Journal of
Photopolymer

Science and Technology
Volume 36 Number 5

2023

JOURNAL OF PHOTOPOLYMER SCIENCE AND TECHNOLOGY
Home Page https://www.spst-photopolymer.org
https://www.jstage.jst.go.jp/browse/photopolymer

Journal of Photopolymer Science and Technology publishes papers on the scientific progress and the technical development of photopolymers.

Editorial Board

Information for Contributors

Submit Manuscripts to the SPST Homepage (Journal --> Submission of Papers --> Editorial Manager). Submission is a representation that the manuscript has not been published previously elsewhere. The manuscript should be accompanied by a statement transferring copyright from the authors (or their employers-whoever holds the copyright) to the Society of Photopolymer Science and Technology. A suitable form for copyright transfer is available from the SPST Homepage. This written transfer of copyright, which previously was assumed to be implicit in the act of submitting a manuscript, is necessary under the Japan copyright law. Further information may be obtained from the "Manual for Manuscript Writing" at the SPST Homepage.

Proofs and All Correspondence: Concerning papers in the process of publication should be addressed to the Editorial Office.

Manuscript Preparation: All the papers submitted are reproduced electronically as they were. For this reason, the manuscripts should be prepared according to the Manual for Manuscript Writings shown at the SPST Homepage.

Subscription Price (Airmail Postage included):
¥12,000 (in Japan), US$ 150.00 (for Foreign)

Subscriptions, renewals, and address changes should be addressed to the Editorial Office. For the address changes, please send both old and new addresses and, if possible, include a mailing label from the wrapper of recent issue. Requests from subscribers for missing journal issues will be honored without charge only if received within six months of the issue's actual date of publication; otherwise, the issue may be purchased at the single-copy price.

Publication Charge (Reprint Order): To support a part of the cost of publication of journal pages, the author's institution is requested to pay a page charge of ¥3,000 per page (with a one-page minimum) and an article charge of ¥12,000 per article. The page charge (if honored) entitles the author to 50 free reprints. For Errata the minimum page charge is ¥3,000, with no articles charge and no free reprints.

The cover designed by M. Tsuda and M. Morishita

JOURNAL

OF

PHOTOPOLYMER SCIENCE

AND

TECHNOLOGY

Volume 36   Number 5

2023

Synthesis of Monomers Having a 2-Hydroxypyridyl Group and Their Application to Photo-adhesive Materials

Masahiro Furutani*, Wataru Usui, and Chiharu Nishibata

Department of Chemistry and Biology, National Institute of Technology,
Fukui College, Geshi-cho, Sabae, Fukui 916-8507, Japan
*furutani@fukui-nct.ac.jp

A novel photo-adhesive material containing 2-hydroxypyridyl groups was prepared with a radical photo-initiator and a methacryl monomer having a 2-hydroxypyridyl group. The methacryl monomer was obtained as a stable colorless liquid. It seemed that 2-hydroxypyridyl group of the methacryl monomer took mainly the ractim-type structure in solution, resulting from its tautomerization reaction. Photo-adhesion was achieved between a glass substrate and another one (glass or dissimilar materials), after 1 J/cm^2 of UV irradiation at a wavelength of 365 nm. Shear stress up to 6.2 MPa was recorded, and thermal dismantlement of the sample was also observed. Furthermore, using residue of the adhesive layer on each substrate, re-adhesion was performed with gentle heating.
Keywords: 2-Hydroxypyridyl group, Photo-adhesive material, Tautomerization reaction, Dissimilar material, Thermal dismantlement

1. Introduction

In industry, photo-adhesion is one of important technologies, because it realizes area-selective adhesion in a short time without heating. Photo-adhesive materials have been studied and developed for application to printing [1], coating [2], and medical materials [3,4]. On the other hand, photo-adhesion for dissimilar materials has also been required for multi-material industrial products. Some photo-adhesive polymers bearing catechol groups were developed [5,6], which were possible to adhere various kinds of substrates by using chemical properties of catechol groups [7].

We have developed photo-adhesive monomers having a 2-mercaptopyridyl (2-MP) group [8] or a 2,2'-dipyridyl disulfide (PySSPy) moiety [9-12], analogues of catechol structure. Photo-adhesive samples fabricated with these monomers showed somewhat strong shear stress with copper substrate, probably due to interaction between copper and sulfur or nitrogen atoms of the monomers. However, the density of 2-MP groups or PySSPy moieties was low (less than 5 mol%) in the adhesive layer, because these monomers were all solid compounds that needed to use with another liquid (meth)acrylate monomers.
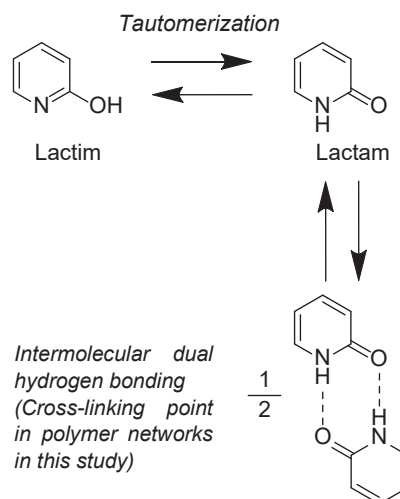
Scheme 1. Tautomerization and intermolecular dual hydrogen bonding of 2-hydroxypyridine (2-HP).

2-Hydroxypyridine is one of *ortho*-position substituted pyridines that equilibrate between enol- and keto-tautomers (Scheme 1) [13,14]. The ratio between two tautomers would be changed by temperature and concentration [15]. It is also known that lactam tautomers form dual hydrogen bonds [16], which is affected by solvents [15]. In this work, 2-hydroxypyridyl (2-HP) groups were introduced into an adhesive layer as key functional

group that mimicked its chemical structure through tautomerization reaction for adaptation toward any adhesive layer-substrate interfaces. Two 2-HP monomers, **1** and **2**, were designed and synthesized, to use in a radical UV curing process (Fig. 1). In the adhesive layer, it was expected that 2-HP groups form cross-linking points through their non-covalent bonding. Thermal dismantlement and subsequent re-adhesion were also examined with gentle heating treatment.

2. Experimental

2-Hydroxynicotinic acid, thionyl chloride, 2-hydroxyethyl acrylate (HEA), 2-hydroxyethyl methacrylate (HEMA), Omnirad651 (2,2-di-methoxy-2-phenylacetophenone, a radical photo-initiator), Omnirad819 (phenylbis(2,4,6-trimethyl-benzoyl)phosphine oxide, a radical photo-initiator), and concentrated nitric acid were purchased from Tokyo Chemical Industry Co., Ltd. (Tokyo, Japan). *N,N*-Dimethylformamide (DMF), triethylamine, and tetrahydrofuran (THF) were purchased from FUJIFILM Wako Pure Chemical Corporation (Osaka, Japan). Magnesium sulfate ($MgSO_4$, anhydrous), methanol (MeOH), chloroform ($CHCl_3$), and acetone were purchased from NACALAI TESQUE, Inc. (Kyoto, Japan). All reagents were used without further purification.

Glass substrate (1 mm thick) was purchased from AS ONE Corporation (Osaka, Japan). Copper (Cu, 0.3 mm thick), stainless (SUS, 0.1 mm thick), and aluminum (Al, 0.3 mm thick) substrates were purchased from HIKARI CO., Ltd. (Osaka, Japan). These substrates were ultra-sonicated with acetone and then $CHCl_3$ for 15 min each. Treated-Cu was prepared according to the literature [17], with immersion Cu substrates into concentrated nitric acid for 30 sec. After washing with distilled water, the substrates were used for photo-adhesion experiments as early as possible. Polypropylene (PP) was purchased from Acrysunday Co., Ltd. (Tokyo, Japan), which was wiped with paper-wastes before photo-adhesion. Calcium fluoride (CaF_2) substrate was purchased from Pier Optics Co., Ltd. (Gunma, Japan) that was wiped with $CHCl_3$-immersed paper-wastes before FT-IR spectral experiments.

^{1}H- and ^{13}C-NMR spectra were recorded using a Bruker AVANCEIII. UV-Vis spectra were recorded using an Agilent Technologies Cary60. FT-IR spectral measurements were performed using a Perkin Elmer Spectrum100. Photo-adhesion experiments were performed with
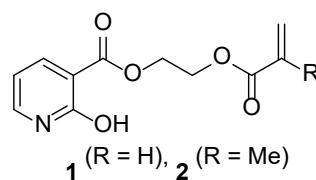
Fig. 1. Chemical structures of adhesive monomer **1** and monomer **2** synthesized in this study.

3UV™-36UVLamp (Analytik Jena AG) and UIT-250/UVD-C365 ultraviolet radiometer (Ushio Inc.). Shear stress was recorded using an MCT-2150 (A&D, Co., Ltd., tensile rate: 10 mm/min).

Synthesis of **1**. Thionyl chloride (2.7 mL, 37.2 mmol) and DMF (1.02 g) were added to 2-hydroxynicotinic acid (503 mg, 3.62 mmol), and the solution was stirred at room temperature for 3 h. Unreacted thionyl chloride was removed by evaporation. HEA (1.72 g, 14.8 mmol) and triethylamine (0.57 g, 5.62 mmol) in THF (20 mL) were then added to the residue, followed by stirring under nitrogen atmosphere at room temperature for 5 days. After evaporating, the residue was dissolved into $CHCl_3$, and washed with brine three times. The organic layer was dried with $MgSO_4$ before silica gel column chromatography ($CHCl_3$, three times), to obtain **1** in a 0.7% yield as a colorless liquid. ^{1}H-NMR (400 MHz, $CDCl_3$): δ 4.59 (4H, m, $-CH_2CH_2-$), 5.88 (1H, m, $=CH_2$), 6.15 (1H, m, $-CH=$), 6.46 (1H, m, $=CH_2$), 7.34 (1H, m, Py-H), 8.18 (1H, m, Py-H), 8.53 (1H, m, Py-H). ^{13}C-NMR (100 MHz, $CDCl_3$): δ 62, 64, 122, 127, 128, 132, 140, 150, 152, 164, 166.

Synthesis of **2**. Thionyl chloride (11 mL, 152 mmol) and DMF (0.34 g) were added to 2-hydroxynicotinic acid (506 mg, 3.64 mmol), and the solution was stirred at room temperature for 3.5 h. Unreacted thionyl chloride was removed by evaporation. HEMA (1.69 g, 13.0 mmol) and triethylamine (0.58 g, 5.69 mmol) in THF (20 mL) were then added to the residue, followed by stirring under nitrogen atmosphere at room temperature for 10 days. After evaporating, the residue was dissolved into $CHCl_3$, and washed with brine three times. The organic layer was dried with $MgSO_4$ before silica gel column chromatography ($CHCl_3$, twice), to obtain **2** in a 33% yield as a colorless liquid. ^{1}H-NMR (400 MHz, $CDCl_3$): δ 1.98 (3H, s, $-CH_3$), 4.59 (4H, m, $-CH_2CH_2-$), 5.64 (1H, m, $=CH_2$), 6.18 (1H, m, $=CH_2$), 7.37 (1H, m, Py-H), 8.19 (1H, m, Py-H), 8.56 (1H, m, Py-H). ^{13}C-NMR (100 MHz, $CDCl_3$): δ 18, 62, 64, 122, 126, 126, 136, 140, 150,

152, 164, 167.

Tautomerization behavior of **2** in solution. CHCl₃ or MeOH solution (0.05 mM each) of **2** was prepared, and was subjected to UV-Vis spectral measurements at room temperature.

Photo-adhesion of dissimilar materials using **2**. Omnirad651 (2 wt%) was added to **2**, and these were dissolved with at least amount of THF. The solution was dropped on a substrate (glass, Cu, treated-Cu, SUS, Al, or PP), and sandwiched with another glass substrate. UV irradiation (2.9 mW/cm^2, 1 J/cm^2) was performed at a wavelength of 365 nm, to prepare photo-adhesive samples. Two or three samples were prepared with each pair of substrates. Adhesion area was 8.5-27 mm^2. A glass-glass adhesive sample was heated on a hot-plate to dismantle the adhesive layer. The dismantled substrates were superposed again, which was subjected to gentle heating and subsequent air cooling. Shear stress was measured with the re-adhesive sample.

Molecular state of **2** in the adhesive layer. A drop of solution prepared for photo-adhesion experiments was sandwiched with two CaF₂ substrates. FT-IR spectra of the sample were recorded before and after UV irradiation (wavelength: 365 nm, 2.8 mW/cm^2, 1 J/cm^2). The sample was then heated to 200°C on a hot-plate, followed by FT-IR spectral measurements during cooling the sample.

3. Results and discussion
3.1. Synthesis of adhesive monomers
After synthesis and repeated purification, monomer **1** was obtained in a very low yield, probably due to side reactions of the acryloyl groups. A THF solution containing HEA, **1** (5 mol% toward HEA), and Omnirad819 was too unstable to stock as photo-adhesive liquid material. On the other hand, by using methacryloyl group instead of the acryloyl group, monomer **2** was obtained in a middle yield as a stable compound. Monomer **2** could stock in a refrigerator at least five months.

Interestingly, both monomers were colorless liquid, implying no intermolecular hydrogen bonding at 2-HP groups. This result encouraged us to use monomer **2** without HEMA in preparation of our photo-adhesive material.

3.2. Tautomerization behavior in solution
As shown in Fig. 2, monomer **2** had a UV-Vis spectral peak around 270 nm in CHCl₃ as well as
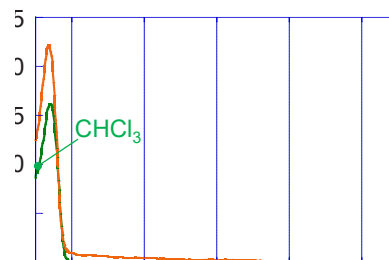
Fig. 2. UV-Vis spectra of monomer **2** in solution (CHCl₃ or MeOH, concentration: 0.05 mM).
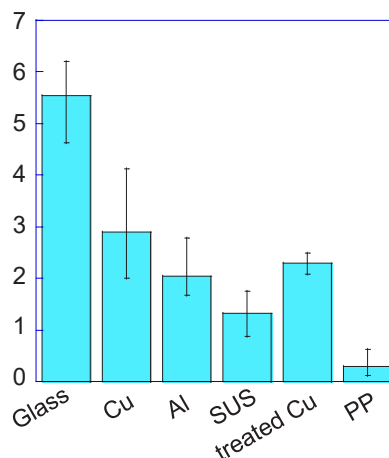
Fig. 3. Results on the shear stress test of photo-adhesive samples fabricated with monomer **2**, Omnirad651, and at least amount of THF. UV irradiation energy was 1 J/cm^2 at a wavelength of 365 nm. Height of each bar is the average value (n = 2 or 3). Upper and lower parts of each error bar are the maximum and minimum values.

MeOH solution. This peak indicated that monomer **2** existed as the lactim tautomer [18]. Chemical shifts of peaks of 2-HP group in the ^{1}H-NMR spectrum were 8.56, 8.19 and 7.37 ppm. The shifts to relative lower magnet field would also support the presence of the lactim tautomer in CDCl₃ solution [8,19]. In the UV-Vis spectrum of MeOH solution, a slight shoulder was also observed around 300 nm, suggesting that a part of monomer **2** would be lactam tautomer.

3.3. Photo-adhesion of dissimilar materials using **2**
Photo-adhesion between glass-glass, (-metals, or -PP) was achieved (Fig. 3). Interfacial failure was observed, basically at the side of metals or PP. The maximum shear stress (6.2 MPa) was recorded with a glass-glass adhesive sample where cohesive failure was observed. Heating another glass-glass adhesive sample, it was dismantled at 108°C. The adhesive residue on each substrate was fused

at 70°C, and 3.0 MPa of shear stress was recorded.

3.4. Molecular state in the adhesive layer

After UV irradiation, a peak at 1638 cm^{-1} was disappeared in FT-IR spectral measurements, indicating consumption of methacryloyl groups in radical polymerization reactions (Fig. 4). On the other hand, before UV irradiation, peaks at 1740 and 1722 cm^{-1} were assigned to 2-hydroxy-nicotinate moiety and methacryloyl group, respectively. A weak peak around 1700 cm^{-1} could be assigned to amide moiety of the lactam tautomer of 2-HP group [20]. FT-IR spectrum of the UV-cured film at 80°C was compared with that at room temperature. The peak of 2-hydroxy-nicotinate moiety seemed to shift slightly to high wavenumber field by heating (data not shown), implying cleavage of an intramolecular hydrogen bond between hydroxy group of lactim tautomer and 2-hydroxynicotinate carbonyl moiety [15].

4. Conclusion

A methacryl monomer having a 2-HP group was obtained as a stable colorless liquid, and used as main component of a photo-adhesive material. To improve adhesive strength and adjust thermal dismantlement conditions, optimization of the composition is under investigation.

Acknowledgement

Fig. 4. FT-IR spectra of a photo-adhesive material containing monomer **2** and Omnirad651, after (upper) and before (lower) 1 J/cm^2 of UV irradiation at a wavelength of 365 nm.

References
1. C. Mendes-Felipe, J. Oliveira, I. Etxebarria, J. L. Vilas-Vilela, and S. Lanceros-Mendez, *Adv. Mater. Technol.*, **4** (2019) 1800618.
2. L. D. Agnol, F. T. G. Dias, H. L. Ornaghi Jr., M. Sangermano, and O. Bianchi, *Prog. Org. Coat.*, **154** (2021) 106156.
3. Y. Hong, F. Zhou, Y. Hua, X. Zhang, C. Ni, D. Pan, Y. Zhang, D. Jiang, L. Yang, Q. Lin, Y. Zou, D. Yu, D. E. Arnot, X. Zou, L. Zhu, S. Zhang, and H. Ouyang, *Nat. Commun.*, **10** (2019) 2060.
4. Y. Ma, J. Yao, Q. Liu, T. Han, J. Zhao, X. Ma, Y. Tong, G. Jin, K. Qu, B. Li, and F. Xu, *Adv. Funct. Mater.*, **30** (2020) 2001820.
5. J. Nishida, M. Kobayashi, and A. Takahara, *ACS Macro Lett.*, **2** (2013) 112.
6. M. Kohri, S. Yamazaki, S. Irie, N. Teramoto, T. Taniguchi, and K. Kishikawa, *ACS Omega*, **3** (2018) 16626.
7. J. Saiz-Poseu, J. Mancedo-Aracil, F. Nador, F. Busqué, and D. Ruiz-Molina, *Angew. Chem. Int. Ed.*, **58** (2019) 696.
8. M. Furutani, D. Fujihira, and K. Arimitsu, *J. Photopolym. Sci. Technol.*, **33** (2020), 261.
9. M. Furutani, K. Endo, and K. Arimitsu, *Mater. Technol.*, **37** (2019) 27.
10. M. Furutani, K. Nakayama, K. Okuma, and K. Arimitsu, *J. Photopolym. Sci. Technol.*, **32** (2019), 619.
11. M. Furutani, K. Nakayama, K. Okuma, and K. Arimitsu, *J. Polym. Res.*, **29** (2022), 245.
12. M. Furutani and R. Senkyo, *J. Photopolym. Sci. Technol.*, **35** (2022), 337.
13. S. Stoyanov, I. Petkov, L. Antonov, and T. Stoyanova, *Can. J. Chem.*, **68** (1990) 1482.
14. M. H. Krackov, C. M. Lee, and H. G. Mautner, *J. Am. Chem. Soc.*, **87** (1965) 892.
15. P. Beak, J. B. Covington, S. G. Smith, J. M. White, and J. M. Zeigler, *J. Org. Chem.*, **45** (1980) 1354.
16. P. Beak, J. B. Covington, and S. C. Smith, *J. Am. Chem. Soc.*, **98** (1976) 8284.
17. "Part twenty two: Wood, adhesives, in Annual book of ASTM standards", ed. By American Society for Testing and Materials, Philadelphia, PA, (1976) 767.
18. P. Beak, F. S. Fry Jr., J. Lee, and F. Steele, *J. Am. Chem. Soc.*, **98** (1976) 171.
19. D. W. Aksnes and H. Kryvi, *Acta Chem. Scand.*, **26** (1972) 2255.
20. R. M. Silverstein, G. C. Bassler, and T. C. Morrill, "Spectrometric identification of organic compounds, fifth ed.", John Wiley & Sons, Inc., New York (1991) p12.

Communication

Resist Removal Using Laser Irradiation Combined with Ozone Water Treatment

Ryohei Yasukuni[1*], Atsushi Koizumi[1], Masashi Mizutani[2], Tomoya Nakao[1], Masashi Yoshimura[3], Hideo Horibe[2], and Tomosumi Kamimura[1]

[1]Department of Electronics and Information Systems Engineering, Osaka Institute of Technology, 5-16-1 Ohmiya, Asahi-ku, Osaka, 535-8585, Japan
[2]Department of Applied Chemistry and Bioengineering, Graduate School of Engineering, Osaka Metropolitan University, 3-3-138 Sugimoto, Sumiyoshi, Osaka, 558-8585, Japan
[3]ILE, Osaka University, 2-6 Yamadaoka, Suita, Osaka 565-0871, Japan
*ryohei.yasukuni@oit.ac.jp

Laser induced resist stripping technique in water is interesting for both fast and environment-friendly resist removal. However, small pieces of the deposited resist still remain or reattach on the silicon (Si) wafer after laser irradiation. In order to eliminate the remaining resist on the Si wafer surface in environment-friendly way, the effects of ozone water and ozone microbubble water treatments were investigated. The laser induced resist stripping area was effectively expanded by 1.27 times in 600 sec by the immersion treatment in ozone water. Furthermore, combination of ozone microbubbles and flowing water treatment enhanced the resist removal rate by about 20% each. These results demonstrated that the synergy of the laser induced effect, the ozone microbubble and flowing water treatment has a great potential for fast and environment-friendly resist removal technique.

Keywords: Resist removal, Laser induced resist stripping, Ozone treatment, Ozone microbubble treatment

1. Introduction

The growing market in the semiconductor industry requires new processing technologies in order to achieve more efficient production lines, and higher yields. At the same time, reducing the environmental impact of the manufacturing process is one of the key issues for a sustainable society [1, 2].

There are several steps in the semiconductor manufacturing: resist coating, exposure, development, etching, ion implantation, and resist removal. Regarding the last step, the conventional wet process causes high environmental impact because it uses large amount of chemicals such as sulfuric acid, hydrogen peroxide, and amine solvents. Oxygen plasma ashing is increasingly being used as a safe and environment-friendly method although the removal rate is relatively slower than the wet processes [3].

We have proposed a pulsed laser irradiation technique as an alternative to the above conventional resist removal methods [4, 5]. In this laser induced resist stripping, a ns laser pulse was sent to a resist material deposited on a silicon (Si) wafer. The laser pulse energy absorbed by the Si wafer causes a rapid temperature rise. As a result, the thermoelastic compressive stress increases within the short pulse duration due to the difference in thermal expansion coefficient. Consequently, the coated resist material is stripped from the Si wafer at the laser irradiated area.

We have also reported that the laser induced resist stripping is easier and more convenient in water than in normal atmosphere conditions for the following reasons.

First, the laser induced damage threshold of the Si wafer is higher in water than in normal atmosphere conditions, and the risk of the laser

induced damage on the Si surface is lower [6].

Second, a finite element analysis and time-resolved imaging of the laser induced resist stripping phenomena in water showed that higher compressive stress was generated in water, which improved the resist stripping efficiency [7-9].

To date, large areas of diazonaphthoquinone (DNQ) /novolak resists and poly(4-vinylphenol) (PVP) coated on Si wafers have been successfully stripped by scanning laser pulses in water. In addition, novolak resists implanted with ions such as boron, phosphorus and arsenic, which are generally more difficult to remove from the Si wafer, could also be stripped without laser induced surface damage [10-12].

As described above, the laser induced resist stripping technique is of interest for both fast and environment-friendly resist removal. One problem with this technique is that small pieces of the deposited resist still remain or reattach on the Si wafer after laser irradiation. Therefore, further cleaning processes, which is also environment-friendly, is required.

For this purpose, ozone water treatment would be a possible choice. Ozone produces reactive oxygen species (ROS): peroxides, superoxide, hydroxyl radical, and singlet oxygen, which oxidize organic molecules and clean a surface. Of these ROS, the hydroxyl radical has the strongest oxidation power, capable of breaking even a carbon-carbon single bond. It has also been reported that ozone microbubbles stimulate the production of hydroxyl radicals due to a reaction between ozone and hydroxide ions at an interface of the shrinking microbubbles. In fact, ozone microbubble water has been shown to remove high dose ion implanted photoresist. Therefore, ozone water and ozone microbubble treatments are expected to effectively clean the remaining resist on the Si wafer [13].

In this work, we investigated the effects of the ozone water and ozone microbubble water treatments on the remaining resist after laser induced resist stripping toward an efficient resist removal technique.

2. Experimental

Positive-tone DNQ / novolak resist of OFPR-800LB (Tokyo Ohka Kogyo Co., Ltd.) was used as the resist material. The Si wafer was first treated with hexamethyldisiloxane (HMDS) to have a hydrophobic surface by spin-coating (10 s at 500 rpm then 20 s at 2000 rpm) and prebake at 100℃

for 1 min. Subsequently, OFPR- 800LB was spin-coated on the HMDS treated Si wafer (for 5 s at 300 rpm then 20 s at 2500 rpm). As shown in Fig. 1, the prepared resist coated Si wafer was immersed in a container filled with water, and placed on a precision stage. The surface profile and thickness of the coated resist was measured with a stylus surface profilometer (Dektak 6M, Bruker). The resist stripping was performed using a pulsed Nd:YAG laser (Surelite, Amplitude) with a wavelength of 532 nm and a pulse duration of 8 ns. The output laser pulse with Gaussian beam pattern was focused through a lens (f = 300 mm) and the beam diameter was 220 μm at the sample position located 320 mm from the lens.
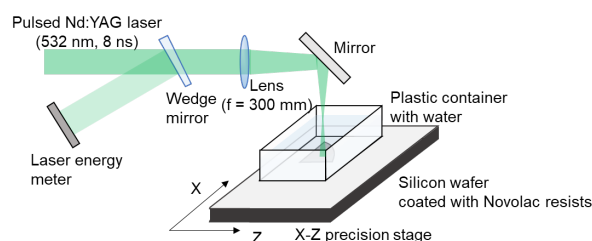
Fig. 1. A schematic illustration of the laser irradiating system for the resist stripping.

The laser induced resist stripping was performed using a "1-on-1" method, where the laser spot was moved with each shot. The laser pulse energy was adjusted with an attenuator consisting of a polarizer and a half-wave plate. A part of laser pulse was led to a laser energy meter with a wedge mirror to monitor fluctuations in pulse energy. The minimum laser pulse energies that can strip the novolak resist from the Si wafer in water and that can cause damage to the Si surface in water have previously been estimated to be 0.18 and 0.52 J/cm^2 respectively. In this experiment, we used 0.4 J/cm^2 for the resist stripping to obtain a better efficiency for stripping without surface damage. The resist stripping area after the laser irradiation was confirmed with a digital microscope (VHX-950F, KEYENCE).

Ozone water was produced by a pressurized dissolution system shown in Fig. 2. Ozone gas was generated from oxygen (5.0 L/min)/nitrogen (0.5 L/min) gas by an ozone generator and dissolved in water through a dissolution tank at a pressure of about 0.5 MPa. Ozone water in a reservoir was circulated by a bellows cylinder pump (ΣP-15D-V, Sigma Technology Inc.) at a flow rate of 2.1 L/min to maintain the ozone concertation at 36 mg/L which was monitored by an UV absorption measurement with an ozone sensor (EBARA

JITSUGYO CO., LTD.). The temperature of the ozone water was maintained at 12°C. The ozone microbubble was generated by a decompression nozzle (ShigenKK). The size distribution of generated microbubble has been reported elsewhere [13]. Briefly, the bubble size shows two peaks: a sharp peak around 15 μm in diameter and a broader peak around 40 μm. The resist coated Si wafers were exposed to the ozone water or ozone microbubble water in two different ways: immersion treatment and flowing water treatment as shown in Fig. 3.
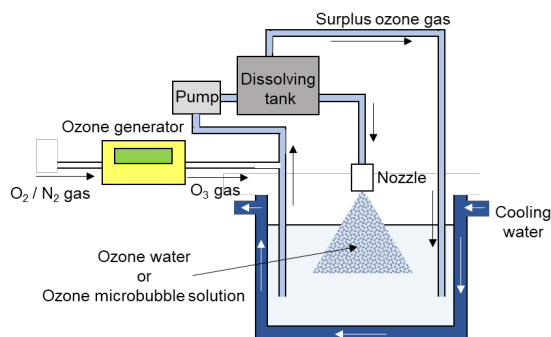
Fig. 2. A schematic illustration of the ozone water and ozone microbubble water production system. The nozzle was used for ozone microbubble production only.
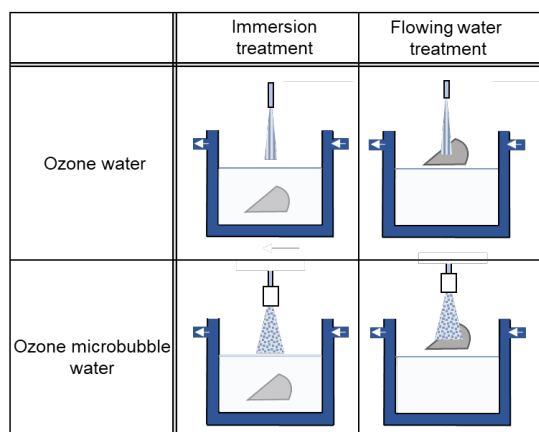
Fig. 3. Schematic diagrams of four types of post laser treatments.

3. Results and discussion

The effects of the ozone water on the resist removal were first verified by immersion and flowing water treatments using resist coated bulk Si wafer without laser irradiations. The resist coated Si wafer before the treatments is shown in Fig. 4(a). The stylus profilometer measurement showed that the resist film thickness was about 1.1 μm and was homogeneous throughout the Si wafer.

After the immersion treatment in ozone water, resist removal from the edge of the Si wafer was confirmed (Fig.4(b)). On the other hand, when the flowing water treatment was applied, the resist removal was occurred also from the center where the ozone water hit on the Si wafer (Fig.4(c)).
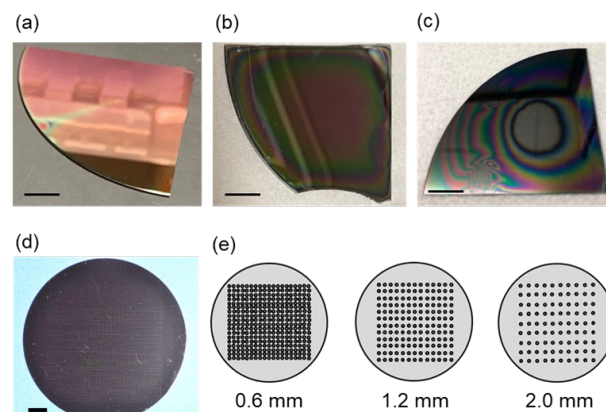
Fig. 4. Photographs of the Si wafer coated with novolak resist (a) without any treatment, (b) 10 min after immersion treatment in ozone water, and (c) 5 min after flowing water treatment with ozone water. (d) Photographs of the resist film on the Si wafer after laser induced resist stripping. (e) The schematic images of three sample prepared with a laser irradiation at 0.6, 1.2 and 2.0 mm intervals. Scale bars indicate 1 cm for all images.

The effects of ozone water and ozone microbubble treatments after the laser induced resist stripping were then investigated. The resist removal efficiency was compared between the resist film stripped by irradiating laser pulses at 0.6, 1.2 and 2.0 mm intervals as illustrated in Fig. 4d, e. However, there were no clear differences for the total removal time under these conditions. Therefore, we observed each resist stripping spot under the microscope to confirm effects of the ozone treatments.

Figure 5 shows representative images of the resist stripping areas before and after the ozone water and ozone microbubble water treatments. The grayish white areas in the images where Si surface appear are regarded as the resist stripped areas.

In the immersion case, the resist stripped areas were enlarged with both ozone water and ozone microbubble water. The flowing water treatment results show an increase in the resist stripped areas with both ozone water and ozone microbubble water as in the immersion treatment. The resist stripped areas were fitted with a circle and the

diameter was used as the area size.

The time evolution of the resist stripped areas during the ozone water and ozone microbubble water treatments are displayed in Fig. 6. The immersion treatments for 600 s expanded the resist stripped areas by 1.27 times with the ozone water, and 1.42 times with the ozone microbubble water. The flowing water treatments for 180 s have a better efficiency than the immersion cases and the magnifications were by 1.43 and 1.57 times after the ozone water and ozone microbubble water respectively.
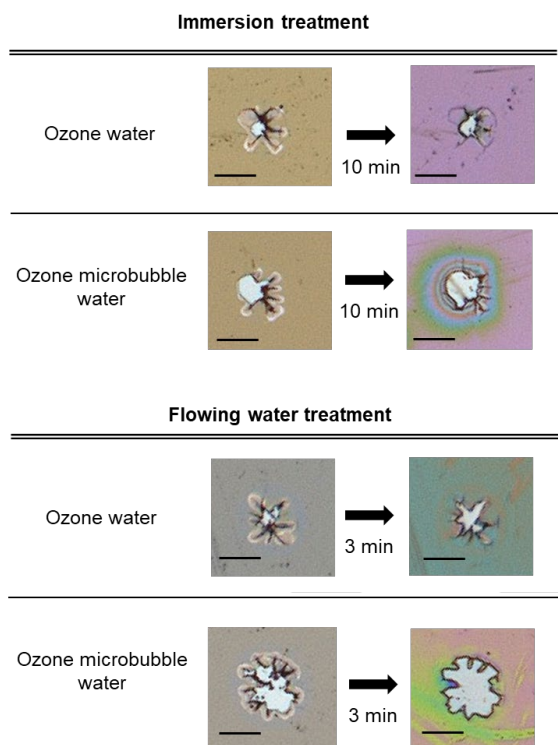
Fig. 5. Representative transmission images of the resist stripping area before and after immersion and flowing water treatments with ozone water and ozone microbubble water. Scale bars indicate 100 μm for all images.

It should be noted that we did not observe any effects when oxygen water or oxygen microbubble water was used for the resist removal. These control experiments indicate that ozone and ozone microbubbles play a key role in resist removal, but not the oxygen and physical effects of the microbubble. The final magnifications of each condition are summarized in Fig. 6(c).

In all cases, the degree of expansion of the resist stripped area is much larger than the resist thickness of 1.1 μm, indicating different removal rates in the in-plane and thickness directions.
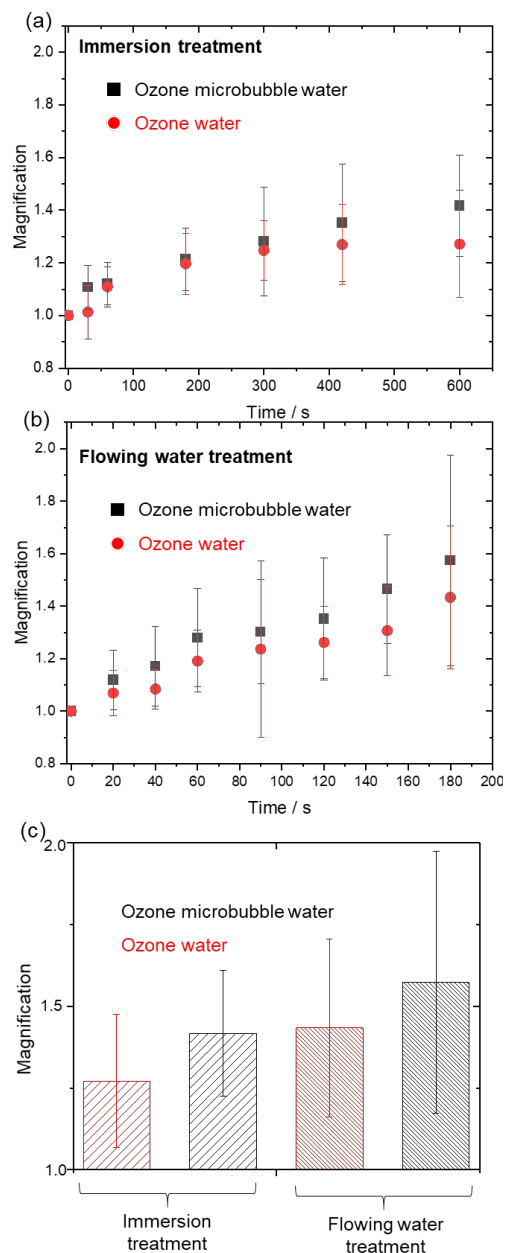
Fig. 6. Temporal variation of the magnification of the resist stripped areas during ozone water and ozone microbubble water treatments. (a) average of 10 spots under the immersion treatment. (b) average of 20 spots under the flowing water treatment. The error bars indicate standard deviation. (c) The comparison of maximum magnifications in (a) and (b).

One reason for this anisotropic removal may be as follows. In Fig. 5, white lines can be seen surrounding the resist stripped area before all treatments. The shape of these lines has a certain correspondence with the resist stripped area after the treatments. When a resist film was ablated by a laser pulse, only the center of the laser irradiated area was removed. At the same time, the periphery

of the removed area would also be cracked or detached from the surface by thermoelastic stress generation. Such cracks or detachments could be considered to be quickly eliminated.

Another possible hypothesis could be a residual stress in the resist. As is mentioned in Fig. 4(b), the faster resist removal was also observed at the edge of the bulk Si wafer. It is known that thin films bonded to a substrate have in-plane residual stresses [14]. Due to the residual stresses, film delamination is initiated along the film edge. Therefore, once the resist film is delaminated from the edge of the Si wafer or the resist stripped area, ROS will penetrate between the resist and the Si wafer, which might accelerate the resist removal.

Regarding the better efficiency of the flowing water treatment compared to the immersion treatment, it would be explained that the removed resist layer was continuously rinsed by the flowing ozone water and the resist surface was always exposed to fresh ozone water.

Finally, the removal of the resist is more effective with the microbubbles. In general, the lifetime of hydroxyl radical is quite short, so the microbubbles should collapse near the resist surface. As we can see a clear effect of the microbubbles, it is assumed that sufficient amount of hydroxyl radical has reached to the resist surface for both immersion and flowing water treatments.

4. Conclusion

In order to develop an efficient and environment-friendly resist removal technique, we investigated the effects of the ozone water and ozone microbubble water treatments on the remaining resist after laser induced resist stripping.

The laser induced resist stripping area was effectively expanded by the ozone water immersion treatment probably due to the resist cracking and detachment by laser irradiation and/or the residual stress in the resist film. Using ozone microbubbles and flowing water treatment each enhanced the resist removal rate by about 10%. The flowing ozone microbubble water treatment showed the maximum improvement of 20% compared to the ozone water immersion treatment.

These results demonstrated that the synergy of the laser induced effect, the ozone microbubble and the flowing water treatment has a great potential for fast and environment-friendly resist removal technique. However, at the present stage, the improvement is limited around the laser irradiated area. In order to put this laser induced resist stripping technique into practical applications, further optimization of the system, such as laser irradiation intervals and ozone treatments condition, is required.

References

1. J. M. Havard, N. Vladimirov, J. M. Frechet, S. Yamada, C.G. Wilson, and J. D. Byers, *Macromolecules,* **32** (1999) 86.
2. J. Y. Park, J. M. Yun, and J. B. Kim, *J. Polym. Sci. Part A*, **46** (2008) 7534.
3. B. Thedjoisworo, D. Cheung, and V. Crist, *J. Vac. Sci. Technol. B,* **31** (2013) 021206
4. H. Horibe, M. Fujita, I. Nishiyama, and A. Yoshikado, *J. Appl. Phys.*, **44** (2005) 8673.
5. H. Horibe, T. Kamimura, T. Hata, M. Yamamoto, I. Yamato, O. Nigo, M. Fujita, A. Yoshikado, and K. Yoshida, *Polym. J.*, **37** (2005) 813.
6. T. Kamimura, K. Nuno, Y. Kuroki, T. Yamashiro, S. Tsujimoto, R. Nakamura, S. Takagi, T. Nishiyama, and H. Horibe, *J. Photopolym. Sci. Technol.*, **29** (2016) 633.
7. T. Kamimura, H. Kuramae, T. Yamashiro, K. Nuno, Y. Umeda, S. Tsujimoto, R. Nakamura, T. Nishiyama, and H. Horibe, *J. Photopolym. Sci. Technol.*, **30** (2017) 291.
8. T. Kamimura, Y. Umeda, H. Kuramae, K. Nuno, R. Nakamura, and H. Horibe, *J. Photopolym. Sci. Technol.*, **31** (2018) 4
9. T. Kamimura, H. Muraoka, Y. Matsura, and H. Horibe, *J. Photopolym. Sci. Technol.*, **25** (2012) 741.
10. T. Kamimura, Y. Kuroki, T. Kiriyama, H. Muraoka, T. Nishiyama, Y. Harada, H. Kuramae, and H. Horibe, *J. Photopolym. Sci. Technol.*, **27** (2014) 237.
11. T. Kamimura, Y. Kuroki, T. Murakami, K. Nuno, M. Akimoto, Y. Harada, T. Nishiyama, and H. Horibe, *J. Photopolym. Sci. Technol.*, **28** (2015) 307.
12. T. Kamimura, N. Nishioka, Y. Umeda, D. Shima, Y. Funamoto, Y. Harada, M. Yoshimura, R. Nakamura, and H. Horibe, *J. Photopolym. Sci. Technol.*, **32** (2019) 603.
13. M. Takahashi, H. Ishikawa, T. Asano, and H. Horibe, *J. Phys. Chem. C,* **116** (2012) 12578.
14. H. H. Yu, M. Y. He, and J. W. Hutchinson, Acta Mater. **49** (2001) 93.

Surface Nanopatterning of Bioabsorbable Materials Using Thermal Imprinting Technology

Mano Ando[1], Rio Yamagishi[1], Sayaka Miura[1], Yuna Hachikubo[1],
Tsugumi Murashita[1], Naoto Sugino[2], Takao Kameda[2],
Yoshiyuki Yokoyama[3], Yuki Kawano[3], Kaori Yasuda[1], and Satoshi Takei[1*]

[1] *Department of Pharmaceutical Engineering,*
Toyama Prefectural University, Imizu, Toyama 939-0398, Japan
[2] *Futuristic Technology Department, Sanko Gosei, Nanto, Toyama 939-1852, Japan*
[3] *Toyama Industrial Technology Research and Development Center,*
Takaoka, Toyama 933-0981, Japan
*takeis@pu-toyama.ac.jp

Our research aimed to develop a bioabsorbable material, a mixed compound of polyglycolic acid and polylactic acid, by surface nanopatterning using thermal imprinting technology and utilize it for life science and medical applications. Bioabsorbable materials such as polyglycolic acid and polylactic acid are one of the most difficult materials to surface nanofabricate in terms of melting point and flowability. Therefore, gas generated during processing was allowed to permeate through a porous cyclodextrin-based gas-permeable mold, and surface nanopatterning with a projection height of 1−2 μm and a pitch of 1.24 μm was successfully performed. Surface nanopatterning at a thermal imprint firing temperature of 50°C is expected to enhance the surface modification of bioabsorbable materials, which may be used in a wide range of applications.
Keywords: Bioabsorbable materials, Bioabsorbable thermal nanoimprint material, Surface nanopatterning, Gas-permeable mold, Thermal nanoimprint lithography

1. Introduction

Significant recent advances in biodegradable materials have increased their demand worldwide [1-4]. Currently, biodegradable materials are attracting attention from two perspectives: bioabsorbable materials, which are "materials that can be degraded and absorbed *in vivo*," and biodegradable materials, which are "materials that can be degraded by the action of microbes, such as bacteria and fungi." This research focuses on bioabsorbable materials.

Bioabsorbable materials are important in the medical field and are increasingly in demand in pharmaceuticals and tissue engineering products [5-7]. They include natural biopolymers, such as proteins and polysaccharides, and synthetic polymers, such as polyglycolic acid, polylactic acid, and polycaprolactone. Among these, polyglycolic acid, polylactic acid, and polycaprolactone are typical polymers of bioabsorbable materials [8,9].

These materials are hydrolyzed to nontoxic compounds either *in vivo* by hydrolysis of the ester main chain and excretion by the kidney as urine or *ex vivo* as water and carbon dioxide. Thus, bioabsorbable materials have excellent biocompatibility owing to *in vivo* hydrolysis and hence have been applied in absorbable sutures for medical use [10,11], surgical implant materials [12-15], and drug delivery systems [16-21].

However, surface-processing of bioabsorbable materials with high-resolution nanopatterns, such as nanoimprint lithography and hot embossing, is difficult. For example, polyglycolic acid is highly crystalline and hard, has significantly inferior physical properties in terms of impact resistance, and has insufficient dissolution stability, making it prone to gas formation during dissolution processing [22, 23]. Polylactic acid has weak heat resistance (melting point ~170°C), has poor flowability, and
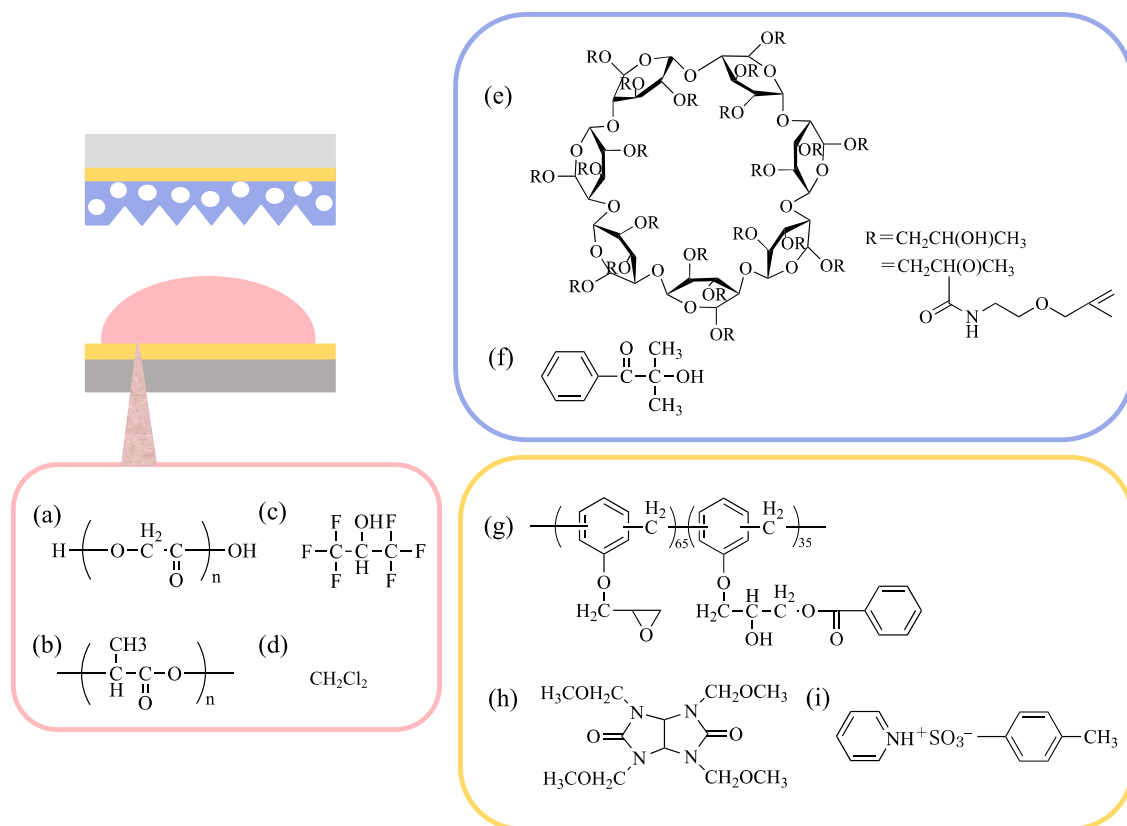
Fig. 1. (a)~(d) The composition of the bioabsorbable thermal nanoimprint material. (e) and (f) depict the composition of the porous cyclodextrin-based mold material. (g)~(i) depict the composition of the novolac adhesive primer employed.

poor mold release properties [24-26]. Likewise, polycaprolactone has a low melting point of about 60°C, which limits its applicability [27]. Due to these reasons, nanopattern processing of bioabsorbable materials with nanopatterns, is difficult.

The objective of this research was to develop a bioabsorbable material for applications such as anti-adhesive films, surgical sutures, antibacterial films, and water-repellent tapes by surface nanopatterning process using thermal imprinting technology. We attempted to improve molding defects by utilizing gas-permeable molds consisting of porous cyclodextrins with an average pore size ~0.7 nm to allow the permeation of gases generated during molding and Holy Land absorbent thermal nanoimprinting material, a mixed compound of polyglycolic acid and polylactic acid. Additionally, we developed a surface nanopatterning process with a pitch of 1.24 μm and a height of 1.9 μm by nanoimprint lithography.

2. Experimental

2.1. Mixing bioabsorbable thermal nanoimprint materials

Figures 1 (a)~(d) depict the composition of the bioabsorbable thermal nanoimprint material used in this study. (a) 45 wt% polyglycolic acid (Merck), (b) 5 wt% polylactic acid (Merck), (c) 42 wt% 1,1,1,3,3,3-hexafluoro-2-propanol (Tokyo Kasei) as a volatile solvent to increase their fluidity, and (d) 8 wt% dichloromethane (Tokyo Kasei) were mixed.

2.2. Synthesis of porous cyclodextrin-based mold material

Figures 1 (e) and (f) depict the composition of the porous cyclodextrin-based mold material [28-30] synthesized in this research. (e) 35% (w/w) of 2-hydroxypropyl-β-cyclodextrin (Cyclochem), (f) 35% (w/w) of 2-methacryloyloxyalkyl isocyanate (Showa Denko), and methyl ethyl ketone were mixed. Triethylamine (Tokyo Kasei) was added to the mixture at a concentration of 5 wt%. The solution was stirred at 60 °C for 6 h in a multi-nitrogen environment for a water-inhibition chemical reaction. Since the solution was very low in concentration, it was thickened using a rotary evaporator and collected through two extraction and drying procedures to obtain the β-cyclodextrin derivative. The β-cyclodextrin derivative was blended with additives, including 2-hydroxy-2-methyl-1-phenyl-

Fig. 2.   Schematic showing the thermal nanoimprint lithography process

1-propanone as a UV polymerization initiator, and radical polymerized to obtain porous cyclodextrin-based mold material.

2.3. Generation of novolac adhesive underlayment

Figures 1 (g)~(i) depict the composition of the novolac adhesive primer employed in this study. The primer consists of (g) novolac resin with hydroxyl and epoxy groups, (h) tetrakis (methoxymethyl) glycolyl, (i) pyridinium p-toluene sulfonate as a thermal initiator, and other additives. Epoxy novolac re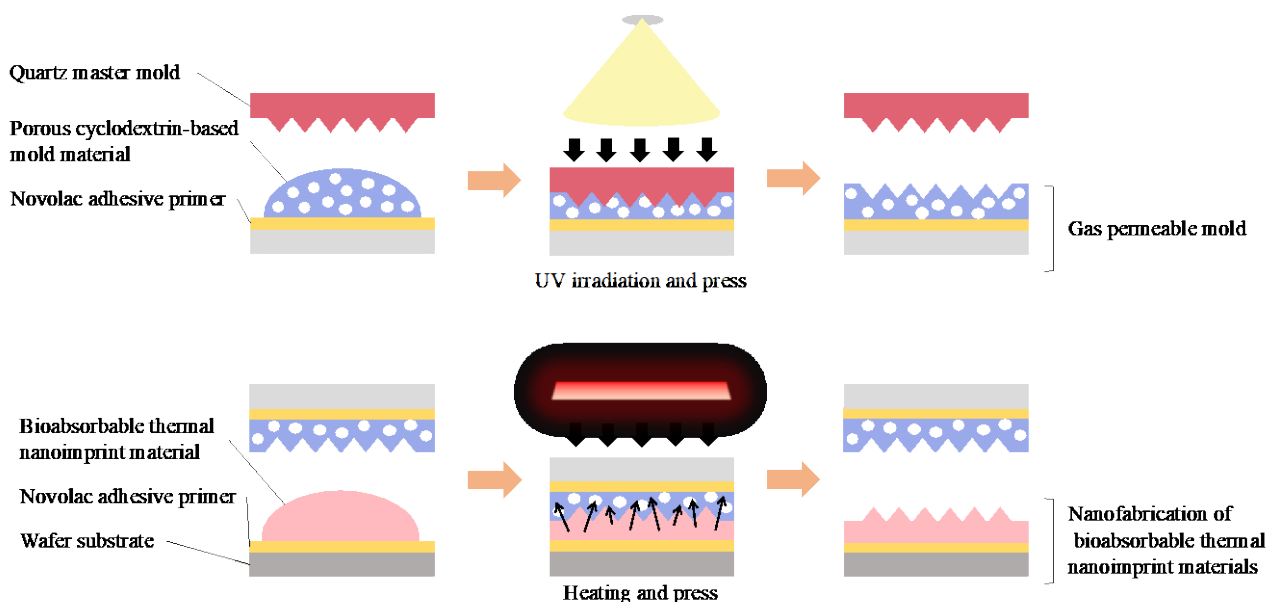sin (DOW D.E.N.) and benzoic acid (Tokyo Kasei) were made to react at 98°C for 12 h to initiate addition chemical reaction using benzyltriethylammonium chloride as a catalyst to produce a novolac resin with hydroxyl and epoxy groups [31]. Additionally, by adding tetrakis (methoxymethyl) glycolyl, the hydroxyl groups in the resulting novolac resin were cross-linked with aminoplast.

2.4 Thermal nanoimprint lithography process

Figures 2 depict the double nanoimprint lithography process consisting of the following steps: i) the fabrication of a porous cyclodextrin gas-permeable mold using a quartz master mold with a dense pattern of needles of 1.24 µm pitch and 1.9 µm height and ii) the transfer of this quartz master mold onto a bioabsorbable material.

The quartz master molds were drawn using an electron beam lithography system (CABL-8000TPU, Crestec) with water-developable resist material. First, the surface of the quartz master mold having a size

of 10 mm^2 per side was hydrophilically treated for 5 min using an ozone generator (LTOZ-180, Litho Tech Japan). The mold was then treated with a fluorinated self-assembled monolayer (DS-831TH, DURASUE) for a minute, dried for another minute, and then coated with a mold release film. Next, the surface-treated quartz master mold was rinsed with DS-TH (DURASURF, Harbeth) for a minute and then dried for another minute. Finally, a step and flash imprint lithography system (Molecular Imprint IMPRIO) was used to fabricate the surface patterning structures on the porous cyclodextrin-based gas-permeable molds. Experimental conditions were as follows: patterning size of 10 mm^2 per side on a master quartz mold, total solution volume of 0.5 ml, pre-exposure delay time of 90 s, exposure time of 120 s, imprint force of 100 N, and wafer size of 150 mm. Using the quartz master mold, a gas-permeable mold with a 1.24 µm pitch and 1.9 µm height was fabricated.

Next, vacuum thermal imprint lithography was performed using an imprint test machine (Litho Tech Japan LTNIP). As described in Section 2.1, 1,1,1,3,3,3-hexafluoro-2-propanol (as a volatile solvent to enhance flowability) was mixed with 42 wt% of 1,1,1,3,3,3-hexafluoro-2-propanol and 8 wt% of dichloromethane. Then, the bioabsorbable thermal nanoimprint material, a mixture of polyglycolic acid and polylactic acid containing 8 wt% dichloromethane, was mixed. The solution was brought in contact with a porous cyclodextrin-based gas-permeable mold for 90 s at room temperature

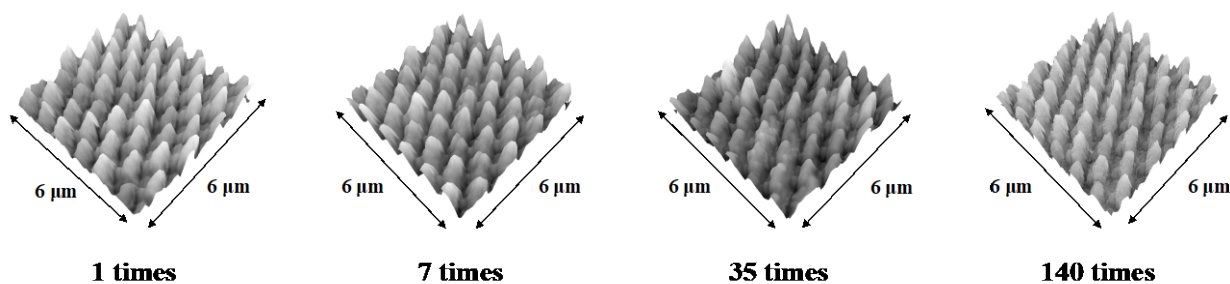**1 times**　　　**7 times**　　　**35 times**　　　**140 times**

Fig. 3.　SPM images of the bioabsorbable thermal nanoimprint material obtained using gas-permeable mold

and imprinted with a force of 500 N. The heat was transferred by vacuum at 50°C for 15 min to remove volatile solvents from the bioabsorbable thermal nanoimprint material. Finally, we demolded the material using the gas-permeable mold to obtain surface-patterned polyglycolic acid and polylactic acid structures, which were repeated 140 times, and the results of imprinting the material 1, 7, 35, and 140 times were observed with a scanning probe microscope (SPM; SPM-9700, Shimazu Corporation).

2.5. Young's modulus measurement

Young's modulus measurements were performed on TiO_2–SiO_2 gas-permeable mold, SiO_2 mold, cellulose mold, cyclodextrin mold, quartz, polymethyl methacrylate, and polyethylene using a dynamic ultra-micro hardness tester (DUH-211, SHIMAZU) [32].

2.6. Oxygen permeability measurement

Oxygen permeability measurements were performed on TiO_2–SiO_2 gas-permeable mold, cyclodextrin gas-permeable mold, quartz, polymethyl methacrylate, and polyethylene using a differential pressure gas permeability measuring system (GTR-11, GTR Tec) at a sample thickness of approximately 100 μm and a temperature of 40°C.

2.7. Light transmittance measurement

A spectrometer (V-650, JASCO) was used to measure the light transmittance before patterning of cyclodextrin gas-permeable molds with a sample thickness of 10 μm. Wavelengths were measured from 250 to 900 nm.

3. Results
3.1. Measurements of thermal nanoimprint lithography using gas-permeable molds

Figures 3 shows thermal SPM images of the bioabsorbable material after nanoimprint lithography using gas-permeable molds performed several times. The results of imprinting the material 1, 7, 35, and 140 times are shown. For a gas-permeable mold with a 1.24 μm pitch and 1.9 μm height structure, the heights obtained were 1.86 ± 0.34 μm, 1.87 ± 0.35 μm, 1.70 ± 0.45 μm, and 1.59 ± 0.42 μm, respectively. These results show that there was no significant difference in the surface nanopatterning process for the materials imprinted different number of times. As compared to the material imprinted once, the material imprinted 140 times had lower height; however, as this difference was in the micrometer range, it was concluded that the surface nanopatterning process was accomplished. Consequently, the bioabsorbable thermal nanoimprint material was proven to be capable of surface nanopatterning.

3.2. Measurements of thermal nanoimprint lithography using nongas permeable quartz molds

As explained in Section 2.4, in thermal nanoimprint lithography using a nongas permeable quartz mold, a mixture of polyglycolic acid and polylactic acid containing 42 wt% 1,1,1,3,3,3-hexafluoro-2-propanol and 8 wt% dichloromethane as the volatile solvent was used. Figure 4 shows SPM images of molding defects in the bioabsorbable thermal nanoimprint material, a mixture of polyglycolic acid and polylactic acid containing 42 wt% 1,1,1,3,3,3-hexafluoro-2-propanol and 8 wt% dichloromethane, with a height of 0.82 ± 0.27 μm for a gas-permeable mold with a 1.24 μm pitch structure. The volatile solvents added to maintain flowability have a small molecular weight, which causes gas formation when heated, resulting in molding defects. In other words, in contrast to Section 3.1, it has been demonstrated that gas-permeable molds can permeate the gases generated during molding.

3.3. Young's modulus measurement results

The results of Young's modulus measurements for
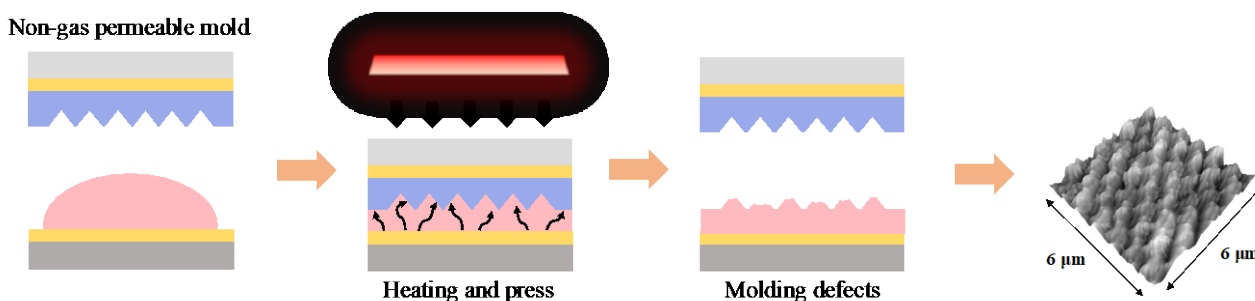
Fig. 4. SPM image of molding failure of the bioabsorbable thermal nanoimprint material using nongas permeable quartz mold

cyclodextrin mold, quartz, TiO_2–SiO_2 gas-permeable mold, SiO_2 mold, polyethylene, cellulose mold and polymethyl methacrylate were 2.8, 72, 0.97, 0.32, 0.27, 1.6, and 2.7 GPa, respectively, as shown in Figure 5. Young's modulus for the cyclodextrin mold was almost equal to that for polymethyl methacrylate, which has excellent processability, formability, and weather resistance. For future large scale microfabrication of bioabsorbable materials, cyclodextrin molds will be easy materials to handle when modifying mold size and shape.
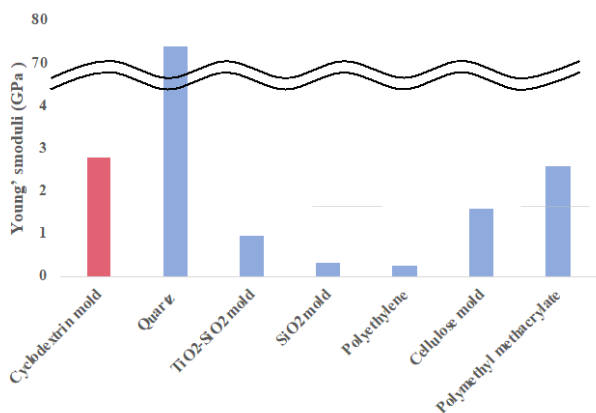
Fig. 5. Young's modulus measurements

3.4. Oxygen gas transmission measurement results
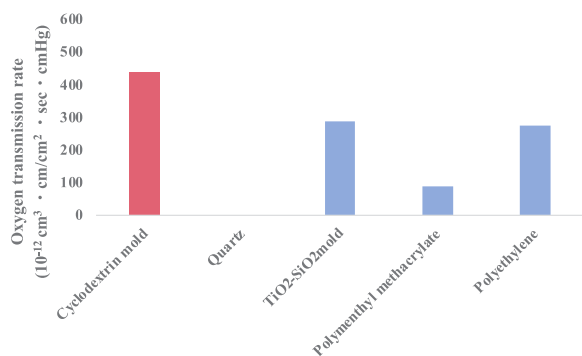
Fig. 6. Oxygen permeability measurement results

The results of oxygen permeability measurements for the cyclodextrin gas-permeable mold, quartz, TiO_2–SiO_2 gas-permeable mold, polymethyl methacrylate, and polyethylene are shown in Figure 6. Quartz is used in conventional mold, however, is found to be impermeable by gases. The cyclodextrin gas-permeable mold had a gas permeability advantage over polyethylene, a general-purpose plastic with high-performance gas permeability, and had the highest gas permeability among the molds studied.

3.5. Results of light transmission measurement

The results of light transmittance measurement for cyclodextrin gas-transparent mold before the patterning at wavelengths 250–900 nm are shown in Figure 7. The cyclodextrin gas-transmitting molds exhibited high light transmittance of over 98% for wavel engths 300–900 nm. This indicates that the cyclodextrin gas-permeable molds are also applicable for optical nanoimprint lithography, and there is a prospect for surface nanopatterning of bioabsorbable materials by optical nanoimprint lithography.
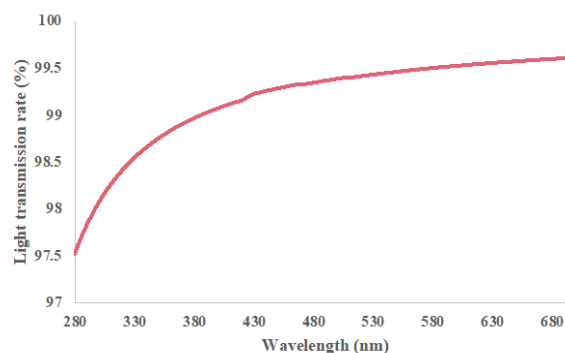
Fig. 7. Results of light transmittance measurements

4. Conclusion

Utilizing the cyclodextrin gas-permeable mold, we have succeeded in surface nanopatterning of bioabsorbable materials, which are mixtures of

polyglycolic and polylactic acids containing 1,1,1,3,3,3-hexafluoro-2-propanol and dichloromethane as volatile solvents. This research found that surface nanopatterning can further improve the properties of bioabsorbable materials, not only polyglycolic acid and polylactic acid, and may contribute to life science and medical applications. Furthermore, it was elaborated that value addition to any material is possible by utilizing the nanoimprint lithography method using cyclodextrin gas-permeable molds.

Acknowledgement

References

1. M. R. Havstad, *Plast. Waste Recycl.*, (2020) 97.
2. E. S. Hosseini, S. Dervin, P. Ganguly, and R. Dahiya, *ACS Appl. Bio Mater.*, **4** (2020) 163.
3. J. Baranwal, B. Barse, A. Fais, G. L. Delogu, and. A. Kumar, *Polymers*, **14** (2022) 983.
4. C. I. A. La Fuente, B. C. Maniglia, and C. C. Tadini, *Packag. Technol. Sci.*, **36** (2023) 81.
5. A. Prasad, *Mater. Today: Proc.*, **44** (2021) 2447.
6. S. W. On, SW. Cho, S. H. Byun, and B. E. Yang, *Biomedicines*, **8** (2020) 300.
7. N. Reshma and O. Dudko, *The Scientific Heritage*, **62** (2021) 13.
8. E. L. Boland, C. J. Shine, N. Kelly, C. A. Sweeney, and P. E. McHugh, *Ann. Biomed. Eng.*, **44** (2016) 341.
9. Y. H. An, S. K. Woolf, and R. J. Friedman, *Biomaterials*, **21** (2000) 2635.
10. J. M. Seitz, M. Durisin, J. Goldman, and J. W. Drelich, *Adv. Healthcare Mater.*, **4** (2015) 1915.
11. D. Das, N. Mulchandani, A. Kumar, and V. Katiyar, *Advances in Sustainable Polymer*, (2020) 121.
12. C. Li, H. Lv, Y. Du, W. Zhu, W. Yang, X. Wang, J. Wang, and W. Chen, *Regener. Ther.*, **19** (2022) 9.
13. S. D. Rousselle, Y. Ramot, A. Nyska, and N. D. Jackson, *Toxicol. Pathol.*, **47** (2019) 358.
14. L. Pisecky, M. Luger, A. Klasan, T. Gotterbarm, M. C. Klotz, and R. Hochgatterer, *EFORT Open Rev*, **6** (2021) 1132.
15. L. Figueiredo, R. Fonseca, L. F. Pinto, F. C. Ferreira, A. Almeida, and A. Rodrigues, *J. Mech. Behav. Biomed. Mater.*, **103** (2020) 103572.
16. S. K. Prajapati, A. Jain, and S. Jain, *Eur. Polym. J.*, ***120*** (2019) 109191.
17. P. Jana, M. Shyam, S. Singh, V. Jayaprakash, and. A. Dev, *Eur. Polym. J.*, **142** (2021) 110155.
18. K. Aoki, and N. Saito, *Pharmaceutics*, **12** (2020). 95.
19. Y. K. Sung and S. W. Kim, *Biomater. Res.*, **24.** (2020) 1.
20. H. Idrees, S. Z. J. Zaidi, A. Sabir, R. U. Khan, X. Zhang, and S. U. Hassan, *Nanomaterials*, **10** (2020) 1970.
21. Y. Su, B. Zhang, R. Sun, W. Liu, Q. Zhu, X. Zhang, R. Wang and C. Chen, *Drug delivery*, **28** (2021) 1397.
22. D. Niu, P. Xu, J. Li, W. Yang, T. Liu, and P. Ma, Strong, *Polymer*, **264** (2023) 125532.
23. D. Y. Niu, P. W. Xu, S. J. Xu, J. X. Li, W. J. Yang, and P. M. Ma, *Chin. J. Polym. Sci.*, **1** (2022).
24. R. Yang, H. Cao, P. Zhang, L. Chen, G. Zou, X. Zhang, and J. Li, *ACS Appl. Polym. Mater.*, **3** (2020) 299.
25. X. Zhao, J. Liu, J. Li, X. Liang, W. Zhou, and S. Peng, *Int. J. Biol. Macromol.*, (2022).
26. H. Zheng, Z. Sun, and H. Zhang. *J. Thermoplast. Compos. Mater.*, **33** (2020) 1383.
27. N. Zheng, H. Y. Liu, J. Gao, Y. M. Mai, *Composites, Part B*, **171** (2019) 320.
28. S. Takei and M. Hanabata, *AIP Advances*, **7** (2017) 035110.
29. S. Takei, and M. Hanabata, *Applied Physics Letters*, **107** (2015) 141904.
30. S. Takei, S. Nakajima, and M. Hanabata, *Microelectronic Engineering*, **190** (2018) 68.
31. S. Takei, T. Ogawa, R. Deschner and C.G. Willson, *Microelectronic engineering*, **116** (2014) 44.
32. R. Yamagishi, S. Miura, K. Yasuda, N. Sugino, T. Kameda, Y. Kawano, Y. Yokoyama, and S. Takei, *Applied Physics Express*, **15** (2022) 046502.

Photoactive Compounds Effects on Removal Rate for Polystyrene-type Polymers by H_2/O_2 Mixture Activated by Hot Tungsten Wire

Masashi Yamamoto[1*], Koki Akita[1], Tomohiro Maniwa[1], Machi Asakawa[1], Tomokazu Shikama[1], Shiro Nagaoka[2], Hironobu Umemoto[3], and Hideo Horibe[4]

[1] *National Institute of Technology, Kagawa College, Department of Electrical and Computer Engineering, 335 Chokushi-cho, Takamatsu, Kagawa 761-8058, Japan*
[2] *Osaka Prefecture University, Department of Physics and Electronics, 1-1 Gakuen-cho, Naka-ku, Sakai, Osaka 599-8531, Japan*
[3] *Shizuoka University, Johoku, Naka, Hamamatsu, Shizuoka 432-8561, Japan*
[4] *Osaka City University, Department of Physics and Electronics, 3-3-138 Sugimoto-cho, Sumiyoshi-ku, Osaka 558-8585, Japan*
*m-yamamoto@t.kagawa-nct.ac.jp

We earlier reported that the removal rate of positive-tone novolac photoresist was enhanced compared to that of a pure hydrogen system when a H_2/O_2 gas mixture is activated by a hot tungsten filament. However, when the added oxygen amount was increased to more than 1.0%, the removal rate decreased considerably. We specifically examined cross-linking between novolac resin and photoactive compound (PAC), which are the main photoresist components, as one cause of this decrease in the removal rate. For examination in this study, the "PAC-mediated cross-linking model" was proposed to identify the cross-linking site on novolac resin. To investigate functional group interaction with PAC, we examined the removability of polystyrene-based polymers with various PAC contents. For poly(vinyl phenol), which has an OH group at the terminal end on side chain, a markedly decreased removal rate was confirmed with increased added oxygen when the PAC content was 18.7 wt%. This decrease was never observed in others. For the commercial positive-tone novolac photoresist, the decreased removal rate under excessive oxygen addition might be ascribed to cross-linking, which can be formed by mediating PACs near OH groups on the main chain of novolac resin.
Keywords: Crosslinking, H_2/O_2 mixture, Photoactive compound (PAC), Polystyrene-type polymer, Radical, Removal

1. Introduction

The environmental burdens and costs caused by harmful chemicals used for photoresist removal processes during conventional semiconductor manufacturing are regarded as important shortcomings. To overcome these difficulties, we have studied an "environmentally friendly" photoresist removal method using radicals generated by activating H_2/O_2 mixed gas on a hot filament surface [1–4]. This method allows oxidizing O radicals and OH radicals to coexist in a reducing H radical atmosphere [5–7]. The high reactivity of OH radicals is well known [8, 9]. We

have reported a positive-tone novolac photoresist with a removal rate that is enhanced by an optimum added oxygen amount: its oxygen gas flow rate to hydrogen gas flow rate is 0.5–1.0% [1]. When the oxygen added amount is increased beyond 1.0%, the removal rate decreases considerably with increasing substrate temperature.

Generally speaking, the removal rate is synonymous with the rate of decomposition reactions. Fundamentally, according to the Arrhenius equation, it must increase concomitantly with increasing substrate temperature. When a hot tungsten filament is used as a catalyst, the H radical

production decreases along with increased added oxygen because the oxygen is a catalytic poison [5]. The removal rate is directly proportional to hydrogen radical production [10]. Nevertheless, this marked decrease is not explainable solely by the decreased production. Clarifying the factors causing the removal rate decrease is important to improve the rate further.

In our recent study, we used activated H_2/O_2 mixed gas to examine the removal rate of pseudo-photoresists, which comprise novolac resin with various contents of photoactive compound (PAC) [4]. Results show that the decrease in the removal rate which occurred for a given excess added oxygen amount varied with the PAC content. According to work by Hanabata et al., diazonaphthoquinone (DNQ) on PACs is generally placed to cap the functional groups in the novolac resin because of dissolution inhibition of the aqueous base developer [11–13]. The chemical structure of novolac resin is characterized by its benzene rings and functional groups such as H, OH, and CH_3. To investigate the functional group interaction with PAC, we examined the removability of polystyrene-based polymers: polystyrene (PS), poly(vinyl phenol) (PVP), and poly(4-methylstyrene) (4-PMS). For this study, we suggest the "PAC-mediated cross-linking model" to elucidate the cross-linking site on novolac resin and to discuss causes of the decrease in the removal rate of positive-tone novolac photoresists.

2. Experimental

2.1 Preparation of PS-based polymers

As PS-based polymers, PS (M_W = 35,000; Sigma-Aldrich Corp. LLC), PVP (M_W = 89,000–98,000; Sigma-Aldrich Corp. LLC), and 4-PMS (average $M_W \approx$ 72,000; Sigma-Aldrich Corp. LLC) were used. Solids (polymer and PAC) were dissolved in liquid (propylene glycol methyl ether acetate (PGMEA), guaranteed reagent grade; Kanto Chemical Co. Inc.) at a ratio of 78 wt% (liquid) / 22 wt% (solid) [14]. The PAC used was naphthoquinone diazo esterified with 2, 3, 4, 4'-tetrahydroxybenzophenone. The esterification ratio of PAC is 75%. Generally speaking, the amount of PAC in positive-tone novolac photoresists is about 20% of the solid content. The PAC contents were, respectively, 0, 9.4, and 18.7 wt% of solids in the pseudo-photoresist.

These polymer solutions were spin-coated onto a Si wafer using a spin coater (K-359 S-1; Kyowa Riken Co., Ltd.) at 2.6×10^3 rpm for 20 s and were prebaked in an oven (CLO-2AH; Koyo Thermo Systems) at 100 °C for 60 s. The initial photoresist film thickness was 1.2 μm, as measured using a

surface texture measuring instrument (Surfcom 480A; Tokyo Seimitsu Co. Ltd.).

2.2 Removal rate examination

The apparatus and the procedure used for experimentation were similar to those described elsewhere [1–4]. The H_2 gas (≥99.99%; Takamatsu Teisan) flow rate was fixed at 100 sccm using a mass flow controller. (SEC-400MK2; STEC Inc.). The O_2 gas (≥99.5%; Iwatani Ind. Gases Corp.) flow rate was varied between 0 and 1.5 sccm using another mass flow controller (SEC-400MK3; STEC Inc.): i.e., the amount of added oxygen (flow rate ratio of O_2 to H_2) was varied between 0 and 1.5%. The typical total pressure under processing was 2.7 kPa, as measured using a vacuum gauge (Baratron 622A12TAE; MKS Instruments Inc.). A resistively heated coiled tungsten filament (99.9%, 0.5 mm diameter; The Nilaco Corp.) was used for radical production. The total filament length was 0.36 m. The number of turns in the coiled section was 12 times, with 28 mm length and 8 mm diameter. The substrate–filament distance was set to 20 mm. A DC current source (EX-750L2; Takasago Ltd.) was used to heat the filaments. The filament temperature, set to 1600 °C, was measured through a quartz window using a two-wavelength (0.80 and 1.05 μm) infrared radiation thermometer.

Changes in film thickness were evaluated using thin film interference of the photoresist [1–4]. By thin film interference, the peaks and valleys of the reflected light intensity were observed alternately during changes in film thickness. The film thicknesses are calculable from the reflected light intensity. Green laser light from an optical source (520 nm, 150 mW, Civil Laser; Naku Technology Co. Ltd.) entered the center of the stage at an incident angle against the substrate surface of 76°. A Si photodiode (S1787-04; Hamamatsu Photonics KK) in reverse bias was used as a photodetector to measure the intensity of light reflected from the substrate. Its cathode was connected to +5 V DC through a 60 kΩ resistor. The reflected light intensity was ascertained by correcting the voltage across the resistor.

We heated the substrate using a substrate stage heater to evaluate the removal rate dependence on the substrate surface temperature. A sheath thermocouple (TKφ1.6 × L300; AS One Corp.) was used to measure the surface temperature. The thermocouple was placed on the substrate surface at 20 mm distance from the stage center. The temperature and film thickness were measured

simultaneously at 0.2 s intervals. The temperature was averaged every 2 s. The removal rate was calculated from the average decrease in film thickness during 2 s.

3. Results and Discussion

Figure 1 portrays the relation between the removal rate and the substrate surface temperature for each pure polymer. For either polymer, the removal rate with oxygen was slightly higher than without oxygen. In the case without PAC, the removal rates never decreased, even if the substrate temperature was increased, under added oxygen amounts up to 1.5 sccm. A hump found for the PVP removal rate at 150–210°C is discussed later.

Figure 2 shows the relation between the removal rate and the substrate surface temperature for polymers with PAC 9.4 wt%. For PS and 4-PMS, the removal rate with oxygen was slightly higher than that without oxygen, as shown also for Figs. 1(a) and 1(b). However, the removal rates of PVP increased at temperatures higher 250°C when adding oxygen. This substrate temperature dependence of the removal rate differed from that shown in Fig. 1(c). Even with PAC 9.4 wt%, despite some minor differences, the removal rates never decreased even with increased substrate temperature, as shown also in Fig. 1.

Figure 3 presents the relation between the removal rate and the substrate surface temperature for polymers with PAC 18.7 wt%. For PS and 4-PMS, the removal rate with oxygen was slightly higher than that without oxygen, exhibiting similar results to those shown in Figs. 1(a) and 1(b) and Figs. 2(a) and 2(b). However, for PVP, a clear decrease in the removal rate was apparent at temperatures higher than 220°C when the added oxygen amount was 1.5 sccm (Fig. 3(c)). This decrease is a similar phenomenon to that reported from our recent study [4].

Next we discuss the removability of polymers with various PAC contents with respect to the added oxygen amount. In consideration of the results depicted in Fig. 3(c), we specifically examined the removal rate achieved when the substrate temperature was 275 °C. Figure 4 shows the relation between the removal rate and the added oxygen amount for polymers with and without PAC. To compare polymers easily, these removal rates were normalized by the removal rate achieved under a pure hydrogen system. Namely, the removal rates without oxygen addition for each polymer were normalized to become 1. In the case without PAC, as presented in Fig. 4(a), the removal rate of either polymer increased even if the substrate temperature

was increased. From Fig. 4(a), exhibiting the case of only the polymer, the removal rate for either polymer was almost constant even if the added oxygen amount was increased. This tendency resembles that in the case in which only novolac resin was used [4]. When the PAC content was 9.4
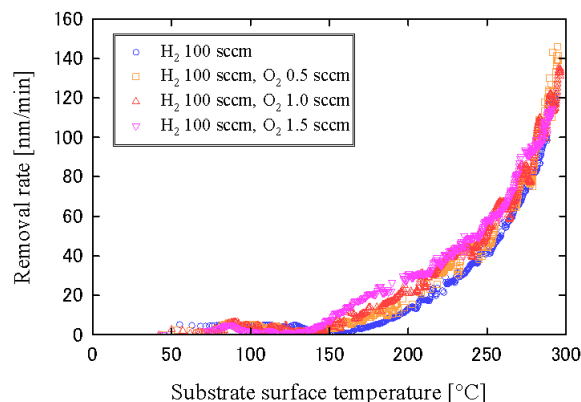
(a) PS (PAC 0 wt%)
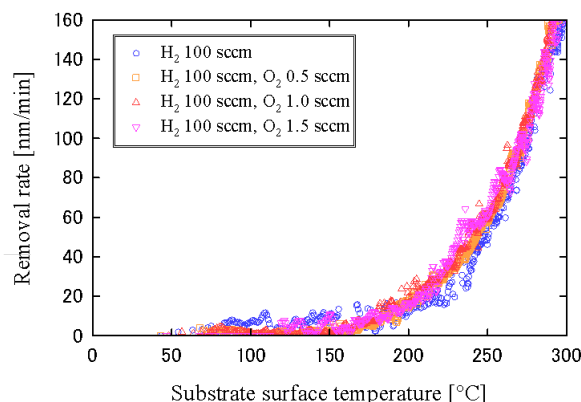
(b) 4-PMS (PAC 0 wt%)
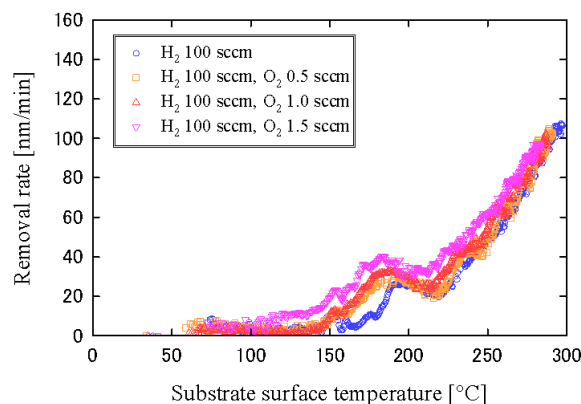
(c) PVP (PAC 0 wt%)

Fig. 1. Removal rate relation to the substrate surface temperature for each pure polymer.

wt%, a difference in removal rates between polymers was found for the added oxygen amount of 0.5 sccm. The removal rate was in the order of 4-PMS > PVP > PS. When the added oxygen amount was other than 0.5 sccm, the removal rate was similar to that of polymer alone. When the PAC

content was 18.7 wt% (Fig. 4(c)), the difference of the removal rates between polymers was greater than that with PAC 9.4 wt%. The dependence of the removal rate for PS was similar to the dependences presented in Figs. 4(a) and 4(b). This removal rate was independent of the added oxygen amount. The

(a) PS with PAC 9.4 wt%

(b) 4-PMS with PAC 9.4 wt%

(c) PVP with PAC 9.4 wt%
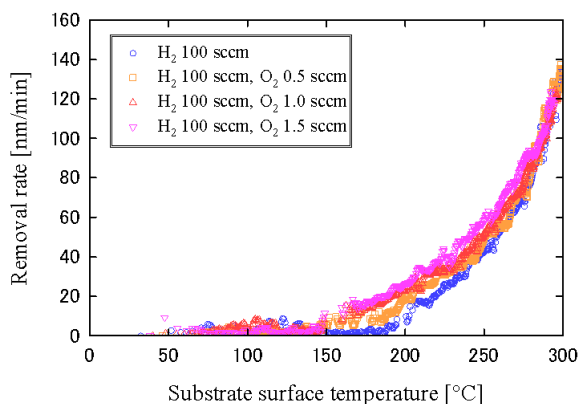
Fig. 2. Removal rate relation to the substrate surface temperature for polymers with PAC 9.4 wt%.
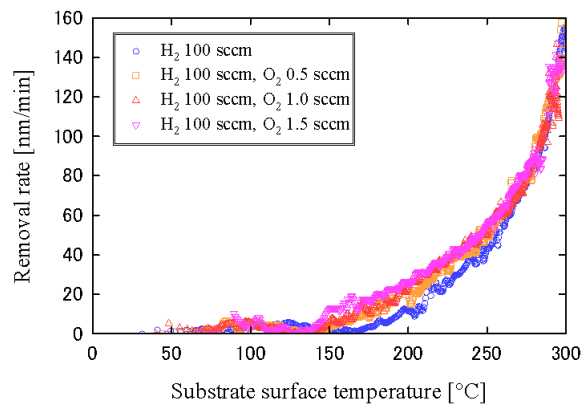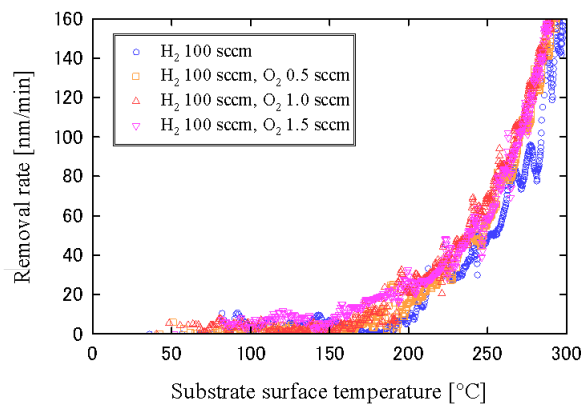
(a) PS with PAC 18.7 wt%

(b) 4-PMS with PAC 18.7 wt%

(c) PVP with PAC 18.7 wt%

Fig. 3. Removal rate relation to the substrate surface temperature for polymers with PAC 18.7 wt%.

removal rate for 4-PMS was 20–60% higher than that found for a pure hydrogen system when the added oxygen amount was greater than 0.5 sccm.
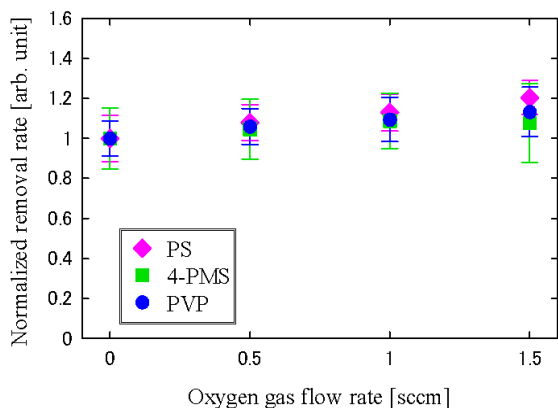
(a) PAC 0 wt%
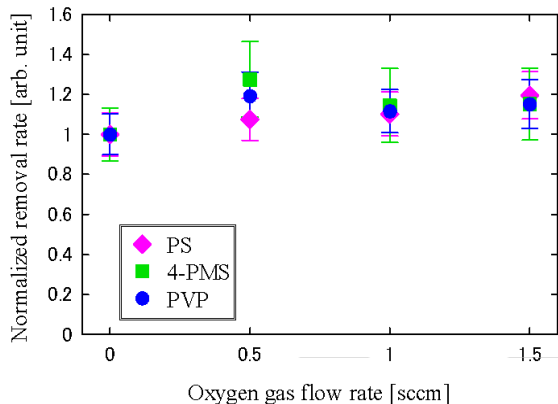
(b) PAC 9.4 wit%
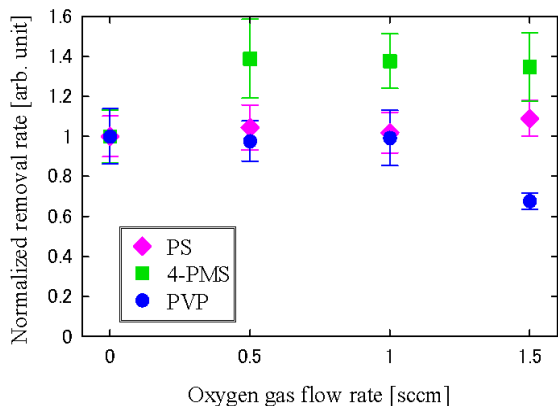
(c) PAC 18.7 wt%

Fig. 4. Relation between the normalized removal rate and the oxygen additive amount. The substrate temperature is 275 °C. Each removal rate was normalized by the removal rate for a pure hydrogen system.

The removal rate for PVP was almost constant at amounts up to 1.0 sccm, but it decreased considerably at 1.5 sccm.

PS-based polymers are categorized as vinyl polymers with a benzene ring in their side chain. They have a slightly different chemical structure at the end of the side chain. The respective terminal groups of PS, 4-PMS, and PVP are H, CH_3, and OH. These polymers are categorized as main chain cross-linking polymers because hydrogen in their α-position is desorbed and neighboring polymers cross-link there by external inputs such as electrons and heat [15]. The removal rate was found to be independent of the terminal group of side chain in the case without PAC, as portrayed in Fig. 4(a). The function of main chain cross-linking can be dominant. The PS removal rate was found to be independent of the PAC content and the added oxygen amount. This independence must be ascribed to benzene ring resonance stabilization.

In the case of 4-PMS with PAC 18.7 wt%, the removal rate with added oxygen of more than 0.5 sccm was increased by 20–40% compared to that without oxygen addition. This removal rate improvement was not observed when PAC was not contained. Actually, according to one earlier report [13], 4-PMS can also be classified as a side-chain scission polymer because its CH_3 group can be the benzene ring decay site. Hanabata *et al*. reported that DNQ, when placed near OH groups on the novolac resin, causes inhibition dissolution in a general novolac photoresist [11–13]. Actually, PAC might be positioned near the CH_3 group, as are OH groups. Free space between molecular chains with PACs can increase beyond that without PACs. The CH_3 groups can be attacked more easily by reactive species. In oxygen-added systems, OH radicals, which are highly reactive [8, 9], are produced together with H and O radicals. Not only are O radicals less abundant; they are also less reactive than H radicals. Their contribution to the removal processes must be minor [1, 16]. The CH_3 group attacked by the active species becomes $CH_2{}^*$; it can play a role as a decay site for benzene rings on side chains. Reactions with H radicals are classifiable as H abstraction reactions and H addition reactions, but H addition reactions are generally the major type because it is an energetically favorable reaction [17–19]. The H-radical density decreases along with increased added oxygen amounts when using a hot tungsten catalyst [5]. The abstraction reaction of hydrogen by OH radicals must induce an increase in the removal rate. Therefore, the removal rate of 4-PMS can be enhanced beyond those of PS and PVP.

By contrast, in the case of PVP with PAC 18.7

wt%, the removal rate was constant when the added oxygen amount was less than 1.0 sccm. The removal rate was considerably lower, by approximately 30%, when the added oxygen amount was 1.5 sccm. This decrease in the removal rate was never observed in PVP with PAC 0 wt% or 9.4 wt%. For PVP, PAC must be positioned near the OH group, as is true for the general novolac photoresist [11–13]. Free space between molecular chains might increase; consequently, the OH groups can be attacked more easily by reactive species, as in CH_3 groups in 4-PMS. Then, OH or H, or both, can desorb from the terminal end of phenol structure on a side chain in PVP by thermal stimulation, H abstraction reactions by OH radicals, and H addition reactions by H radicals, and so on. Then, dangling bonds, i.e., phenoxy radicals and phenyl radicals, are produced on the side chain. The hump at 150–210°C presented in Figs. 1(c), 2(c), and 3(c) might be ascribed to shrinking of the film thickness by desorbing and light cross-linking. These radicalized sites might also form a cross-linkage structure by mediating PAC. When the amount of added oxygen is slight, H radicals must be provided sufficiently on the polymer surface. The dangling bonds, if produced, might be terminated by H radicals before cross-linking. Consequently, the cross-linking is preventable. Moreover, the decrease in the removal rate is minor even if the temperature is raised, as presented in Fig. 2(c). However, the addition of an excessive amount of O_2 decreases H-radical production considerably. In such a case, not only the cross-linking via side chains (thermal cross-linking) but also cross-linking through PACs must proceed because the H termination of their dangling bonds can be suppressed. Accordingly, the removal rate can be inferred to decrease at high temperatures, as presented in Fig. 3(c).

For a commercial positive-tone novolac photoresist, we have demonstrated that the photoresist removal rate increased with added oxygen up to 0.5–1.0 sccm; it then decreased gradually beyond that amount [1]. Introduction of excessive oxygen, i.e., of more than 1.5 sccm, decreases H radical production by the catalytic poisoning effect of O atoms on the catalyst surface [5]. To date, we have inferred that this removal rate decrease is attributable to a decrease in H radical production because the removal rate increases in direct proportion to H radical production [10]. However, because this decrease was remarkable in the high substrate temperature range, explaining it solely by the hydrogen radical decrease is difficult.

In this experiment environment, the photoresist removal rate generally changes according to the Arrhenius equation with respect to the surface temperature [10, 20]. The removal rate decrease in the high temperature range is different behavior from that implied by the Arrhenius equation. In fact, the removal reaction is a competition reaction, comprising reactions of decomposition by radicals, but also thermal cross-linking and PAC-mediated cross-linking. The resin, even if independent, is hardened thermally. Higher temperatures promote its cross-linking [21, 22].

We have reported the removal rates of pseudo-photoresists containing various amounts of PAC using a tungsten-filament-activated H_2/O_2 gas mixture [4]. The removal rate of novolac resin never decreases, even when the added oxygen amount increases to 1.5 sccm and the substrate temperature increases to a high temperature. The removal rate decreases at temperatures higher than 250 °C when oxygen is added up to 2.0 sccm. We confirmed that cross-linkage, by which the π-conjugated system increases, proceeds from UV spectra of these pure resin substrates. For PAC 18.7 wt%, the removal rate decreased at higher temperatures when the added oxygen amount was 1.5 sccm, as shown in Fig. 3(c)). The UV spectra induced by π-conjugated system are never observed. To build diazo coupling with the novolac resin, PAC must be positioned near the OH group in this pseudo-novolac photoresist, as one must do also for the general novolac photoresist [11–13]. Free space between molecular chains might increase compared to a material with no PAC content. The OH groups can be attacked more easily by reactive species, as can OH groups in PVP. Moreover, OH or H, or both, can desorb from the novolac resin. In a novolac resin with PAC 18.7 wt% (pseudo-photoresist), a cross-linkage in which the π-conjugated system remains unchanged can be formed by mediating PACs near these desorbed sites.

Based on the results obtained from this study, we can discuss commercial photoresist removability when adding oxygen. Strictly speaking, the three-dimensional arrangement of the chemical structure must be considered, but here we simplify that point. We specifically examined three characteristics of the novolac resin chemical structure: (1) the benzene ring, (2) CH_3 group on the benzene ring, and (3) OH groups on the benzene ring. For this study, PS, 4-PMS, and PVP are useful to discuss differences of removal rates with oxygen addition from the viewpoint of interaction between functional groups and PACs. As portrayed in Fig. 4, the removal rate without PACs depends little on the added oxygen amount for either group. The CH_3 groups with PACs enhance the removal rate as a decay site for a benzene ring on a side chain. The

OH groups with PACs cause a decline in the removal rate as a cross-linkage site between polymer chains. Consequently, the photoresist removal rate might increase with the added oxygen amount up to 1.0 sccm by the interaction of CH_3 and PACs; the rate might then decrease gradually because of OH and PAC interaction. Commercial photoresists are not simple binary mixing systems similar to novolac resin and PAC because various trace additives are blended. For this reason, the pseudo-photoresist cannot be treated strictly as equivalent to a commercial photoresist. However, there must be some measure of correlation between them. For commercial photoresists, a decrease in the removal rate at high substrate temperatures with excessive oxygen addition might be ascribed to PAC-mediated cross-linking.

4. Conclusion

This study examined removal rates of PS-based polymers with various contents of photoactive compound (PAC) using activated H_2/O_2 mixed gas. Based on the findings, we discuss the causes of decreased removal rates for a novolac photoresist. The results of this study are presented below.

(a) The PS removal rate was independent not only of the PAC content but also of the added oxygen amount. Even with excessive oxygen addition of 1.5 sccm, the removal rate never decreased.

(b) The 4-PMS removal rate without PAC was independent of the added oxygen amount. When the PAC content was 18.7 wt%, the removal rate with oxygen addition of more than 0.5 sccm increased to 20–40% more than that without added oxygen. This increase was more prominent than that with PAC 9.4 wt%.

(c) The PVP removal rate was found to be dependent on the PAC content and on the added oxygen amount. When the PAC content was 18.7 wt%, the removal rate was constant for added oxygen amounts of less than 1.0 sccm. However, the removal rate decreased considerably by approximately 30% when the added oxygen amount was 1.5 sccm. This decrease was never observed for PVP with PAC 9.4 wt% or without PAC.

For a commercial positive-tone novolac photoresist, the decrease in the removal rate found at high substrate temperatures under excessive oxygen addition might be ascribed to cross-linking, which can be formed by mediating PACs near OH groups on the main chain of novolac resin.

References

1. M. Yamamoto, H. Umemoto, K. Ohdaira, T. Shikama, T. Nishiyama, and H. Horibe, *Jpn. J. Appl. Phys.,* **55** (2016) 076503/1-5.
2. M. Yamamoto, T. Taki, T. Sunada, T. Shikama, S. Nagaoka, H. Umemoto, and H. Horibe, *J. Photopolym. Sci. Technol.,* **31** (2018) 419.
3. M. Yamamoto, T. Shiroi, T. Shikama, S. Nagaoka, H. Umemoto, and H. Horibe, *J. Photopolym. Sci. Technol.,* **32** (2019) 609.
4. K. Akita, S. Sogo, R. Sogame, M. Yamamoto, S. Nagaoka, H. Umemoto, and H. Horibe, *J. Photopolym. Sci. Technol.,* **34** (2021) 499.
5. H. Umemoto and M. Moridera, *J. Appl. Phys.,* **103** (2008) 034905.
6. H. Umemoto, H. Kusanagi, K. Nishimura, and M. Ushijima, *Thin Solid Films*, **517** (2009) 3446.
7. H. Umemoto and H. Kusanagi, *Open Chem. Phys. J.,* **2** (2009) 32.
8. H. Sugimitsu, "Ozone no Kiso to Oyo (Basis and Application of Ozone)", Korin, Tokyo, (1996) 20 (in Japanese).
9. S. Fujimura, K. Shinagawa, M. T. Suzuki, and M. Nakamura, *J. Vac. Sci. Technol. B*, **9** (1991) 357.
10. M. Yamamoto, T. Maruoka, A. Kono, H. Horibe, and H. Umemoto, *Appl. Phys. Express*, **3** (2010) 026501.
11. M. Hanabata, Y. Uetani and A. Furuta, *J. Vac. Sci. Technol. B*, **7** (1989) 640.
12. M. Hanabata, F. Oi and A. Furuta, *Proc. SPIE.,* **1466** (1991) 132.
13. A. Furuta and M. Hanabata, *J. Photopolym. Sci. Technol.,* **2** (1989) 383.
14. M. Yamamoto, R. Kitai, Y. Horibe, A. Sekiguchi, and H. Tanaka, *J. Photopolym. Sci. Technol.,* **22** (2009) 357.
15. A. A. Miller, E. J. Lawton and J. S. Balwit, *J. Polym. Sci.,* **14** (1954) 530.
16. M. Yamamoto, K. Akita, S. Nagaoka, H. Umemoto, and H. Horibe, *J. Photopolym. Sci. Technol.,* **33** (2020) 433.
17. J. M. Nicovich, and A. R. Ravishankara, *J. Phys. Chem.,* **88** (1984) 2534.
18. C. Barckholtz, T. A. Barchholtz, and C .M.

Hadad, *J. Phys. Chem. A*, **105** (2001) 140.

19. A. M. Mebel, M. C. Lin, T. Yu, and K. Morokuma, *J. Phys. Chem. A*, **101** (1997) 3189.

20. M. Yamamoto, T. Maruoka, A. Kono, H. Horibe, and H. Umemoto, *Jpn. J. Appl. Phys.,* **49** (2010) 016701.

21. T. Maruoka, Y. Goto, M. Yamamoto, H. Horibe, E. Kusano, K. Takao, and S. Tagawa, *J. Photopolym. Sci. Technol.,* **22** (2009) 325.

22. M. Yamamoto, H. Horibe, H. Umemoto, K. Takao, E. Kusano, M. Kase, and S. Tagawa, *Jpn. J. Appl. Phys.,* **48** (2009) 026503.

Friction Dynamics of Commercial Artificial Hair

Momoka Sano[1], Shyuko Konno[1], Koji Asanuma[2], and Yoshimune Nonomura[1*]

[1]*Department of Applied Chemistry, Chemical Engineering, and Biochemical Engineering,
Graduate School of Science and Engineering, Yamagata University,
4-3-16 Jonan, Yonezawa 992-8510, Japan*
[2]*Department of Resin Processing Research, Division of Polymer Solution,
Denka Company Limited, 2-13-1, Kamakuradai, Kanagawa 247-8510, Japan*
[*]nonoy@yz.yamagata-u.ac.jp

Frictional property is one of the most important physical factors in designing artificial hair. Using a sinusoidal motion friction evaluation system, the frictions of eight commercial artificial hairs and natural human hair were evaluated when they were rubbed with an artificial finger. The friction profiles of all artificial hairs exhibited very general stable patterns: the outward and homeward frictional behaviors were similar and no significant oscillations were observed. The frictional forces of human hair and artificial hair derived from human hair were smaller than that of hair fabricated from synthetic fibers. In addition, the shape of the artificial hairs, particularly whether they were straight or wavy, significantly affected the friction parameters. These findings will be useful for understanding the characteristics of artificial hair to control its tactile texture.
Keywords: Artificial hair, Human hair, Synthetic resin, Morphology, Friction

1. Introduction
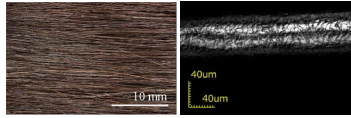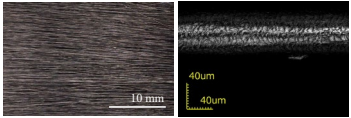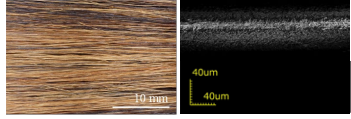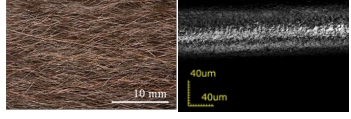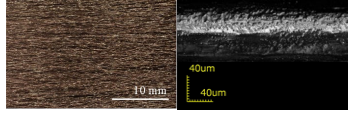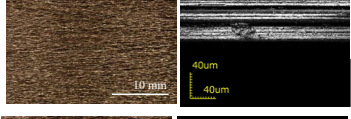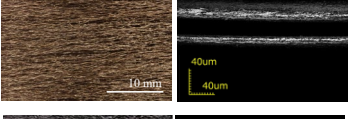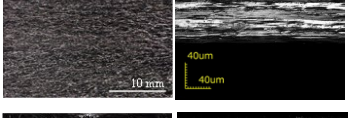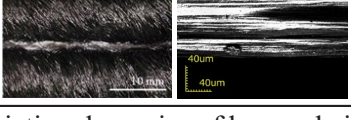
Artificial hair refers to hair made of synthetic fibers. It has advantages over human hair, such as lower cost, easier maintenance, reduced susceptibility to fading in sunlight, and lighter weight [1]. However, it also has disadvantages, such as unnatural appearance and movement and poorer texture compared to human hair. Synthetic fibers with controlled luster have been developed for application as artificial hair that resembles human hair in appearance and tactile feel [2]. Artificial hair derived from polyvinyl chloride (PVC) [3,4], polyethylene terephthalate (PET) [4,5], polyacrylonitrile (PAN) [6-8], and protein [9] have been reported.

Many studies have reported on the friction of synthetic fibers and natural fibers, such as wool and cotton. In many cases, the friction tests were evaluated between single fibers [10–13] or between cylinders and fibers [14–17]. Bowden and Tabor studied the effect of the shape of the fiber on the friction force (F) and reported that the friction coefficient (μ) of synthetic fibers is determined by the vertical force and diameter of the fiber [18].

Mogahzy and Gupta found that the F of circular fibers is greater than that of non-circular fibers [19]. Schic showed that the wettability of lubricant on the fiber surface and the viscosity of the lubricant have a significant effect on the friction phenomenon [20]. Nakashima and Ohta proposed a friction evaluation method that accounts for the reciprocating motion during the weaving process [21]. The friction of artificial hair is important in evaluating and controlling the tactile texture. LaTorre et al. evaluated artificial hair made of collagen film using atomic force microscopy and reported a μ value was about eight times greater than that of untreated human hair [22]. Yasmin et al. quantitatively evaluated the effect of PVC and modacrylic coatings on the friction of fibers [23].

Previous studies on F have been performed with the contact probe sliding at a constant velocity. We have obtained some limited information under such conditions, including F and its temporal change. In contrast, when the sliding velocity is constantly changing, a single measurement can yield several dynamic data points, such as the frictional phenomena at the beginning of the motion, the

Table 1. Characteristics and images of human hair and artificial hair.

Material	Raw thread	Fineness / d	λ / mm	A / mm	d / mm	Image
Human hair						
H	—	56 ± 12	—	—	—	
Artificial hair						
S₁	Human hair	66 ± 17	—	—	—	
S₂	Human hair	64 ± 17	—	—	—	
LW₁	Human hair	61 ± 15	12.61 ± 1.13	0.80 ± 0.23	—	
SW₁	PVC	49 ± 5	3.92 ± 0.01	0.17 ± 0.01	—	
SW₂	PVC	43 ± 4	3.66 ± 0.10	0.17 ± 0.02	—	
SW₃	PVC	39 ± 8	3.75 ± 0.09	0.21 ± 0.01	—	
SW₄	PVC	51 ± 6	5.49 ± 0.14	0.35 ± 0.05	—	
C	PVC	56 ± 8	—	—	11.31 ± 1.15	

dependence of frictional forces on velocity over a wide range, and hysteresis, which reflects the dependence on forces previously applied to the object. Therefore, we have developed a sinusoidal motion friction evaluation system that can evaluate friction dynamics under nonlinear motion [24, 25]. We can obtain the delay time (δ), which is the time lag between the motion of the contact probe and the mechanical response at the start of the movement, as well as the viscosity coefficient (C), which can quantify velocity dependence across several scales. To date, we have clarified the mechanism of tactile sensation of cosmetic sponges, powders, leather, and cloth using this sinusoidal motion friction evaluation system [26–32].

In this study, the friction dynamics of human hair and commercially available artificial hair were evaluated using a sinusoidal motion friction evaluation system to determine the effects of material and morphology. The subject of this evaluation included both human hair-derived and synthetic fiber-derived artificial hair. The present findings are useful for the characterization and design of artificial hair.

2. Experimental
2.1. Materials
The images and laser micrographs of human hair and artificial hair are shown in Table 1. Human hair was labeled as **H**, while artificial hairs were
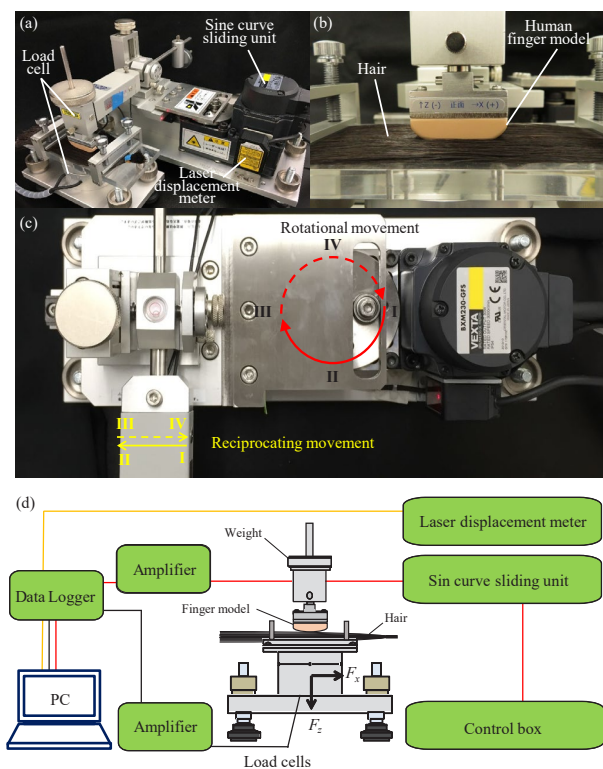
Fig. 1 Sinusoidal motion friction evaluation system. (a) Overall view, (b) contact probe of human finger model on human hair, (c) conversion from the rotational movement of an eccentric disk to the sinusoidal reciprocating movement of the contact probe, and (d) conceptual diagram.

classified as straight hair (**S**) without waviness, large wavy hair (**LW**), small wavy hair (**SW**), and curly hair (**C**). Fineness (f, the thickness of the yarn) was expressed in denier, which is the weight in g per 9 km. The wavelength (λ) and amplitude (A) of the waves for **LW** and **SW**, and the radius of curvature (r) of **C** were measured using ImageJ image analysis software (U.S. National Laboratory, Bethesda, USA). Three locations on the hair were randomly selected and the results obtained at each location were averaged to determine these parameters. The materials of the different hairs were as follows: **H** (Beaulax Co. Ltd., Saitama, Japan), $\underline{S_1}$ (raw thread = human hair), $\underline{S_2}$ (human hair), **LW** (human hair), $\underline{SW_1}$ (PVC), $\underline{SW_2}$ (PVC), $\underline{SW_3}$ (PVC), $\underline{SW_4}$ (PVC), and **C** (PVC).

H was evaluated after washing with a 1-wt% aqueous solution of sodium polyoxyethylene lauryl ether sulfate (Kao Corporation, Emeril 270J, 70% active ingredient). The hair bundles were soaked in 50 mL of the aqueous solution for 2 min and then rinsed with a large amount of tap water for 3 min. The wet hair bundle was placed between paper towels and a 1200 g weight was placed on it for 10 s to remove the water. The hair was then combed
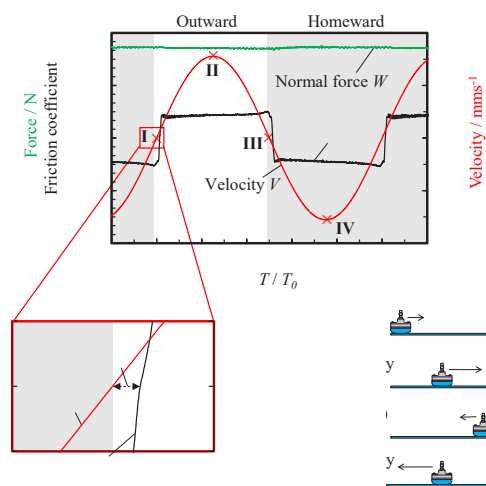
Fig. 2 Temporal profile of the friction coefficient (μ) (black line), velocity (yellow line), and normal force (green line) of the artificial hair sample, $\underline{SW_1}$, at $\omega = 2.1$ rad s^{-1} and $W = 0.98$ N, and the movement of the contact probe at each time.

and allowed to dry naturally overnight. Artificial hair was used without washing because of the lubricant oil on the surface.

2.2. Friction evaluation

Using the sinusoidal motion friction evaluation system, we evaluated the F of the human and artificial hairs. Figure 1 shows a photograph and a schematic of the device. The sinusoidal motion was achieved using the scotch-yoke mechanism, in which the rotational movement of an eccentric disk was converted into the sinusoidal reciprocating movement of the contact probe [24, 25].

We evaluated F when the hair bundles on a pedestal were rubbed with a polyurethane contact probe. The contact probe replicated the geometry and mechanical properties of an actual human finger, and the probe surface contained 29 grooves (depth: 0.15 mm) carved at 0.5 mm intervals [33]. F was measured after the roots and ends of the hair bundles were fixed and pinned. The following measurement conditions were used: sliding width = 30 mm, $W =$ 0.98 N, number of reciprocations = 11, and disk rotation speed = 2.1 rad s^{-1} (maximum velocity = 30 mm s^{-1}). The above evaluations were performed at 25°C ± 0.5°C and 50% ± 5% relative humidity. To confirm the reproducibility, three hair bundles of the same type were evaluated three times each under one condition. The friction parameters were calculated based on the friction profile of the second reciprocating movement of the probe over the hair. The static friction coefficient (μ_s) was defined as the
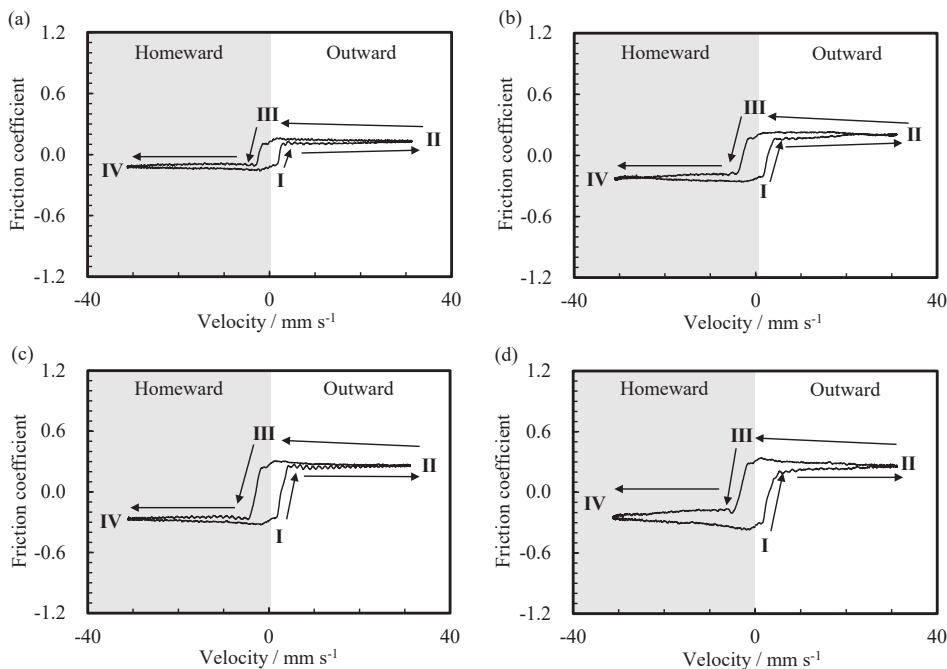
Fig. 3 Frictional patterns of human hair and artificial hair at $\omega = 2.1$ rad s^{-1} and $W =$ 0.98 N. (a) **S$_2$**, (b) **LW$_1$**, (c) **SW$_1$**, and (d) **C**. Refer to Figure 2 for description of I, II, III, and IV.

maximum value in the initial process of the sliding method. The kinetic friction coefficient (μ_k) was defined as the average of the sliding process without the initial process.

3. Results

3.1. Typical friction profile of artificial hair

Fig. 2 shows the temporal profile of μ, friction velocity, and W when artificial hair, **SW$_1$**, was rubbed with a contact probe under sinusoidal motion. The positive velocity region indicates the outward μ in the reciprocating motion of the contact probe, and the negative region indicates the homeward μ. In this case, the outward friction is in the direction from the root to the tip of the hair, and the homeward friction is in the direction from the tip to the root. The friction coefficient of **SW$_1$** exhibited a profile we named the "stable pattern". This pattern is defined as a profile in which no large oscillations of F are observed with similar frictional behavior on the outward and homeward directions [27]. We previously reported that various temporal profiles of frictional forces are observed on soft material surfaces due to surface deformation during the sliding process [27-32]. This poorly changing profile represents the typical pattern observed on most material surfaces. μ_s was 0.27 and μ_k was 0.33 for the outward direction, while μ_s and μ_k for the homeward direction were 0.23 and 0.31, respectively. The response of F to the movement of

the contact probe was delayed by a time difference (Δt). The normalized δ, which was calculated by dividing Δt by the friction time (T_0) for one reciprocating movement, was 0.014 for the outward direction and 0.016 for the homeward direction.

Figure 3a shows the relationship between μ and the velocity when a straight hair, **S$_2$**, is rubbed by a contact probe. Under the conditions of an angular velocity (ω) of 2.1 rad s^{-1} and a W of 0.98 N, μ_s reached 0.11 at a velocity of 3.0 mm s^{-1} in the outward direction, and μ_k remained almost the same at a maximum velocity of 30 mm s^{-1} (state II). Figure 3b shows the relationship between μ and the velocity of **LW**. In the outward direction, μ_s reached 0.19 at a velocity of 4.0 mm s^{-1}, and μ_k remained almost the same at 30 mm s^{-1} (state II). Figure 3c shows the relationship between μ and velocity of **SW$_1$**. In the outward direction, μ reached 0.27 at 4.3 mm s^{-1} and increased with acceleration, and μ_k was 0.34 at 30 mm s^{-1} (state II). In the homeward direction, μ reached 0.22 at a velocity of -4.8 mm s^{-1} and increased with acceleration, and μ_k was 0.33 at -30 mm s^{-1}. In the case of this artificial hair, small oscillations were observed. Figure 3d shows the relationship between μ and the velocity of **C**. In the outward direction, μ reached 0.19 at 5.3 mm s^{-1}, increased with velocity, and was 0.25 at 30 mm s^{-1} (state II).

3.2. Dependence of friction force on vertical force

Figure 4a shows the relationship between F and W. The F of human hair and artificial hair increased with W. The F obtained under each condition was analyzed based on the power law shown in equation (1).

$$F = aW^n \tag{1},$$

where a and n are constants. When $n = 1$, a is the friction coefficient, which follows Coulomb–Amonton's law, a general law for solid surfaces. Figure 5 shows a and n for all the hairs.

In the case of <u>**H**</u>, because of the presence of the cuticle, F was significantly different for the reciprocating movement: $a = 0.22$ in the outward direction along the cuticle, and $a = 0.51$ in the homeward direction against the cuticle. On the other hand, the a and n values of artificial hair were almost the same for the reciprocating movement. Fibers derived from human hair had smaller a values than those derived from synthetic fibers, such as PVC and modacrylic: the minimum and maximum a values for both human hair-derived fibers, <u>**S₂**</u> and <u>**LW₁**</u>, were 0.12 ± 0.01 and 0.20 ± 0.00, respectively. The artificial hair derived from synthetic fiber with the smallest a value was <u>**SW₃**</u> ($a = 0.21 \pm 0.01$), whereas the hair with the largest a value was <u>**SW₁**</u> ($a = 0.31 \pm 0.00$).

3.3. Dependence of delay time on vertical force

Figure 4b shows the relationship between δ and W, in which δ increased with the increase of W. The obtained δ was analyzed using the following linear model.

$$\delta = cW + d \tag{2},$$

where c and d are constants. A linear relationship was observed for all cases. The coefficient of determination (R^2) was $0.880\sim > 0.999$. Figure 6 shows the c and d values. The c values of <u>**H**</u> also differed greatly between the outward and homeward directions due to the presence of the cuticle. The c value was 0.011 in the outward direction along the cuticle and 0.007 in the homeward direction against the cuticle. The c and d values of the artificial hair were almost the same for the reciprocating movement. The human hair-derived fiber had a smaller c value than the artificial hair made of synthetic fiber: the c values of both human hair-derived fibers, <u>**S₂**</u> and <u>**LW₁**</u>, were a minimum of 0.002 ± 0.000, and a maximum of 0.004 ± 0.000, respectively. In contrast, the c values of the synthetic fibers, <u>**SW₃**</u> and <u>**SW₄**</u>, were a minimum and maximum of 0.005 ± 0.000 and 0.011 ± 0.001, respectively.

4. Discussion
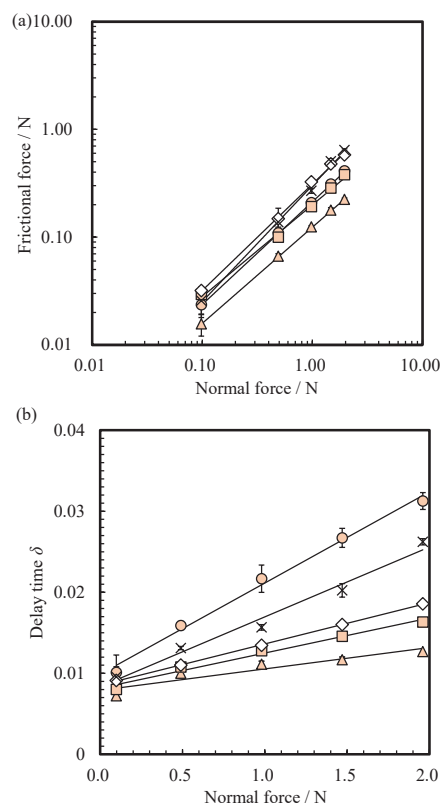
Fig. 4 Relationship between friction parameters and normal force. (a) Friction force (F) and (b) delay time (δ) at each normal force: ○ = human hair (<u>**H**</u>), △ = straight hair (<u>**S₂**</u>), □ = large wave hair (<u>**LW₁**</u>), ◇ = small wave hair (<u>**SW₁**</u>), × = curly hair (<u>**C**</u>).

Fig. 5 Friction parameters, a and n, of human hair and artificial hair. Raw thread material is human hair (orange) and raw thread material is artificial fiber (white), ○ = human hair, △ = straight hair, □ = large wave hair, ◇ = small wave hair, × = curly hair.

The friction profiles of all the artificial hairs, including <u>**S₁**</u>, <u>**S₂**</u>, and <u>**LW₁**</u>, which were derived from human hair, showed a stable pattern with similar frictional behavior in the outward and homeward directions, and no significant oscillations in F were

observed (Fig. 3). These profiles were quite different from previously reported data on human hair. When untreated human hair was subjected to sinusoidal motion with a contact probe, oscillatory phenomena with a frequency of 50–70 Hz were observed in a homeward direction because the human hair surface has a coarse cuticle [32]. This difference is caused by the shape of the artificial hairs. The laser microscope image in Table 1 shows that the surface of the artificial hairs was smooth and no cuticle-like bumps were observed. Cuticles on the human hair surface were probably removed during the process of preparing the artificial hair.

The raw material and shape of the artificial hair were reflected in the parameters related to friction dynamics. Fibers derived from human hair had smaller a and c values than those derived from synthetic fibers such as PVC and modacrylic. Human hair and human hair-derived artificial hair had lower F values than those composed of synthetic fibers. The friction force of the fiber is expressed by the following equation [18].

$$\mu = kW^{-\beta}D^{2\beta} \qquad (3),$$

where W and D are the vertical force and diameter of the fiber, respectively, and k and β are constants. According to Equation (3), μ increases with greater hair thickness. However, the results of this study are only partially consistent with this rule. There are two reasons for this. The first is the difference in surface energy and adhesion force among materials. In general, high surface energy leads to high F because the adhesion force at the real contact point, where the materials are in direct contact with each other, is greater [34]. Korte et al. suggested that the surface energies of natural and bleached human hair were ~24 and ~44 mN m^{-1}, respectively [35]. On the other hand, the energies of PVC and poly (methyl acrylate) were 41.9 and 41.0 mN m^{-1}, respectively [36]; therefore, there is no significant difference in the surface energies of artificial hair derived from human hair and artificial hair made of synthetic fibers.

The second factor is the morphology of the artificial hair, particularly the waving. The shape of the hair has a great influence on the number of contact points and the true contact area with the contact probe. In the case of the artificial hairs derived from human hair, **S_1**, **S_2**, and **LW**, the contact probe was able to move smoothly over the hairs because they were straight or had large weaves of centimeter-order. However, the artificial hairs made of synthetic fibers all consisted of fine weaves or curls in the millimeter-order. Bumps of this size are capable of trapping fingerprint-like patterns on the surface of the contact probe, which may have

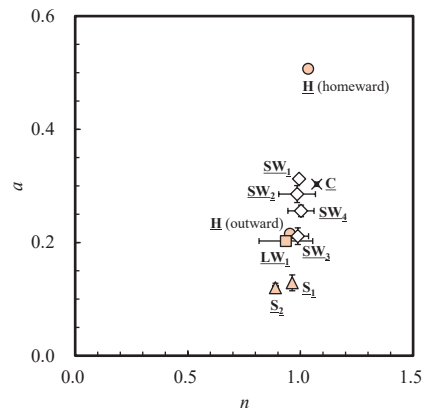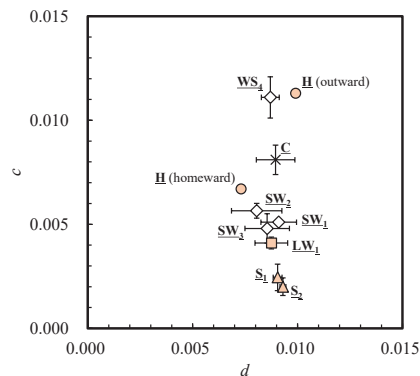Fig. 6 Friction parameters, d and c, of human hair and artificial hair. Raw thread material is human hair (orange) and raw thread material is synthetic fiber (white), ○ = human hair, △ = straight hair, □ = large wave hair, ◇ = small wave hair, × = curly hair.

resulted in larger a and c values. The roughness of a solid surface has a significant effect on friction. In the case of the finger model, it has been reported that the roughness of the surface of the object to be touched has a decisive influence not only on the magnitude of F but also on the temporal profile [28, 33, 37].

The frictional properties determined in this study may affect the tactile texture of the artificial hair. Previous studies have reported that smoothness or slipperiness is enhanced when the μ and the change in the kinetic friction process are small, while coarseness is enhanced when the surface is uneven [28, 38, 39]. In the present study, the artificial hairs derived from human hair, **S_1**, **S_2**, and **LW_1**, had significantly smaller a values, reflecting the dependence of F on W. These results suggest that the tactile texture of these artificial hairs is smooth.

5. Conclusion

We evaluated the friction of commercial artificial hairs using a sinusoidal motion friction evaluation system in which a finger model contact probe slides under a sinusoidal motion that mimics human tactile motion. The friction force depended on the material of the fiber: a and c were smaller for the artificial hair derived from human hair and larger for synthetic fibers. From the results of this study, we have succeeded in developing a new evaluation method for artificial hair that can reflect the shape and material of the artificial hair. This evaluation method will be useful for the development of artificial hair with good touch and feel.

Acknowledgement

References

1. S. Saed, O. Ibrahim, and W. F. Bergfeld, *Int. J. Women's Dermatol.* **2** (2016) 122.
2. E. R. Kaswell, *Text. Chem. Color.* **27** (1995) 21.
3. I. S. *Kim*, H. M. Cho, J. Koh, and J. P. Kim, *J. Appl. Polym. Sci.* **90** (2003), 3896.
4. Y. Liu, H. C. Kim, and Y. S. Chung, *Fibers Polym.* **8** (2007) 363.
5. H. C. Kim, D. H. Kim, J. Park, J. C. Lim, and Y. W. Park, *Fibers Polym.* **10** (2009) 594.
6. X. Zeng, J. Hu, J. Zhao, Y. Zhang, and D. Pan, *J. Appl. Polym. Sci.* 106 (2007) 2267.
7. K. Badii, J. S. Church, G. Golkarnarenji, M. Naebe, and H. Khayyam, *Polym. Degrad. Stabil.* **131** (2016) 53.
8. Y. Wang and W. Yin, *Physics Proc.* **18** (2011) 202.
9. L. Yang, J. Guo, S. Zhang, and Y. Gong, *Int. J. Biol. Macromol.* **99** (2017) 166.
10. N. Gralén and B. Olofsson, *Text. Res. J.* **17** (1947) 488.
11. J. Lindberg and N. Gralén, *Text. Res. J.* **18** (1948) 287.
12. J. Lindberg, *Text. Res. J.* **18** (1948) 470.
13. H. G. Howell, *J. Text. Inst.* 42 (1951) 521.
14. R. S. Merkel, *Text. Res. J.* **33** (1963) 84.
15. M. J. Schick, *Text.* Res. *J.* **43** (1973) 103.
16. C. Rubenstein, *Wear* **2** (1959) 296.
17. B. Lincoln, *J. Text. Inst.* **45** (1954), 92.
18. F. P. Bowden and D. Tabor, *Brit. J. Appl. Phys.* **17** (1966) 1521.
19. Y. E. EI Mogahzy and B. S. Gupta, *Text. Res. J.* **63 (**1993) 219.
20. M. J.Schic, *Text. Res. J.* **43** (1973) 342.
21. T. Nakashima and K. Ohta, *J. Text. Mach. Soc. Jpn.* **12** (1966) 185.
22. C. LaTorre and B. Bhushan, *Ultramicroscopy* **105** (2005) 155.
23. R. Yasmin and H. Kweon, *Int. J. of Integr. Eng.* **12** (2020) 216.
24. Y. Aita, N. Asanuma, A. Takahashi, H. Mayama, and Y. Nonomura, *AIP Adv.* **7** (2017) 045005.
25. Y.Aita, N. Asanuma, H. Mayama, and Y. Nonomura, *Chem. Lett.* **47** (2018) 767.
26. N. Asanuma, Y. Aita, and Y. Nonomura, *J. Oleo Sci.* **67** (2018) 1117.
27. K. Shinomiya, H. Mayama, and Y. Nonomura, *Langmuir* **34** (2018) 12723.
28. K. Kikegawa, R. Kuhara, J. Kwon, M. Sakamoto, R. Tsuchiya, N. Nagatani, and Y. Nonomura, *R. Soc. Open Sci.* **6** (2019) 190039.
29. Y. Nonomura and H. Ouchi, *J. Oleo Sci.* **69** (2020) 461.
30. K. Kikuchi, H. Mayama, and Y. Nonomura, *Langmuir* **37** (2021) 8045.
31. Y. Sakata, H. Mayama, and Y. Nonomura, *Int. J. Cosmet. Sci.* **44** (2022) 20.
32. M. Sano, H. Mayama, and Y. Nonomura, *J. Surfact.* Deterg. https://doi.org/10.1002/jsde.12634.
33. K. Kuramitsu, T. Nomura, S. Nomura, T. Maeno, and Y. Nonomura, *Chem. Lett.* **42** (2013) 284.
34. K. L.Johnson, K. Kendall, and A. D. Roberts, *Proc. R. Soc. Lond. A* **324** (1971) 301.
35. M. Korte, S. Akari, H. Kühn, N. Baghdadli, H. Möhwald, and G. S. Luengo, *Langmuir* **30** (2014), 12124.
36. J. Brandrup, E. H. Immergut, and E. A. Grulke, Polymer Handbook 4th Edition, Wiley-Interscience, 2003, p. VI 521-541.
37. A. Takahashi, A. Yamaguchi, and Y. Nonomura, *Chem. Lett.* **43** (2014) 1899.
38. S. Okamoto, H. Nagano, and Y. Yamada, *IEEE Trans. Haptics*, **6** (2013) 81.
39. Y. Kato, R. Kuhara, M. Sakamoto, R. Tsuchiya, N. Nagatani, and Y. Nonomura, *J. Oleo Sci.* **70** (2021) 195.

Preparation of Polyimide-TiO$_2$ Hybrid Films by Synthesis of Polyamic Acid Having Carboxylic Acid Group Sidechains in the Presence of TiO$_2$

Yuuki Hodozuka and Atsushi Morikawa[*]

*Department of Biomolecular Functional Engineering, Ibaraki University, 4-12-1,
Nakanarusawa, Hitachi, Ibaraki, 316-8511, Japan
atsushi.morikawa.reg@vc.ibaraki.ac.jp

Polyimide-TiO$_2$ hybrid films, **PICOOH-TiO$_2$s**, were prepared by the synthesis of polyamic acid having carboxylic acid group sidechains in the presence of TiO$_2$. TiO$_2$ and benzophenonetetracarboxylic dianhydride (BTDA) were added to a solution of 3,5-diaminobenzoic acid and 4,4'-oxydianiline(ODA) in NMP and stirred at room temperature for 24 h, 220 h, and 410 h. The NMP solutions were cast onto a glass plate and dried at 70 $^{\circ}$C, and thermal cyclodehydration of the polyamic acid was performed by successive heating at 100 $^{\circ}$C for 1 h, 200 $^{\circ}$C for 1 h, and 300 $^{\circ}$C for 1 h. T_g values of polyimides in the polyimide-TiO$_2$ hybrid films, **PICOOH-TiO$_2$-24**, prepared by stirring for 24 h after the addition of TiO$_2$ and BTDA, **PICOOH-TiO$_2$-220** prepared by stirring for 220 h, and **PICOOH-TiO$_2$-410** prepared by stirring for 410 h, were 284 $^{\circ}$C, 361 $^{\circ}$C, and 377 $^{\circ}$C, respectively. The T_g values became higher with increased stirring time after the addition of TiO$_2$ and BTDA, exhibiting stirring time dependence.
Keywords: Carboxylic acid group sidechains, 3,5-Diaminobenzoic acid, TiO$_2$, Polyimide-TiO$_2$ hybrid film, PICOOH-TiO$_2$, Stirring time dependence

1. Introduction

Polyimides are reliable high temperature polymers that exhibit superior mechanical and electrical properties [1-2]. Because of these excellent characteristics, polyimides have been used in the aerospace industry and for electric and heat resistance applications [3-7].

Organic-inorganic hybrids are attractive materials because they possess desirable characteristics that are associated with organic and inorganic compounds such as heat, mechanical, and electrical advantages [8]. The thermal stability of organic compounds is enhanced through the incorporation of inorganic moieties in the hybrid material. In this regard, hybridizations of organic materials with inorganic compounds have focused on the modification of polyimides to improve their properties [9-16]. However, preparation without a connection between the polyimide and inorganic material resulted in films that were opaque due to phase separation and exhibited poor mechanical properties relative to pristine polyimide [9].

Polyimide-Ti connections have been prepared by the reaction between organic functional groups and alkoxytitanium using the sol-gel method. For example, in the preparation of polyimide-TiO$_2$ hybrid material, polyimide-TiO$_2$ connections were created by the sol-gel reaction of titanium butoxide in a solution of polyimide with hydroxy group sidechains [16], the sol-gel reaction of titanium isopropoxide in a solution of aminopropyltrimethoxysilane terminated polyimide [13], the sol-gel reaction of titanium butoxide in a solution of a polyimide with carboxylic acid end groups [14] and using silica-modified anatase-type TiO$_2$ nanoparticles [15] to obtain transparent and tough material.

In this study, **PICOOH-TiO$_2$s** were prepared from polyamic acid having carboxylic acid group sidechains synthesized in the presence of commercially available TiO$_2$ with particle size of 30 nm [17-18]. The polyimide-Ti connection was not produced by the sol-gel method simply by stirring TiO$_2$ in the solution of polyamic acid having

carboxylic acid group sidechains. The carboxylic acid must first undergo an esterification reaction with the Ti-O bond as shown in eqns. (1) and (2) [19-20]. With the esterification reaction, a cross-linked structure though TiO_2 is produced in the polyamic acid solution since the TiO_2 surface has many Ti-O bonds. The polyimide molecule, which is finally formed, is restricted in motion, with a high T_g. The relation between the T_g value of the restricted polyimide in **PICOOH-TiO_2** and the stirring time after the addition of TiO_2 and BTDA to the solution of 3,5-diaminobenzoic acid and ODA,

which indicated the progression of the reaction, was examined.
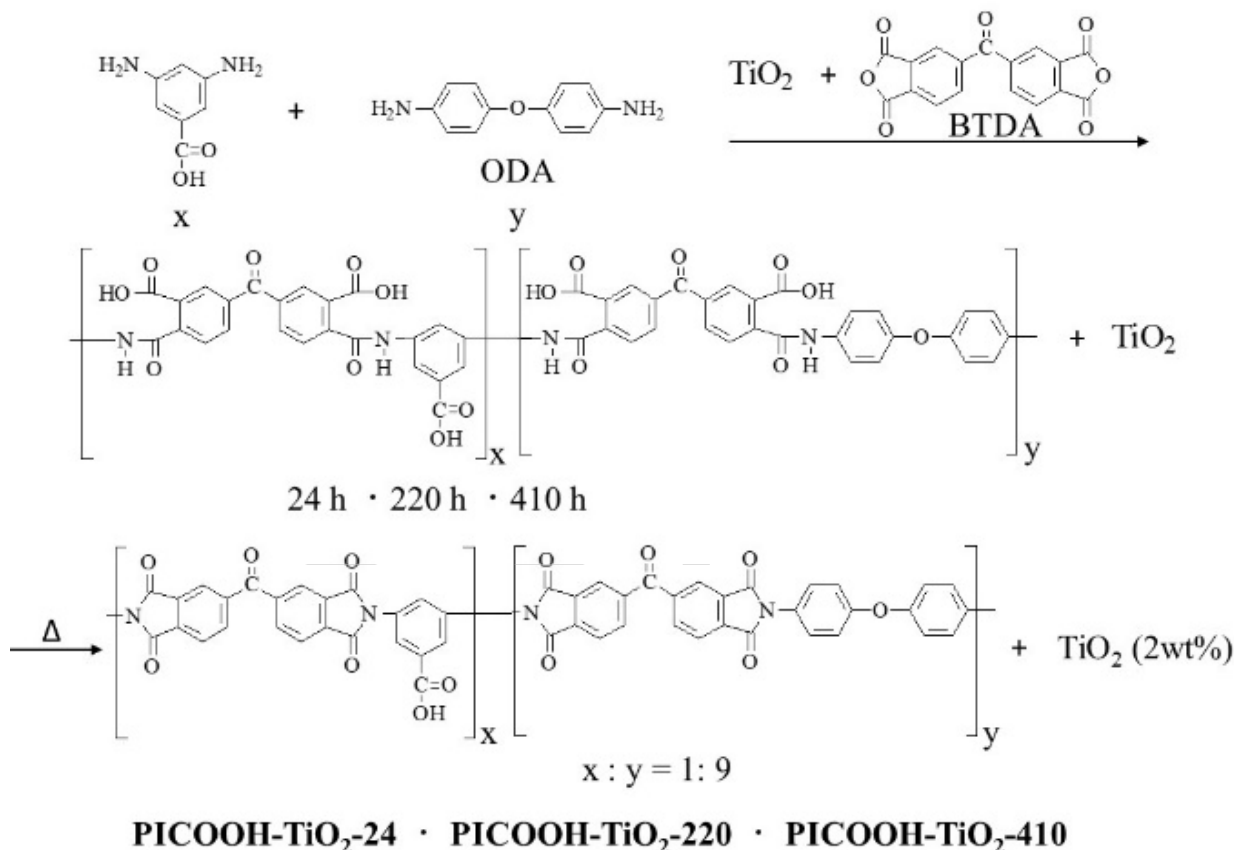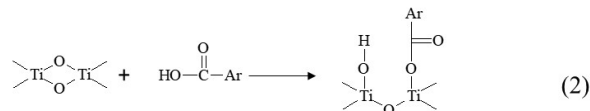
Figure 1. Preparation of polyimide-TiO2 hybrid fims.

2. Experimental

2.1. Materials

ODA, 3,5-diaminobenzic acid and BTDA were obtained commercially. TiO_2 was purchased from Art Science Co., Ltd.

2.2. Preparation of **PICOOH-TiO_2s**

In a three necked flask, 0.051 g of TiO_2 was added to a solution of 0.902 g (4.5 mmol) of ODA and 0.075 g (0.5 mmol) of 3,5-diaminobenzoic acid in 20 mL of NMP. Next, 1.611 g (5.0 mmol) of BTDA was added to the solution, which was then stirred at room temperature under nitrogen. After stirring for 24 h, part of the resulting viscous solution was poured into 200 mL of methanol. The precipitated polymer was filtered, washed with methanol, dried under vacuum, and measured the inherent viscosity. The NMP solution was cast onto a glass plate and dried at 70 °C. The thermal cyclodehydration of the polyamic acid was performed by successive heating at 100 °C for 1 h, 200 °C for 1 h, 300 °C for 1 h under vacuum. The stirring was continued, and reprecipitation of polyamic acid and the preparation of polyimide film were carried out after stirring for 220 h and 410 h.

The IR spectrum exhibited absorption bands at 1780 cm^{-1} (C=O), 1720 cm^{-1} (C=O), 1360 cm^{-1} (C-N), and 1680 cm^{-1} (O=C-OH).

2.3. Measurement

IR spectra were recorded on a Shimadzu spectrometer IR 435. For thermogravimetry (TG), a Rigaku thermal analysis station TG 8110 was used and measurements were made at a heating rate 10 $^{\circ}$C min^{-1} in air. Dynamic mechanical analysis (DMA) was performed with the Advanced Rheometric Expansion System at 1.0 Hz at 5 $^{\circ}$C min^{-1}. The inherent viscosities of the polyamic acids were measured at 0.5 dL-1 in NMP at 30 $^{\circ}$C.

3. Results and discussion

Preparation of **PICOOH-TiO$_2$s** was performed by the synthesis of polyamic acid having carboxylic acid group sidechains in the presence of TiO$_2$ as shown in Figure 1. TiO$_2$ and BTDA were added to a solution of ODA and 3,5-diaminobenzoic acid (ODA:3,5-diaminobenzoic acid = 9:1 M equivalents) in NMP at room temperature. The mixture was stirred for 6 h and became viscous due to the formation of polyamic acid (1.10 dL g^{-1}). The polyamic acid solution was stirred for 24 h, 220 h, and 410 h after the addition of TiO$_2$ and BTDA to examine the stirring time dependence of the T_g value of the polyimide in **PICOOH-TiO$_2$**. The inherent viscosities of the polyamic acid after stirring for 24 h, 220 h, and 410 h were 1.05, 1.03, and 1.04, respectively. No large variation was observed, and the solution of the polyamic acid was stable during stirring with TiO$_2$. The solutions were cast onto a glass plate and dried. The thermal conversion of polyamic acids was performed by successive heating of the precursor polymers in the form of films at 100 $^{\circ}$C for 1 h, at 200 $^{\circ}$C for 1 h, and finally 300 $^{\circ}$C for 1 h under vacuum, and the resulting transparent polyimide- TiO$_2$ hybrid films, **PICOOH-TiO$_2$-24**, **PICOOH-TiO$_2$-220**, and **PICOOH-TiO$_2$-410**, respectively, were obtained. They contained 2 wt% TiO$_2$.

The formation of the polyimide was confirmed by the appearance of IR bands at 1780, 1720, and 1360 cm^{-1} which are characteristic of an imide group, and 1680 cm^{-1} which is characteristic of a carboxylic acid group. It was difficult to confirm the existence of TiO$_2$ by IR and SEM due to its low content.

Figure 2 shows TG curves of the polyimide having carboxylic acid group sidechains and **PICOOH-TiO$_2$-220** in air. The weight loss was observed at about 420 $^{\circ}$C, and the 10% weight loss temperature was 535 $^{\circ}$C. The final weight residue of **PICOOH-TiO$_2$-220** at 800 $^{\circ}$C was 2%, equal to the TiO$_2$ content. Stirring time of TiO$_2$ in the solution of the polyamic acid having carboxylic acid group sidechains did not have a great influence on the TG behavior.
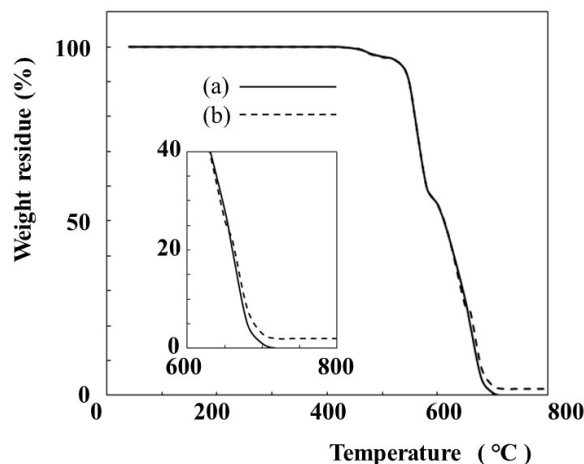
Figure 2. TG curves of the polyimide containing carboxylic acid group sidechains (a), and PICOOH-TiO$_2$-24 (b).

Figure 3 shows DMA curves of **PICOOH-TiO$_2$s**. That of the polyimide having carboxylic acid group sidechains without TiO$_2$ is also shown in Figure 3. In the tan δ spectra, single peaks corresponding to T_g of the polyimides were observed, and T_g values of the polyimide without TiO$_2$, **PICOOH-TiO$_2$-24**, **PICOOH-TiO$_2$-220**, and **PICOOH-TiO$_2$-410** were 274 $^{\circ}$C, 284 $^{\circ}$C, 361 $^{\circ}$C and 377 $^{\circ}$C, respectively. T_g values of **PICOOH-TiO$_2$s** were higher than that of the polyimide without TiO$_2$ and were higher with increasing stirring time of TiO$_2$ in the solution the polyamic acid having carboxylic acid group sidechains.

Regarding the temperature dependence storage modulus, a highly modulus glass transition region was followed by a decrease of the modulus at the T_g, and the E of **PICOOH-TiO$_2$s** decreased at higher temperature with increasing stirring time of TiO$_2$ in the solution of the polyamic acid having carboxylic acid sidechains.
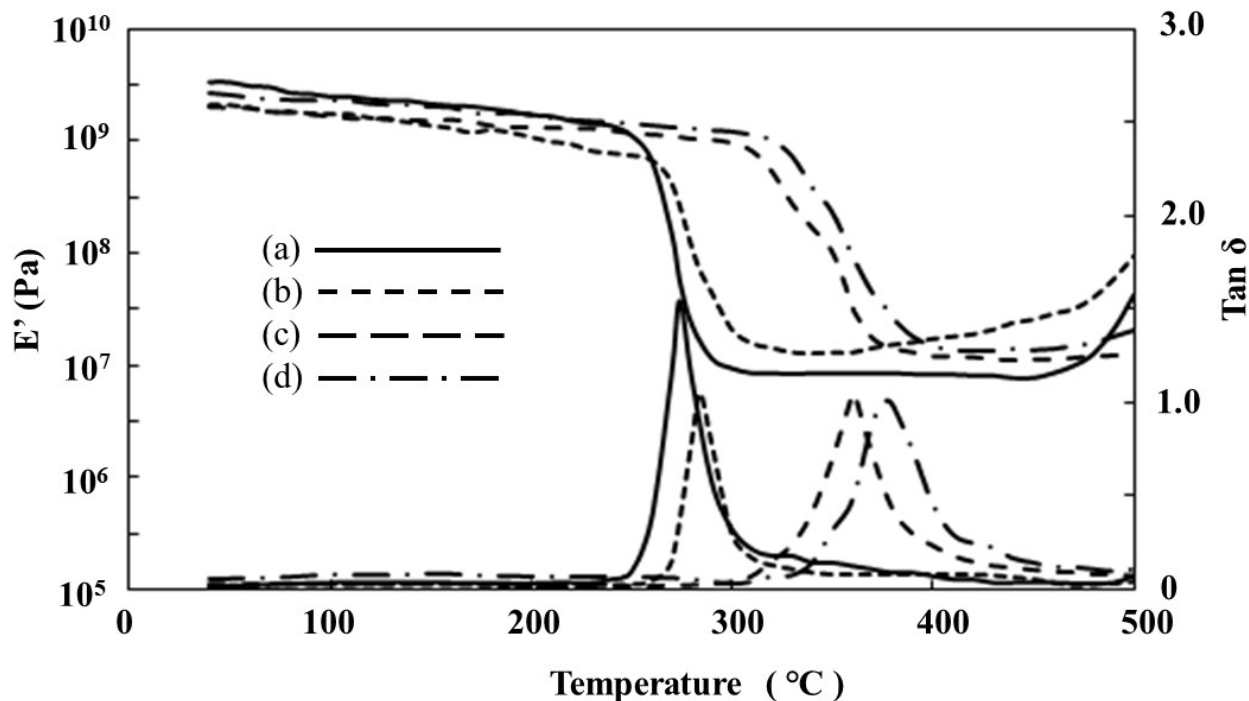
Figure 3. Dynamic mechanichal behaviors of the polyimide having carboxylic acid group sidechains (a), and PICOOH-TiO$_2$-24 (b), PICOOH- TiO$_2$-220 (c) and PICOOH- TiO$_2$-410 (d).
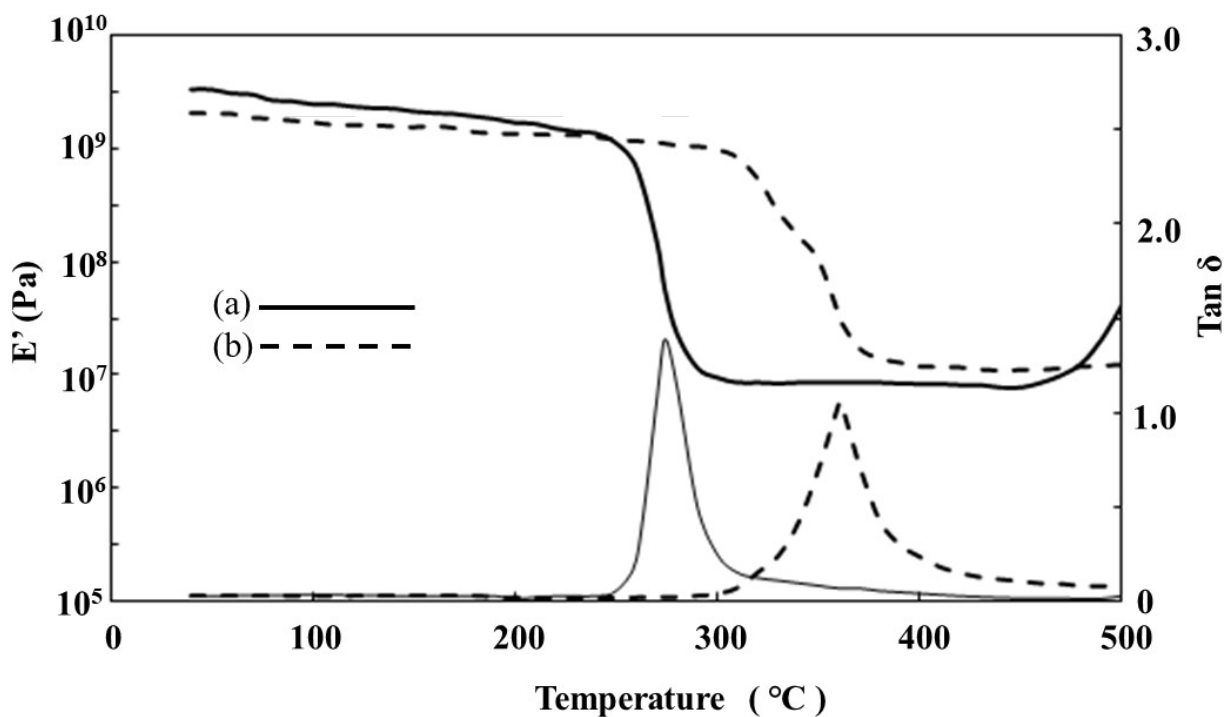
Figure 4. Dynamic mechanichal behaviors of the BTDA-ODA polyimide-TiO$_2$-220 hybrid film without carboxylic acid   (a) and PICOOH- TiO$_2$-220 (b).

The DNA behavior of the **BTDA-ODA polyimide-TiO₂-220** hybrid film without carboxylic acid group sidechains prepared by stirring for 220 h after the addition of TiO₂ and BTDA was compared with that of **PICOOH-TiO₂-220** (Figure 4). The T_g value of **BTDA-ODA polyimide-TiO₂-220** was much lower at 274 ºC, whereas the polyimide mobility was thought to be restricted by the cross-linked structure produced from the reaction of TiO₂ and carboxylic acid group sidechains in **PICOOH-TiO₂-220**. Ti-O-Ti and Ti-OH groups on the surface of TiO₂ reacted with carboxylic acid group sidechains as shown in eqns. (1) and (2) [19-20], respectively, and crosslinks were thought to form as shown in Figure 5.

4. Conclusion

Polyimide-TiO₂ hybrid films with polyimide-TiO₂ connections were prepared by the synthesis of the polyamic acid having carboxylic acid group sidechains in the presence of TiO₂. T_g values of the polyimide in the polyimide-TiO₂ hybrid films were higher with increased stirring time after the addition of TiO₂ and BTDA, even in the hybrid film having only 2% TiO₂ content much higher than the pristine polyimide. The dependence of the polyimide T_g on the stirring time of TiO₂ in the solution of the polyamic acid having carboxylic acid group sidechains was observed.

Figure 5. Reaction between carboxylic acid group sidechains and TiO₂.

References

1. D.-J. Liaw, K.-L. Wang, Y.-C. Huang, K.-R. Lee, T.-Y. Lai, and C.-S. Ha, *Prog. Polym. Sci.*, **37** (2012) 907.
2. A. Morikawa, "*High Performance Polymers and Engineered Plastics*", V. Mittal, Ed., Wiley, Salem, **7**(2011) 205.
3. R. Yokota, S. Yamamoto, M. Hasegawa, H. Yamaguchi, H. Ozawa, and R. Satoh, *High Perform. Polym.*, **13** (2001) S61.
4. M. Miyauchi, Y. Ishida, T. Ogasawara and R. Yokota, *Polym. J.*, **45** (2013) 594.
5. M. Ogino, T. Ohashi, H. Yoshida, D. Nagayama, T. Kubota, A. Morikawa, and K. Ono, *J. Photopolym.Sci. and Technol.*, **27** (2014) 155.
6. A. Morikawa, K. Suzuki, and K. Asano, *J. Photopolym.Sci. and Technol.*, **28** (2015) 151.
7. A. Morikawa, K. Suzuki, and K. Asano, *J. Photopolym.Sci. and Technol.*, **29** (2016) 231.
8. K. Haraguchi, *J. Network Polymer. Japan*, **21** (2000) 84 (in Japanease).
9. A. Morikawa, Y. Iyoku, M. Kakimoto and Y. Imai, *Polym. J.*, **24** (1992) 107.
10. A. Morikawa, Y. Iyoku, M. Kakimoto and Y. Imai, *J. Mater. Chem.*, **2(7)** (1992) 679.
11. P. Sysel, R. Pulec, and M. Maryska, *Polym. J.*,

29 (1997) 607.

12. Y. Shiina and A. Morikawa, *Reactive and Functional Polymers*, **71** (2011)85.

13. C.-M. Chang, C.-L. Chang, C.-C. Chang, *Macromol. Mater. Eng.*, **291** (2006) 1521.

14. H.-W. Sauc and W.-C. Chen: *J. Mater. Chem.*, **18** (2008) 1139.

15. J. Liu, Y. Nakamura, T. Ogura, Y. Shibasaki, S. Ando, and M. Ueda, *Chem. Mater.*, **20** (2008) 271.

16. G. Liou, P. Lin, H. Yen, Y. Yu and W. Chen, *J. Polym. Sci: Part A: Polym. Chem.,* **48** (2010) 1433.

17. The website of industry-academia-government collaboration results presentation. http://www.artkagaku.co.jp/pdf/siryou2.pdf(citr 2023. February 14) (in Japanease).

18. Y. Hasegawa, 2000, Development and Application of Inorganic-Organic Hybrid Materials (Muki Yuuki Haiburiddo Zenkutai no Seramikkusuka to Sonoouyou, 169) Tokyo, CMC Publishing Co., Ltd (in Japanease).

19. S. Okazaki and K. Kuramochi, *The Chemical Society of Japan*, **7** (1982) 1141 (in Japanese).

20. H. Nishikiori, and Y. Kato, *Journal of Flux Grouth*, **6** (2011) 12 (in Japanese).

Preparation of poly(methyl methacrylate) photochromic microcapsules containing spiro-pyran by solvent volatilization

Jian Gao[1], Jiansheng Dong[1], and Yunjie Yin[1*]

[1.] *Key Laboratory of Eco-Textile, Ministry of Education, College of Textile Science and Engineering Jiangnan University, Wuxi 214122, China*
*yinyunjie@jiangnan.edu.cn

In this study, poly(methyl methacrylate) (PMMA) microcapsules containing photochromic spiro-pyran dyes were prepared by the solvent volatilization method. The effects of different core-to-shell ratios, emulsifier dosage and temperature on the yield, size and morphology of PMMA microcapsules were investigated. The results showed that the highest yield was achieved when the core-to-shell ratio was 2:1, the amount of emulsifier was about 2% of the aqueous phase, and the volatilization temperature should be controlled at about 35 °C. Scanning electron microscopy (SEM) images and particle size analysis showed that spherical microcapsules were formed with an average particle size of about 2 µm. The photochromic microcapsules have excellent thermal stability and can withstand a temperature of 300 °C; the color change response performance is excellent and the color can reach saturation within 14 s. The prepared photochromic microcapsules were screen printed on cotton fabric, and scanning electron microscope (SEM) images showed that there was an attachment between the photochromic microcapsules and the fibers. The K/S values of the printed cotton fabrics were almost unchanged by UV light cyclic irradiation for 30 consecutive times, indicating that the printed cotton fabrics have excellent color change and fatigue resistance. The photochromic fabric responds quickly to color change under UV light irradiation and reaches saturation color depth after 30 s.
Keywords: Photochromic microcapsule, Solvent evaporation method, Spiro-pyran, Polymethyl methacrylate, Photochromic fabric

1. Introduction

Photochromic compounds can change their color under the irradiation of light, mainly because the compound changes its molecular structure under the action of a certain wavelength of light, which leads to the change of its characteristic absorption peak [1]. Photochromic compounds can be divided into two categories according to the difference in molecular structure, namely inorganic color-changing compounds and organic color-changing compounds [2]. Due to the difference in structure, the mechanism of color change after light exposure varies greatly between compounds. Inorganic photochromic compounds mainly include metal halides and transition metal oxides. Organic photochromic compounds mainly include spiro-pyrans, azobenzenes, diarylvinyls, and salicylaldehyde Schiff bases [3].

Spiro-pyran as an organic photochromic compound was one of the first to be studied in organic photochromic materials and one of the most widely used [4]. Under UV irradiation, the molecular structure of spiro-pyran is disrupted, the ring is opened, and isomerization occurs to display the color. After removal of UV light, the open-ring structure can be restored to a colorless closed-ring structure under the action of visible light [5]. However, spiro-pyran-based optically variable materials also have some defects that limit their applications, especially the poor fatigue resistance of spiro-pyran-based materials. Spiro-pyran is prone to ring-opening reactions under UV excitation, and it is susceptible to photodegradation due to external influences and consumption [6]. The problem that needs to be solved for spiro-pyran is to improve its color-changing properties and resistance to low fatigue [7]. One solution is to encapsulate the photochromic dyes in microcapsules of micro-nano composite particles, which can improve the applicability of photochromic materials and improve their fatigue resistance [8].Si

[9] et al. used spiro-pyran compound as the core material and chitosan as the shell material, and prepared intelligent photochromic chitosan microcapsules through emulsification and chemical crosslinking technology. The test confirmed that the microencapsulated spiro-pyran had high fatigue resistance.

Microcapsules are structures in which micron-sized substances are wrapped in a polymer film to form microspheres. Microcapsules have the appearance of spherical particles with an average particle size ranging from 1 to 500 μm [10]. The substance encapsulated in the polymer film is generally referred to as the core material, including the solid, liquid or gas encapsulated in the shell material, and the polymer film is the shell material, which is generally an inert polymeric material [11]. LV [12] et al. successfully prepared microcapsules with E7 as core and PMMA as shell through solvent evaporation, indicating that the morphology of microcapsules mainly depends on the mass ratio of core material and shell material.

In this study, the photochromic microcapsules were prepared by the solvent volatilization method, which is simpler and easier to operate than other methods. In the preparation of photochromic microcapsules, photochromic spiro-pyran dyes were selected as the core material and polymethyl methacrylate as the shell material. Polymethyl methacrylate, which has good mechanical strength and excellent optical properties, is the material used to ensure the stability and light transmission of the microcapsules. The prepared microcapsules can reduce the external influence on the core material and change the physical and chemical properties of the core material [13]. In addition to the simplicity and ease of preparation of microcapsules by solvent volatilization, it is easier to control the factors affecting the preparation of microcapsules, including the amount of emulsifier, the temperature during volatilization, and the mass ratio of core and shell materials [14]. And there are no other chemical reactions during the preparation of microcapsules

that cause unfavorable factors to the photochromic material and the molding of microcapsules [15]. The shell material of microcapsules is polymethyl methacrylate, although it has the advantages of excellent light transmission, good weather resistance, and good stability, but the polymethyl methacrylate microcapsules prepared by solvent volatilization method still have the disadvantage of low yield and microcapsules due to the instability of volatilization process species [16].

2. Experiment

2.1. Materials

Spiro-pyran dye; polymethyl methacrylate; n-octane; methylene chloride; polyvinyl alcohol 1788; anhydrous ethanol, all from Sinopharm Chemical Reagent (Shanghai) Co., Ltd.

2.2. Preparation of photochromic microcapsules

The photochromic microcapsules were prepared by the solvent volatilization method as shown in Figure 1. Measure 0.05 g of spiro-pyran photochromic dye dissolved in 10 g of n-octane and sonicate for 30 min to dissolve it completely. Measure 0.5 g PMMA dissolved in 5 g dichloromethane. When PMMA was completely dissolved, a certain proportion of n-octane solution containing the photochromic dye was selected and added dropwise to dichloromethane containing PMMA as the oil phase. A certain amount of polyvinyl alcohol 1788 (PVA 1788) was dissolved in water under high temperature stirring as the aqueous phase. After the aqueous phase was cooled to room temperature, the oil phase was added to the aqueous phase, and then the oil-water mixture was homogenized for 10 min to emulsify. The dichloromethane in the emulsion was slowly evaporated off at a suitable temperature. The evaporated emulsion was centrifuged, and the lower layer after centrifugation was the prepared microencapsulated sample. The samples were removed and washed three times with 30 % ethanol solution and finally the samples were freeze-dried.
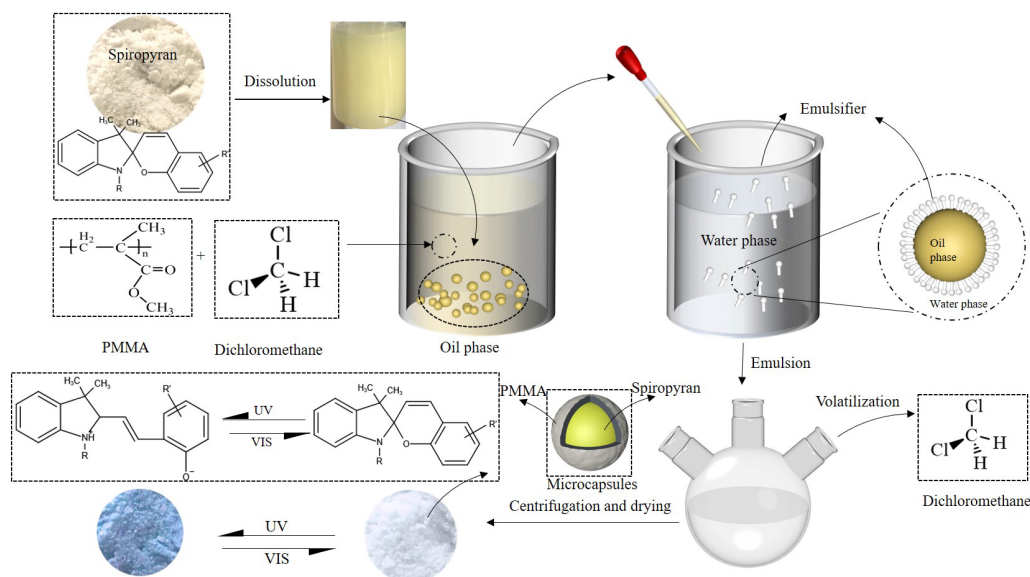
Fig. 1. Schematic diagram of the preparation of PMMA photochromic microcapsule

2.3. Screen printing of cotton fabric with PMMA photochromic microcapsule

Printing paste is composed of 2 wt% synthetic thickener, 12 wt% adhesive, 10 wt% PMMA photochromic microcapsules and 76 wt% deionized water. After mixing the printing paste evenly, select the appropriate printing mesh to scrape onto the fabric. Dry the printed fabric in an oven at 80 °C for 15 min. Finally, the printed fabric is baked in an oven at 120 °C for 3 min.
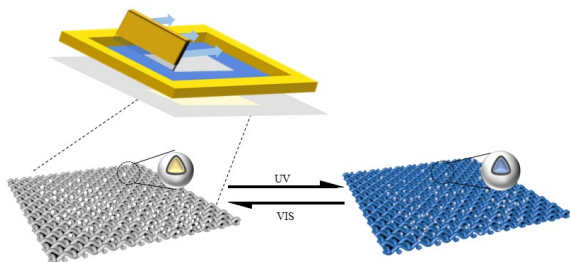
Fig. 2. Flow chart of the preparation process of photochromic fabric

2.4. Testing and Characterization

The optically variable microcapsule products, optically variable materials, shell materials and solvents with different core shell ratios were tested by Fourier infrared spectrometer. The total reflection method was used at room temperature, and the scanning spectrum range was $3500 \sim 500$ cm^{-1}. The surface morphology of PMMA photochromic microcapsules with different core-to-shell ratios and the photochromic microcapsule printing fabric were observed by scanning electron microscopy (SEM), and the SEM images of each sample were captured by a SU1510 scanning electron microscope (Hitachi, Ltd.). The particle size and particle size distribution of PMMA photochromic microcapsules were measured by zeta potential and particle size analyzer (Brookhaven Co., Ltd., USA). The UV-Vis absorption spectra of the photochromic materials before and after light exposure were tested by UV-Vis spectrophotometer. The test wavelength range was from 200 to 600 nm. The color parameter values (K/S values, CIE-Lab values) involved in the photochromic behavior and light fatigue resistance of PMMA microcapsules and fabrics were determined using an Xrite-8400 spectrophotometer (x-rite Ltd., USA) with a D65 light source and a 10° standard observer. Thermogravimetric analysis of PMMA photochromic microcapsule samples and solvents was performed using a Q5000IR thermogravimetric analyzer (TA Instruments, Ltd., American) from 25 to 600 °C (scan rate of 10 °C/min) under a nitrogen gas flow.

3. Results and discussion
3.1. Preparation and Yield of PMMA Photochromic Microcapsules

In the preparation and experimental exploration of microcapsules, six different core shell ratios of 1:3, 1:2, 1:1, 2:1, 3:1 and 4:1 were selected, and the corresponding yields were calculated, and the encapsulation effect in the preparation process of

microcapsules was preliminarily measured. The different core-to-shell ratios have a great influence on the light-change microcapsules, which will not only affect the particle size of microcapsules, but also affect the surface morphology and retaliation effect of microcapsules, and finally affect the yield of microcapsule vegetation [17]. As can be seen from Table 1, when the amount of core material is less and the amount of shell material is more, the yield of the prepared microcapsules is higher and can reach about 50 % of the mass of input core and shell material. Due to the low hardness of PMMA surface, the microcapsules are easily broken after molding, which leads to the decrease of the yield of microcapsules. When the core material is unchanged, increasing the amount of shell material will make the shell of microcapsules thicker, which will increase the stability of microcapsules and will not break during emulsion mixing and volatilization, thus increasing the yield of photochromic microcapsules. However, thicker shell material will firstly lead to larger particle size of microcapsules and will also affect the color change performance of photochromic microcapsules to some extent, as will be seen later in the investigation. Therefore, when the core-to-shell ratio is 2:1, the yield of microcapsules is 44.3 %, which can meet the yield requirement in the production process and also ensure the uniform particle size of microcapsules as well as the excellent color-changing performance.

Table 1. Process formula difference and yield of different core-shell ratios for preparing microcapsules

Experiment number	Core shell ratio	Spiro-pyran + n-octane (core)/g	PMMA (shell)/g	Yield
1	1：3	0.167	0.5	49.6 %
2	1：2	0.25	0.5	56.1 %
3	1：1	0.5	0.5	45.9 %
4	2：1	1.0	0.5	44.3 %
5	3：1	1.5	0.5	18.6 %
6	4：1	2.0	0.5	16.9 %

In the preparation of microcapsules by solvent volatilization method, the formation of stable emulsion is one of the keys to the preparation of microcapsules, so the amount of emulsifier also plays a very important role in the preparation of microcapsules [18]. In the process of preparing microcapsules by solvent volatilization method, the dichloromethane solvent in the oil phase continuously decreases due to the volatilization of the solvent, which gradually increases the viscosity

of the oil phase, thus causing the aggregation and adhesion between adjacent droplets and affecting the formation of microcapsules [19] As can be seen from Table 2, in general, the stability of the emulsion increases within a certain range with the increase in the amount of emulsifier, and therefore the yield of microcapsules increases accordingly. However, when there is more emulsifier, the output of microcapsules will not increase linearly, and part of the emulsifier may remain on the shell material of microcapsules, making it difficult to clean the sample and affecting the surface morphology of microcapsules [20,21]. Therefore, the dosage of emulsifier should be kept within a reasonable range. In this experiment, polyvinyl alcohol 1788 (PVA 1788) was used as the emulsifier in the process of preparing microcapsules by solvent volatilization method, and the highest yield of prepared microcapsules was about 46 % when the amount of emulsifier was about 2 %, indicating that the emulsifier had a better emulsification effect on the system at this time.

Table 2. Different emulsifier dosages for the preparation of microcapsules and their yields

Experiment number	Core shell ratio	Emulsifier dosage (compared to water)	Yield
1	2：1	1.0 %	44.3 %
2	2：1	1.3 %	44.1 %
3	2：1	1.7 %	45.7 %
4	2：1	2.1 %	46.4 %
5	2：1	2.5 %	40.3 %

The organic solvent used to prepare microcapsules by solvent volatilization method is dichloromethane, which has a boiling point of 39.8 °C and is volatile. When the volatilization temperature is too low, the rate of solvent volatilization is slow and the time to prepare microcapsules will be prolonged, resulting in lower experimental efficiency. Moreover, the boiling point of dichloromethane is low, and when the temperature at volatilization exceeds the boiling point of the organic solvent, the dichloromethane solution present in the system will boil violently, which affects the preparation of microcapsules. In addition, when the temperature of the aqueous phase is high, the dripping of the oil phase will also lead to the precipitation of the membrane material and prevent the formation of microcapsules. As can be seen from Table 3, the temperature at volatilization is too low, resulting in long volatilization time and low efficiency, and it is impossible to accurately judge

whether the solvent is volatilized, which is not conducive to the formation of microcapsules. The volatilization temperature was chosen to be higher at 40 °C. The high temperature may also affect the stability of the emulsion, and the violent volatilization of the solvent may cause the shell material of the microcapsules to break and not exist stably. During the experiment, the volatilization temperature was generally chosen between 30 °C ~35 °C according to the characteristics of the selected dichloromethane solvent, and according to the high yield of microcapsules in Table 3, therefore the volatilization temperature of 35 °C was chosen as more appropriate.

Table 3. Differences in the process formula and yield of microcapsules prepared at different volatilization temperatures

Experiment number	Core shell ratio	Volatile temperature (°C)	Volatilization time	Yield
1	2：1	20	12 h	35.4 %
2	2：1	25	10 h	36.8 %
3	2：1	30	8 h	38.8 %
4	2：1	35	6 h	44.1 %
5	2：1	40	4 h	28.4 %

3.2. Characterization of PMMA microcapsules

In the experimental process of preparing photochromic microcapsules, the core and shell materials are dissolved in an organic solvent to form an oil phase. The oil phase is dispersed in the aqueous phase and then undergoes a series of processes such as emulsification. Dichloromethane solvent is completely volatile in the oil phase, so the quality of the core and shell inputs directly determines the amount of microcapsule encapsulation and directly affects the morphology of the microcapsules. The morphological characteristics of PMMA photochromic microcapsules were analyzed using SEM, as shown in Figure 3.

From the SEM images of microcapsules, it can be seen that when the core-to-shell ratio is 1:3 or 1:2, as in Figure 3(a, b, c), some microcapsules have larger particle size and some have smaller particle size, and the factors of uneven particle size may be caused by excessive shell material adsorbed on the surface of microcapsules and uneven emulsification. Some irregularly shaped microcapsules adsorbed some impurities on the surface, and these impurities may be the residues after the microcapsules rupture. As shown in Figure 3(d), when the core-to-shell ratio is 2:1, the microcapsules when more regular spherical structure with more uniform particle size. As the core-to-shell ratio increases, as shown in Figure 3(e, f), the particle size of microcapsules decreases with the reduction of core material, but the encapsulation rate of photochromic microcapsules is lower at this time, and the surface of microcapsules often appears depressed or broken. In summary, when the core-to-shell ratio is 2:1, the surface morphological characteristics of the prepared PMMA microcapsules are better and can meet the application of printing in textiles.
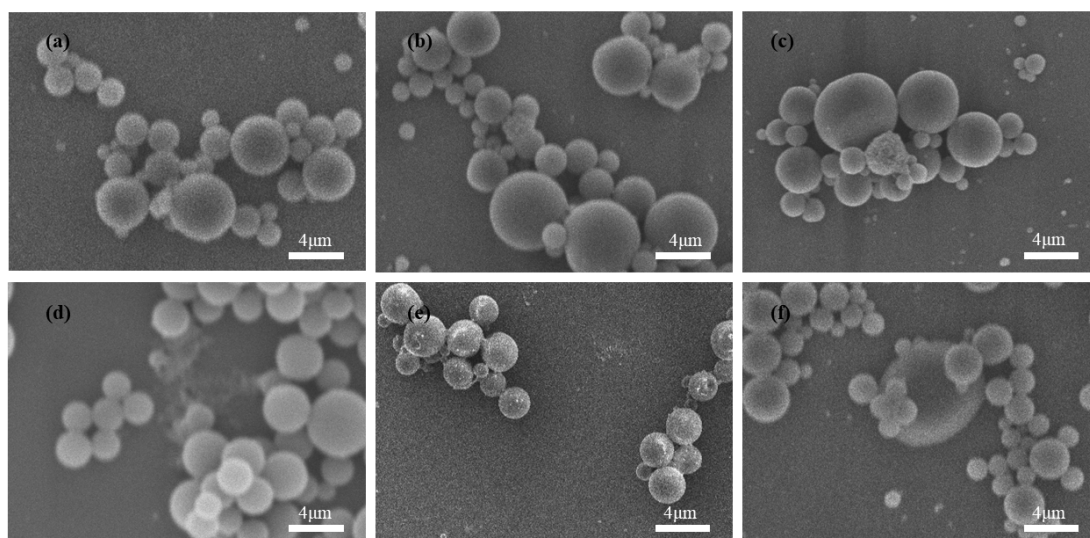

Fig. 3. SEM images of PMMA microcapsules with different core-to-shell ratios: (a) 1:1, (b) 1:2, (c) 1:3, (d) 2:1, (e) 3:1 and (f) 4:1.

In this experiment, microcapsules with different core-shell ratios were prepared by controlling the amount of emulsifier and other factors such as constant volatilization temperature, and particle sizes with different core-shell ratios were tested by particle size analyzer, as shown in Figure 4 (a). It can be seen that the average particle size of most microcapsules is about 1.5-2 μm. When the core shell ratio is 1:3, due to the excessive amount of shell material, the surface of microcapsules can be attached to more shell material, resulting in the average particle size of photochromic microcapsules is relatively large, about 3.5 μm; Due to the existence of more shell polymers may lead to the existence of non-uniformity in the emulsification process, the particle size distribution is relatively wide. When the core shell ratio is 2:1, the average particle size is about 2 μm, the particle size decreases and the distribution is more uniform. When the core shell ratio is 1:1 and 3:1, the distribution is the most uniform. When the core-shell ratio was 4:1, most of the microcapsules were destroyed due to the thin shell material of the tested microcapsule sample, and only a small part of microcapsules with a particle size of about 1 μm or some impurities existed. It can be seen that with the increase of core shell ratio, the particle size of microcapsules gradually decreases,

the particle size distribution gradually Narrows, and the particle size of microcapsules gradually tends to be uniform.

Figure 4 shows the TGA curves of PMMA (curve a), PMMA microcapsules (curve b), n-octane (curve c) and blank microcapsules (curve d), respectively. From the TGA curves of PMMA microcapsules, there was a small weight loss at about 95 °C, probably due to the loss of moisture, and the decomposition of the shell material PMMA started at about 250 °C, and the decomposition of the core material n-octane started at about 400 °C. The first mass loss was 24.88 %, the second mass loss was 72.39 %, and the remaining mass was 2.73 %. One of the major weight losses starts around 300 °C, which is caused by the decomposition of PMMA. the rapid thermal decomposition after 400 °C is attributed to the thermal decomposition of n-octane, the main solvent in part of the shell and core materials. The degradation of the TGA profile of the blank microcapsules at 170 °C relative to the microcapsules is probably due to the rupture of the shell material. From the figure, it can be seen that PMMA as the shell material covers the photochromic dyes with good thermal stability, which has a protective effect on the photochromic dyes.
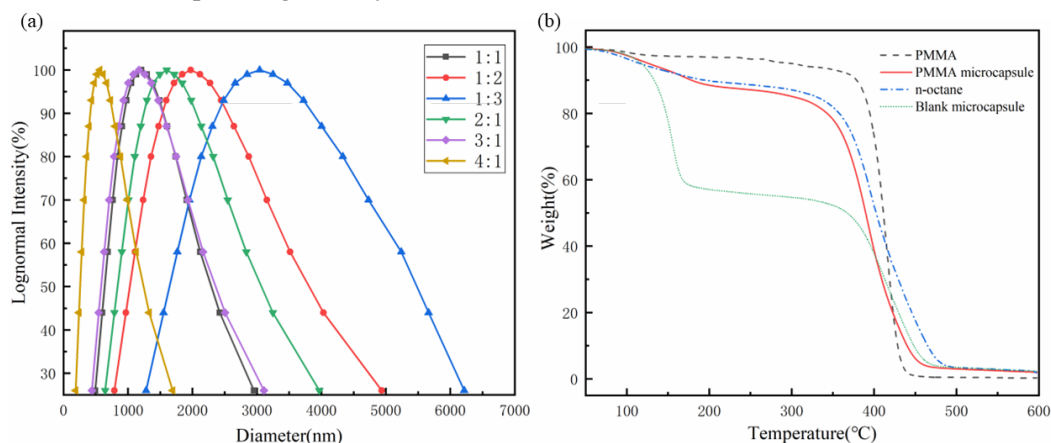
Fig. 4. Particle size distribution of PMMA microcapsules with different core-to-shell ratios (a); TGA curves of PMMA microcapsules, PMMA, n-octane and blank microcapsules (b).

From Figure 5(a, b), it can be seen that the PMMA microcapsules show the peak at 2990 cm^{-1} as the absorption peak of methyl group (C-H), another absorption peak of methylene group around 2950 cm^{-1}, the peak at 1750 cm^{-1} as the absorption peak of carbonyl group (C=O), and the absorption peak of ether bond (C-O-C) at 1100~1300 cm^{-1}. Combined with the infrared spectrum of PMMA, it shows that the surface coating material of the microcapsules is PMMA. From Figure 5(b), it can be seen that the

absorption peaks of PMMA microcapsules are approximately the same as those of PMMA, and the characteristic absorption peaks of photochromic dyes and n-octane are not present, which can indicate that the presence of photochromic dyes and n-octane is in the form of encapsulation in microcapsules with PMMA as the shell material.
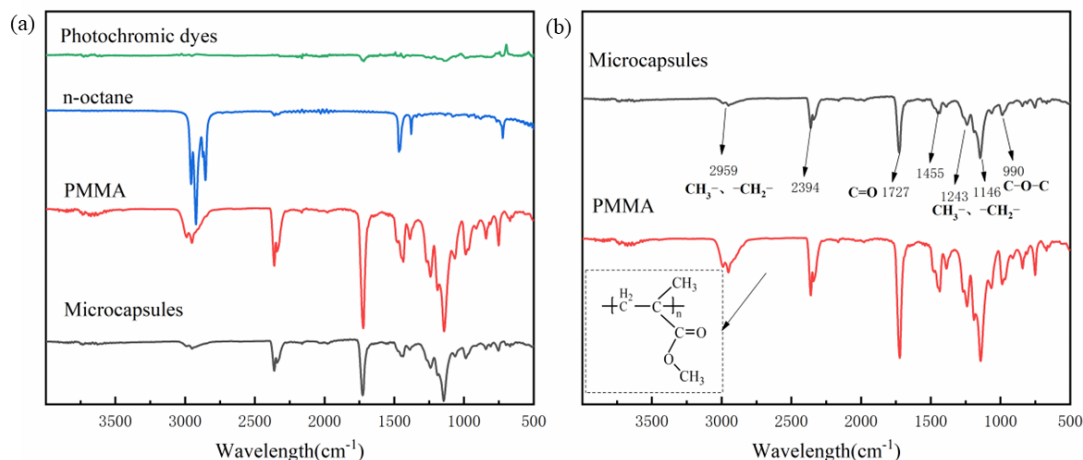
Fig. 5. FTIR spectra of photochromic dyes, n-octane, PMMA and microcapsules (a); FTIR spectra of PMMA microcapsules and PMMA (b).

3.3. The photochromic properties of PMMA microcapsules

The spiro-pyran photochromic dye used in this experiment is a yellow powder, and the solution of the photochromic dye formed by dissolving the dye in n-octane appears purplish-red under UV irradiation. It was encapsulated in poly(methyl methacrylate) (PMMA) by solvent evaporation to form microcapsules with a core-shell structure, which peculiarly appeared blue under UV irradiation.

In Figure 6(a), the photochromic dyes have absorption peaks in the visible band from 380 to 420 nm and in the UV irradiation from 550 to 620 nm, and the absorption peaks in the UV region are located around 250 nm with strong absorption peaks. This indicates that there is a benzene ring in the structural system of the dye, which is a conjugated system containing two or more double bonds. Combined with the structure of the dye and the mechanism of color change, it indicates that the dye absorbs UV light at around 250 nm and undergoes

ring-opening reaction and color change. In Fig. 6(c), the photochromic dyes reacted rapidly to UV light, and obvious color changes occurred at 2 s of irradiation, reaching the maximum value within about 8 s. This indicates that the photochromic dyes are sensitive to color changes. In Figure 6(b), the microcapsules containing the photochromic dye did not change color before UV irradiation, and after UV irradiation, the spiro-pyran dye in the microcapsules underwent a ring-opening reaction, showing an obvious absorption peak at about 550 nm, resulting in a color change of the microcapsules. In Figure 6(d), it can be seen that the microcapsules can reach the saturation value of the color within 14 s, which is due to the fact that the shell material, while acting as a protection for the core material, undergoes some reflection or diffuse reflection when irradiated by light, which can cause the photochromic spiro-pyran dye in the core material to absorb less energy than that absorbed directly by the spiro-pyran dye under the same irradiation intensity and time.
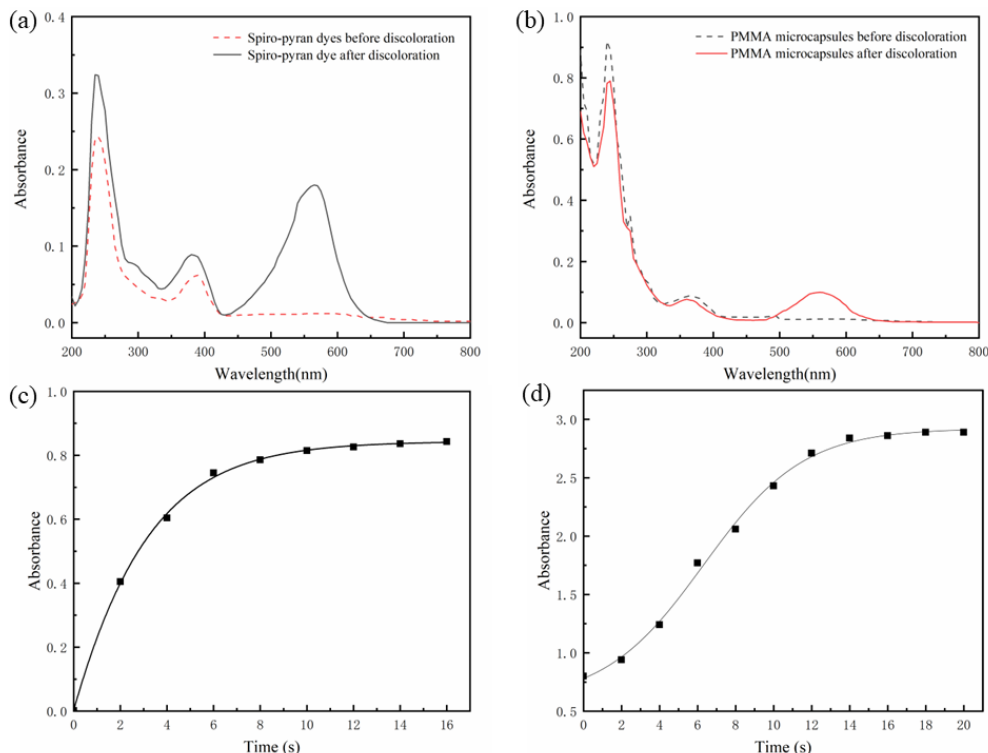
Fig. 6. UV-Vis spectra of spiro-pyran photochromic dyes (a) and photochromic microcapsules (b) before and after discoloration; color change response time of spiro-pyran dyes (c) and photochromic microcapsules (d).

3.4. Photochromic properties and fatigue resistance of printed cotton fabrics

The most commonly used methods of combining photochromic materials with fabrics are mainly printing and dyeing. When there is no affinity between the optically variable material and the fabric, it is usually necessary to make the optically variable material into optically variable microcapsules, and then fix it on the fiber by adding a binder. The so-called coating process of microcapsules is to mix the prepared optically variable microcapsules with the prepared coating solution through the method of pigment printing, stir evenly to become a paste, and then apply the printing on the fabric by screen printing. The surface is placed in a dryer to dry the fabric to obtain a fabric with a microcapsule coating.

In the experiment, photochromic microcapsules with a core-to-shell ratio of 2:1 were selected as the printing material, mixed with binders to form a color paste, and printed on cotton fabrics to make photochromic fabric samples. After microcapsule finishing, the fabric changed from white to violet-blue after UV irradiation (Figure 7), and the color change was sensitive and long-lasting. The surface microscopic morphology of the printed cotton fabric under the action of photochromic microcapsules with 10 % PMMA microcapsules and 12 % adhesive is shown in Figure 8. These images show that the surface of cotton fabric is cross-linked with this large number of microcapsules attached. the morphology of PMMA photochromic microcapsules on cotton fabric did not change and remained well spherical.

Fig. 7. Photochromic properties of printed cotton fabrics

Fig. 8. SEM image of a cotton fabric printed with PMMA microcapsules.

After photochromic microencapsulated printing of cotton fabrics, the fabric surface changed from white to blue after UV light irradiation, and the color change was sensitive. The photochromic fabric was exposed to light for different times, and for the first 5 s, the K/S value was tested with a colorimetric color-matching instrument. 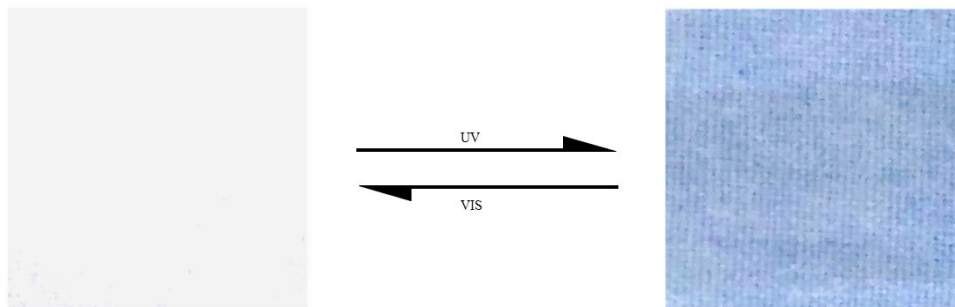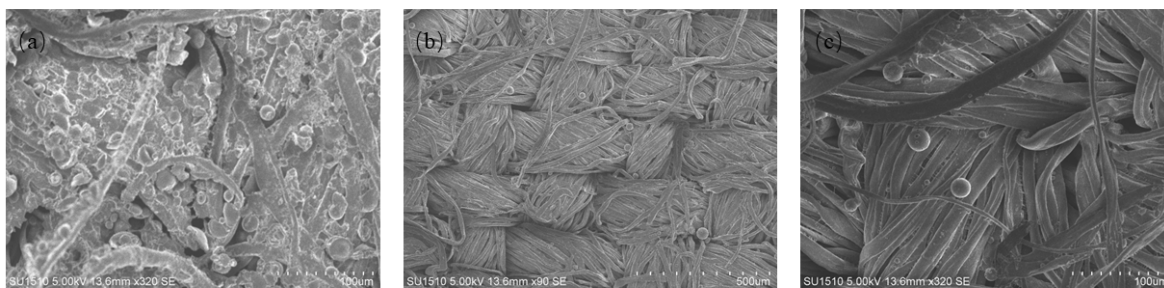After the fabric is completely faded, the UV irradiation time is increased in turn for 5 s, and the test is repeated 6 times until the color of the photochromic fabric is no longer deepened. In this way, the light saturation time of photochromic fabrics and the color depth of photochromic fabrics under UV light were explored.

The color of the photochromic fabric gradually deepened with increasing UV light time. The microencapsulated coated fabric has a fast photochromic effect under light and its fading rate is slow, indicating that the photochromic material treated by microencapsulation has a certain photochromic stability to the fabric. From Fig. 9 (a), it can be seen that with the increase of irradiation time, the K/S value of the photochromic fabric gradually increases and the color gradually becomes darker. In 30 s, the K/S value of the photochromic fabric reaches its maximum value and no longer increases significantly, indicating that the color of the photochromic fabric is saturated at this time, so the light saturation time is 30 s.
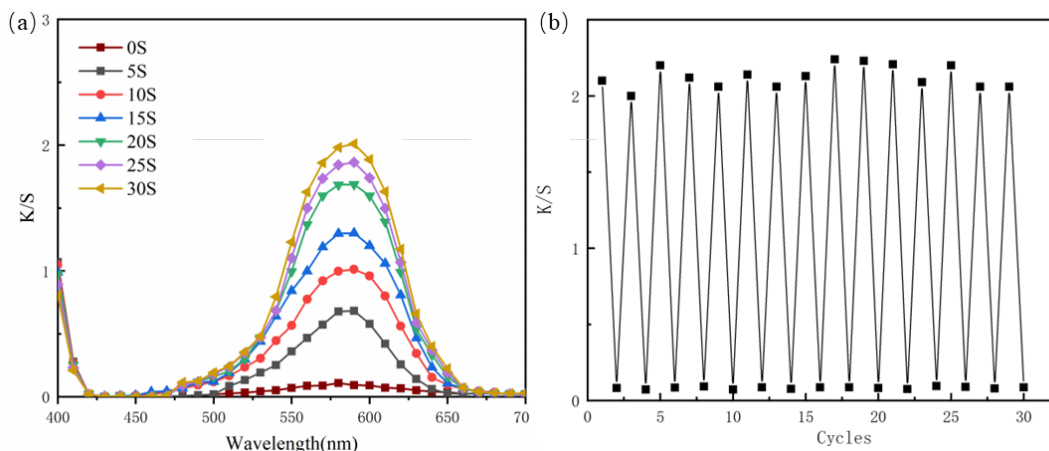
Fig. 9. K/S values of PMMA microcapsules under different UV light irradiation times (a); K/S values of PMMA microcapsules irradiated by UV-visible light cycle (b).

4. Conclusions

The best preparation process conditions for microcapsules with methyl methacrylate as the shell material covered with spiro-pyran photochromic dyes by solvent volatilization method are: the core-to-shell ratio is 2:1, the amount of emulsifier is about 2 % of the aqueous phase, and the temperature during volatilization should be controlled at about 35 °C. The microcapsules prepared in this way have high yield, complete morphology, good thermal stability, and good protection for the core material. The microcapsules present a regular spherical structure with a particle size of about 2 μm, sensitive to discoloration after UV irradiation, and the color reaches saturation in about 14 s. The microcapsules were printed onto the fabric and still had good color change properties after 30 cycles of UV irradiation and fading, indicating that the prepared microcapsules have good color change and fatigue resistance. These excellent properties will help it to be well applied in the field of smart garments.

Conflict of interest

The authors declare that they have no known competing financial interests or personal relationships that could have appeared to influence the work reported in this paper.

References

1. M. Raeesi, Z. Alinejad, V. Hamrang, and A. R. Mahdavian, J. *J Colloid Interf Sci*, **578** (2020) 379.
2. A. Julia-Lopez, D. Ruiz-Molina, J. Hernando, and C. Roscini, J. *Acs Appl Mater Interf*, **11** (2019) 11884.
3. B. Di Credico, G. Griffini, M. Levi, and S. Turni, J. *Acs Appl Mater Interf*, **5** (2013) 6628.
4. S. X. Wu, J. Fan, W. Wang, and D. Yu, J. *Colloid Surface A*, **632** (2022) 127760.
5. O. Topbas, A. M. Sariisik, G. Erkan, and O. Ek, J. *Iran Polym J*, **29** (2020) 117.
6. G. F. Zhang, T. Chen, C. Li, W. L. Gong, M. P. Aldred, and M. Q. Zhu, J. *Chinese J Org Chem*, **33** (2013) 927.
7. E. B. Kang, H. Cho, M. Z. A. Islamy, I. In, and S. Y. Park, J. *Surf Interface Anal*, **49** (2017) 759.
8. J. Kadokawa, Y. Tanaka, Y. Yamashita, and K. Yamamoto, J. *Eur Polym J*, **48** (2012) 549.
9. L. L. Si, Y. Y. Zhang, Y. J. Yin, and C. X. Chao, J. *Prog Org Coat*, **151** (2021) 106080.
10. A. Gerbreders, J. Teteris, E. Aleksejeva, and A. Danilovs, J. *J Optoelectron Adv M*, **11** (2009) 2155.
11. X. Xia, R. Shi, J. H. Huang, Y. B. Li, Y. Zuo, and J. D. Li, J. *J Appl Biomater Func*, **18** (2020).
12. K. Lv, D. Liu, W. Li, S. Tang, and X. Zhou, J. *Mol Cryst Liq Cryst*, **557** (2012) 217.
13. A. Sari, C. Alkan, and A. Karaipekli, J. *Appl Energ*, **87** (2010) 1529.
14. T. Feczko, O. Varga, M. Kovacs, T. Vidoczy, and B. Voncina, J. *J Photoch Photobio A*, **222** (2011) 293.
15. S. Ataei, A. Hassan, P. Azari, B. Pingguan-Murphy, R. Yahya, W. J. Basirun, and N. Shahabudin, J. *Smart Mater Struct*, **29** (2020).
16. R. Al-Shannaq, M. Farid, S. Al-Muhtaseb, and J. Kurdi, J. *Sol Energ Mat Sol C*, **132** (2015) 311.
17. F. Ahangaran, M. Hayaty, A. H. Navarchian, and F. Picchioni, J. *Polym Test*, **64** (2017) 330.
18. R. Barbaz-Isfahani, S. Saber-Samandari, and M. Salehi, J. *Int J Biol Macromol*, **200** (2022) 532.
19. X. M. Pan, R. Mercade-Prieto, D. York, J. A. Preece, and Z. B. Zhang, J. *Ind Eng Chem Res*, **52** (2013) 11253.
20. F. -L. Jin, and S. -J. Park, J. *J Ind Eng Chem*, **13** (2007) 608.
21. Q. Meng, S. L. Zhong, J. Wang, Y. Gao, and X. J. Cui, J. *Carbohyd Polym*, **300** (2023) 120265.

Resist Characteristic of Chemically Amplified Three-Component Novolac Resist Containing a Dissolution Inhibitor with Different Protection Ratio

Katsuaki Takashima and Hideo Horibe*

*Department of Chemistry and Bioengineering, Graduate School of Engineering,
Osaka Metropolitan University, 3-3-138 Sumiyoshi-ku, Osaka 558-8585, Japan*
**hhoribe@omu.ac.jp*

We have developed a three-component novolac resist incorporating a chemical amplification mechanism. The three components are a novolac resin, a dissolution inhibitor, and a photoacid generator. In this study, we investigated the change in dissolution rate and resist characteristic by reducing the number of protecting groups on the dissolution inhibitor. The dissolution inhibitor is a compound obtained by protecting some of the three hydroxyl groups of the dissolution accelerator (DA), which is a phenol derivative, with tBoc groups. From the dissolution rate of the polymer film, tBoc-DI-1(33%) in which one of the three hydroxyl groups was protected with tBoc group and DA showed dissolution promoting ability. tBoc-DI-2(67%) in which two of the three hydroxyl groups were protected with tBoc groups and tBoc-DI(100%) in which the three hydroxyl groups were completely protected exhibited dissolution inhibition ability. Mixtures of fully protected tBoc-DI(100%) and DA and tBoc-DI(X%) with randomly protected hydroxyl groups on DA have the same sensitivity, but the resolution of tBoc-DI(X%) was better. This is probably because tBoc-DI(100%) has a very large ability to suppress dissolution.
Keywords: Novolac resin, Dissolution inhibitor, Positive resist, Chemically amplified resist

1. Introduction

Semiconductors are used in various devices and have become essential to our lives. Semiconductors are required to have finer circuit patterns in order to achieve functionality and miniaturization [1-6]. Photoresist, a photosensitive polymer, can create fine patterns on the surface of semiconductors. Formation of a circuit pattern using a photoresist is generally performed by the following multiple processes. A resist film is applied to the oxide film on the silicon substrate. A pattern is formed by exposing the resist film through a mask, transferring the pattern, and developing the resist film. A circuit pattern can be formed by removing the exposed oxide film by etching, implanting ions, and removing the resist. Photoresists whose solubility in a developer change upon exposure are required to have improved sensitivity and resolution.

We have developed a three-component chemically amplified resist consisting of a base polymer, a dissolution inhibitor (DI), and a photoacid generator (PAG) [7,8]. The base polymer is a novolac resin, DI is a monomer that reacts with acid to become hydrophilic, and PAG is a compound that generates protons upon exposure. Before exposure, the resist does not dissolve in the developer due to the interaction between the novolac resin and DI [9-11]. After exposure, the acid generated from PAG reacts with DI, converting DI into a dissolution accelerator (DA). In the exposed area, the interaction between the novolac resin and DI is eliminated, and the resist becomes soluble in the developer because DA is hydrophilic. When DI changes to DA, protons are regenerated and act as catalysts. Mechanisms in which protons act as catalysts are called chemically amplified mechanisms [12-14]. The chemical amplification mechanism is expected to improve sensitivity and resolution compared to

two-component novolac resist: novolac resin and diazonaphthoquionone derivative [15-18]. DA can promote the solubility of the novolak resin in the exposed area of the chemically amplified three-component resist [19]. This is probably because DA, being a monomer, dissolves in the developer faster than the novolac resin, increasing the contact area between the novolac resin and the developer. In this study, we synthesized *t*Boc-protected DIs and investigated the changes in the solubility of the photoresist in developer by varying the protection rate, and attempted to improve the resist characteristic. We also investigated the solubility of a mixture of DI with a protection rate of 100% and DA with a protection rate of 0%, and improved the sensitivity while maintaining the resolution.

2. Experimental

m/p-Cresol Novolac (*m/p* = 6/4) resin (M_w 4,200-5,600) supplied by Asahi Yukizai Corp. was used as a base polymer. Propylene glycol monomethylether acetate (PGMEA) was used a solvent for base resin. 2-Methyl-α-[2-[[(propylsulfonyl)oxy]imino]-3(2H)-thienylidene]benzeneacetonitrile (product name : Irgacure PAG 103) was obtained from BASF and used as a photoacid generator. 2.38% of tetramethylammonium hydroxide (TMAH) aqueous solution was used as a developer. 4,4'-[1-[4-[1-(4-hydroxyphenyl)-1-methylethyl]phenyl]ethylidene]bis[phenol] was used as a DA. *t*Boc-DI was synthesized by reacting DA with di-*tert*-butyl dicarbonate in acetone in the presence of 4-dimethylaminopyridine (DMAP) [20]. The protection rate of *t*Boc-DI(X%) (X = 100, 91, 78,

68, 49) was adjusted by changing the stoichiometric amount of di-*tert*-butyl dicarbonate to DA. The *t*Boc-DI-1(33%) and *t*Boc-DI-2(67%) were purified by silica gel column chromatography. The chemical structure of *t*Boc-DI-1(33%), *t*Boc-DI-2(67%), and *t*Boc-DI(X%) are shown in Scheme 1. *t*Boc-DI-1(33%) is a compound in which one of the three hydroxyl groups is protected with a *t*Boc group, and *t*Boc-DI-2(67%) is a compound in which two of the three hydroxyl groups are protected with a *t*Boc group. *t*Boc-DI(X%) is a mixture of DA, *t*Boc-DI-1(33%), *t*Boc-DI-2(67%) and *t*Boc-DI(100%).

The polymer solution was prepared by dissolving novolac resin in PGMEA with a concentration of 23 wt%. *t*Boc-DI or DA was added to the polymer solution at a concentration of 0.1 to 0.5 mmol/g per weight of novolac resin. *t*Boc-DI(100%, 91%) and a mixture of *t*Boc-DI(100%) + DA were dissolved in polymer solution at 80 °C. Other DIs were dissolved in polymer solution at room temperature. The resist solution was then prepared by adding 3 wt% of the PAG to the polymer solution containing *t*Boc-DI.

The prepared solution was spin-coated on a three inches silicon wafer. After spin-coating, the wafer was prebake on a hot plate at 100 ℃ for 1 min. The film thickness remained solution was measured using stylus surface profilometer (Bruker Co. Ltd., Dektak XT). The prebake resist was then exposed and baked again at 100 ℃ for 2 min. All films were developed again with 2.38% of TMAH aqueous solution for 1 min. The film thickness remained after development was measured. The exposure conducted using M-1S (Mikasa Co. Ltd.).
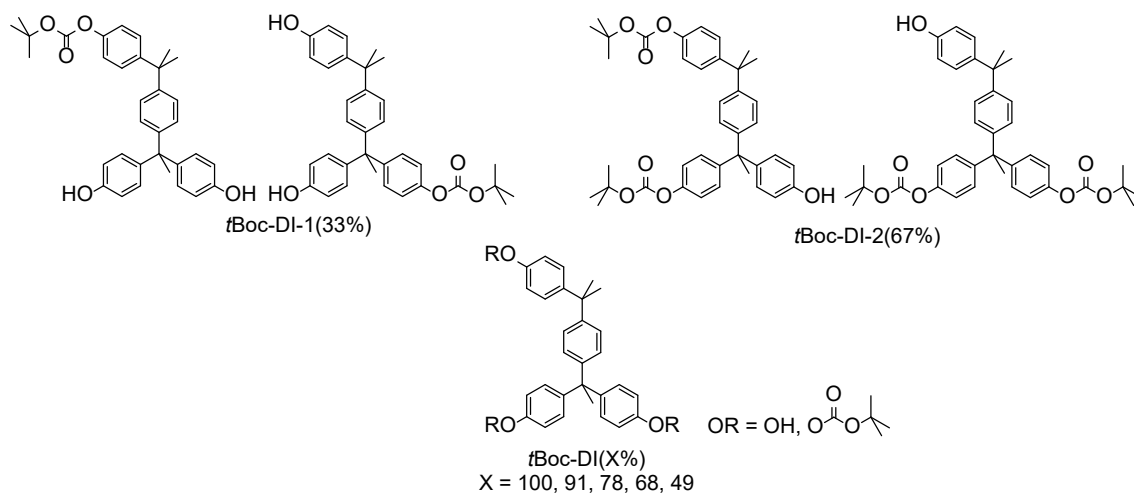
Scheme 1. Chemical structure of *t*Boc-DI-1(33%), *t*Boc-DI-2(67%), and *t*Boc-DI(X%).

3. Results and discussion

From the Alkali dissolution rate (ADR) of the polymer film containing *t*Boc-DI or DA, the ability of DI to inhibit dissolution of novolac resin was evaluated. ADR was calculated from the decrease in film thickness of polymer films developed under non-exposure. The correlation between the ADR of the polymer film and the amount of *t*Boc-DI(X%) per gram of polymer was shown in Fig. 1. ADR decreased with increasing amounts of *t*Boc-DI (X%) added. At a loading of 0.3 mmol/g of *t*Boc-DI (X%), at least about 80% of *t*Boc groups were required to inhibit dissolution of the polymer film. The ADR was similarly calculated for polymer films in which a mixture of *t*Boc-DI (100%) and DA was dissolved (Fig. 1). *t*Boc-DI (100%) + DA = Y% (Y = 100, 91, 78, 68, 49, 0) was added to the polymer solution so that the number of functional groups was the same as that of *t*Boc-DI(X%). As *t*Boc-DI(100%) + DA increased, dissolution of the polymer film could be suppressed. A loading of 0.3 mmol/g of *t*Boc-DI(100%) + DA required more than 68% of *t*Boc groups to prevent dissolution of the polymer film. The mixture of *t*Boc-DI(100%) + DA had a greater ability to inhibit dissolution than *t*Boc-DI(X%) at any protection rate. In addition, when the protection rate decreased, the difference in ADR between the mixture and *t*Boc-DI (X%) increased. This trend was attributed to the fact that *t*Boc-DI (X%) contained *t*Boc-DI-1(33%) and *t*Boc-DI-2(67%), while *t*Boc-DI (100%) + DA did not. From the difference in composition between tBoc-DI (X%) and DA + tBoc-DI (100%) and the results of ADR, tBoc-DI (100%) is expected to have a significantly greater ability to inhibit dissolution than *t*Boc-DI-1(33%) and *t*Boc-DI-2(67%).

Therefore, the ADR of polymer films containing *t*Boc-DI with different numbers of *t*Boc protecting groups was also investigated (Fig. 2). Increasing amounts of DA and *t*Boc-DI-1(33%) accelerated the dissolution of the film, while increasing amounts of *t*Boc-DI-2(67%) and *t*Boc-DI(100%) inhibited film dissolution. It was found that DI exhibits dissolution-enhancing ability when it has 0 or 1 *t*Boc group and exhibits dissolution-suppressing ability when it has 2 or 3 *t*Boc groups.
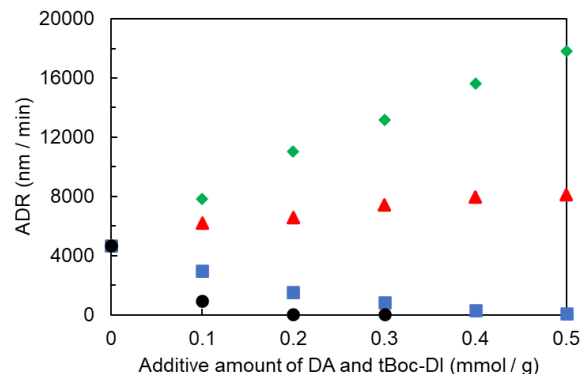
Fig. 2. ADR of polymer films containing DA(♦), *t*Boc-DI-1(33%)(▲), *t*Boc-DI-2(67%)(■), *t*Boc-DI(100%)(●).

The effect of protection rate of tBoc was investigated using *t*Boc-DI(X%) on resist characteristics. The sensitivity curve is shown in Fig. 3. Sensitivity improved as the protection rate decreased. At X = 100, 91 and 78, the sensitivities are 55, 50 and 45 mJ/cm^2, respectively. This is because DA and *t*Boc-DI-1(33%), which promote dissolution, tend to increase as the protection rate decreases.
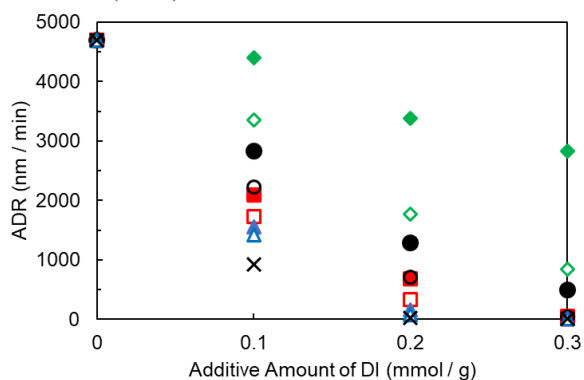
Fig. 1. ADR of polymer films containing *t*Boc-DI(X%) (X = 100(✕), 91(▲), 78(■), 68(●), 49(♦)), *t*Boc-DI(100%) + DA =Y% (Y = 91(△), 78(□), 68(○), 49(◇)).
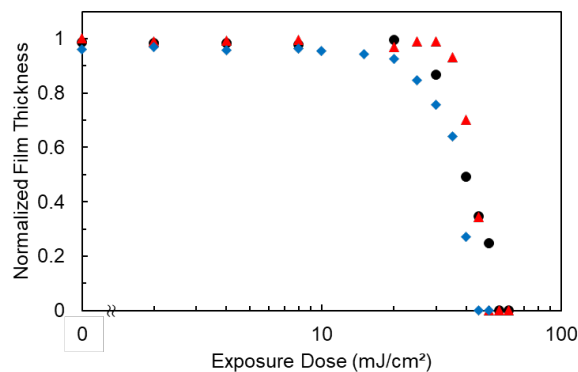
Fig. 3. Sensitivity curves of Novolac resist including *t*Boc-DI(X%) (X = 100(●), 91(▲), 78(♦)).

The sensitivity curve of the resist to which

tBoc-DI(100%) + DI = Y% was added is shown in Fig. 4. The smaller the value of Y, the better the sensitivity. At Y = 100, 91, 78, and 68, the sensitivities were 55, 50, 45, and 40 mJ/cm^2, respectively. As tBoc-DI(100%) is deprotected, the ability of DI to inhibit dissolution decreases. As the ratio of tBoc-DI(100%) becomes smaller, the ability to inhibit dissolution tends to become smaller. In addition, since the added amount of DA was increased, the resist sensitivity was improved.
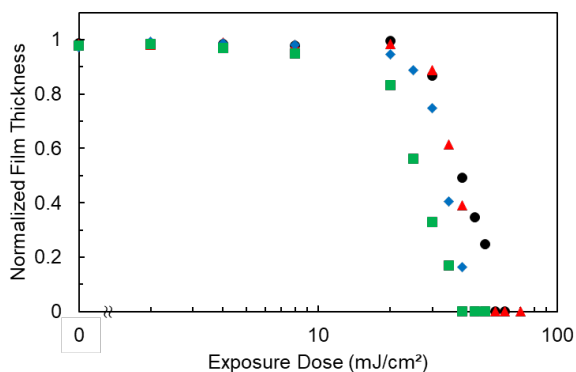
Fig. 4. Sensitivity curves of Novolac resist including tBoc-DI(100%) + DA = Y% (Y = 100(●), 91(▲), 78(◆), 68(■)).

There was no difference between Figs. 3 and 4, and tBoc-DI(X%) and tBoc-DI(100%) + DA = Y% with the same protection rate had the same sensitivity (Table 1). This is because tBoc-DI(100%) of the mixture is deprotected and becomes a state like tBoc-DI(X%), and both resists have almost the same dissolution rate in the exposed area.

Table 1. Sensitivity of Novolac resist containing tBoc-DI(X%) or tBoc-DI(100%) + DA.

tBoc-DI(X%)	X = 100	X = 91	X = 78	
Sensitivity (mJ/cm^2)	55	50	45	
tBoc-DI(100%) + DA = Y%	Y = 100	Y = 91	Y = 78	Y = 68
Sensitivity (mJ/cm^2)	55	50	45	40

Finally, the pattern of the photoresist for which the sensitivity curve was created was confirmed with an optical microscope (Figs. 5-10). Patterns were created by irradiating exposure doses 1.5-2.5 times the sensitivity. A pattern of 4 μm or 3 μm could be formed at any protection rate of tBoc-DI(X%) and at any ratio of tBoc-DI(100%) +

DA = Y%. However, incomplete 2μm patterns are formed in Figs. 6, 7, and 10. Therefore, the resist containing tBoc-DI(X%) has slightly better resolution than the resist containing tBoc-DI(100%) + DA. This difference is due to the difference in the dissolution rate of the exposed area. In the resist containing tBoc-DI(100%) + DA, a large amount of tBoc-DI(100%) exists in the exposed area. On the other hand, in the resist containing tBoc-DI(X%), tBoc-DI(100%) is less and tBoc-DI-1(33%) is relatively present in the exposed area. The results of ADR show that tBoc-DI(100%) has a large ability to inhibit dissolution, so tBoc-DI(100%) + DA has a relatively lower dissolution rate in the exposed area than tBoc-DI(X%). Even with tBoc-DI(100%) + DA = 68%, a relatively large amount of DA is present, and the dissolution speed of the exposed area is thought to be high. It is considered that a slight difference in resolution was observed due to the difference in the composition of the exposed portion.
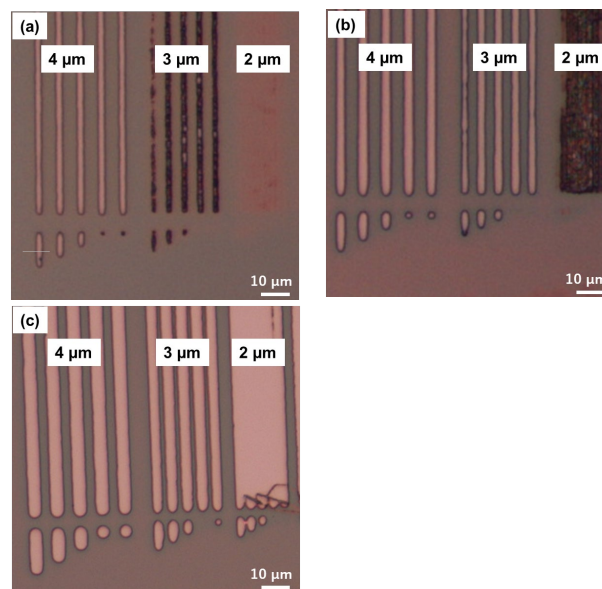
Fig. 5. Pattern image of resist containing tBoc-DI(100%) at an exposure dose of (a) Eth × 1.5 = 83 mJ/cm^2, (b) Eth × 2.0 = 110 mJ/cm^2, (c) Eth × 2.2 = 121 mJ/cm^2.
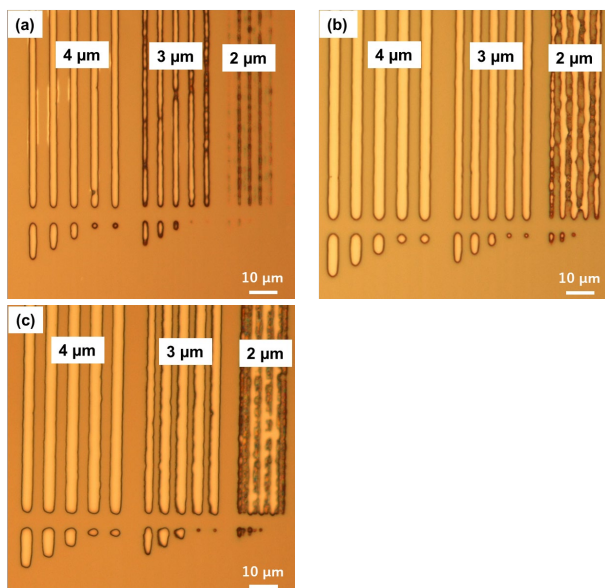
Fig. 6. Pattern image of resist containing *t*Boc-DI(91%) at an exposure dose of (a) Eth $\times$ 1.5 = 75 mJ/cm², (b) Eth $\times$ 2.0 = 100 mJ/cm², (c) Eth $\times$ 2.5 = 125 mJ/cm².

Fig. 8. Pattern image of resist containing *t*Boc-DI(100%) + DA = 91% at an exposure dose of (a) Eth $\times$ 1.5 = 75 mJ/cm², (b) Eth $\times$ 1.7 = 85 mJ/cm², (c) Eth $\times$ 2.0 = 100 mJ/cm².
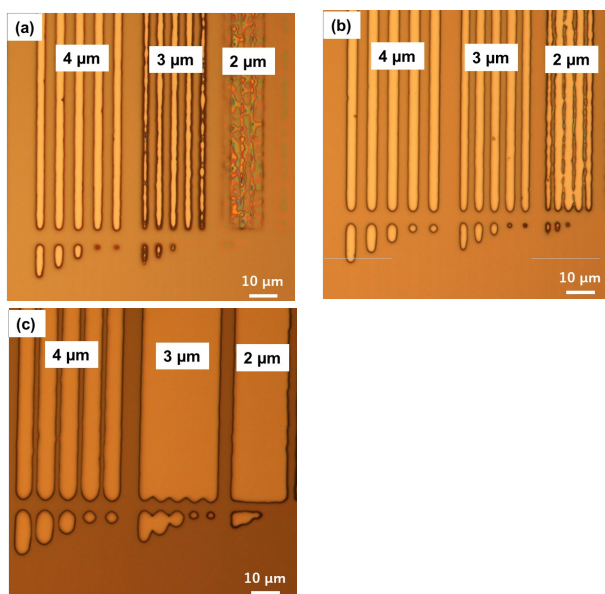
Fig. 7. Pattern image of resist containing *t*Boc-DI(78%) at an exposure dose of (a) Eth $\times$ 1.5 = 68 mJ/cm², (b) Eth $\times$ 1.7 = 77 mJ/cm², (c) Eth $\times$ 2.0 = 90 mJ/cm².
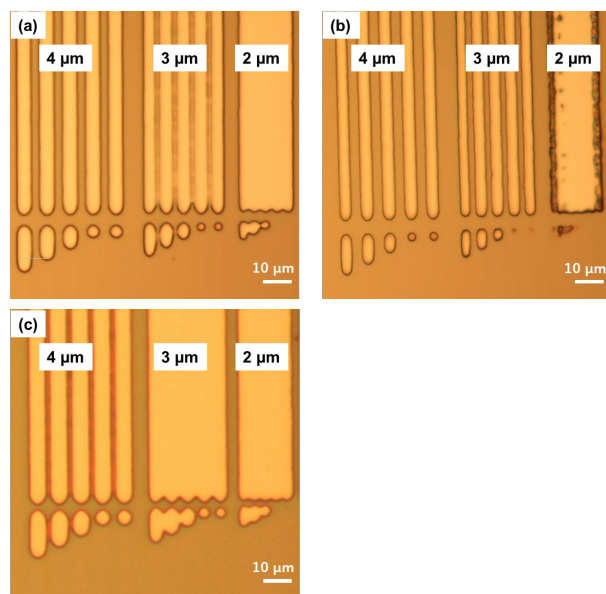
Fig. 9. Pattern image of resist containing *t*Boc-DI(100%) + DA = 78% at an exposure dose of (a) Eth $\times$ 1.5 = 68 mJ/cm², (b) Eth $\times$ 2.0 = 90 mJ/cm², (c) Eth $\times$ 2.2 = 99 mJ/cm².
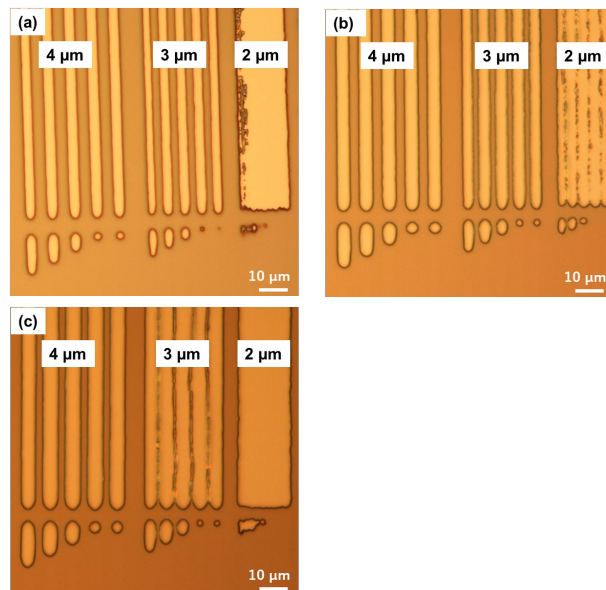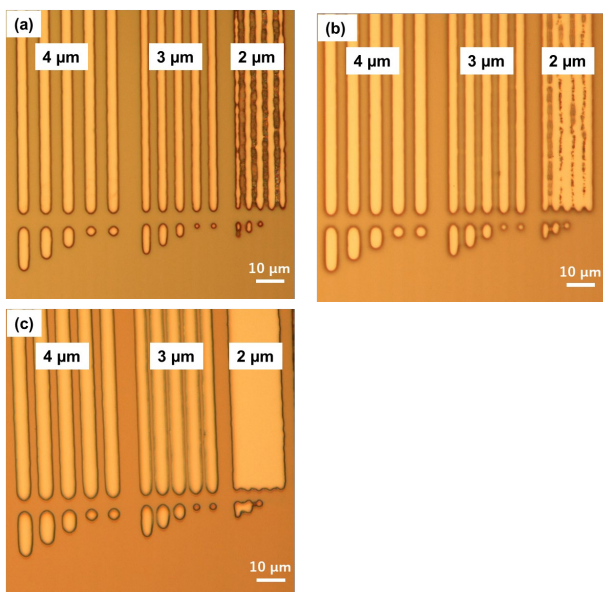
Fig. 10. Pattern image of resist containing tBoc-DI(100%) + DA = 68% at an exposure dose of (a) Eth $\times$ 1.8 = 54 mJ/cm^2, (b) Eth $\times$ 1.9 = 57 mJ/cm^2, (c) Eth $\times$ 2.0 = 60 mJ/cm^2.

4. Conclusion

A three-component novolac resist incorporating a chemical amplification mechanism was developed. The ability to inhibit dissolution decreased as the protective ratio of DI decreased and the ratio of DA increased. DA and tBoc-DI-1(33%) were found to promote dissolution, while tBoc-DI-2(67%) and tBoc-DI (100%) were found to inhibit dissolution. Even if the protection ratio of DI was lowered and the ratio of DA was increased, the sensitivity of the photoresist could be improved. Resist containing tBoc-DI(X%) gave slightly better resolution than resist containing tBoc-DI(100%) + DA due to a small difference in the dissolution rate of the exposed area.

References

1. R. Haruta, *J. Inst. Electri. Electron. Eng.*, **10** (2007) 353.
2. G. Mago, *J. Surf. Finish. Soc. Jpn.,* **65** (2014) 349.
3. K. Sakai, K. Nakahira, M. Ueda, and K. Kitami, *J. JSPE.*, **83** (2017) 125.
4. K. Takagi, *J. Surf. Finish. Soc. Jpn.*, **61** (2010) 350.
5. K. Torimyama, K. Okamoto, S. Kohara, and Y. Orii, *Trans JIEP.*, **14** (2011) 372.
6. R. Schaller, *IEEE Spectrum.*, **34** (1997) 52.
7. D. R. McKean, S. A. MacDonald, T. D. Johnson, N. J. Clecak, and C. G. Willson, *Chem. Mater.*, **2** (1990) 619.
8. L. Schlegel, T. Ueno, H. Shiraishi, N. Hayashi, and T. Iwatanagi, *Chem. Mater.*, **2** (1990) 299.
9. H. Y. Shih and A. Reiser, *Macromolecules*, **28** (1995) 5595.
10. M. Endo, M. Sasago, and K. Ogawa, *Kobunshi Ronbunshu*, **45** (1988) 771.
11. H. Honda, B. T. Seauchemin, Jr., R. J. Hurditch, A. J. Blakeney, Y. Kawabe, and T. Kokubo, *Proc. SPIE*, **1262** (1990) 492.
12. H. Ito, C. G. Willson, and J.M. J. Frechet, 1982 *Symposium on VLSI Technology*, Oiso, Japan, 1982.
13. H. Ito and G. G. Willson, *Polym. Eng. Sci.*, **23** (1983) 1012.
14. E. Reichmanis, F. M. Houlihan, O. Nalamasu, and T. X. Neenan, *Chem. Mater.*, **3** (1991) 394.
15. S. A. MacDonald, C. G. Willson, and J. M. J. Frechet, *Acc. Chem. Res.*, **27** (1994) 151.
16. K. Doki, H. Miyamoto, A. Tsuji, A. Matsumoto, K. Hasegawa, and A. Fukuda, *Kobunshi Ronbunshu*, **53** (1996) 231.
17. M. Hanabata and A. Fukuda, *Kobunshi Ronbunshu*, **45** (1988) 803.
18. A. Yokota, M. Nishida, M. Furuta, and S. Asaumi, *Kobunshi Ronbunshu*, **51** (1994) 309.
19. H. Ito, T. Nakatama, M. Sherwood, D. Miller, and M. Ueda, *Chem. Mater.*, **20** (2008) 341.
20. H. Horibe, T. Kumada, and S. Kubota, *Kobunshi Ronbunshu*, **53** (1996) 133.

Clarification of Degradation of Aromatic Compounds by Oxygen Microbubbles Water

Masaki Mizutani and Hideo Horibe*

Graduate School of Engineering, Osaka Metropolitan University,
3-3-138 Sugimoto, Sumiyoshi-ku, Osaka 558-8585, Japan
*hhoribe @omu.ac.jp

Microbubbles (MBs) are tiny bubbles with a particle size of 1 - 100 μm. It has been reported that MBs have excellent gas dissolving ability, and hydroxyl radicals are generated when microbubbles collapse in water. Therefore, we aimed to decompose persistent organic compounds using hydroxyl radicals generated by MBs collapse. In this study, we evaluated the degradation of the aromatic compounds methylene blue and salicylic acid by oxygen MBs water. Methylene blue was used as a hydroxyl radical detector, and we investigated the conditions under which hydroxyl radicals were generated most frequently. We confirmed that hydroxyl radicals were generated most frequently when oxygen MBs water generated by the gas-liquid revolving system was circulated under acidic conditions. The presence of cations such as copper and hydrogen ions affects the stability of MBs, and the shear stress caused by the swirling liquid flow is thought to promote MB crushing. Treatment of salicylic acid under these conditions reduced the Total Organic Carbon (TOC) of salicylic acid by about 40%. In addition ,From the intermediate products, we confirmed that salicylic acid and hydroxyl radicals undergo substitution reactions according to the orientation of the functional group.
Keywords: oxygen microbubble, hydroxyl radicals, methylene blue, salicylic acid

1. Introduction

MBs are tiny bubbles with a diameter of 1-100 μm and possess remarkable properties differing from those of normal bubbles. Firstly, rising speed of MBs in the water is slow, which follow scheme (Stokes equation) (1)).

$$u_B = \frac{d_B{}^2 (\rho_L - \rho_G)\, g}{18\, \mu_L} \qquad (1)$$

Rising speed of microbubbles is given as (1), where u_B is the rising speed and d_B is the diameter. In addition, ρ_L and ρ_G are liquid and gas density, μ_L is liquid viscosity coefficient and g is gravitational acceleration. Due to the large diameter of normal bubbles, they float quickly in water, reach the gas-liquid interface, and disappear after a few seconds. On the other hand, since the microbubbles have a small diameter, the rising speed is small, and the bubble collapses while shrinking. And,

microbubbles can efficiently dissolve internal gas with surrounding liquid because internal gas pressure is increased by surface tension at the gas-liquid interface [1,2]. The size of bubble affects the pressure difference between the inside and outside of the bubble. The equation (Young-Laplace equation, (2)) is shown below.

$$\Delta p = \frac{4\sigma}{d_B} \qquad (2)$$

The interfacial tension between gas phase and liquid phase is given as (2), where Δp is pressure difference between inside and outside, σ is the surface tension between water and air and d_B is the diameter of the bubble. From this equation, the smaller the diameter, the larger the pressure difference. Since microbubbles shrink over time, the pressure difference becomes larger. This effect is called the self-pressurization effect. The most

interesting property of MBs is their ability to generate hydroxyl radicals. A possible reason for the formation of hydroxyl radicals is the electric double layer, which has been reported to be negatively charged in water by zeta potential measurements. Therefore, MBs form an electric double layer consisting of hydroxide ions and cations in water, and it is thought that when MBs contract and collapse in water, the surrounding hydroxide ions react to form hydroxyl radicals (Fig.1). The standard redox potential of hydroxyl radicals is much higher than that of oxidants such as ozone and hydrogen peroxide. The hydroxyl radicals non-selectively decompose organic compounds. Therefore, it is thought that MBs are useful for decomposing persistent organic compounds [3-13].

In this study, the aromatic compounds methylene blue and salicylic acid were decomposed with oxygen MBs to confirm the effect of MBs [14-17].
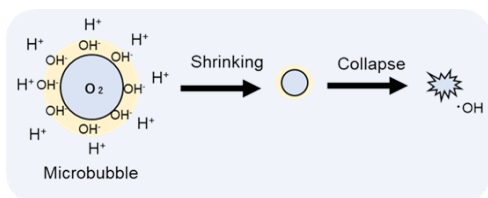
Fig. 1. Mechanism of hydroxyl radical generated from microbubbles.

2. Experimental
2.1. Oxygen MB generation systems

Fig. 2 shows a schematic diagram of the oxygen MB generator. MBs were generated using pressurized dissolution method (a) and the gas-liquid revolving method (b).

(a)Oxygen gas was dissolved by pressurizing with 0.5 MPa using a bellows pump (ΣP - 15 D - V, Sigma Technology Co.). An oxygen aqueous solution in a supersaturated state was generated and opened to the atmosphere through a dispersion nozzle to generate MBs.(All of this equipment is made of Teflon.)

(b)A gas-liquid two-phase swirling flow is generated in the nozzle, which is designed so that the swirling velocity increases as it approaches the center. When the gas-liquid is sucked in from the center of the nozzle, it is torn into small pieces by the swirling liquid flow and discharged externally from the discharge port. It collides with stationary gas-liquid outside the device, and the impact disperses the bubbles to generate MBs. (This device

has exposed copper and stainless steel.)

(a)
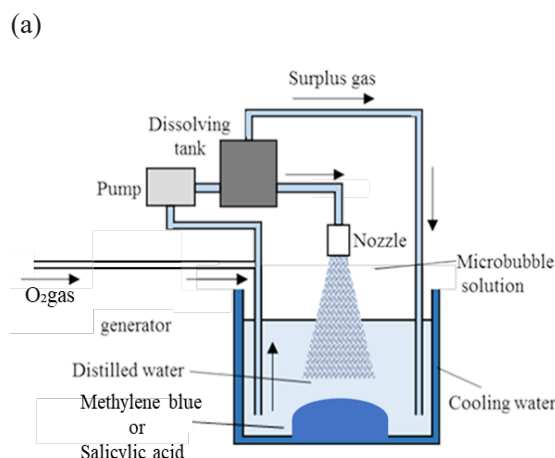
Fig. 2-a. Schematic illustration of oxygen MBs generation system using pressurized dissolution method.

(b)
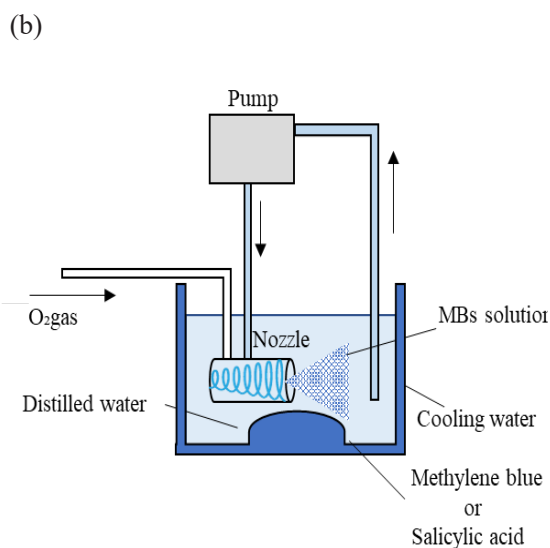
Fig. 2-b. Schematic illustration of oxygen MBs generation system using gas-liquid revolving method.

2.2. Decomposition treatment
2.2.1 Treatment method of methylene blue by oxygen MBs

Oxygen MBs were generated in 3 L of distilled water at a stabilized temperature of 15 ± 1 °C. A total of 0.01 mmol of methylene blue (Wako Pure Chemical Industries) was dissolved in the oxygen MBs water and stirred for 120 minutes. The decomposition rate and decomposition products of methylene blue were measured using Ultraviolet-Visible Absorption Spectroscopy (UV/Vis). The pH

of the aqueous methylene blue solution was adjusted using hydrochloric acid (4 mL, Wako Pure Chemical Industries). Additionally, the pressurized dissolution method involved treating copper sheets (100 cm², 0.5 mm) immersed in oxygen MBs water.

2.2.2 Treatment method of salicylic acid by oxygen MBs

Oxygen MBs were generated using the gas-liquid revolving method in 3 L of distilled water at a stabilized temperature of 15 ± 1 °C. Hydrochloric acid (4 mL) and 1 mmol of salicylic acid (Wako Pure Chemical Industries) were dissolved in the oxygen MBs water and stirred for 180 minutes. The degradation rate of salicylic acid was measured using High Performance Liquid Chromatography (HPLC), UV/Vis, and TOC. Additionally, Infrared Absorption Spectrometry (IR) and Nuclear Magnetic Resonance (NMR) were used to confirm changes in the chemical structure.

3. Results and Discussion

3.1. Detection of hydroxyl radicals with methylene blue

The UV/Vis peak of the methylene blue solution (665 nm) is presented in Fig. 3 Methylene blue is known to change its absorption wavelength at the UV/Vis peak by undergoing demethylation or substitution reactions with hydroxyl radicals [18-20]. Figure 4 illustrates the changes in aqueous methylene blue solution treated with oxygen MBs water under various conditions, showing the peak intensity change at 665 nm, the absorption wavelength of methylene blue, obtained by UV/Vis measurement. The greatest change in peak intensity was observed after 120 minutes of oxygen MBs water treatment when the sample was treated with oxygen MBs water in the gas-liquid revolving method under acidic conditions. This could be attributed to the crushing environment of the MBs

Fig. 4. Plot of A_t/A_0 , where A_t is the absorbance at 665 nm in UV/Vis with the treatment time, of methylene blue aqueous solution by oxygen MBs water (black),with HCl (blue),with copper plate (green),with HCl and copper plate (red).
(The solid line is the gas-liquid revolving method and the dashed line is pressurized dissolution method.)

where the metal is exposed, and shear stress is always present.

3.2.1 Decomposition of salicylic acid by oxygen MBs

Fig. 5,6,7 depict the HPLC ,UV/Vis, and TOC changes of the aqueous solution, respectively, when salicylic acid was decomposed in oxygen MBs water using the gas-liquid revolving method under acidic conditions (pH 2) for 180 minutes.

According to HPLC measurements presented in Fig. 5, salicylic acid was found to degrade by 60% after treatment with oxygenated MBs water. Dihydroxybenzoic acid was also observed as a decomposition product. Plus, the formation of

Fig. 3. The UV/Vis of methylene blue aqueous without treatment.
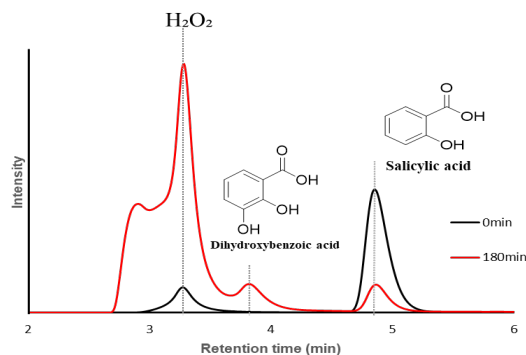
Fig. 5. HPLC chromatograms of untreated (black) and salicylic acid solution treated with oxygen MBs (red).

hyadrogen peroxide, which is believed to be a dimerization of OH radicals, was also detected.

UV/Vis measurements showed that the salicylic acid degraded by 35% after 180 minutes of treatment with oxygenated MBs water (Fig. 6). Additionally, the peak derived from salicylic acid was observed to shift to the long-wavelength side. Similar to the HPLC results, it is believed that salicylic acid underwent the substitution reaction with hydroxyl radicals to form dihydroxybenzoic acid.
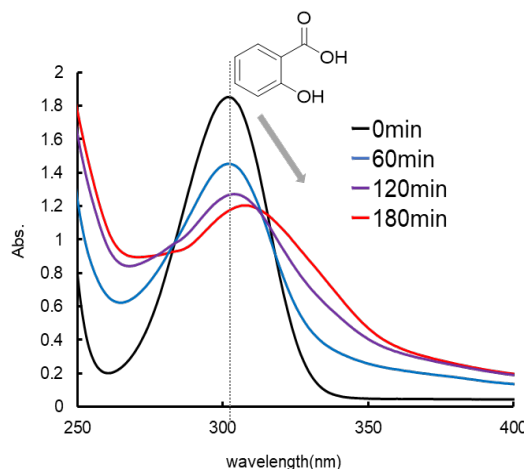
Fig. 6. The UV/Vis of salicylic acid aqueous treated with oxygen MBs for 180min.

Fig. 7 depicts the time course of total organic carbon (TOC) for salicylic acid solutions treated with oxygen MBs water. The experiments were conducted in triplicate, and the error bars indicate the range of error. It is evident from the figure that, after 180 minutes of treatment time, the TOC had decreased by 10-40%.
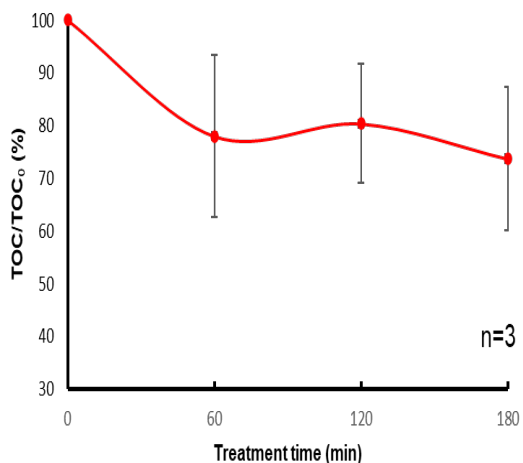
Fig. 7. TOC of aqueous solution of salicylic acid after the treatment by oxygen MBs water.

The degradation of salicylic acid by oxygen MBs water treatment was confirmed by HPLC, UV/Vis, and TOC analysis. However, to fully understand the degradation mechanism, it is essential to confirm any changes in the chemical structure of salicylic acid.

3.2.2 Changes in the chemical structure of treated salicylic acid

The alteration in the chemical structure of salicylic acid, subjected to oxygen MBs water treatment in the gas-liquid revolving system under acidic conditions, was verified by IR and NMR analyses.

To perform IR and NMR measurements, the treated salicylic acid solution was extracted using diethyl ether and the solvent was allowed to stand and evaporate. IR measurements showed no change in the functional group of salicylic acid treatment with oxygen MBs water (Fig. 8). Therefore, it is possible that aromatics similar in chemical structure to salicylic acid are formed.
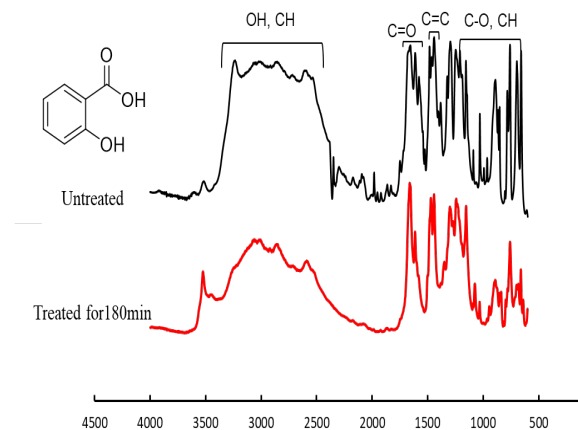
Fig. 8. FT-IR of untreated (black) and salicylic acid solution treated with oxygen MBs (red).

The NMR results for salicylic acid after 180 minutes of treatment are shown in Fig. 9. NMR of untreated salicylic acid and (2,3)(2,5)-dihydroxybenzoic acid are also shown. NMR measurements confirmed that treatment of salicylic acid with oxygen MBs produces dihydroxybenzoic acid with an attached hydroxyl group. The functional groups of salicylic acid, carboxy and hydroxyl groups, are meta oriented and ortho- and para- oriented, respectively. Therefore, the hydroxyl group was added to the 3- or 5-position of the benzene ring according to the orientation.
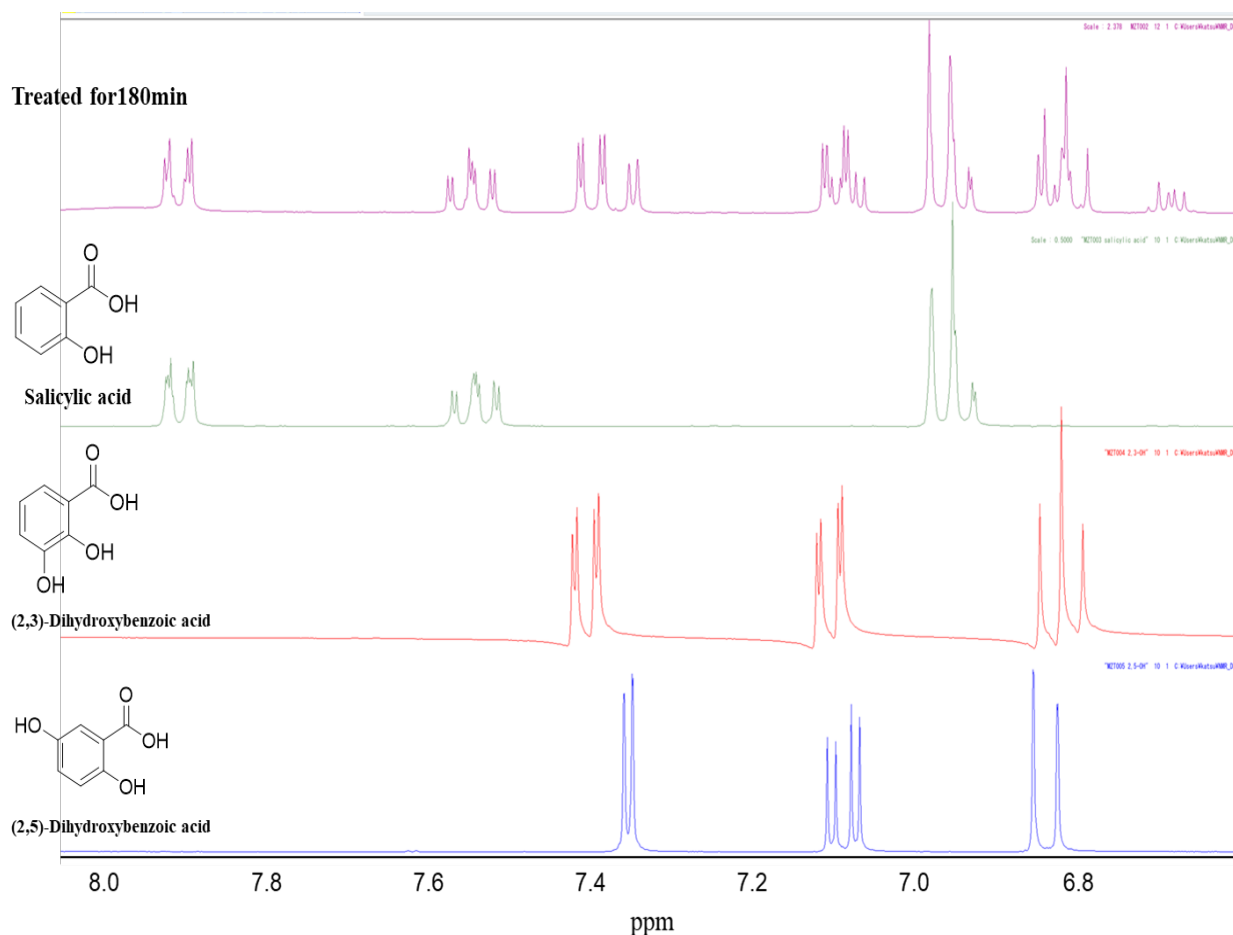
Fig. 9. NMR spectra of salicylic acid treated with oxygen MBs for 180 min and untreated salicylic acid and dihydroxybenzoic acid.

4. Conclusion

The results using methylene blue as a detection agent for hydroxyl radicals showed that oxygen MBs water generated by the gas-liquid revolving method under acidic conditions produced the highest amount of hydroxyl radicals. Since hydroxyl radicals are generated when MB decays, it is suggested that MB decays easily under acidic conditions and in the gas-liquid revolving method. It is believed that the presence of cations such as copper and hydrogen ions affects the stability of MBs, and that the shear stress caused by the swirling flow of the liquid promotes the MBs' disintegration.

When salicylic acid was treated for 180 minutes under the conditions that generated the most hydroxyl radicals, TOC was reduced by 40%. In addition, HPLC showed a 60% reduction in the peak and a 35% reduction in the UV/Vis peak. In addition, NMR measurements confirmed the formation of dihydroxybenzoic acid, although IR could not confirm this. Therefore, it is suggested that the hydroxyl radicals generated by the oxygen

MBs water undergo substitution reactions on the benzene ring according to the orientation of the functional group. In the future, we plan to extend the treatment time to investigate the extent to which hydroxyl radicals react with salicylic acid.

5. References
1. M. Takahashi, K. Chiba, and P. Li, *J. Phys. Chem. B*, **111** (2007), 1343.
2. P. Li, H. Tsuge, and K. Itoh, *Ind. Eng. Chem. Res*., **48** (2009), 8048.
3. H. Tsuge, Ed. *The Latest Technology on Microbubbles and Nanobubbles*, CMC Publishing Co.: Tokyo (2007), p 109.
4. J. S. Park, K. Kurata, *Hort. Tech.*, **19** (2009), 212.
5. F. De Smedt, S. De Gendt, M. Heyns, C. Vinckier, *J. Electrochem. Soc.*, **148** (2001), G487−G493.
6. H. Vankerckhoven, F. De Smedt, B. Van Herp, M. Claes, S. De Gendt, M. M. Heyns, C. Vinckier, *Ozone: Sci. Eng.*, **24** (2002), 391.

7. H. Vankerckhoven, F. De Smedt, M. Claes, S. De Gendt, M. M. Heyns, C. Vinckier, *Solid State Phenom*., **92** (2003), 101.

8. D. M. Knotter, M. Marsman, P. Meeusen, G. Gogg, S. Nelson, *Solid State Phenom*., **92** (2003), 223.

9. S. Noda, M. Miyamoto, H. Horibe, I. Oya, M. Kuzumoto, T. Kataoka, *J. Electrochem. Soc*., **150** (9) (2003), G537.

10. M. N. Kawaguchi, J. S. Papanu, B. Su, M. Castle, A. Ai-Bayati, *J. Vac. Sci. Technol*. B, **24** (2006), 657.

11. H. Horibe, M. Yamamoto, T. Ichikawa, T. Kamimura, S. Tagawa, *J. Photopolym. Sci. Technol*., **20** (2007), 315.

12. H. Horibe, M. Yamamoto, Y. Goto, T. Miura, S. Tagawa, *Jpn. J. Appl. Phys.*, **48** (2009), 026505.

13. Q. Wang, T. Shen and S. Tong, *Ind. Eng. Chem. Res.,* **55** (2016), 10513-10522

14. K. Matsuura, T. Nishiyama, E. Sato, M. Yamamoto, T. Kamimura, M. Takahashi, K. Koike, and H. Horibe, *J. Photopolym. Sci. Technol.*, **29** (2016) 623.

15. T. Nishiyama, K. Matsuura, E. Sato, N. Kometani, and H. Horibe, *J. Photopolym. Sci. Technol.*, **30** (2017) 285.

16. T. Miyazaki, E. Sato, and H. Horibe, *J. Photopolym. Sci. Technol.*, **31** (2018) 409.

17. G. H. Kelsall, S. Tang, A. L. Smith and S. Yudakul., *J. Chem. Soc., Faraday Trans,* **92** (1996), 3879-3885.

18. W Kuan, et al.,*J.Photoenergy*,849-916 (2013)

19. F. Ogata, Y. Uematsu, T. Nakamura, and N. Kawasaki, *Yakugaku Zasshi* **140**, 1463-1470 (2020)

20. H.H.K. Yoon, J.S. Noh, C.H. Kwon, M. Muhammed, M. Mater. *Chem. Phys*. **95** （2006） 79.

Erratum to "Synthesis, Properties, and Photovoltaic Characteristics of Arch- and S-shaped Naphthobisthiadiazole-based Acceptors" [J. Photopolym. Sci. Technol. 34 (2021) 285-290]

Hiroyuki Mayama

Editorial Office in Department of Chemistry,
Asahikawa Medical University,
2-1-1-1 Midorigaoka-higashi, Asahikawa, Hokkaido 078-8510 Japan

The author deeply apologize to Dr. Jinnai and Prof. Ie about the partially missing errors in Figs. 3 and 6 in the paper entitled "Synthesis, Properties, and Photovoltaic Characteristics of Arch- and S-shaped Naphthobisthiadiazole-based Acceptors Specific Interaction of Phospholipid Polymer with C-reactive Protein" in Vol. 34, No. 3 (2021), pages 285-290. The correct Figs. 3 and 6 should be as shown here.
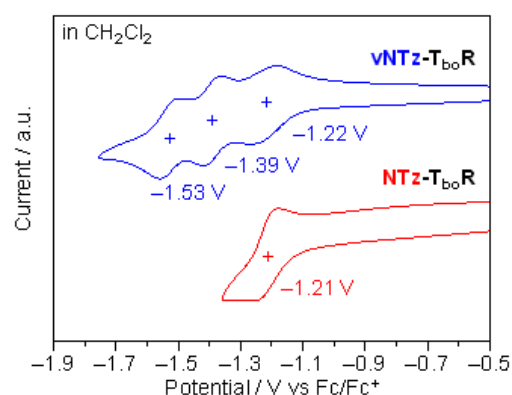
Fig. 3 Cyclic voltammograms of **vNTz-T$_{bo}$R** and **NTz-T$_{bo}$R**.
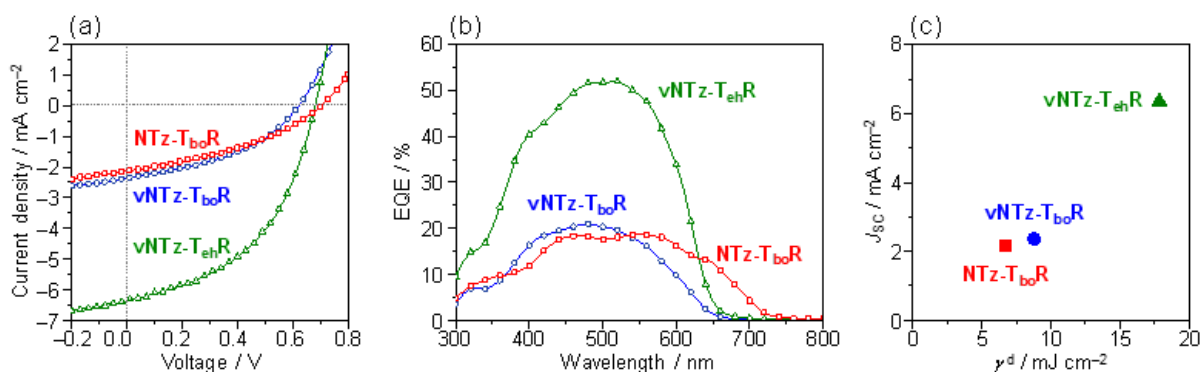
Fig. 6 (a) *J–V* characteristic and (b) external quantum efficiency spectra of OSC devices. (c) Plot of γ^d vs J_{SC} values for acceptor materials used in this study.

Technical Paper

Theory of Photodecomposable Base in Chemically Amplified Resist

Mark Neisser[1,2,*]

[1] *School of Integrated Circuits, Tsinghua University, Beijing, China*
[2] *International Innovation Center of Tsinghua University, Shanghai, N. 602 Tongpu Road, Putuo District, Shanghai, China*
*mark@neissers.net, markTHU@mail.tsinghua.edu.cn

Photo-decomposable bases (PDBs) are basic materials that turn into neutral ones photochemically. TWE calculate the slope of the latent acid gradient after base neutralization and before diffusion and show that this gradient is generally larger when PDB is used instead of traditional non-photosensitive quencher. The gradient generally improves as more PDB is added. Two different limiting cases are calculated; one where the PDB and PAG do not compete for photons or secondary electrons but instead photolyze independently and one where the do compete. The first case may be encountered in chemically amplified resists where the overall optical absorbance is low and photons react directly with the PAG and PDB. The second case is likely to encountered in EUV lithography where replacing conventional base with PDB does not change the EUV absorbance of the resist. The calculations show that the PDB will probably give a large improvement in latent acid gradient in the second case.
Keywords: Photo-decomposable base, Photoresist, PDB, EUV resist, latent image

1. Introduction

A photo-decomposable base (PDB) is a basic material that reacts with actinic light and decomposes to a neutral compound. When added to a chemically amplified resist, a PDB acts remains in the unexposed areas of resist but is decomposed in exposed areas. A prototype material like this is triphenyl sulfonium hydroxide, but other materials have been reported.[1] The hydroxide anion in triphenyl sulfonium hydroxide is quite basic. When photolyzed it turns into neutral sulfur containing compounds and water, thus destroying it as a base. These materials were first proposed as

of chemically amplified resists containing PDB along with some related simulations.

2. Mechanism of Action

Figure 1 shows an aerial image and the simulated concentrations of acid, blocked polymer and quencher (base) in a chemically amplified resist when printing 65nm lines and spaces with ArF immersion lithography. The simulation uses ordinary (non-photosensitive) quencher and assumed no acid diffusion in order to show the expected acid and base distribution after neutralization and before PEB. In the areas
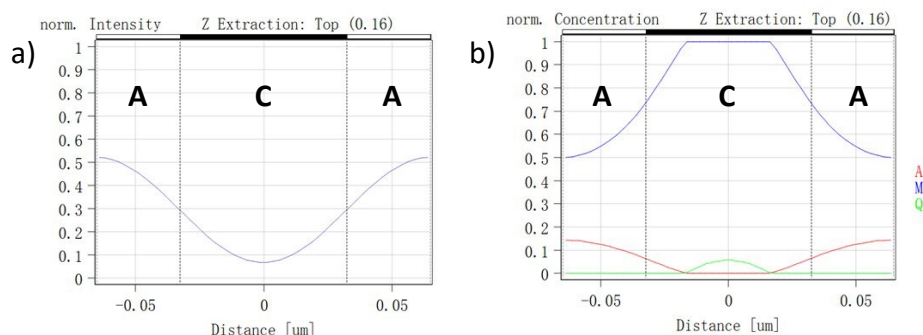
Figure 1: a) simulated 65nm line and space aerial image from ArF exposure b) Acid (A), base (Q) and polymer deprotection assuming no acid diffusion from the same aerial image

additives to chemically amplified resists by Funato et al.[2, 3] They reported that these materials improved the film stability and delay time stability of chemically amplified resists. Photo-speed was not reduced as much by the PDB as it was by an equivalent amount of conventional base. Nalamasu and coworkers also reported improved delay time stability[4] by using PDB as did Padmanaban and coworkers.[5] Other reports then suggested that use of PDB can improve depth of focus and profile [6] or improve line width roughness (LWR) or critical dimension uniformity (CDU).[7] Work reporting on the simulation of photoresists has shown that they can provide significant benefit to LWR.[8] In a series of papers, Kozawa reported molecular level simulations of the latent image after diffusion that explore the best diffusion properties and concentrations for the use of PDB in EUV and e-beam resists.[9-14]. This paper reports a theoretical study of the formulation parameters

labeled "A", which are the brightest areas of the image, the amount of photo-generated acid is much larger than the initial base concentration and neutralizes all of the base. In the dark area in the middle labeled "C" there was not enough acid to neutralize all of the base, so there is no acid concentration in the C region and no polymer deprotection took place.

What happens if PDB is used instead of regular quencher? In the dark area "C" either the PDB will photolyze or the PAG will photolyze but if the exposure is not enough to either create enough acid to neutralize all the PDB or to remove all the PDB then there will not be any acid remaining in those areas and no polymer deprotection will occur. In the bright areas "A", as long as there is more than enough dose to remove all the base or to generate enough acid to neutralize all the base, there will be residual acid in these areas that can catalyze polymer

deprotection. Just like in the case of regular quencher, the areas "A" will have acid but no base and the area "C" will have base but no acid. Unless there is a difference in the image transition zones between dark and light, the PDB will give the same result as conventional base. The literature is clear that substituting PDB for conventional quencher improves photospeed for a given base concentration. If you can load more base for a given photospeed into a resist, one would expect better delay stability. This matches the observations that formulations with PDB have better delay stability. So there is some difference in the transition zones. Should we expect any other difference between the two types of quencher? We address this question below by calculating the slope of the acid concentration after neutralization but before diffusion and polymer deprotection.

3. Calculation assuming PDB and PAG exposure is independent

Assume that the photogenerated acid reacts with base immediately after exposure but that acid diffusion, and base diffusion and polymer deprotection don't happen until the temperature is raised during the PEB. Then the concentration of acid and base are defined by these equations where x is the position across the feature, E(x) is the exposure dose at a particular x position, $[PAG]_0$ is the initial PAG concentration, $[PDB]_0$ is the initial PDB concentration, C_{PAG} is the Dill parameter C for the PAG, C_{PDB} is the Dill parameter C for the PDB, $[PAG]_{E(x)}$ is the concentration of PAG after receiving dose E(x) and $[PDB]_{E(x)}$ is the concentration of PDB after receiving dose E(x). $[H^+]_0$ is the concentration of acid before neutralization and $[H^+]$ is the concentration after reacting with base.

$$[PAG]_{E(x)} = [PAG]_0 \, e^{-C_{PAG}E(x)} \quad \text{and}$$
$$[PDB]_{E(x)} = [PDB]_0 \, e^{-C_{PDB}E(x)}$$

The amount of acid generated is

$$[H^+]_0 = [PAG]_0 (1 - e^{-C_{PAG}E(x)})$$

For the moment, assume that the actual absorbances of both the PAG and PDB are relatively low so that replacing regular quencher with PDB adds absorbance and the PAG and PDB both absorb a similar amount of light in the presence of each other as they would if they were in the resist by themselves. This is probably a reasonable assumption for KrF and ArF resists; but, as discussed below, is probably not reasonable for EUV resists. Then, the total acid after neutralization is the initial concentration of acid minus the unreacted PDB.

$$H^+ = [PAG]_0 (1 - e^{-C_{PAG}E(x)}) - [PDB]_0 e^{-C_{PDB}E(x)} = PAG_0 - PAG_0 e^{-C_{PAG}E(x)} - PDB_0 e^{-C_{PDB}E(x)}$$

Note that if this value is negative, it reflects more base than acid is present. If the base is not photosensitive, then this equation reduces to the following, where $[Base]_0$ is the initial concentration of added base.

$$H^+ = [PAG]_0 - PAG_0 e^{-C_{PAG}E(x)} - Base_0$$

Taking the derivative with respect to x results in equation 1 below
(1)
$$d[H^+]/dx = C_{PAG} \, dE(x)/dx \, (PAG_0) e^{-C_{PAG}E(x)}$$

Where $d[H^+]/dx$ is the slope of the acid concentration at position x before diffusion. For PDB, if the C value for the PDB is the same as for the PAG then equation 2 results after replacing C_{PDB} by C_{PAG}:
(2)
$$d[H^+]/dx = C_{PAG} \, dE(x)/dx \, (PAG_0 + PDB_0) e^{-C_{PAG}E(x)}$$

Comparing equations 1 and 2, one can see that the acid gradient before diffusion will be larger when PDB is used instead of regular quencher if the C values are equal. If this translates into also having a larger acid gradient after diffusion this should provide less LWR.[15] This matches the results of Smith and Biafore, who

reported better LWR for simulated resists that

Figure 2: Latent image slope ratio (LISR) as a function of the ratio of PDB loading to PAG. Different lines indicate the ration of C_{PDB} relative to C_{PAG}. 3a) calculated for 30% PAG conversion 3b) 50% PAG conversion 3c) 70% PAG conversion

used PDB instead of conventional base.

Consider the case where the PAG and PDB do not react with light at the same rate. Let C_{PDB} be n times C_{PAG}. From before we have

$$H^+ = PAG_0 - PAG_0 e^{-C_{PAG}E(x)} - PDB_0 e^{-C_{PDB}E(x)}$$

Differentiating,

$$d[H^+]/dx = dE(x)/dx (C_{PAG}PAG_0 e^{-C_{PAG}E(x)}) + dE(x)/dx (C_{PDB}PDB_0) e^{-C_{PDB}E(x)})$$

$$d[H^+]/dx = dE(x)/dx (C_{PAG}PAG_0 e^{-C_{PAG}E(x)}) + dE(x)/dx (nC_{PAG}PDB_0) e^{-nC_{PAG}E(x)})$$

Giving equation 3

(3)
$$d[H^+]/dx = dE(x)/dx * C_{PAG} * e^{-C_{PAG}E(x)}(PAG_0 + n * PDB_0 * e^{-(n-1)C_{PAG}E(x)})$$

In order to simplify, remember that $e^{-C_{PAG}E(x)}$ is a fraction that represents how much PAG remains unexposed at position x, and call this number PPR (percent PAG remaining). Define the ratio of starting PDB and PAG concentrations as f = [PDB]$_0$/[PAG]$_0$. We can divide equation 3 by equation one to get the ratio of the acid gradient before diffusion with PDB to the gradient with conventional base, which is the latent image slope ratio or LISR. Then:

$$LISR = (\frac{PAG_0}{PAG_0}) + (n * PDB_0/PAG_0 * e^{-(n-1)C_{PAG}E(x)}$$

$$LISR = 1 + (n * f * e^{-nC_{PAG}E(x)})/e^{-C_{PAG}E(x)}$$

$$LISR = 1 + (n * f * PPR^n)/PPR$$

We can use this equation to understand the effects of various formulation parameters. Figure 2 shows the effect of different PDB loading on the improvement in the latent image slope before diffusion gained by using PDB. As the loading of PDB relative to PAG increases, the latent image slope improves. This improvement is not sensitive to the ration of C_{PDB} to C_{PAG} nor is it sensitive to the amount of PAG conversion. If a typical conventional base loading is 10% to 20%, there will be some
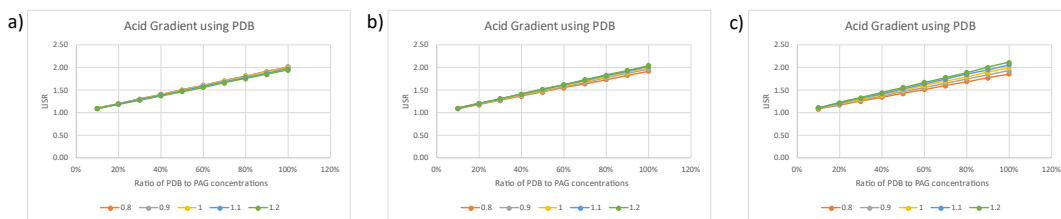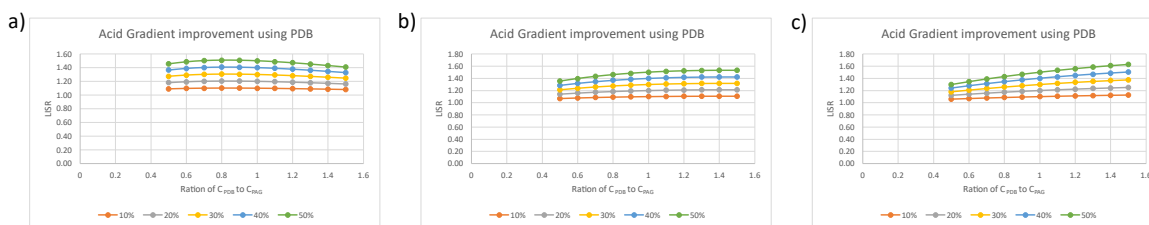

Figure 3: Latent image slope ratio (LISR) as a function of the ratio of C_{PDB} to C_{PAG}. Different lines indicate loading of PDB relative to PAG. 3a) calculated for 30% PAG conversion 3b) 50% PAG conversion 3c) 70% PAG conversion

improvement in latent image slope, by using PDB but a larger amount of PDB will be better. Figure 3 shows the dependance of the improvement using PDB on the ration of C_{PDB} to C_{PAG}. There is not much sensitivity unless the x position is such that the PAG is mostly converted to acid. As discussed below, lower PAG conversions are more likely. So as long as the PDB converts photochemically at a rate within 50% of that the PAG, a significant latent image slope improvement should result from using PDB.

4. Calculation where PDB and PAG exposure competes

In the calculations above, it was assumed that adding PDB instead of conventional base added absorption to the resist and thus the C_{PAG} and C_{PDB} values determined independently for the two photosensitive materials could be assumed to be independent when the two materials are together in the same formulation. But this may not be the case in some situations, particularly for EUV resists. In EUV resists the entire matrix of the resist absorbs EUV photons and then generates secondary electrons which will react with the PDB and PAG. Adding PDB instead of conventional base will not increase light absorption. The PDB and PAG will then probably compete to react with the primary and secondary electrons generated by the EUV absorption. Under these conditions the effective dose for the PDB and PAG will be reduced by the absorption of the other photosensitive component. Define p as the fraction of the incident photons or electrons that the PDB captures compared to what the PAG captures. This reaction ratio isn't specified by the variables already considered. But C values are related to absorption and the quantum yield. For EUV, the matrix mostly absorbs photons and then generates secondary electrons. Making the approximation that the PDB and PAG both generate base and acid efficiently once reacting with an electron, then one can approximate the ration of absorbances by the ratio of the C values. For ArF or KrF, the absorption values and quantum yields could both be different from

each other and this may not be as good an assumption.

Then, at the start of exposure, the PDB will receive a dose of

$$\frac{C_{PDB}}{C_{PDB} + C_{PAG}} * E(x) = p * E(x)$$

And the PAG will receive a dose of

$$\frac{C_{PAG}}{C_{PDB} + C_{PAG}} * E(x) = (1 - p) * E(x)$$

As the exposure continues, the ratio of remaining PAG and PDB could change, with the photosensitive material that reacts faster reducing its concentration relative to the other one. This will change the reactance ratio and adjust it so there is less difference in reaction rates. That would be more like the case examined before. So let's assume this ratio is fixed and use the math below to estimate how much competition for photons or secondary electrons could change the effects of PDB addition. This should be the limiting case for this mechanism. Using similar logic as before, one obtains

$$H^+ = PAG_0 - PAG_0 e^{-C_{PAG}*(1-p)*E(x)} - PDB_0 e^{-C_{PDB}*p*E(x)}$$

And differentiating,

$$d[H^+]/dx = dE(x)/dx (C_{PAG} * (1 - p) * PAG_0 * e^{-C_{PAG}*(1-p)*E(x)}) + dE(x)/dx (C_{PDB} * p * PDB_0)e^{-C_{PDB}*p*E(x)}$$

If C_{PDB} is a multiple of C_{PAG}, say n * C_{PAG}, then this gives equation 3.

Figure 4: Latent image slope ratio (LISR) as a function of the ratio of PDB loading to PAG assuming competition between PAG and PDB for photoreaction.   Different lines indicate the ration of C_{PDB} relative to C_{PAG}. 3a) calculated for 30% PAG conversion 3b) 50% PAG conversion 3c) 70% PAG conversion

$$d[H^+]/dx = dE(x)/dx (C_{PAG} * (1-p) * PAG_0 * e^{-C_{PAG}*(1-p)*E(x)}) + dE(x)/dx (n * C_{PAG} * p * PDB_0)e^{-n*C_{PAG}*p*E(x)}$$

(3)

$$d[H^+]/dx = dE(x)/dx * C_{PAG} * e^{-C_{PAG}*E(x)} * ((1-p) * [PAG]_0 e^{-C_{PAG}*p*E(x)} + n * p * PDB_0 * e^{-(np-1)*C_{PAG}*E(x)})$$

In this case the percentage PAG remaining will be $e^{-C_{PAG}*(1-p)*E(x)} = PPR'$ (to differentiate it from the previous definition of PPR). The equation for the case of no PDB is the same equation 1 as before.

(1)

$$d[H^+]/dx = C_{PAG} * dE(x)/dx * (PAG_0) * e^{-C_{PAG}E(x)}$$

Dividing equation 3 by equation 1 gives the LISR, the improvement in slope by substituting PDB for conventional quencher.

$$LISR = ((1-p) * [PAG]_0 * e^{-C_{PAG}*p*E(x)} + \frac{n*p*([PDB]_0)}{[PAG]_0}) * e^{-(np-1)*C_{PAG}*E(x)})$$

Substituting as before we get equation 4

$$LISR = (1-p)/PPR' + (n * p * f * PPR'^{np})/PPR'$$

So far, we have not derived p, but if we use the assumption described above, we can relate p to n.   Simple math shows that then p = n/(n+1). We can then calculate the LISR as before, except that we use PPR' instead of PPR.   The results are shown in Figure 4.

When the PAG conversion is low, the improvement in the latent image slope is better than calculated before, but when the PAG conversion is high it is worse.   How much PAG conversion is expected?   Figure 6 shows the unexposed PAG concentration as a function of position for the simulations shown in figure 1. Most of the PAG is not converted to acid.   The maximum conversion to acid is around 40%. Figure 4a is thus probably a more realistic case than 4b or 4c. The values of LISR in Figure 4a are bigger than the values in figure 2a. Note that no matter what percent of PAG is decomposed, in all cases a higher PDB loading gives a better improvement in the latent image log slope.
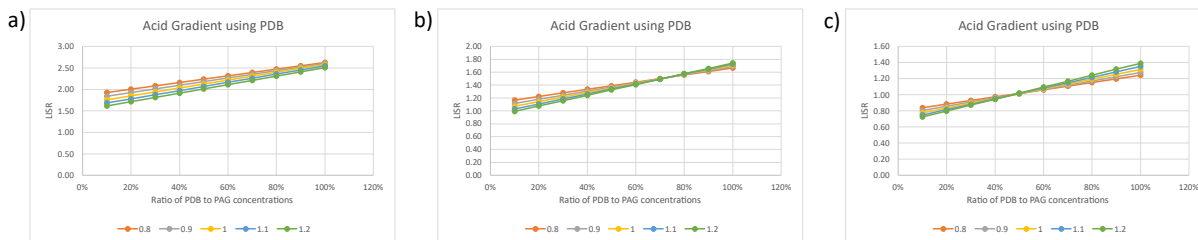

Figure 5: Latent image slope ratio (LISR) as a function ratio of the ratio of C_{PDB} to C_{PAG} assuming competition between PAG and PDB for photoreaction. Different lines indicate loading of PDB relative to PAG. 3a) calculated for 30% PAG conversion 3b) 50% PAG conversion 3c) 70% PAG conversion

(4)
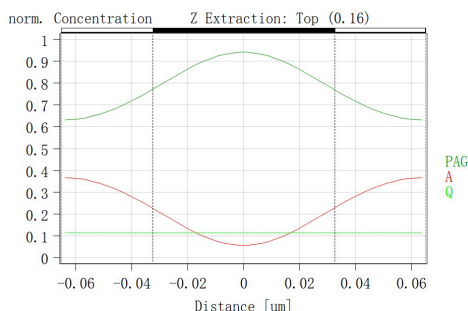
Figure 6: a) Acid, PAG and quencher concentrations after exposure and before neutralization and deprotection, in the case corresponding to figure 1.

This result suggests that PDB will provide a bigger boost in latent image slope when the PAB and PDB compete for photodecomposition. PDB may be more effective in EUV resists than ArF or KrF ones. Also, in EUV, unlike ArF or KrF, using PDB instead of conventional base will most likely not affect EUV absorbance of the resist significantly. The added absorbance might be expected to affect resist characteristics such as sidewall slope in KrF or ArF resists but is not expected to do so for EUV resists.

We can also examine the ratio of C_{PDB} to C_{PAG} for resists where PAG and PDB compete for decomposition. This is shown in figure 5. The effect of percent PAG conversion is more pronounced than the result in figure 3. As discussed above, the 30% or 50% cases are probably more realistic at the feature edge. A high C_{PDB} compared to C_{PAG} does not seem necessary for a beneficial effect.

It should be noted that there seems to be no data on the C values for PDBs in the literature nor any test procedure for determining them. There also is no data on relative reaction rates when both are present in a photoresist. Such data would be useful in examining which cases analyzed above are applicable to what types of resist.

5. Conclusions

Examining the effect of PDB compared to ordinary quencher, we find that PDB compared

to conventional base increases the acid gradient in the boundary regions between light and dark. This would be expected to improve the LWR of patterned resist. Such an improvement would is valuable for ArF resist and more valuable for EUV resist. The amount of improvement in the acid gradient depends on whether the PDB and PAG compete for photons or compete for photogenerated electrons. When the presence of one reduces the photolysis of the other, the effect of adding PDB compared to conventional base is larger. In EUV, not only are photons scarce, but the entire photoresist matrix absorbs EUV photons and generates electrons that cause the PAG and PDB to decompose. Given a fixed and limited number of electrons produced by exposure, the presence of PDB should reduce the rate at which the PAG generates acid. The mathematics above suggests that PDB will therefore be more effective in reducing EUV LWR than in reducing ArF LWR.

6. Acknowledgement

References

[1] C. Liu and C. Chang, US patent application 2014/0011133 A1, pany ublished January 9, 2014.

[2] Satoru Funato, N. Kawasaki, Yoshiaki Kinoshita, Seiya Masuda, Hiroshi Okazaki, Munirathna Padmanaban, T. Yamamoto, Georg Pawlowski, "Application of photodecomposable base concept to two-component deep-UV chemically amplified resists," Proc. SPIE 2724, Advances in Resist Technology and Processing XIII, (14 June 1996); https://doi.org/10.1117/12.241816

[3] S. Funato, Y. Kinoshita, T. Kudo, S. Masuda, H. Okazaki, M. Padmanaban,K. J. Przybilla, N. Suehiro, and G. Pawlowski, J. Photopolym. Sci. Technol., 8, 543 (1995).

[4] O. Nalamasu, F. M. Houlihan, R. A. Cirelli, A. G. Timko, G. P. Watson, R. S. Hutton, J. M. Kometani, E. Reichmanis, A. Gabor, A. Medina, and S.Slater, J. Vac. Sci. Technol. B 16, 3716 (1998).

[5] Munirathna Padmanaban, Jun-Bom Bae, Michelle M. Cook, Woo-Kyu Kim, Axel Klauck-Jacobs, Takanori Kudo, M. Dalil Rahman, Ralph R. Dammel, Jeff D. Byers, "Application of photodecomposable base concept to 193-nm resists," Proc. SPIE 3999, Advances in Resist Technology and Processing XVII, (23 June 2000); https://doi.org/10.1117/12.388278

[6] S. F. Chen, L. L. Chang, Y. H. Chang, C. C. Huang, C. Y. Chang, and Y. Ku, Proc. SPIE 8325, 83250O (2012)

[7] J. Thackeray, J. Cameron, V. Jain, P. LaBeaume, S. Coley, O. Ongayi, M. Wagner, A. Rachford, and J. Biafore, J. Photopolym. Sci. Technol. 26, 605 (2013).

[8] John J. Biafore, Mark D. Smith, "Application of stochastic modeling to resist optimization problems," Proc. SPIE 8325, Advances in Resist Materials and Processing Technology XXIX, 83250H (14 March 2012); https://doi.org/10.1117/12.916518

[9] Takahiro Kozawa 2014 Jpn. J. Appl. Phys. 53 066508.

[10] Takahiro Kozawa et al 2017 Jpn. J. Appl. Phys. 56 066501.

[11] Takahiro Kozawa 2015 Jpn. J. Appl. Phys. 54 056502.

[12] Takahiro Kozawa 2017 Jpn. J. Appl. Phys. 56 046502.

[13] Takahiro Kozawa 2015 Jpn. J. Appl. Phys. 54 126501.

[14] Takahiro Kozawa et al 2018 Jpn. J. Appl. Phys. 57 056501.

[15] Takahiro Kozawa et al 2010 Appl. Phys. Express 3 036501.

Manipulation of Polymer Solubility: Crosslinking, Thermal Activation and Variable-Temperature Bakes

Jacob Sitterly, Justin Nhan and Robert Brainard*

State University of New York Polytechnic Institute, 257 Fuller Rd. Albany, NY 12203
* rbrainard@sunypoly.edu

A two-layer polymeric stack is designed to be converted to a three-layer stack using sequential bakes. The three-layer stack is composed of layers that are (bottom to top): insoluble, soluble, and insoluble in 0.26 N TMAH developer. The two-layer stack is composed of a bottom layer that is a 193-nm positive tone resist containing a thermal acid generator (TAG) and, optionally, a crosslinker. The top layer contains a t-butyl acrylate monomer that can be deprotected by catalytic acid. During the sequential bakes, the TAG is designed to decompose to generate an acid that diffuses into the top layer. Diffusion lengths of 20-30 nm have been demonstrated. Additionally, the Arrhenius activation parameters are described for the acid-catalyzed deprotection of two esters in combination with strong and weak sulfonic acids. Surprisingly, the rates of these reactions are dictated more by their entropy than by their enthalpy.
Keywords: Polymer, Solubility, Development, Deprotection, Crosslinking, Thermal acid generator

1. INTRODUCTION

Controlling the solubility of polymer films is essential to many pattering schemes used in the manufacture of integrated circuits [1-4]. Two ubiquitous polymer films are the chemically amplified positive- and negative-tone photoresists. Conventional positive-tone chemically-amplified photoresists are initially insoluble in aqueous developer. Through exposure and generation of strong acids that catalyze the transformation of esters into carboxylic acids, these films become soluble in aqueous developer (Figure 1A) [5].

This change in solubility is key to the imaging capability of positive-tone resists. Acid-catalyzed negative-tone resists are initially soluble in aqueous developer and are typically transformed into films that are insoluble in aqueous developer through reactions that involve crosslinking (Figure 1B) [6].

In addition to photochemically-generated acids used in both positive and negative photoresists, researchers have also used thermal acid generators (TAGs) [7] and acid amplifiers (AAs) to create acid that can participate in deblocking reactions and cross-linking reactions (Figure 1C).
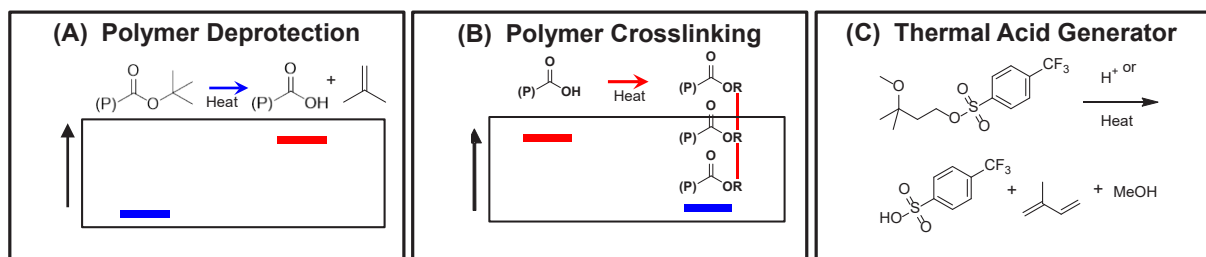
Fig. 1. Three reactions used to study diffusion and reaction of acid causing a solubility switch through catalyzed deprotection and crosslinking. (A) The catalyzed deprotection of an ester to form a carboxylic acid with increased TMAH solubility. (B) The crosslinking reaction of carboxylic acids and -OH polymer groups that results in a decrease in TMAH solubility. (C) The thermal decomposition of an AA that creates a weak acid.

Acid amplifiers are compounds that decompose in the presence of acid to create a new acid [8-9]. These compounds have predictable decomposition temperatures so they can also function as thermal acid generators.

Here, one of our key objectives is to create a two-layer stack of polymeric films composed of specifically-designed polymers, PAGs, TAGs, and base that can be transformed into a three-layer coating by careful use of low-, medium- and high-temperature bakes (Figure 2). Central to the proper functioning of this two-layer stack is our ability to promote specifically-identified reactions at specific temperatures. These reactions include: acid catalyzed deprotection reactions (Figure 1A), crosslinking reactions (Figure 1B) and thermal decomposition of acid amplifiers or TAGs (Figure 1C). Our second key objective is to conduct a detailed kinetic study of the acid-catalyzed deprotection of esters in solution using ^{1}H NMR. As acid catalyzed deprotection reactions are at the heart of many DUV, 193-nm and EUV positive-tone photoresists (Figure 1A), there are many important kinetic studies in the literature. For the most part, these studies have been done in polymeric films and evaluated using FTIR [10-16].

Our work here, however, has been done using acetate esters of t-butyl alcohol (to model t-butyl acrylate monomers in DUV polymers) and of methyl adamantyl alcohol (to model MAMA monomers in 193-nm polymers). The reactions studied in this model system differ from reactions occurring in the polymeric films of DUV and 193-nm resists in two important ways: (1) our reactions occur in solution instead of viscous, solid-phase polymer films; and (2) our reactions involve small molecules instead of polymeric side chains.

Despite the obvious differences between our model system and actual photoresists, our model system provides a few distinct advantages. First, our solution-phase model system exactly maps into over a century of research into solution-phase chemical kinetics [17] allowing us to make direct comparisons to this body of work, particularly in the area of the interpretation of entropy. Second, as the viscosity of our medium (C_6D_6/CD_3CN mixture) is quite low, we can study the kinetics of our reactions without the complications of molecular diffusion masking the kinetics of the acid-catalyzed reactions which can occur in reactions in polymeric films.

2. EXPERIMENTAL

2.1. Synthesis and Formulation Preparation.

All thin films were prepared by spin-coating (<5 wt% solid) formulations on 100-mm silicon wafers at 1000-2000 RPM after 0.20 um PTFE or Nylon filtration. We coated bottom layer formulation from a mixture of Ethyl Lactate and PMA and coated the overcoat polymer from a mixture of MIBC and NBA. We synthesized TAG by an established procedure [8]. We synthesized MaAco by an established procedure [18]. We obtained crosslinkers and polymers from commercial sources. We synthesized custom crosslinkers in DCM at RT with 2H, 2M, 3H or 3M alcohol (1 mol), triethylamine (1.5 mol) and 1,3,5-benzenetricarboxylate (0.5 mol), stirred under N2 for 4 hours, washed 3x with sat. NaHCO$_3$ (aq) then DI 5x, organic phase dried over Na$_2$SO$_4$, filtered and solvent removed under vacuum.

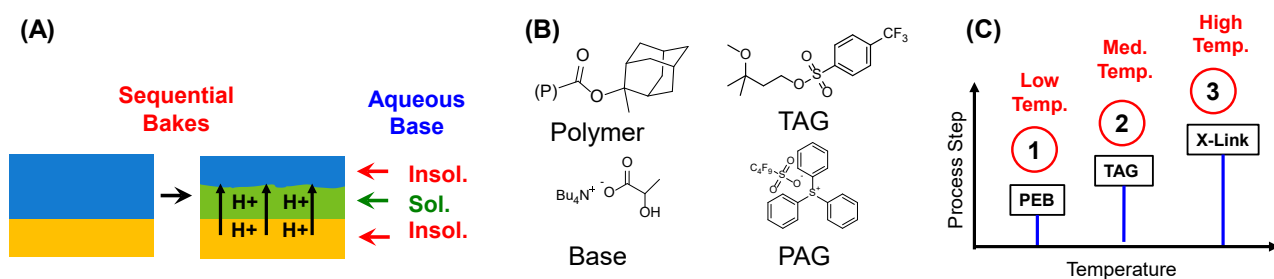Fig. 2. (A) Bilayer of polymer thin films fabricated to study diffusion and reaction of acid, that causes a solubility switch through acid catalyzed deprotection and crosslinking. (B) The materials selected for the bottom layer that follows the three-step baking process with separated chemical reactions shown in (C).

2.2. Isolated Bakes.

These studies incorporated 10 wt% of TAG, 4 wt% PAG and 1.25 wt% TBAL base with respect to total solids (<5 wt% total solids in solution) in polymer thin films baked up to 200 °C in individual steps and developed in organic Hexane:MIBC 60:40 and aqueous TMAH developers to evaluate reaction and solubility switch.

2.3. Sequential Bakes.

These studies incorporated 10 wt% of TAG, 4 wt% PAG, 1.25 wt% TBAL base and up to 10 wt% crosslinker with respect to total solids (<5 wt% total solids in solution) in polymer thin films baked up to 200 °C in sequential steps, each bake condition was followed by the next higher temperature condition, and developed in Hexane:MIBC 60:40 and TMAH to evaluate reaction and solubility switch.

2.4. Two-Layer Film Studies.

Two-layer studies utilized a bottom single-layer of polymer described above that is overcoated with a deprotectable TBA polymer from an organic solvent (MIBC) that does not dissolve the first layer. The two-layer stack was baked to promote thermal acid generation, diffusion and selective polymer deprotection of the top layer.   Development of this bilayer in organic solvent (Hexane:MIBC) removed only protected polymer and revealed the extent of diffusion and reaction by comparing bottom layer starting thickness and thickness after organic development.   Development in aqueous TMAH after organic development revealed baking conditions that caused deprotection when the bottom layer dissolved in TMAH.

2.5. Solution Kinetic Studies.

This work used ^{1}H NMR to study polymer deprotection kinetics using analogous molecules. We synthesized acetate analogs that represented deprotectable units in methacrylate polymer using an established procedure.18   We prepared 100 mM sample of each ester with 1 mM Acid in C6D6/CD3CN 90/10 mixture in 5 mm NMR tubes sealed under vacuum.   We measured the concentration of ester and decomposition products vs. time by immersing samples in an oil bath between 60 and 150 °C to evaluate the kinetics of decomposition.

3.   RESULTS AND DISCUSSION

The research presented here falls into two parts: (1) We describe the development of the components needed to build a two-layer stack that can be converted to a three-layer stack via acid diffusion from the bottom to the top layer and only controlled by using three bakes of increasing temperature (Figure 2).   Each step in the development of this system is explored, with the initial studies conducted using single-polymer films and then ultimately two-layer stacks.   (2) We describe the detailed kinetics of acid-catalyzed deprotection of two esters catalyzed using a strong acid (from our PAG) and a relatively week acid (from our TAG).

3.1. Conversion of a Two-Layer Stack to a Three-Layer Stack.

In this section, we describe our stepwise approach to developing a system in which a two-layer polymeric stack can be converted into a three-layer stack by using a sequence of three bakes of increasing temperature (Figure 2C).   The two-layer coating is composed of a bottom layer and an overcoat layer.   The bottom layer is a modified base-line resist (MAMA-polymer, PAG and base) with additives of a TAG and an optional crosslinker (Figure 2B).   The overcoat is composed of a TBA polymer that can be (a) coated over the bottom layer without dissolving and it and can be (b) deprotected by the acid generated during the thermal decomposition of the TAG (initially in the bottom layer).   The first low-temperature bake is a PEB bake for imaging of the exposed 193-nm resist, that does not activate the TAG.   The second medium-temperature bake is the TAG bake.   In this step the TAG is designed to thermally decompose to generate acid, then this acid is designed to diffuse a finite distance into the overcoat and then catalyze the deprotection of the ester in that polymer (Figure 2A).   This deprotection reaction is designed to convert the overcoat layer from being insoluble in aqueous base and soluble in organic solvent to soluble in aqueous base and insoluble in organic solvent.   The third high-temperature bake is designed to promote cross-linking within the bottom layer and therefore cause the bottom layer to be insoluble in aqueous base despite the previous decomposition of the TAG.   Ultimately, the three-layer stack (bottom to top) should be composed of a layer that is insoluble in aq. base, a layer that is soluble in aq. base, and a layer that is insoluble in aq. base (Figure 2A).

3.1.1. Low-Temperature Bake.

Our baseline 193-nm resist (described in the experimental section), is similar to other recently described open-source resists [6,12,13,17], and will function as a chemically-amplified resist by using a range of bake temperatures that are low enough to prevent PAG thermal decomposition of the PAG yet high enough to enable catalytic ester deprotection using the photogenerated acid (perfluorobutane sulfonic acid).

3.1.2. Medium-Temperature TAG Bake.

In this step the TAG is designed to thermally decompose to generate acid, then this acid is designed to diffuse a finite distance into the overcoat and then catalyze the deprotection of the ester in that polymer. We decided to use an acid amplifier (AA) as our thermal acid generator as their thermal decomposition temperatures can be predictably tuned based on their chemical structures [8-9]. Figure 3 shows twelve AAs that were synthesized and tested for this project. We used Differential Scanning Calorimetry (DSC) to evaluate the decomposition of pure, powdered samples of these AAs. The decomposition temperature of an AA is dependent on its molecular structure. The organic framework can be connected to a hydroxyl or methoxy group via secondary or tertiary linkages. A sulfonic ester serves the role of a precursor to the sulfonic acid generated by this reaction. AA decomposition temperatures decrease with the pKa's of the sulfonic acid generated by the AA. An AA with a methoxy trigger, tertiary body and p-trifluoromethylbenzenesulfonic acid precursor (3M-A) was selected to serve the role of TAG for subsequent experiments.

Fig. 3. The structures and decomposition temperatures of neat TAG measured using DSC (Differential Scanning Calorimetry). We studied two body structures described as tertiary (3) or secondary (2), two trigger structures of methoxy (M) or hydroxy (H) and three acid precursors A-C. The decomposition temperature trends with body and trigger stability and acid pKa.

In the full bilayer stack the TAGs are located in the bottom layer, to evaluate the thermal decomposition of the TAGs in a polymer matrix, we formulated a TAG (3M-A) and base with polymer (Figure 2B) to test acid generation and catalytically polymer deprotection. Figure 4 shows the thickness loss of polymer thin films with additives after baking at several temperatures and durations to find a TAG that would be stable during our low

temperature bake yet would decompose during the medium or high temperature bake. We used solubility in 0.26 N TMAH as a way to detect that the TAG has decomposed and that the thermally-generated acid had deprotected the polymeric ester. The result of this experiment using TAG 3M-A shows that no deprotection of the polymer occurred at low and medium temperatures, yet at high temperatures, the dissolution rate of the polymeric layer increased and 50 nm of the film was removed. Therefore, we had identified a TAG that was stable, yet would decompose and deprotect the polymer at high temperature, as desired.

3.1.3. High Temperature Cross-Linking.

The high-temperature bake is designed to promote cross-linking within the bottom layer, and, therefore, cause the bottom layer to be insoluble in aqueous base despite the previous decomposition of the TAG. The bottom layer must undergo several steps in sequence before the crosslinking can be evaluated: (1) during the low temperature PEB bake the unexposed resist must remain unchanged and therefore insoluble in 0.26 N TMAH; (2) during the medium-temperature bake the TAG should decompose to create acid. This acid is designed to diffuse into the top overcoat, but it will also catalyze the deprotection of the MAMA polymer in the bottom-layer polymer where it originates, and therefore the bottom layer will become soluble in 0.26 N TMAH; (3) during the high-temperature bake the film is designed to crosslink, thereby becoming insoluble in 0.26 N TMAH once again. We used thickness loss in 0.26 N TMAH as a measure of the extent of each of these three reactions. Our ideal response is represented in Figure 5A in which a low temperature bake yields no thickness loss, a medium temperature bake yields a significant thickness loss, and a high-temperature bake yields no thickness loss.

We studied reactions that crosslink polymer thin films using intrinsic polymer crosslinking, commercial/established crosslinkers and custom synthesized additives (Figure 5). Figure 5B shows that we achieved a nearly ideal thickness-loss pattern in a sample without added crosslinker using isolated bakes where each sample was only baked once. Our goal, however, is to get the thickness-loss pattern shown in Figure 5A using sequential bakes, in which a single sample is baked several times at successively increasing temperatures. Figures 5C through 5F show thickness loss results using sequential bakes. Figure 5C shows the thickness loss in a formulation with no added crosslinkers. It does not show any obvious suppression of thickness loss at high temperatures.

The use of custom crosslinker JN1 produces a film that seems to crosslink so efficiently that there is no evidence of increased solubility. Figure 5D and 5F show thickness-loss profiles that match our goals for low and medium temperature bakes and also show a slight decrease in thickness loss as a result of the high-temperature bake.
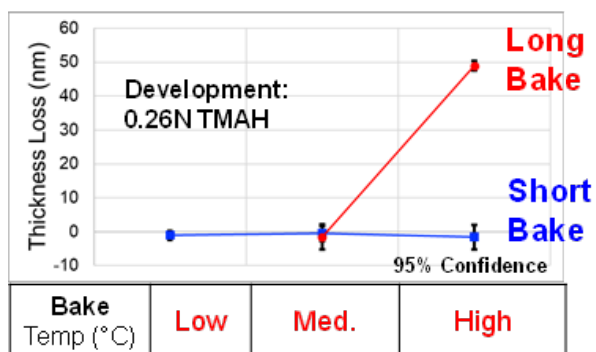

Fig. 4. The thickness loss of single-layer photoresist polymer with TAG, PAG and base after baking and developing in 0.26N TMAH for 60 seconds. Deprotection did not occur when the film was baked at low and medium temperatures, however high temperature and long duration baking caused TAG and catalyzed ester deprotection that increased solubility.
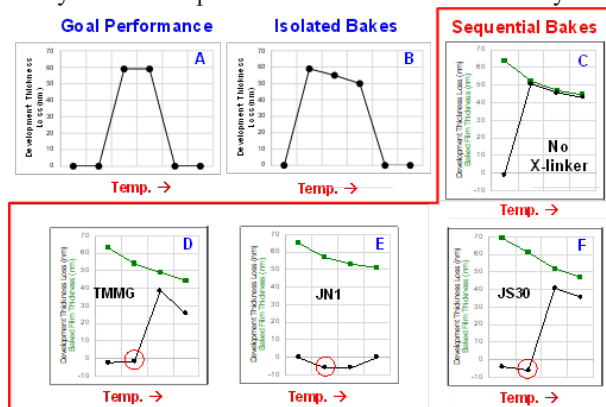
Fig. 5. Thickness loss of polymer film with TAG and crosslinker in TMAH after baking. Isolated bakes use each independent baking step followed by development, while sequential bakes use multiple steps before development. The line composed of green squares shows film thickness after baking and the black squares show film thickness after TMAH development.

Figure 6. The chemical structure of crosslinkers and expected reactions to decrease polymer TMAH solubility. Intrinsic crosslinking of polymer has been demonstrated in polymers containing HadMa6 and using TMMG. We synthesized custom additives based on a multiunit structure containing AA body and trigger.

3.1.4. Diffusion and Reaction in a Two-Layer Stack.

In this section, we describe the use of the full two-layer stack, and a method for evaluating the extent of acid diffusion from the bottom layer into the over-coat polymer. Our procedure is designed to measure the extent of acid diffusion in four steps: (A) the bottom layer consisting of polymer, PAG, base and TAG (Figure 7) is coated, and its thickness measured; (B) the overcoat polymer is coated and soft-baked; (C) a medium-temperature TAG bake is performed; (D) an organic developer is used to remove the original overcoat polymer but not remove the more polar deprotected polymer. Finally, (E) a development in 0.26 N TMAH selectively removes the deprotected region of the top layer and ensures that the bottom layer does not undergo deprotection. The difference in thickness between steps A and D yield the extent of acid diffusion.

Fig. 7. The two-layer process used to study diffusion and reaction of acid that causes a solubility switch through acid catalyzed deprotection. The TAG bake generates acid in the bottom layer than diffuses to the top layer and causes deprotection reactions that increases polymer TMAH solubility and reduces organic developer solubility. Organic development removes only protected polymer to reveal the extent of diffusion and reaction in overcoat polymer.

Figure 8 depicts three possible outcomes from this experiment: (A) Bake temperature/times are insufficient to deprotect the TAG and therefor there is no change in thickness from the original coated film to the film after organic development. (B) Bake temperature/times are sufficient to decompose the TAG, thereby producing acid that diffuses into the top layer converting its TBA esters into carboxylic acids. (C) Bake temperature/times are too high and the TAG decomposition causes all esters in the film to decompose, yielding a film that can be completely dissolved in TMAH.

Figure 9 shows the experimental results of acid diffusion vs. bake temperature/time. The data shows all three results depicted in Figure 8: The low thickness loss are samples in which the TAG did not decompose (Figure 8A), Complete thickness loss at around 40 nm show that complete thickness loss occurred (Figure 8C). Most important, are the three points occurring at intermediate bake conditions. These three points indicate that the amount of acid diffusion into the top layer is ~25 nm.
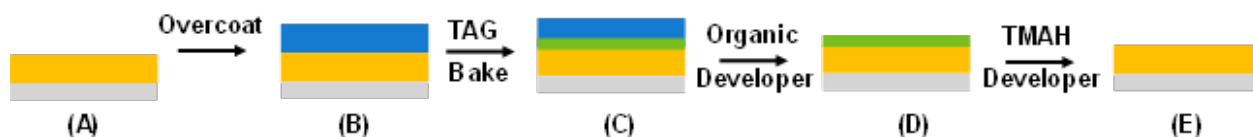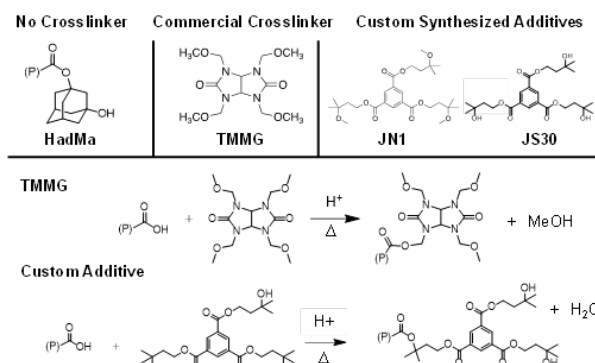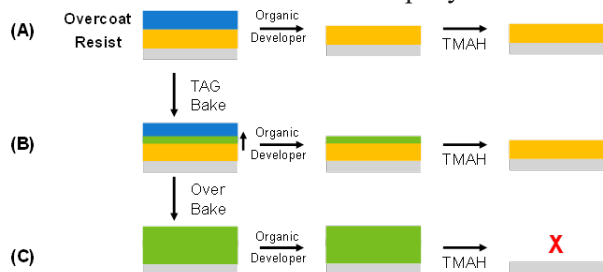

Fig. 8. The bilayer used to study diffusion and reaction of acid that causes a solubility switch through acid catalyzed deprotection. The TAG generates acid in the bottom layer, diffuses to the top layer and causes deprotection reactions that increases polymer TMAH solubility and reduces organic developer solubility. Organic development removes only protected polymer to reveal the extent of diffusion and reaction polymer.
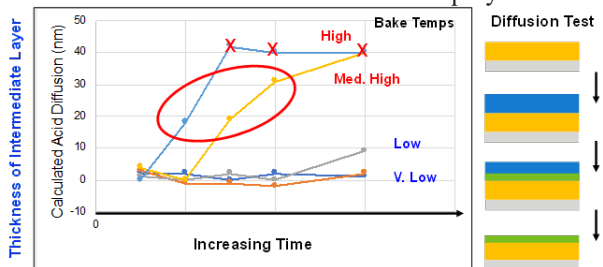

Fig. 9. The calculated extent of acid diffusion and overcoated TBA polymer reaction in a bilayer with TAG in the bottom layer. Increasing baking time and temperature promotes TAG decomposition and polymer deprotection. Intermediate baking conditions resulted in 20-30 nm of diffusion and deprotection of the overcoat without deprotection of the bottom layer, while high temperature and long duration bakes cause unfavorable deprotection of the bottom layer.

3.2. Solution-Phase Kinetics of Acid-Catalyzed Ester Deprotection.

In the first part of this paper, we constructed a two-layer stack that was designed to be converted into a three-layer stack through a series of sequential bake steps of increasing temperature, thereby promoting specifically-identified reactions at each temperature. Along with cross-linking, these reactions include acid-catalyzed deprotection of two esters: polymer-bound t-butyl acrylate and methyl-adamantyl methacrylate. Two acids served the role as catalysts: perfluorobutane-sulfonic acid (or Nonaflate acid) and p-trifluoromethyl-benzenesulfonic acid. These acids are strong (pKa = -3.6) and relatively weak (pKa = -1.1), respectively. In this section, we describe a detailed study of the kinetics of these acid-catalyzed deprotection reactions in solution-phase in sealed NMR tubes. Instead of polymer-bound esters we used acetate analogs to simplify the ^{1}H NMR spectra and so that the concentrations could be high (Figure 10). Solutions consisted of 100 mM and 1 mM concentrations of ester and sulfonic acid, respectively, in a mixture of C_6D_6/CD_3CN solvent. Solutions were sealed in 5-mm NMR tubes and immersed in oil baths for 5-30 minutes, and the extent of reaction was followed by ^{1}H NMR.

First-order reaction kinetics over several temperatures is shown for each combination of acid and ester (Figure 11). The adamantyl ester (MaAc) with the strongest acid (nonaflate acid) showed at the fastest reaction rate, while the TBA ester with the weaker acid decomposed with the slowest rate. The natural log of the rate constants were plotted against the reciprocal of temperature in Kelvin (1/T) yielding four activation energy plots (Figures 12 and 13B). A summary of the results of these plots is shown in Figure 13A. Unexpectedly, the reaction with the fastest reaction rate has the highest activation energy (MaAc/NfOH; 27 kcal/mol). Similarly, the reaction with the slowest rate, has the lowest activation energy (TBA/p-$CF_3C_6H_4SO_3H$; 17 kcal/mol). This is surprising as the activation energy of a reaction is quite frequently assumed to be inversely related to reaction rate. However, this line of thinking ignores the entropic contributions which is related to the pre-exponential factor, A. This value is shown as log(A) in Figure 13A, and shown graphically as the y-intercepts in Figure 13B. Solution-phase studies over the years, provide some correlations of log(A) values with the molecularity of reactions. For example, log(A) values of 9-13 are characteristic of unimolecular reactions (one

remaining as one particle in the transition state) and log(A) values of 13-16 are characteristic of reactions in which two particles are generated from one in the transition state [19]. Our fastest reaction has a log(A) of 14 and our slowest reaction has a log(A) of 6. Our simple interpretation of these two reactions is that the faster reaction has very little change in entropy from the starting materials to the rate-limiting transition state; whereas our slowest reaction undergoes a process in which the transition state is much more ordered (lower entropy) compared to its starting materials.
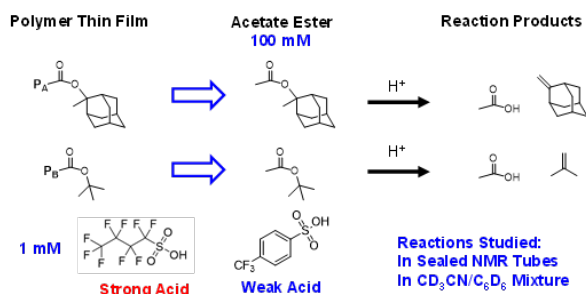
Fig. 10. We synthesized and decomposed compounds resembling the deprotectable part of the polymer to study deprotection reactions catalyzed by different acids. MaAc and TBA were decomposed by weak and strong acid in solution and monitored by ^{1}H NMR to evaluate the kinetics of deprotection.
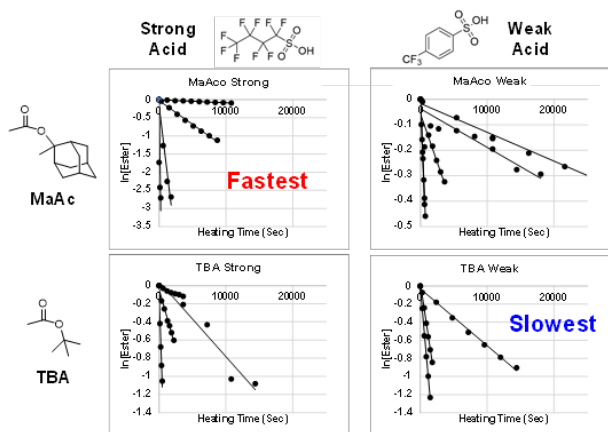
Fig. 11. The kinetics of acid catalyzed ester decomposition monitored by ^{1}H NMR. We plot the natural log of the concentration of ester vs time at multiple temperatures.
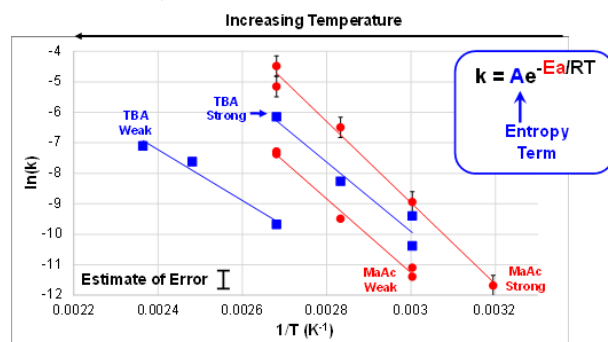
Fig. 12. The Arrhenius plots of acid catalyzed ester deprotection monitored by ^{1}H NMR. We plot the natural log of the rate constant vs reciprocal temperature to extract activation energy Ea and pre-exponential entropic term A.
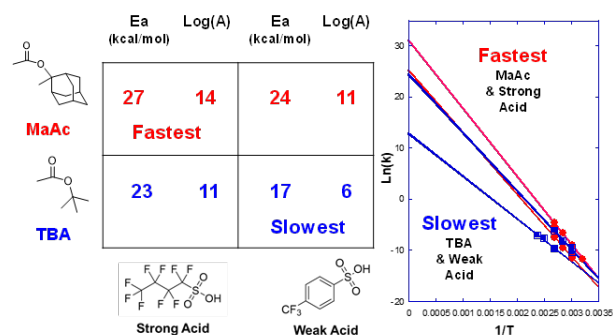
Fig. 13. The activation energy and pre-exponential factors of two esters decomposed with two acids monitored by ^{1}H NMR. We show the natural log of the rate vs reciprocal temperature.

4. CONCLUSION

Controlling the solubility of polymer films is essential to many pattering schemes used in the manufacture of integrated circuits. We have studied acid-catalyzed deprotection, the thermal decomposition of TAGs, and crosslinking in a variety of polymer films and one or two layer structures. In all cases, we use solubility of thse films in either aqueous base or organic solvent as an indicator of the chemical reactions occurring as function of bake temperature. We identified an acid amplifier (3M-A) which was stable during low-temperature PEB bakes, yet thermally decomposes at higher temperatures, yielding acid that would deprotect the adamantyl ester in the 193-nm resist polymer.

Our bottom layer was designed to exhibit three solubility regimes in response to sequential bake steps: low-temperature bake: insoluble in aq. base; medium-temperature bake: soluble in aq. base; and high-temperature bake: insoluble in aq. base. We found that

we could achieve these three solubility regimes if we used isolated bakes without any added crosslinker (Figure 5B). However, we never fully demonstrated the goal solubility profile using sequential backs, as we could not find crosslinkers that would fully shut-down solubility when baked at high temperatures. Using a full two-layer stack, we were able to demonstrate that acid-generated by our TAG would diffuse into the top overcoat layer at distances of 20-30 nm, as desired.

We evaluate the relative reaction rates of four pairs of ester/acid combinations in solution phase in sealed NMR tubes. The most surprising result from this work was that the fastest reaction had the highest activation energy (Ea = 27 kcal/mol) and the slowest reaction had the lowest activation energy (Ea = 17 kcal/mol). The rates of these reactions were primarily driven by changes in entropy rather than changes in enthalpy during the transition states.

ACKNOWLEDGEMENTS

REFERENCES

[1] Willson, C. G., Ito, H., Fréchet, J. M. J., Tessier, T. G. and Houlihan, F. M., "Approaches to the Design of Radiation-Sensitive Polymeric Imaging Systems with Improved Sensitivity and Resolution," J. Electrochem. Soc. 133(1), 181–187 (1986).

[2] Peng, R. C., Huang, I. H., Liu, H. H., Lee, H. J., Lin, J., Lin, A., Chang, A., Lin, B. S.-M. and Lalovic, I., "Process requirements for pitch splitting LELE double patterning at advanced logic technology node," Opt. Microlithogr. XXV 8326(March), 83260X (2012).

[3] Hattori, T., Yokoyama, Y., Kimura, K., Yamanaka, R., Tanaka, T. and Fukuda, H., "Development of high-performance negative-tone resists for 193-nm lithography," J. Photopolym. Sci. Technol. 16(4), 489–498 (2003).

[4] Ito, H. and Willson, C. G., "Chemical amplification in the design of dry developing resist materials," Polym. Eng. Sci. 23(18), 1012–1018 (1983).

[5] Ito, H. and Ueda, M., "Thermolysis and Photochemical Acidolysis of Selected Polymethacrylates," Macromolecules 21(5), 1475–1482 (1988).

[6] Chen, K.-J. R., Huang, W.-S., Li, W.-K. and Varanasi, P. R., "Resist freezing process for double exposure lithography," Adv. Resist Mater. Process. Technol. XXV 6923(March 2008), 69230G (2008).

[7] Perret, D., Simon, J., Gaugiran, S., Cutler, C., Cardolaccia, T., Pikon, A., Guerin, I., Lapeyre, C., Derrough, S., Szmanda, C. and Trefonas, P., "Materials for double patterning strategies: Development and application," Microelectron. Eng. 86(4–6), 757–760 (2009).

[8] Kruger, S. A., Higgins, C., Cardineau, B., Younkin, T. R. and Brainard, R. L., "Catalytic and autocatalytic mechanisms of acid amplifiers for use in EUV photoresists," Chem. Mater. 22(19), 5609–5616 (2010).

[9] Kruger, S., Higgins, C., Gallatin, G. and Brainard, R., "Lithography and chemical modeling of acid amplifiers for use in EUV photoresists," J. Photopolym. Sci. Technol. 24(2), 143–152 (2011).

[10] Kang, S., Wu, W. L., Choi, K. W., De Silva, A., Ober, C. K. and Prabhu, V. M., "Characterization of the photoacid diffusion length and reaction kinetics in EUV photoresists with IR spectroscopy," Macromolecules 43(9), 4275–4286 (2010).

[11] Shinozuka, T., Tsunooka, M., Itani, T. and Shirai, M., "Activation energies for deprotection reaction of chemically amplified resists: A study using in-situ FT-IR spectroscopy," J. Photopolym. Sci. Technol. 15(5), 765–768 (2002).

[12] Ogata, T., Kinoshita, Y., Furuya, S., Matsumaru, S., Takahashi, M., Shiono, D., Dazai, T., Hada, H. and Shirai, M., "Characteristics of low E a 193-nm chemical amplification resists," Adv. Resist Technol. Process. XXIII 6153(March 2006), 615328 (2006).

[13] Ogata, T., Furuya, S., Kasai, K., Hada, H. and Shirai, M., "Low-Ea chemical amplification resists for 193 nm lithography," Japanese J. Appl. Physics, Part 1 Regul. Pap. Short Notes Rev. Pap. 45(6 B), 5450–5455 (2006).

[14] Okoroanyanwu, U., Byers, J. D., Cao, T., Webber, S. E. and Willson, C. G., "Deprotection Kinetics of Alicyclic Polymer Resist Systems Designed for ArF (193 nm) Lithography," ACS Symp. Ser. 706, 174–190 (1998).

[15] Jiang, J., Jung, B., Thompson, M. O. and Ober, C. K., "Chemical reaction and diffusion kinetics during laser-induced submillisecond heating for lithographic applications," J. Vac. Sci. Technol. B 37(4), 041601 (2019).

[16] Okoroanyanwu, U., Byers, J. D., Cao, T., Webber, S. E. and Willson, C. G., "Deprotection Kinetics of Alicyclic Polymer Resist Systems Designed for ArF (193 nm) Lithography," ACS Symp. Ser. 706, 174–190 (1998).

[17] Moelwyn-hughes and Johnson., "the kinetics of the decomposition of diazoacetic ester, catalyzed by acids in aqueous solution.," Trans. Faraday Soc. (1941).

[18] Kolocouris, A., Koch, A., Kleinpeter, E. and Stylianakis, I., "2-Substituted and 2,2-disubstituted adamantane derivatives as models for studying substituent chemical shifts and C-Hax···Yax cyclohexane contacts - results from experimental and theoretical NMR spectroscopic chemical shifts and DFT structures," Tetrahedron 71(16), 2463–2481 (2015).

[19] Robert L. Brainard, Timothy M. Miller, and G. M. W., "Mechanisms of thermal decomposition of trans-chloroneopentylbis(tricyclopentylphosphine)platinum (II)," Organometallics (1986).

Switching the Solubility of Polymers using Intermolecular Reactions and Diffusion of Small Molecules

Jacob Sitterly, Justin Nhan, Moira Niluxsshun, Bharti Sangwan, Stephen Smith, Doug Macleod and Robert Brainard*

State University of New York Polytechnic Institute, 257 Fuller Rd. Albany, NY 12203
*rbrainard@sunypoly.edu

A two-layer polymeric stack is designed to be converted to a three-layer stack via the diffusion of small molecules between layers. The three-layer stack is composed of a bottom layer carboxylic acid (CA-polymer) that is soluble in aqueous TMAH developer; a middle layer of reacted CA-polymer that became soluble in organic developer as a result of reaction with small molecules; and a top layer of nonpolar polymer that is soluble in organic developer. Several small molecules were evaluated for their effectiveness, by combing them with the CA-polymer and evaluated in their effectiveness in decreasing the solubility of this polymer in aqueous base. High molecular weight amines, benzyl bromide combined with nonnucleophilic base, dicyclohexylcarbodiimide, and diisopropylcarbodiimide all are capable of switching the solubility of the CA-polymer. These molecules were used in two-layer stacks to study diffusion, reaction and solubility change. The Tg of the CA-polymer was lowered to promote diffusion of the small molecule from the top to the bottom layers.
Keywords: Polymer, Solubility, Development, Diffusion, Protection, Reaction, Carboxylic acid

1. INTRODUCTION

Controlling the solubility of polymer thin films is essential to photoresist technology [1-2]. Two key concepts in photolithography are (1) changing the solubility of polymers and (2) diffusion of small molecules in polymer thin films. Switching polymer solubility through diffusion has been demonstrated and used to transfer patterns, and to modify existing features [3-9]. Positive-tone chemically amplified photoresists (CAMP) are initially insoluble in aqueous TMAH developer and become soluble upon exposure to light and heat through deprotection reactions of esters (Figure 1A) [13]. The opposite reaction, the protection of carboxylic acid (CA), results in a suppression of aqueous TMAH solubility (Figure 1B).
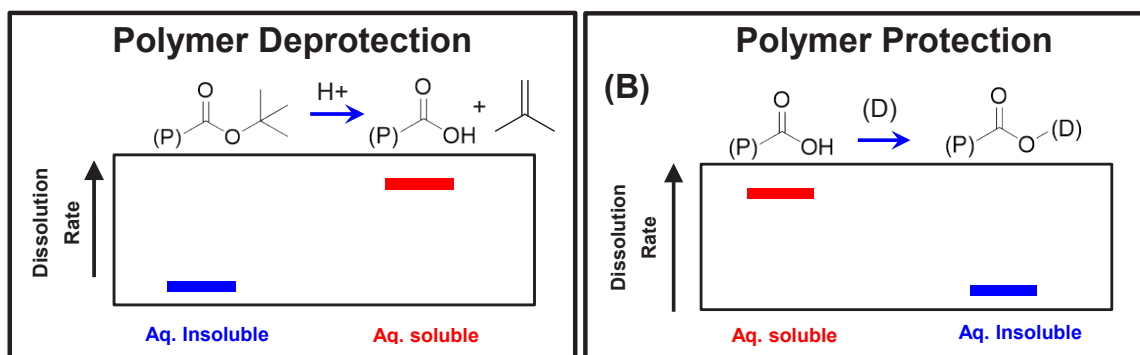

Fig. 1. The two reactions studied in this work to switch the solubility of polymer thin films. A. The acid catalyzed ester deprotection reaction that forms CA and increases thin film solubility in aqueous TMAH. B. The protection reaction of CA with small molecules (D) that decreases thin film solubility in aqueous TMAH.

Here, our goal is to design and create a two-layer polymer stack that has one or more small molecules in the top layer which ultimately will alter solubility of the starting material in the bottom layer, to yield a three-layer stack. The top organic-soluble layer will contain a small molecule and the bottom layer will be composed of a polymer with pendant carboxylic acid groups that is soluble in aqueous base. The small molecule originating in the top layer will diffuse into and react with the bottom layer, thereby creating an intermediate layer that is soluble in organic solvents (Figure 2).

This work is divided into four sections. First, we describe the design, synthesis and evaluation of the two polymers that will be used in our top and bottom layers. Second, we screen several small molecules for their ability to convert the bottom polymer that contains pendant carboxylic acid groups (CA-polymer) from being soluble in aqueous base, to a polymer that is soluble in organic solvents. Third, we evaluate the capacity of small molecules to diffuse from the top donor-polymer into the bottom CA-polymer, thereby creating a three-layer stack. Fourth, we redesign the CA-polymer so that the two-layer stack is more efficient at its conversion to a three-layer stack.
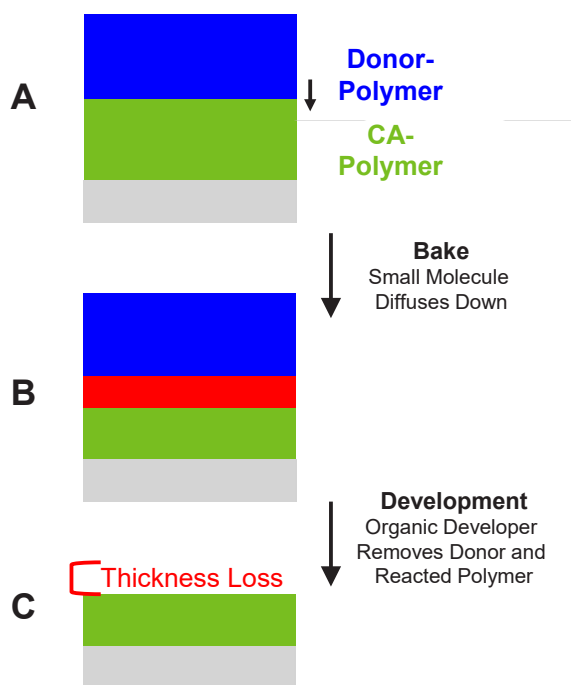
Fig. 2. The two-layer polymer stack to evaluate the formation of a three-layer stack from diffusion and reaction of small molecules. The bake step converted the two-layer stack (2A) to a three-layer stack (2B). The stack was developed in organic n-butyl acetate (NBA) to remove donor-polymer and reacted CA-polymer to determine extent of diffusion and reaction (2C).

2. EXPERIMENTAL

2.1. Polymer Synthesis.

All polymers were synthesized via free radical polymerization at 80 °C for 24 hours with AIBN as an initiator. Solutions of ethyl lactate and monomer were degassed with nitrogen for at least 20 minutes before addition of AIBN and heating under nitrogen to synthesize CA-polymer. The solution was precipitated into cold diethyl ether three times, resolubilized and concentrated in THF each time, and finally dried under vacuum to obtain a fine white powder. CA4-7 were synthesized in the same method with varying monomer composition. Solutions of n-butyl acetate (NBA) and monomer were degassed with nitrogen for at least 20 minutes before addition of AIBN and heating under nitrogen to synthesize donor-polymer.

2.2. Synthesis of Polymer CA-3.

A 1 L round bottom flask was charged with 20.6 grams of methacrylic acid (MAA), 98.4 grams of methyl methacrylate (MMA) and 480 grams of ethyl lactate; separately azobisisobutyronitrile (AIBN) was prepared in 20 grams of ethyl lactate and both solutions were degassed by bubbling nitrogen through solution for 1 hour. The AIBN solution was added to the monomer solution and heated to 80 °C under nitrogen, where it was stirred for 24 hours. The solution was filtered through cotton and concentrated to 500 mL, then added dropwise to 1 L of cold diethyl ether, the solid was collected, solubilized in 500 mL of THF, precipitated and resolubilized twice more and dried under vacuum to obtain a white powder.

2.3. Single-Layer Solubility Switch.

CA-polymer thin films (100-200 nm) were prepared by spin-coating formulations of polymer and additive at 5 wt% solids in ethyl lactate or PM (propylene glycol methyl ether) on 100-mm silicon wafers at 1000-2000 RPM after 0.20 um PTFE filtration. The solubility switch from added small molecules was studied by formulating 5 wt% of solids as additive, or with amines by formulating 1 mole equivalent *vs.* the level of carboxylic acid groups in the CA-polymer. We selected nine amines with a range of carbon-to-nitrogen ratios (C:N) of 6 to 24. Because these amines had MWs of 101 to 354 grams/mole the additives spanned a range of 1.0 to 3.5 wt%. The films were baked at 120 °C for 120 seconds and the thickness loss was measured after development in NBA for 60 seconds and aqueous TMAH [13] for 20 seconds.

2.4. Two-Layer Solubility Switch.

A bottom CA-polymer and overcoated donor-polymer with additives formed a two-layer stack that was baked to promote diffusion and reaction to cause a change in solubility of the bottom layer and form a three-layer stack. CA-polymer thin films (100-200 nm) were prepared by spin-coating formulations of polymer at 5 wt% solids in ethyl lactate or PM (Propylene glycol methyl ether) on 100-mm silicon wafers at 1000-2000 RPM after 0.20 um PTFE filtration. Donor-polymer thin films ((100-200 nm) were prepared by spin-coating formulations of polymer with additives at 5 wt% solids in NBA on CA-polymer at 1000-2000 RPM after 0.20 um Nylon filtration. The stack was baked at 120 °C for 120 seconds and the thickness loss was measured after development in NBA for 60 seconds to compare to starting thickness of CA-polymer. We used small molecule additives up to 20 wt% of solids in donor-polymer to evaluate diffusion and reaction across the two-layer layer interface and extent of a change in solubility.

3. RESULTS AND DISCUSSION

3.1. Two Polymers Used in the Two-Layer Stack.

Our first step in creating the two-layer stack described above and shown in Figure 2, is to design, synthesize and evaluate the two polymers that will be used in these two layers. The polymer used in the top donor-polymer layer must be soluble in n-butyl acetate (NBA) which is used both as the casting solvent and the organic developer. We found that a random copolymer of 60:40 styrene and t-butylmethacrylate (TBMA) had the desired properties of thin film dissolution rates of > 60 nm/s in NBA.

Ultimately, the role played by the CA-polymer in the bottom layer is much more critical to the proper functioning of the two-layer stack than is the role played by the top donor-polymer. To achieve the best CA-polymer required four generations of design and synthesis. In this section, we describe the evaluation of the first three generations of CA-polymer and describe the evaluation of the fourth generation in section 3.D. Our initial development of the CA-polymer focused on achieving the target level of dissolution rate goals. The CA-polymer must (a) contain pendant carboxylic acid groups; (b) be freely soluble in aqueous TMAH [13] and (c) have poor solubility (< 1 nm/s) in NBA. The later point is

required since NBA will be used as the casting solvent for the top layer, and a low solubility in this solvent is required to minimize intermixing at the interface between the two layers.

The first generation of CA-polymer consisted of three random copolymers containing methacrylic acid (MAA) and *t*-butyl acetate (TBA) in which the levels of MAA were 10, 20 and 30 mole %. The three polymers were spin-coated into films and the dissolution rate of these films were measured in NBA. These three polymers easily achieved the solubility goals in aqueous TMAH [13] but were much too soluble in NBA (Figure 3). The second generation of CA-polymers consisted of two random copolymers containing MAA and methyl acrylate (MA) in which the levels of MA were 20 and 30 mole %. These two polymers had dissolution rates (DR) in NBA of ~1 nm/s, which is closer to the target solubility goal in this solvent. Unfortunately, however, these polymers could not be purified by precipitation. The third generation of CA-polymer consisted of a single random copolymer of 20% MAA and 80% methyl methacrylate (MAA). The latter monomer was selected because it has a higher Tg than, MA, and we hoped that this would allow it to be purified by precipitation. This polymer was purified through a precipitation step, has a low solubility in NBA (<0.1 nm/sec) and is called CA-3 (Figure 3).

3.2. Screening Small Molecules in CA-Polymer.

The next step in our goal of building the two-layer stack described above is to evaluate potential small molecules that can diffuse from the top donor-polymer layer to the bottom layer and react with the pendant carboxylic acid groups attached to the CA-polymer thereby converting the top thickness of this layer solubility in aqueous TMAH [13] from soluble to insoluble. To evaluate these small molecules, we blended them directly into the CA-polymer (rather than the top donor-polymer required in our two-stack designed) and evaluated how these molecules converted the solubility of the CA-polymer in aqueous TMAH, from soluble to insoluble, and conversely converted the solubility of this polymer in NBA from insoluble to soluble. We evaluated small molecule amines, reactive molecules and multicomponent additives for reactions with CA-polymer that switched polymer solubility.
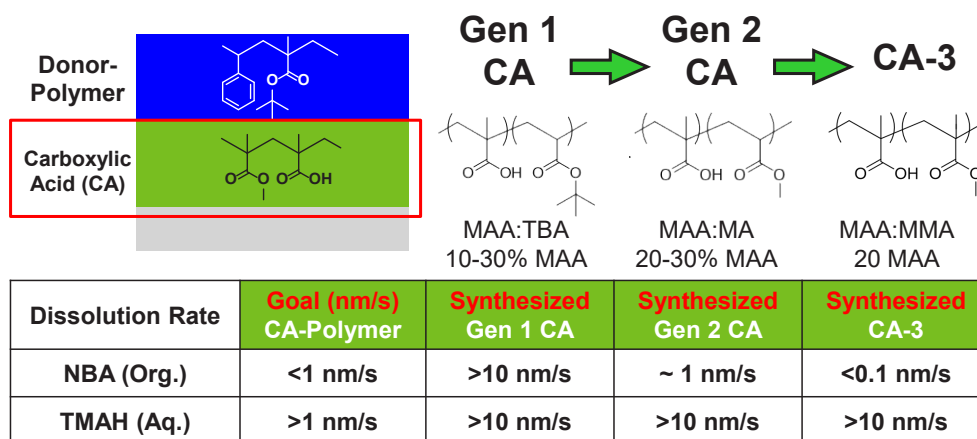
Fig. 3. The CA-polymer was designed and synthesized to dissolve slowly in organic NBA and quickly in aqueous TMAH; representing an exposed positive tone photoresist that deprotected and has carboxylic acid groups. Three generations of CA-polymer were synthesized and evaluated. CA-1: Was three different copolymers composed of MAA:TBA 10-30 mole % MAA and was too soluble in NBA (>10 nm/sec). CA-2: Was three different copolymers composed of MAA:MA 20-30 mole % MAA and was still soluble in NBA (~1 nm/sec). CA-3: Was composed of MAA:MMA 20:80 mole % MAA and met solubility criteria insoluble in NBA (<0.1 nm/sec).

3.2.1. Amines.

We selected nine amines with a range of carbon-to-nitrogen ratios (C:N) of 6 to 24. To a solution of 5 wt% CA-polymer CA-3 were added 1 molar equivalents of amines (*vs.* pendant carboxylic acids in the CA-polymer). Because these amines had MWs of 101 to 354 grams/mole, the actual wt % of these additives spanned a range of 1.0 to 3.5 wt%. Solutions were spin-coated, then baked at 120 °C for 120 seconds to yield films that were 100-200 nm thick. The thickness loss of these films was measured after being dipped into either organic NBA for 60 seconds or aqueous TMAH [13] for 20 seconds. Thickness loss in NBA and aqueous TMAH for these nine amines are shown (Figure 4). A trend of decreasing thickness loss with increasing C:N ratio indicated a solubility switch of CA-polymer. The largest amines studied, trioctylamine and triisooctylamine, prevented dissolution in aqueous developer and increased dissolution in organic NBA developer. The high carbon content amines switched the CA-polymer solubility in the desirable way, likely by decreasing the polarity of the thin film and preventing dissolution in polar aqueous TMAH and enabling dissolution in nonpolar NBA. We noticed exceptions to this trend in octylamine and dioctylamine, shown by the red points in Figure 4. That achieved a reduced aqueous TMAH solubility with relatively low carbon content. This may be due to reactions of primary and secondary amines that can form amides with CA, while tertiary amines are not expected to react this same way

Fig. 4. The CA-polymer single-layer films with amines, baked and developed in: A. NBA; with increasing thickness loss and solubility with C:N ratio. B. aqueous TMAH; with decreasing thickness loss and solubility *vs.* increasing C:N ratio.

3.2.2. Other Small Molecules.

Several other molecules were evaluated for their ability to switch the solubility of the CA-polymer from aqueous TMAH [13] to NBA dissolution. Figure 5A and B show the dissolution rate of pure CA-3 polymer and the goal dissolution rate after bak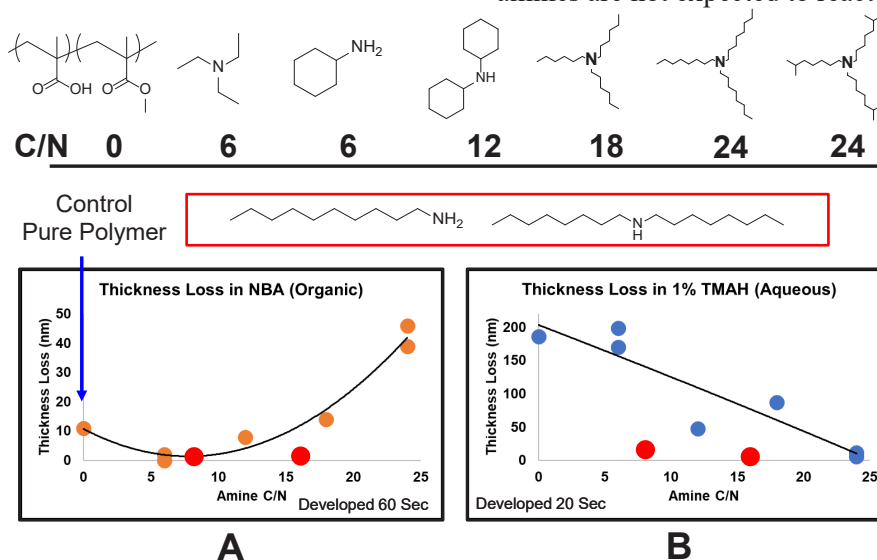ing in the presence of a 5 wt% quantity of the small molecule, respectively. The pure CA-3 polymer has a dissolution rate of 9 nm/s in aqueous TMAH (left-blue column) and < 0.1 nm/s in NBA (right-red column). The goal is for the small molecule to convert the CA-3 polymer into a film that has < 0.1 nm/s in aqueous TMAH and ~10 nm/s in NBA.

The addition of 5 wt% of di-*t*-butyl dicarbonate (DBDC) in the CA-polymer produced a film that had a slightly lower dissolution rate in aqueous TMAH and about the same DR in NBA (Figure 5C). The addition of 5 wt% of benzyl bromide or diisopropylethylamine, had a similar effect: slight suppression of the solubility in aqueous TMAH and very little change to the solubility in NBA (Figures 5D and E, respectively). The addition of 5 wt% each of both benzyl bromide and diisopropylethylamine, however, showed a dramatic change in the solubility of the CA-3 polymer (Figure 5F). The reaction of benzyl bromide and a nonnucleophilic base like diisopropylethylamine with carboxylic acids can form esters (Figure 6) [11].

Figures 5G and 5H show the dissolution rates after baking of CA-3 polymer with addition of 5 wt% of dicyclohexylcarbodiimide (DCC) or diisopropylcarbodiimide (DIC), respectively. We observed a dramatic change in the solubility of the CA-3 polymer, achieving our goal of increasing aqueous TMAH and decreasing organic NBA solubility. We do not currently know the reaction that results in the observed solubility switch, however, the first step in the reaction between DCC and carboxylic acid yields an ester (Figure 7), there is also the possibility that the reaction can produce anhydrides [12].
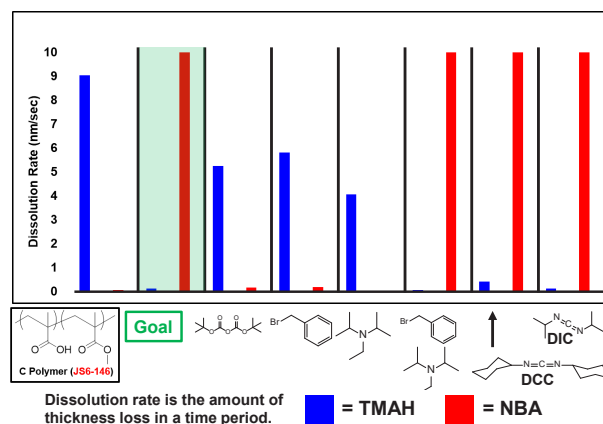
Fig. 5. The DR of CA-polymer single-layer films with small molecules additives baked and developed in aqueous TMAH and NBA. A. The pure CA-polymer dissolved very quickly in aqueous TMAH and very slowly in NBA. B. The goal solubility change of CA-polymer was slow dissolution in aqueous TMAH and rapid dissolution in NBA. C-E. The CA-polymer with molecules that did not increase NBA solubility. F-H. The CA-polymer with molecules that changed aqueous TMAH and NBA solubility.
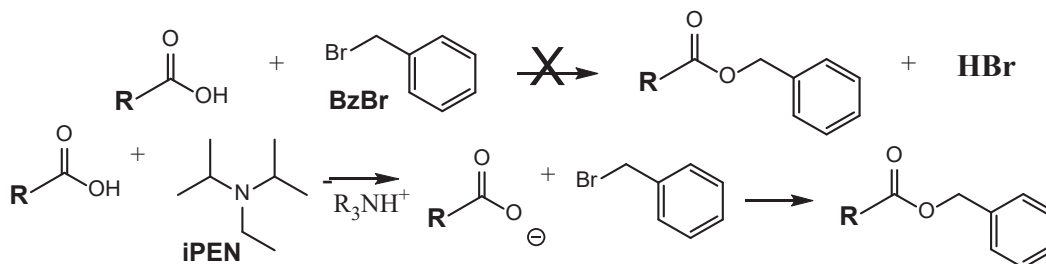
Fig. 6. The first reaction of CA with BzBr is unexpected to result in the formation of an ester or solubility change. The second reaction of CA with BzBr and DIPEA to form an ester of changed solubility in aqueous TMAH and NBA.
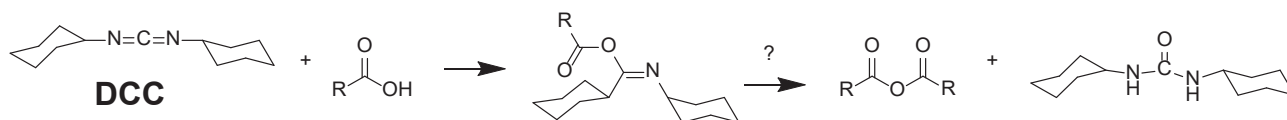
Fig. 7. The first reaction of CA with DCC to form an anhydride would likely not significantly change thin film solubility.

3.3. Two-Layer Diffusion and Reaction

Ultimately, the goal of this work is to create a two-layer polymeric stack that has one or more small molecules in the top layer which ultimately will alter the solubility of the starting material in the bottom layer, to yield a three-layer stack through a process in which a small molecule diffuses from the top to bottom layers. Earlier, we described the development of the polymers used in the top and bottom layers, and the evaluation of several small molecules that were capable of switching the solubility of the bottom polymer. In this section, we assemble the whole two-layer stack and evaluate the ability of the small molecule's ability to diffuse from top to bottom thereby increasing the solubility in NBA of the top portion of the bottom layer. The experimental process for this evaluation is shown in Figure 8 and is described in the experimental section. After the two-layer stack is fabricated, it is subjected to a 120 °C/120 second diffusion bake. After the bake the stack is developed in NBA for 60 seconds. A comparison is made between the original thickness of the bottom film and the remaining film at the end of the process. Since the small molecule has been selected for its ability to convert the NBA-solubility of the CA-polymer from insoluble to soluble, we take the thickness loss as an indication of the diffusion of the small molecule into the bottom layer.

The thicknesses of the initial bottom layer and the thicknesses at the end of the process is shown for several amines (Figure 9). The control condition of polymer with no diffuser (Figure 9A) shows negligible thickness loss compared to starting film thickness (dotted blue line at 180 nm). The ideal thickness loss (Figure 9B) is about 25-45 nm after diffusion bake and development. The amines that switched CA-polymer solubility in single-layer studies were ***unable*** to achieve significant thickness losses in two-layer studies (Figure 9C-F). Similar experimental results were also achieved when using DCC, and no significant thickness loss was observed. The bilayer stack of CA-3 and donor-polymer containing small molecules was unable to achieve the goal thickness loss from diffusion and reaction, this necessitated a reevaluation of the process and materials used in our bilayer stack. In the next section we explore the limitations of diffusion in this system and the steps taken to promote diffusion and reaction.
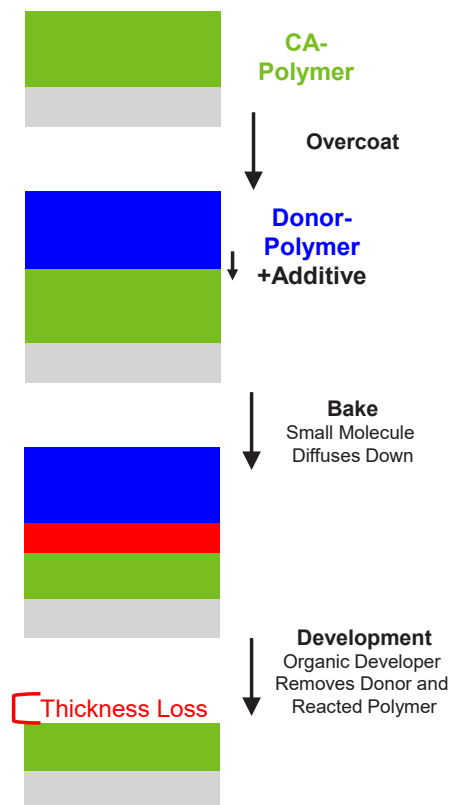
Fig 8. The two-layer process to evaluate CA-polymer thin film thickness loss from diffusion and reaction of small molecules from the top layer to the bottom layer. Starting thickness is compared to the thickness after overcoating, baking and developing to evaluate thickness loss from diffusion and reaction of small molecules from the top to bottom layer.
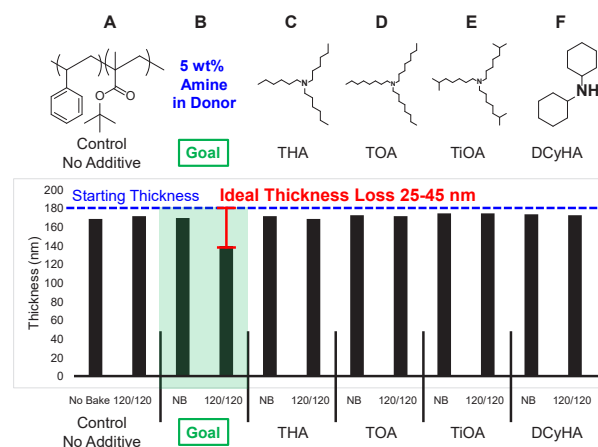
Fig. 9. The thickness loss of CA-polymer after overcoating with donor-polymer containing small molecules, baked and development in NBA for 60 seconds. The starting CA-polymer thickness is shown by the dotted blue line at 180 nm. A: The control condition of polymer with no diffuser demonstrated negligible thickness loss compared to starting film thickness. B: The ideal thickness loss of 25-45 nm after diffusion bake and development. C-F: The amines that changed CA-polymer solubility in single-layer studies; not able to achieve significant thickness loss in two-layer studies.

3.4. CA-Polymer Redesign

We considered three possible reasons why the use of amines or DCC in the two-layer stacks did not show significant thickness loss: (1) The Tg of CA-polymer was too high; (2) the small molecules are too large; and (3) the difference in polarity between donor-polymer and CA-polymer resulted in a sharp interface that limited diffusion between nonpolar and polar polymer films. We, therefore, redesigned the CA-polymer to address the first possibility by creating CA-polymers with lower Tgs than CA-3. A fourth generation of polymers were made in which the MMA monomer was replaced with an MA monomer at levels of 0-40 mole % (Figure 10). The Tgs of these polymers ranged from 88-146 °C and allowed further study with CA-polymer in two-layer stacks.

The CA-polymers with 0-20 mole % MA were tested in a two-layer stack overcoated with donor-polymer containing DCC, baked and developed in NBA (Figure 11). The CA-polymer thickness losses increased with decreasing polymer Tg. We observed high thickness losses with CA-5 when overcoated with DCC in the donor-polymer (~40 nm). We interpret these thickness losses as indicating that the DCC had diffused from the top layer to the bottom layer and reacting with CA-polymer, thereby creating an intermediate layer that is NBA soluble. The CA-5 polymer had the greatest thickness loss of ~40 nm. We further studied the thickness loss of CA-5 polymer in two-layer stacks with varying concentrations of DCC in donor-polymer (Figure 12). We observed increasing thickness loss in NBA with increasing concentration of DCC up to 5 wt% of solids, thereafter the thickness loss decreased. The increasing thickness loss with DCC concentration makes sense, we are unsure why thickness loss decreases with higher levels.

Fig. 11. The CA-polymer thickness loss *vs.* Tg after overcoated with polymer containing 5 wt% DCC, baking at 120 °C for 120 seconds and developing in NBA for 60 seconds. The thickness loss increased with increasing MA concentration and decreasing Tg.
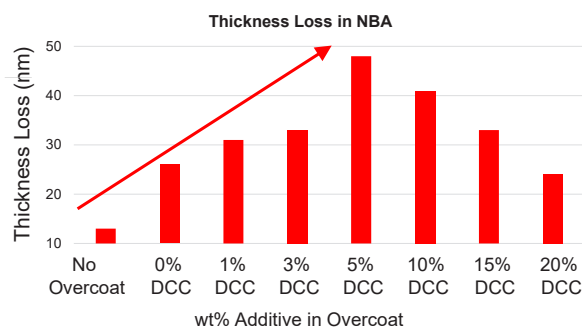
Fig 12. The CA- polymer thickness loss *vs.* DCC concentration in donor-polymer. The two-layer stacks were baked at 120 °C for 120 seconds and developed in NBA for 60 seconds. Increasing thickness loss is observed up to 5 wt

	Polymer	MAA (Mol%)	MMA (Mol%)	MA (Mol%)	Tg (C)
CA3	JS6-146	20	80	0	146
CA4	MN1-50	20	70	10	136
CA5	MN1-49	20	60	20	121
CA6	MN1-48	20	50	30	101
CA7	MN1-26	20	40	40	88

Fig 10. The composition and Tg of CA3-7 polymers containing MAA 20 mole %, MMA 40-80 mole % and MA 0-40 mole %. The Tg decreased with increasing MA concentration.
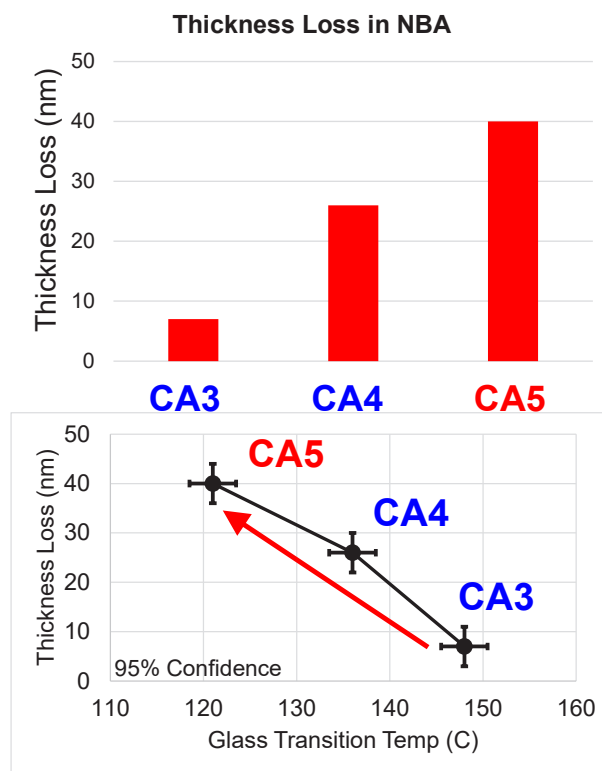
4. CONCLUSIONS

Controlling the solubility of polymer thin films is essential to photoresist technology. We studied small molecules and reactions that switch the solubility of CA-polymer thin films. Single-layer thin film studies were conducted to evaluate reaction and solubility switches in aqueous TMAH [13] and organic NBA. This served as an indicator of chemical reactions occurring as a function of bake temperature. Two-layer thin film studies were designed and conducted to study the diffusion and reaction of small molecules that created a three-layer stack of distinguished solubility.

We synthesized donor-polymer and CA-polymers with varying composition to find materials that dissolved in selected developers and could form a two-layer stack. These polymers were formulated with small molecules, cast as single-layer films and baked to promote and measure reaction and solubility switch. Small molecules that changed CA-polymer solubility in single-layer test were evaluated in a two-layer system through combination with the donor-polymer that was cast on an existing CA-polymer, baked to promote diffusion that resulted in reaction and solubility switch of the CA-polymer. Subsequent development to measured diffusion and a change in solubility by comparison to starting thickness. We were unable to achieve diffusion that resulted in a solubility change with our first three generations of polymers. The CA-polymer was redesigned with increasing MA and decreasing MMA concentration and evaluated in two-layer stacks; in which we observed increasing thickness loss with decreasing polymer Tg. We selected the best performing polymer and further studied diffusion, reaction and solubility change across a two-layer interface in greater detail with DCC.

5. ACKNOWLEDGMENTS

6. REFERENCES AND FOOTNOTES

[1] Ito, H. and Grant Willson, C., "Applications Of Photoinitiators To The Design Of Resists For Semiconductor Manufacturing.," ACS Symp. Ser., 11–23 (1984).

[2] Willson, C. G., Ito, H., Fréchet, J. M. J., Tessier, T. G. and Houlihan, F. M., "Approaches to the Design of Radiation-Sensitive Polymeric Imaging Systems with Improved Sensitivity and Resolution," J. Electrochem. Soc. 133(1), 181–187 (1986).

[3] Al-Khayat, O., Hong, J. K., Geraghty, K. and Neto, C., "'The Good, the Bad, and the Slippery': A Tale of Three Solvents in Polymer Film Dewetting," Macromolecules 49(17), 6590–6598 (2016).

[4] Ordaz, I., Singh, L., Ludovice, P. J. and Henderson, C. L., "Small molecule diffusion in polymer ultra-thin films," Mater. Res. Soc. Symp. Proc. 899, 52–57 (2005).

[5] Hall, D. B. and Torkelson, J. M., "Small molecule probe diffusion in thin and ultrathin supported polymer films," Macromolecules 31(25), 8817–8825 (1998).

[6] Bucknall, D. G., "Influence of interfaces on thin polymer film behaviour," Prog. Mater. Sci. 49(5), 713–786 (2004).

[7] Man, N., Sekiguchi, A. and Matsumoto, Y., "Measurement of acid diffusion from PAG in photoresists by using TOF-SIMS with GCIB," Adv. Patterning Mater. Process. XXXII 9425(March 2015), 94251H (2015).

[8] Li, J., Rochester, C. W., Jacobs, I. E., Friedrich, S., Stroeve, P., Riede, M., "Measurement of Small Molecular Dopant F4TCNQ and C60F36 Diffusion in Organic Bilayer Architectures," ACS Appl. Mater. Interfaces 7(51), 28420–28428 (2015).

[9] Kang, S., Wu, W. L., Choi, K. W., De Silva, A., Ober, C. K. and Prabhu, V. M., "Characterization of the photoacid diffusion length and reaction kinetics in EUV photoresists with IR spectroscopy," Macromolecules 43(9), 4275–4286 (2010).

[10] Perera, G. M., Pandey, Y. N., Patil, A. A., Stein, G. E. and Doxastakis, M., "Reaction kinetics in acid-catalyzed deprotection of polymer films," J. Phys. Chem. C 116(46), 24706–24716 (2012).

[11] [1] Al-Warhi, T. I., Al-Hazimi, H. M. A. and El-Faham, A., "Recent development in peptide coupling reagents," J. Saudi Chem. Soc. 16(2), 97–116 (2012).

[12] Neises, B. and Steglich, W., "Simple Method for the Esterification of Carboxylic Acids," Angew. Chemie Int. Ed. English 17(7), 522–524 (1978).

[13] In this work we use a 1% dilution of 0.26 N Tetramethyl Ammonium Hydroxide (TMAH standard developer) in water. For brevity, we refer to 2.6 mM TMAH as "aqueous TMAH".

Multi-Trigger Resist for EUV lithography

**C. Popescu[1], G. O'Callaghan[1], C. Storey[1], A. McClelland[1],
J. Roth[2], E. Jackson[2], and A.P.G. Robinson[1*]**

[1]Irresistible Materials, Birmingham Research Park, Birmingham, UK
[2]Nano-C, 33 Southwest Park, Westwood, MA, USA
*a.p.g.robinson@bham.ac.uk

Irresistible Materials (IM) is developing a photoresist based on the multi-trigger concept, which is designed to suppress roughness using a new photoresist mechanism incorporating a dose dependent quenching-like behaviour, and which is based on high EUV absorbance molecular, rather than polymeric, materials to maximise resolution. The latest results using the NXE Scanner are discussed here. The second generation (MTR Gen 2) of MTR incorporates more optimised crosslinker and photoacid generator molecules to tune the reaction rates in the multi-trigger mechanism. We have shown that the dose requirement compared to the first generation (MTR Gen1) of high opacity MTR resists previously presented can be significantly reduced without detriment to LWR or resolution. Lines and Spaces at p28 nm can be patterned at doses from 20 mJ/cm² to 50 mJ/cm² dependent on formulation ratio, with optimum LWR (3.95 nm, biased) occurring at 32 mJ/cm², CD 12.1nm, in a MTR Gen2.4 formulation. Similarly, we present p34 & p36 pillars patterned between 20 mJ/cm² and 60 mJ/cm² doses for 17 nm diameter pillars, with a minimum LCDU for 18 nm diameter p36 pillars of 3.6 nm at 45 mJ/cm² (MTR Gen2.4).

Keywords: EUV lithography, Photoresist, Molecular resist, Multi-trigger resist, Chemical amplification, Crosslinking

1. Introduction

Work is ongoing to develop a photoresist that supports the implementation of EUV lithography, and particularly high-NA EUV lithography, with increased focus on novel photoresist mechanisms. As traditional chemically amplified resists (CAR) are expected to reach a performance plateau with respect to low-Z-factor and low defectivity in high-NA, the development of alternative approaches materials becomes necessary [1–3].

The energy of EUV photons is well above the ionization threshold of the resist materials, and thus photochemical approaches are not necessarily optimal in the EUV regime. But the move to secondary electron chemistry allows for new approaches to be developed. However, the mechanism of low energy electron interaction with resist molecules are not yet entirely clear and further work to elucidate the resist mechanism is ongoing [4]. Several approaches to explain photoacid generation have been proposed. These have included the ionization of the general resist matrix leading to electron recombination with photoacid generators producing photoacids either directly [5] or indirectly [6], or internal excitation of the photoacid generator by the secondary electron leading to a photolysis-like behaviour [4,7].

The interface between the resist and the substrate is also affects the performance of the resist. The interaction of the resist with the underlayer can enhance or degrade performance, for instance by modulating the resist adhesion, whilst the generation of secondary electrons in the underlayer may also be important, and thus the chemical and physical properties of the underlayer should be carefully considered [8,9]. Furthermore, the underlayer choice can also affect the metrology

contrast in non-intuitive ways [10].

As industry moves towards the implementation of high-NA EUV to enable further improvements in resolution, it will become increasingly important to consider the overall thickness of the resist/ underlayer stack. It has long been known that the achievable post development film thickness has needed to reduce, as pitch sizes decrease, to avoid pattern collapse [11], and that this trend is accelerating [12]. However, film thicknesses will be further suppressed in High-NA, as the depth of focus of the tool is known to be severely constrained [13]. The metrology issues will also be exacerbated, and optimisation of the underlayer/ photoresist stack will increase, whilst ever thinner photoresists will also introduce pattern transfer challenges [14].

The Multi-Trigger Resist (MTR) is a new platform under development by Irresistible Materials to address the on-going requirements of EUV lithography. MTR is a molecular resist, using a ring-opening polymerization (ROP) mechanism, which additionally includes a unique dose-dependent self-quenching mechanism, known as the multi-trigger mechanism, directly in the chemical pathways, to improve performance. The intrinsic self-quenching mechanism of MTR, which has been described before [15–21] provides an advantage in acid diffusion mitigation and offers a benefit on achieving ultimate resolutions with low line edge roughness.

After the development of the initial prototype of the resist, a high-EUV opacity variant was developed (MTR Gen1). This incorporates non-metal organic high-opacity moieties to improve the capture of EUV photons. XRR Measurements (CXRO) have shown that the absorption can be widely tailored. The prototype (low-opacity) MTR has an absorbance of ~6 μm^{-1}, whilst MTR Gen1 has demonstrated that the absorbance can be tuned between 12 and 18.2 μm^{-1}. Synthesis of even more highly functionalized molecules has been achieved, and projecting from the XRR measurements, it can be calculated, using the CXRO method [22], that absorbances of 20–25 μm^{-1} could be achieved if required. MTR Gen1 is additionally a high-carbon content material with a low Ohnishi number, and shows low post development film thickness loss (~10%), to improve pattern transferability.

The second-generation of the MTR (MTR Gen2) focuses on optimisation of the reaction pathways of

the high-opacity platform [19]. It was demonstrated that good lithographic performance for P28 L/S could be achieved with doses below 20 mJ/cm^2, whilst for hexagonal pillars P36 and P34 were patterned at doses as low as 30 mJ/cm^2 [23,24].

A number of different approaches to optimisation of the chemistry exist, and we have examined three separate routes to significantly improve the MTR Z-factor: by increasing the monomer activation rate (MTR Gen2.1); adjusting the relative ROP initiation and propagation reaction rates (MTR Gen2.2); and by improving the selectivity of the multi-trigger quenching mechanism (MTR Gen2.3) [25].

Here we present further results of the MTR Gen2.1 approach, together with initial results for MTR Gen2.2 & 2.3. In addition, we have examined whether the advantages gained by each approach are independent and show first indications that combining approaches 2.1 and 2.2 lead to further improvements (MTR Gen2.4).

2. Experimental
The resist samples were prepared by dissolving the individual components in ethyl lactate or PGMEA. The solutions were then combined in various weight ratios and concentrations to give a range of formulations. The solutions undergo metal ion removal using 3M Zeta Plus filtration disks to reduce metals to levels appropriate for fab based processing.

The resist was spun onto a commercial organic underlayer, Brewer Scientific Optistack AL412. Use of other underlayers has been described elsewhere [25]. After spin-coating of the resist using a track, samples received a post application bake (PAB) of 80°C for 1 minute, and were exposed using an ASML NXE3400 scanner at imec. After exposure the samples received a post exposure bake of between 60°C and 70°C, and were developed in n-butyl acetate for 30 seconds using a dynamic system with no subsequent rinse. The patterning was observed using Hitachi CD-SEM (CG-5000 or 6300 models) with 500eV and 8pA as beam conditions, and the LWR, LER, LCDU and CER values are biased values unless otherwise stated.
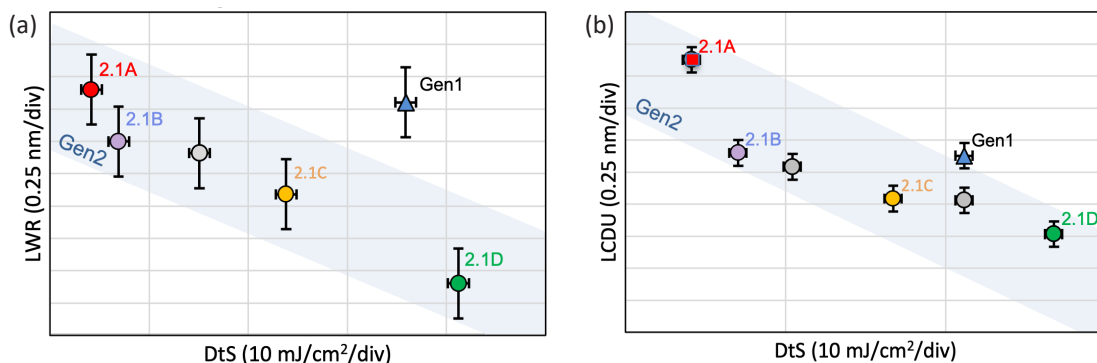
Fig. 1. Comparison in dose range and roughness between MTR Gen1 and MTR Gen2.1. (a) LWR as a function of dose-to-size for MTR Gen2.1 variants (compared to MTR Gen1) for p 28 lines and spaces; (b) LCDU as a function of dose-to-size for MTR Gen2.1 variants (compared to MTR Gen1) for p36 hex pillars. All exposures undertaken on the NXE3400, and with otherwise identical patterning and processing conditions.

3. Results

3.1 Optimisation of MTR Gen2.1 for p28 lines and spaces and p34 & p36 pillars

The optimisation of the MTR Gen2 resists provide a significant performance improvement over MTR Gen1. Fig. 1 shows the LWR as a function of dose-to-size of several formulations of MTR Gen2.1 compared to MTR Gen1. It can be seen that the effect is more marked for p28 line and space (L/S) patterning (Fig. 1 (a)), than for p36 pillars (Fig. 1 (b)). The flexibility of the MTR platform, whereby it is possible to optimise towards either speed or roughness, by varying the relative ratios of the MTR components is maintained in MTR Gen2.

Representative images of P28 L/S and P36 pillars obtained using the fastest formulation of the MTR MTR Gen2.1 series (MTR Gen2.1A) are shown in Fig. 2. The film thickness (FT) for L/S was 20 nm and for pillars the resist FT was 21.5 nm. The dose for L/S was 19 mJ/cm^2 and for pillars 29 mJ/cm^2.
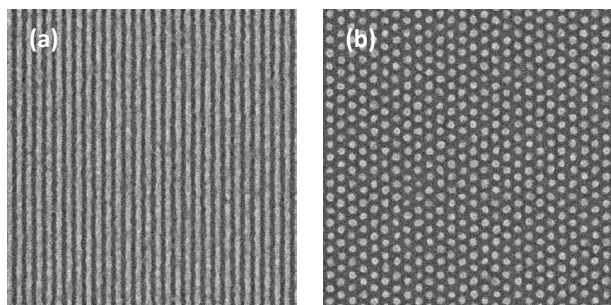
Fig. 2. p28 L/S and p36 hexagonal pillars patterning in MTR Gen 2.1A; (a) Lines: CD 13.1 nm, dose 19 mJ/cm^2; (b) Pillars: CD 18.9 nm, dose 29 mJ/cm^2. Exposed using the NXE3400.

Whilst the MTR Gen2.1A can clearly resolve at the indicated pitches, the roughness is quite high. Due to the tunability of the MTR formulation, the roughness can be modulated relatively easily through formulation changes. MTR Gen2.1B, C, and D, have reduced sensitivity compared to MTR Gen2.1A but roughness and resolution improve.

Fig. 3 shows p34 hexagonal pillars patterned on the NXE3400 using MTR Gen2.1B, C, and D which have incrementally higher dose-to-size. The diameter of the pillars is 18 nm, and the doses are 35 mJ/cm^2 for MTR Gen2.1B, 55 mJ/cm^2 for MTR Gen2.1C and 76 mJ/cm^2 for MTR Gen2.1D.
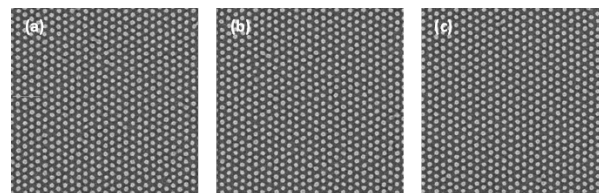
Fig. 3. Hexagonal pillars of CD 18 nm patterned on the NXE3400 at p34: (a) MTR Gen2.1B, dose 35 mJ/cm^2; (b) MTR Gen2.1C, dose 55 mJ/cm^2, and (c) MTR Gen2.1D, dose 76 mJ/cm^2.

For p28 lines and spaces, the same trend is observed with roughness reducing from MTR Gen2.1B to D, with the doses used to obtain these patterns ranging from 25 to 59.5 mJ/cm^2, Fig. 4. The CD for these p28 lines is 13.8 nm, and all exposures were performed on the NXE3400.
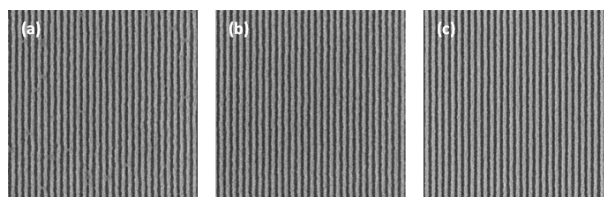
Fig. 4. Lines and spaces of CD 13.8 nm patterned on the NXE3400 a p28: (a) MTR Gen2.1B, dose 25 mJ/cm^2; (b) MTR Gen2.1C, dose 42.5 mJ/cm^2; and (c) MTR Gen2.1D, dose 59.5 mJ/cm^2.

MTR-Gen2.1C		**MTR-Gen2.2**		**MTR-Gen2.3**	
Dose:	24.4mJ/cm²	Dose:	21.2 mJ/cm²	Dose:	31.2mJ/cm²
CD:	12.4 nm	CD:	13.1nm	CD:	13.4 nm
LWR	2.76 nm	LWR	2.61 nm	LWR	3.22nm

Fig. 5. Lines and space patterned at P28 at PSI for MTR Gen2.1C, MTR Gen2.2 and MTR Gen2.3. Each has a different optimisation strategy, and all three out-perform MTR Gen1.

3.2 Results for MTR Gen2.2 – Gen2.3

Evaluation of MTR Gen2.2 optimizations (improved polymerization) and MTR Gen2.3 approaches (better termination selectivity) was undertaken at PSI. As with MTR Gen2.1 both approaches to enhancing the performance of the MTR system show performance improvement over MTR Gen1 as shown in Fig. 5.

3.3. Introducing MTR Gen 2.4

For each of MTR Gen2.1 – 2.3 the optimizations addressed a single aspect of the MTR chemical mechanism to improve performance. MTR Gen2.4 takes the improvements seen in MTR Gen2.1 and MTR Gen2.2 and combines them.

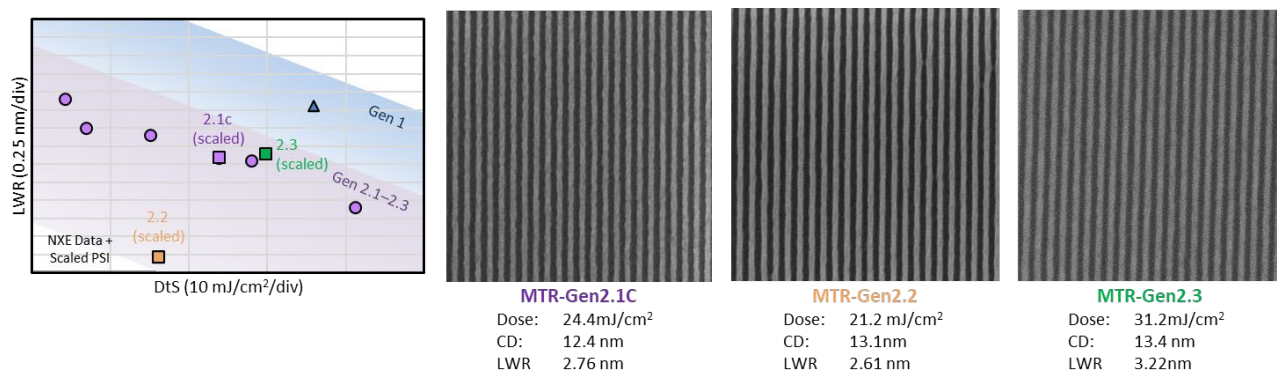Initial results from imec patterning for MTR Gen2.4 shows that additional benefits come from the simultaneous optimization of two reaction mechanisms. Fig. 6 shows p28 lines patterned at 32mJ/cm² to achieve a line width of 12.1nm with a biased LWR of 3.95nm, and a p36 hexagonal array of pillars patterned at 45mJ/cm² with a pillar diameter of 18.3nm and an LCDU of 3.6nm. Compared to previous formulations, the MTR Gen2.4 achieves the same p28 biased LWR as MTR Gen2.1 with a 40% reduction in dose.

4. Conclusion

MTR Resist is a negative tone resist with an intrinsic dose dependent quenching mechanism, which can pattern high resolution patterns with EUV lithography. The lithographic performance of several second-generation MTR formulations was shown. The fastest variant of MTR Gen2.1 was 3 times faster than MTR Gen1, with only a very small increase in LWR in L/S patterning, whilst sensitivity could be doubled for hexagonal pillar patterning whilst maintaining LCDU. MTR Gen2.1 optimizes the monomer activation rate; similar performance enhancement is seen by optimizing the ROP reaction rates (MTR Gen2.2 [20]), or improving the multi-trigger efficiency (MTR Gen2.3; Fig. 5). These performance gains appear to be non-correlated and MTR Gen2.1 & 2.2 can be combined to achieve further improvement (MTR Gen2.4; initial NXE3400 data Fig. 6).

Fig. 6. p28 dense lines and p36 hex pillar patterned with MTR Gen2.4 resist.

References

[1] Nagahara, S., Que Dinh, C., Yoshida, K., Shiraishi, G., Kondo, Y., Yoshihara, K., Nafus, K., Petersen, J.S., De Simone, D., Foubert, P., Vandenberghe, G., Stock, H-J, Meliorisz, B., "EUV resist chemical gradient enhancement by UV flood exposure for improvement in EUV resist resolution, process control, roughness, sensitivity, and stochastic defectivity," *Proc. SPIE*, **11326** (2020) 113260A.

[2] Shirotori, A., Hoshino, M., De Simone, D., Vandenberghe, G., Matsumoto, H., "A novel main chain scission type photoresists for EUV lithography", *Proc SPIE*, **11517** (2020) 115170D.

[3] Sharma, S.K., Kumar, R., Chauhan, M., Moinuddin, M.G., Peter, J., Ghosh, S., Pradeep, C.P., Gonsalves, K.E., "All-new nickel-based Metal Core Organic Cluster (MCOC) resist for N7+ node patterning," *Proc SPIE*, **11326** (2020) 1132604.

[4] Torok, J., Del Re, R., Herbol, H., Das, S., Bocharova, I., Paolucci, A., Ocola, L. E., Ventrice Jr., C., Lifshin E., Denbeaux, G., Brainard, R. L., "Secondary Electrons in EUV Lithography," *J Photopolym. Sci. Technol.*, **26** (2013) 625–634.

[5] Thackeray, J., Cameron, J., Jain, V., LaBeaume, P., Coley S., Ongayi O., Wagner M., Rachford A., Biafore J., "Progress in Resolution, Sensitivity and Critical Dimensional Uniformity of EUV Chemically amplified Resists," *Proc. SPIE*, **8682** (2013) 868213.

[6] Nakano, A., Kozawa, T., Okamoto, K., Tagawa, S., Kai, T., Shimokawa, T., "Acid Generation Mechanism of Poly(4-hydroxystyrene)-Based Chemically Amplified Resists for Post-Optical Lithography: Acid Yield and Deprotonation Behavior of Poly(4-hydroxystyrene) and Poly(4-methoxystyrene)," *Jpn. J. App. Phys.* **45**, (2006) 6866–6871.

[7] Narasimhan, A., Wisehart, L., Grzeskowiak, S., Ocola, L.E., Denbeaux, G., Brainard, R. L., "What we don't know about EUV exposure mechanisms," J Photopolym. Sci. Technol., **30** (2017) 113–120.

[8] Long, L.T., Neureuther, A., Walraff, G., Naulleau, P. "Resist Underlayer Simulations," In *IEUVI TWG April 2022*, 7, (2022), http://ieuvi.org/TWG/ Resist/IEUVI_Resist01.htm (Accessed 13/02/2023).

[9] Raley, A., Huli, L., Grzeskowiak, S., Lutker-Lee, K., Krawicz, A., Feurprier, Y., Liu, E., Kato, K., Nafus, K., Dauendorffer, A., Bae, N., LaRose, J., Metz, A., Hetzer, D., Honda, M., Nishizuka, T., Ko, A., Okada, S., Ido, Y., Onitsuka, T., Kawakami, S., Fujimoto, S., Shimura, S., Dinh, C.Q., Muramatsu, M., Biolsi, P., Mochiki, H. and Nagahara, S., "Outlook for high-NA EUV patterning: a holistic patterning approach to address upcoming challenges," *Proc SPIE*, **12056** (2022) 120560A.

[10] Severi, J., Lorusso, G.F., De Simone, D., Moussa, A., Saib, M., Duflou, R., De Gendta, S., "Chemically amplified resist CDSEM metrology exploration for high NA EUV lithography," *J Micro/Nanopattern. Mater. Metrol.*, **21** (2022) 021207.

[11] Goldfarb, D.L., Bruce, R.L., Bucchignano, J.J., Klaus, D.P., Guillorn, M.A. and Wu, C.J., "Pattern collapse mitigation strategies for EUV lithography," *Proc SPIE,* **8322** (2012) 832205.

[12] Noga, D.E., Lawson, R.A., Lee, C.T., Tolbert, L.M. and Henderson, C.L., "Understanding pattern collapse in high-resolution lithography: impact of feature width on critical stress." *Proc* SPIE, **7273** (2009) 727334.

[13] Burov, A., Pret, A.V. and Gronheid, R., "Depth of focus in high-NA EUV lithography: a simulation study." *Proc SPIE,* **12293** (2022) 122930V.

[14] Fallica, R., De Simone, D., Chen, S., Safdar, M. and Suh, H.S., "Scaling and readiness of underlayers for high-NA EUV lithography," *Proc* SPIE, **12292** (2022) 122920V.

[15] Vesters, Y., McClelland, A., Popescu, C., Dawson, G., Roth, J., Theis, W., de Simone, D., Vandenberghe, G., Robinson, A.P.G, "Multi-trigger resist patterning with ASML NXE3300 EUV scanner," *Proc. SPIE*, **10586** (2018) 1058308.

[16] Popescu, C., Kazazis, D., McClelland, A., Dawson, G., Roth, J., Theis, W., Ekinci, Y., Robinson, A.P.G., "High-resolution EUV lithography using a multi-trigger resist," *Proc SPIE*, **10583** (2018) 105831L.

[17] O'Callaghan, G., Popescu, C., McClelland, A., Kazazis, D., Roth, J., Theis, W., Ekinici, Y., Robinson, A.P. G., "Multi-trigger resist – Novel synthesis improvements for high resolution EUV lithography," *Proc SPIE*, **10960** (2019) 109600C.

[18] Montgomery, W., McClelland A., Ure D., Roth J., Robinson A., "Irresistible Materials multi-trigger resist: the journey towards high volume readiness," *Proc SPIE*, **10143** (2017) 1014328.

[19] Popescu, C., McClelland, A., Kazazis, D., Dawson, G., Roth, R., Ekinci, Y., Theis, W. and Robinson, A. P.G., "Multi-trigger resist for electron beam and extreme ultraviolet lithography," *Proc SPIE*, **10775** (2018) 1077502.

[20] Popescu C., O'Callaghan G., McClelland A., Roth J., Lada T., Robinson A.P.G., "Performance enhancements with high opacity multi-trigger resist," *Proc SPIE*, **11326** (2020) 1132611.

[21] Popescu, C., O'Callaghan, G., McClelland, A., Roth, J., Lada, T., Kudo, T., Dammel, R., Moinpour, M., Cao, Y., Robinson, A. P. G., "Progress in the multi-trigger resist," *Proc SPIE*, **11612** (2021) 116120K.

[22] https://henke.lbl.gov/optical_constants/atten2. html (Accessed 13/02/2023).

[23] Popescu, C., O'Callaghan, G., McClelland, A., Roth, J., Jackson, E., Robinson, A. P. G., "Component optimization in the multi-trigger resist," *Proc SPIE*, **12055** (2022) 120550G.

[24] Popescu, C., O'Callaghan, G., McClelland, A., Storey, C., Roth, J., Jackson, E. and Robinson, A.P.G., " Recent accomplishments in EUV lithography patterning for multi-trigger resist," *Proc SPIE*, **12292** (2022) 122920E.

[25] Popescu, C., O'Callaghan, G., McClelland, A., Storey, C., Roth, J., Jackson, E. and Robinson, A.P.G., "EUV lithography patterning using multi-trigger resist," *Proc SPIE*, **12498** (2023) 1249812.

Compositional Dependence of Charge Carrier Dynamics in Multi-Cation/Halide Wide Bandgap Perovskites

Yieon Park[1], Ryosuke Nishikubo[1,2*], and Akinori Saeki[1,2]

[1] Department of Applied Chemistry, Graduate School of Engineering,
Osaka University, 2-1 Yamadaoka, Suita, Osaka 565-0871, Japan
[2] Innovative Catalysis Science Division, Institute for Open and Transdisciplinary Research
Initiatives (ICS-OTRI), Osaka University, 1-1 Yamadaoka, Suita, Osaka 565-0871, Japan
*nishikubo@chem.eng.osaka-u.ac.jp

Lead halide perovskites (LHPs) have a diverse compositional range owing to various employable A- and X-site ions. However, the effect of underlying charge transport layer (CTLs) on the charge transport properties in the composition-varied LHPs remains uncertain. Herein, we employed optical spectroscopies and time-resolved microwave conductivity (TRMC) to investigate the dependence of the optical and photoconductive properties of various A-site (formamidinium: FA, methylammonium: MA, Cs) and X-site (Br, I) compositions of LHPs with different underlying CTLs. Intriguingly, it was found that tricationic FAMACs-based LHPs showed more efficient charge separation than bicationic FACs- and FAMA-based ones in a regular structure. Conversely, FACs-based LHPs showed more efficient charge separation than the others in an inverted structure, as evidenced by the prolonged lifetime of TRMC decays. In alignment with these TRMC results, FAMACs exhibited higher device performance in a regular structure than inverted structure. Whereas, FACs showed superior performance in an inverted structure. Hence, our study revealed that the optimal device structure is compositionally dependent on the charge carrier dynamics.
Keywords: Perovskite, Widegap, Solar cell, Photoluminescence, Charge carrier dynamics

1. Introduction

Lead halide perovskite (LHP) solar cells have garnered significant interests as flexible, cost-effective, and highly efficient photovoltaics [1–5]. In the past decade, the power conversion efficiency (PCE) of 3-dimensional (ABX_3) perovskite solar cells (PSCs) has been dramatically improved from 10.9% to 25.6% [6–8], which is comparable to that of single crystalline silicon solar cells. Furthermore, the optoelectronic properties of LHPs can be easily modulated by altering their composition. Changing the X-site anion allows for tuning the bandgap to a large extent [9,10]. Br-rich LHPs have relatively wide bandgaps, making them ideal for application as a wide bandgap layer within tandem solar cells as well as indoor solar cells [11,12]. Meanwhile, the addition of small amount of methylammonium (MA) and/or cesium (Cs) cations to a

formamidinium (FA)-based LHP has been found to effectively enhance the device performance and stability [13,14]. To date, various A-site-engineered compositions such as FAMACs, FACs, and FAMA have been identified as highly efficient compositions [15–17].

Considering the possibility of various compositions, exploring the optimal combination of the A- and X-site is of particular importance. As for narrow bandgap (NG) LHPs with low Br contents (Br ratio < 30%), FAMACs- and FAMA-based ones have demonstrated impressive PCEs of 22~25% [16–20]. For wide bandgap (WG) LHPs with larger Br-contents (Br ratio > 30%), high PCEs have been more commonly reported in FAMACs- and FACs-based ones [11, 21–23]. However, there is a significant lack of insight into the compositional dependence of LHPs on their optoelectronic

properties.

Additionally, the dependence of device structure, whether regular or inverted, is another significant contributing factor to its performance. For a regular structure, TiO_2 and SnO_2 have been widely employed as underlying electron transport materials (ETMs). For an inverted structure, PEDOT:PSS, poly(9,9-bis(3'-(*N,N*-dimethyl)-*N*-ethylammoinium-propyl-2,7-fluorene)-*alt*-2,7-(9,9-dioctylfluorene)) dibromide coated on poly-triarylamine (PTAA/PFN-Br bilayer), and self-assembled monolayers (SAMs) have been commonly utilized as the underlying hole transport materials (HTMs). Recently, for WG inverted PSCs, devices with PTAA(/PFN-Br) [12, 21, 24–26] and SAMs [27–30] have demonstrated particularly high PCE. FAMACs- and FACs-based WG LHPs have exhibited relatively high PCE exceeding 18% [11]. Despite the remarkable improvements in WG-PSCs, the optimal A-site composition is still not comprehensively understood. To clarify this, the compositional dependence of the charge transport properties with different underlying layers needs to be elucidated.

Conventionally, photoluminescence (PL) spectroscopy and current density (*J*)-voltage (*V*) measurement are one of effective methods to investigate the charge recombination property. However, it is often difficult to distinguish between the effects of the LHP quality and the charge transfer when PL is measured on a perovskite film overlying a CTL. This is because improvements of perovskite quality such as an increase in crystal size and a suppression of traps enhances the PL intensity, while an efficient charge transfer from LHPs to ETMs or HTMs causes PL quenching. These opposing effects are difficult to separate from the PL intensity. Meanwhile, *J-V* measurements offers useful parameters, namely short-circuit *J* (J_{SC}), open-circuit *V* (V_{OC}), fill factor (FF), shunt resistance (R_{Sh}), series resistance (R_S), and ideal factor (*n*). However, the effect coming from each layer cannot be directly separated. In this viewpoints, time-resolved microwave conductivity (TRMC) measurement is a highly effective evaluation method [31–33]. A TRMC signal intensity and decay represent a transient conductivity (the product of charge mobility and density) and lifetime, respectively. Moreover, measuring LHPs with/without charge transport layer provides a reliable indicator of charge transport [34]. Hence, the film quality and charge separation can be separately evaluated.

In this report, we investigated a range of LHPs with different A-site (FAMACs, FACs, FAMA) and X-site (Br ratio = 20, 33, 50%) compositions, grown on different underlying layers (mesoporous (mp)-TiO_2 and PTAA/PFN-Br) using UV-vis, X-ray diffraction (XRD), PL, TRMC, and device measurements. By comparing PL, TRMC, and *J-V* measurement outcomes, we revealed the dependence of optimal LHP compositions for different device structures. When overlying the mp-TiO_2 scaffold layer, FAMACs-LHPs exhibited ~4.7 and ~8.6 times increase in PL intensity and TRMC signal lifetime, respectively, compared to those of FAMACs-LHPs coated on PTAA/PFN-Br. These can be attributed to the superior LHPs quality when FAMACs-LHPs are coated on mp-TiO_2. Besides, FACs-LHPs on PTAA showed the prominent enhancement of PL intensity (3.6 times higher than that of FACs-LHPs on mp-TiO_2) and TRMC signal lifetime (2.6 times longer than that of FAMACs-LHPs on PTAA/PFN-Br). As a result, FAMACs- and FACs- LHPs were identified as suitable for the regular and inverted structures, respectively. We further discuss the conjunction of PSC performance with the charge carrier dynamics.

2. Experimental

The fabrication procedure of regular PSCs follows our previous report [35]. A fluorine-doped tin oxide (FTO)/glass substrate was cleaned with detergent, deionized water, and isopropyl alcohol, followed by UV-ozone treatment. Compact TiO_2 and mp-TiO_2 layers were deposited onto the FTO/glass via spray pyrolysis and spin-coating, respectively, followed by sintering at 500 °C for 20 min. 1 M precursor solutions of LHPs with the compositions of $FA_{0.8}MA_{0.15}Cs_{0.05}PbBr_xI_{(1-x)}$, $FA_{0.9}Cs_{0.1}PbBr_xI_{(1-x)}$, and $FA_{0.85}MA_{0.15}PbBr_xI_{(1-x)}$ (*x* = 0.20, 0.33, 0.50) were prepared by dissolving the stoichiometric ratios of FAI, MABr, CsI, PbI_2, and $PbBr_2$ (Tokyo Chemical Inc., TCI) into *N,N*-dimethylformamide (DMF): dimethyl sulfoxide (DMSO) = 4:1 mixed solution. The solution was spin-coated at 1000 rpm for 10 s and 4500 rpm for 30s. During the spin, chlorobenzene (CB) was dropped, and subsequently annealed at 100 °C for 30 min. 50 nm-thick HTM layers were prepared from 2,2',7,7'-Tetrakis-(N,N-di-4-methoxyphenylamino)-9,9'-spirobifluorene (SpiroOMeTAD, Borun New Material) in CB (78.2 mg mL^{-1}) with 52 mol% of Lithium bis(trifluoromethanesulfonyl)imide (LiTFSI, Sigma-Aldrich) and 5.4 mol% tris(2-(1H-pyrazol-1-

yl)-4-*tert*-butylpyridine)cobalt(III) tris(bis(trifluoromethylsulfonyl)imide) (FK209, Sigma-Aldrich) relative to SpiroOMeTAD dissolved in acetonitrile (Sigma-Aldrich, anhydrous, 99.8%) and 2.9 vol% 4-*tert*-buthypyridine (Sigma-Aldrich, 98%) relative to the solution volume. Finally, a 100 nm-thick stripe-shaped gold electrode was thermally deposited in a vacuum chamber.

For inverted PSCs, PTAA toluene solution (1.75 mg mL^{-1}) and PFN-Br methanol solution (0.5 mg mL^{-1}) were sequentially spin-coated onto cleaned indium tin oxide (ITO)/glass substrates with the spinning rate of 6000 for 20 s and 5000 rpm for 20 s [21]. LHPs were deposited and annealed with the same manner with regular structure. Fullerene (C$_{60}$, 20 nm), bathocuproine (BCP, 8 nm), and Ag electrode (100 nm) were sequentially deposited in vacuum.

J-V measurements were performed using a source-meter unit (ADCMT Corp., 6241A) under AM 1.5 G solar illumination at 100 mW cm^{-2} (1 sun, monitored by a calibrated standard cell, Bunko Keiki BS-520BK) from a 300 W solar simulator (SAN-EI Corp., XES-301S). The size of the active area was defined by a black metal mask with a square hole (2 × 2 mm^2). External quantum efficiency (EQE) spectra were measured using a Bunko Keiki model SM-250KD equipped with a Keithley model 2401 source meter. The monochromated light power was calibrated by a silicon photovoltaic cell, Bunko Keiki model S1337-1010BQ.

For TRMC measurements, perovskite, mp-TiO$_2$, HTM, and their composite layers were prepared in the same manner as the devices on a quartz substrate. The sample was set in a resonant cavity and probed by continuous microwaves at ca. 9.1 GHz. The excitation laser from an optical parametric oscillator (OPO, Continuum Inc., Panther) seeded by the third harmonic generation of a Nd:YAG laser (Continuum Inc., Surelite II, 5–8 ns pulse duration, 10 Hz) was set at 500 nm at $I_0 = 3.84 \times 10^{10}$ photons cm^{-2} pulse^{-1}. The photoconductivity transient $\Delta\sigma$ is converted to the product of the quantum efficiency (φ) and the sum of charge carrier mobilities, $\Sigma\mu$ (= $\mu_h + \mu_e$) by $\varphi\Sigma\mu = \Delta\sigma (eI_0F_{light})^{-1}$, where e and F_{Light} are the unit charge of a single electron and a correction (or filling) factor, respectively.

3. Results and discussion

3.1. Optical and structural characterizations

Photoabsorption spectra of LHP films with various A-site and X-site compositions (3 × 3 = 9)
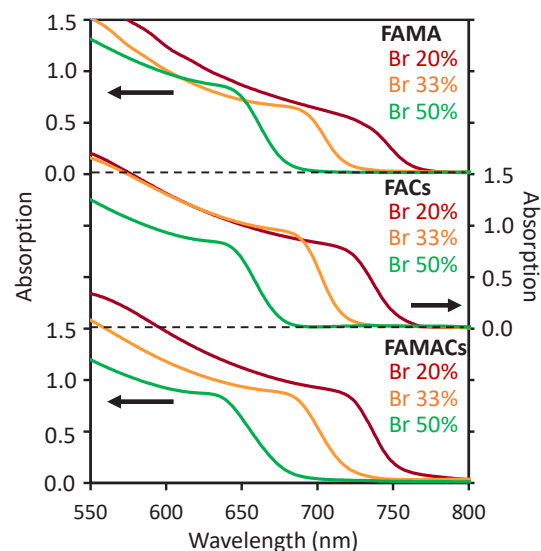
Fig. 1. Photoabsorption spectra of mixed LHP films. All the films were deposited on mp-TiO$_2$.
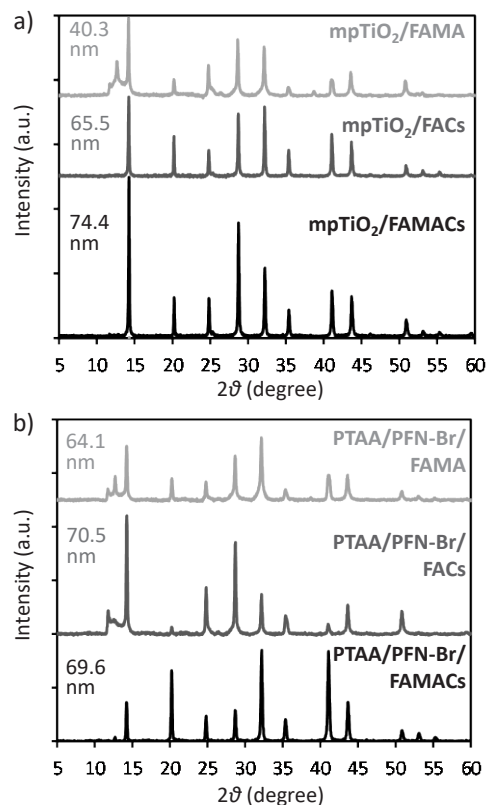
Fig. 2. XRD patterns of Br-33% LHP films deposited on **(a)** mp-TiO$_2$ and **(b)** PTAA/PFN-Br. The crystal size calculated at 14.5° peak by Sherrer's equation were shown in the graphs.

Table 1. E_g (unit: eV) of LHPs with various A-site and X-site compositions calculated from Fig. 1.

Br content	FAMACs	FACs	FAMA
Br 20%	1.66	1.66	1.64
Br 33%	1.73	1.78	1.74
Br 50%	1.85	1.86	1.84
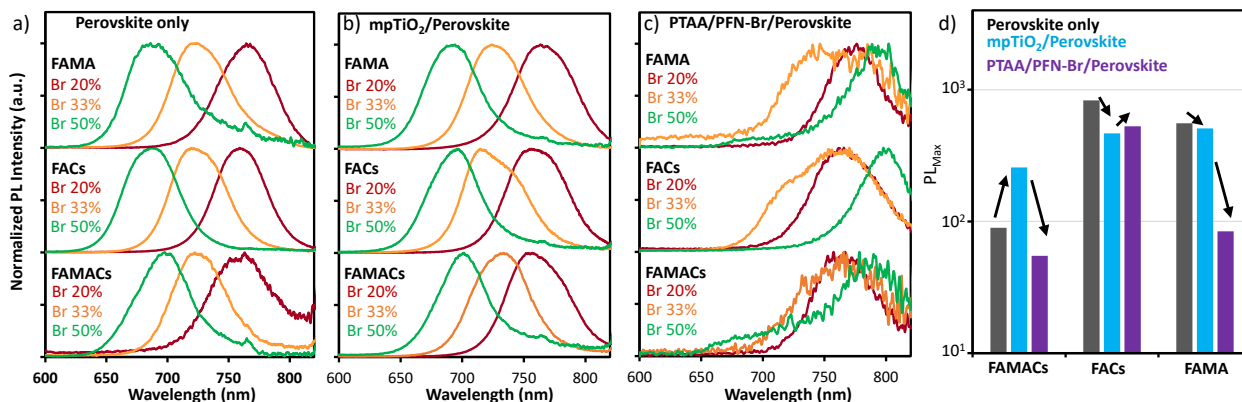
Fig. 3. PL spectra of **(a)** LHP single films, **(b)** mp-TiO$_2$/LHP films, and **(c)** PTAA/PFN-Br/LHP films (λ_{ex} = 500 nm). **(d)** The summary of PL peak intensity of Br-33% LHP films deposited on various scaffold layers.

were measured (Fig 1). The bandgaps (E_g) calculated from the absorption edges were mostly independent on A-site cations, as its majority was occupied by FA (>0.80) (Table 1). In contrast, changing the ratio of Br (20, 33, and 50%) in the X-site caused significant differences in the E_g values. The Br-33% LHPs provided suitable E_g for tandem solar cells combined with Pb-Sn mixed LHPs or CIGS.

XRD measurements were performed on Br-33% LHPs to identify their crystal phase (Fig. 2). The expected formation of LHP phase was confirmed in all the samples. Among the LHP films on mp-TiO$_2$, FAMACs-LHP exhibited the largest XRD intensity and crystal size calculated at 14.5° peak by Sherrer's equation, indicating a higher crystallinity than the others (Fig. 2a). However, among the PTAA/PFN-Br/LHP samples, a FACs-LHP film exhibited the highest crystallinity (Fig. 2b). Such dependence of the crystallinity on the LHP composition as well as the underlying scaffold layer engenders curiosity in their optoelectronic properties.

PL measurements were carried out on a total of 27 films with a 3 × 3 × 3 matrix of A-site compositions, X-site compositions, and the underlying layers (Figs. 3a–3c). The relative PL peak intensities are presented in Fig. 3d. While there were no observable peak separation from the pristine LHP films and mp-TiO$_2$/LHP films, noticeable tails in the near infrared (IR) region were detected from Br-50% samples, suggesting a significant halide segregation in high Br-ratio LHPs (Fig. 3a, 3b). In a comparison between pristine LHPs and mp-TiO$_2$/LHPs, a FAMACs-LHP exhibited a notable increase in PL intensity upon combining with mp-TiO$_2$ (Fig. 3d). This PL

enhancement could arise from either (i) an inefficient electron transfer from LHP to TiO$_2$ or (ii) a reduced defect density. However, distinguishing these possibilities based on the PL results alone is difficult. In contrast, FACs- and FAMA-based LHPs showed the decrease of PL intensity by combining with mp-TiO$_2$, because the effect of electron transfer to TiO$_2$ was more prominent than that of film quality improvement.

Alternatively, PTAA/PFN-Br/LHP films demonstrated the significant stokes shift especially in Br-50% samples (Fig. 3c), indicating more significant halide segregation. Notably, the Br-33% samples showed larger blue shift of PL compared to Br-20%, along with peak splits. This result indicates that the defect formation associated with halide segregation is significant in PTAA/PFN-Br/LHPs. However, FACs-LHP on PTAA/PFN-Br showed a higher PL intensity than that on mp-TiO$_2$, which is an opposite behavior from what was seen in the FAMACs- and FAMA-LHPs (Fig. 3d). This also probably owes to the effect of either reduced defects or an inefficient hole transfer. To distinguish these effects, further detailed study of charge carrier dynamics was required.

3.2. Charge carrier dynamics

TRMC measurement was performed for the forementioned 27 LHPs films (Fig. 4a–4c). All the Br-20% and 33% pristine films exhibited high TRMC signal ($\varphi\Sigma\mu_{max}$) of 30–50 cm^2 V^{-1} s^{-1}. Although this is marginally lower than that of the LHPs with lower Br ratios (Br: 0~10%) [33,34], they are much higher than other organic and inorganic semiconductor films [31,32,36,37]. The decay lifetimes (τ) calculated by double exponential fitting are summarized in Fig. 4d–4f and Table 2.
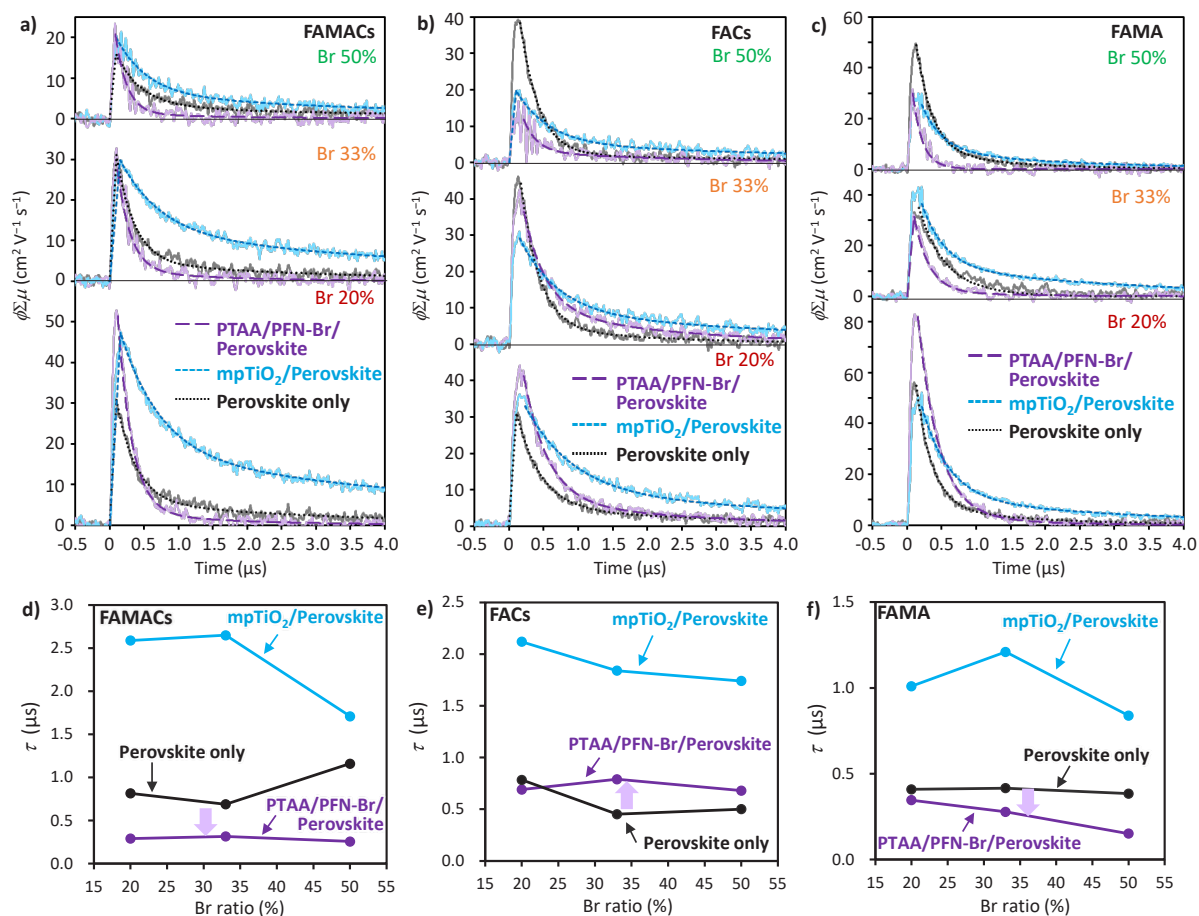
Fig. 4. TRMC transients of **(a)** FAMACs-LHPs, **(b)** FACs-LHPs, and **(c)** FAMA-LHPs with various Br ratio and underlying layers (λ_{ex} = 500 nm, photon density: 3.84×10^{10} photons cm^{-2} pulse^{-1}). The solid and dotted lines are original data and double exponential fitting ($y = \alpha_1 \exp(t / \tau_1) + \alpha_2 \exp(t / \tau_2)$), respectively. The corresponding decay lifetimes ($\tau = (\alpha_1\tau_1 + \alpha_2\tau_2) / (\alpha_1 + \alpha_2)$) of **(d)** FAMACs-LHPs, **(e)** FACs-LHPs, and **(f)** FAMA-LHPs.

Among the mp-TiO$_2$/LHP films, FAMACs-LHPs with Br-content of 20 and 33% showed the significantly longer τ than those of the others, indicating particularly efficient charge separation and low defect density. Thus, the forementioned increased PL intensity of the mp-TiO$_2$/FAMACs-LHPs can as well be explained by the decreased defect, rather than the insufficient charge transfer. The enhanced crystalline feature observed in XRD of mp-TiO$_2$/FAMACs-LHP is also consistent with this TRMC result. In sharp contrast, FAMACs- and FAMA-LHPs deposited on PTAA/PFN-Br showed significant decrease in their τ relative to the corresponding pristine LHPs, indicating more significant nonradiative recombination than mp-TiO$_2$/LHP films. Besides, FACs-LHPs on PTAA/PFN-Br showed much improved τ, indicating their effective defect suppression. It should be noted that these TRMC results rationally explain the reason of the improved PL intensity in mp-TiO$_2$/FAMACs-LHPs and PTAA/PFNBr/FACs-LHPs as the suppression of recombination.

3.3. Device evaluation
    For solar cell measurements, we focused on FAMACs- and FACs-LHPs (Br-33%) because of

Table 2. The TRMC decay lifetimes (τ in µs) of LHPs with various A-site and X-site compositions and underlying layers (perovskite only: (i), mp-TiO$_2$/LHPs: (ii), PTAA/PFNBr/LHPs: (iii)).

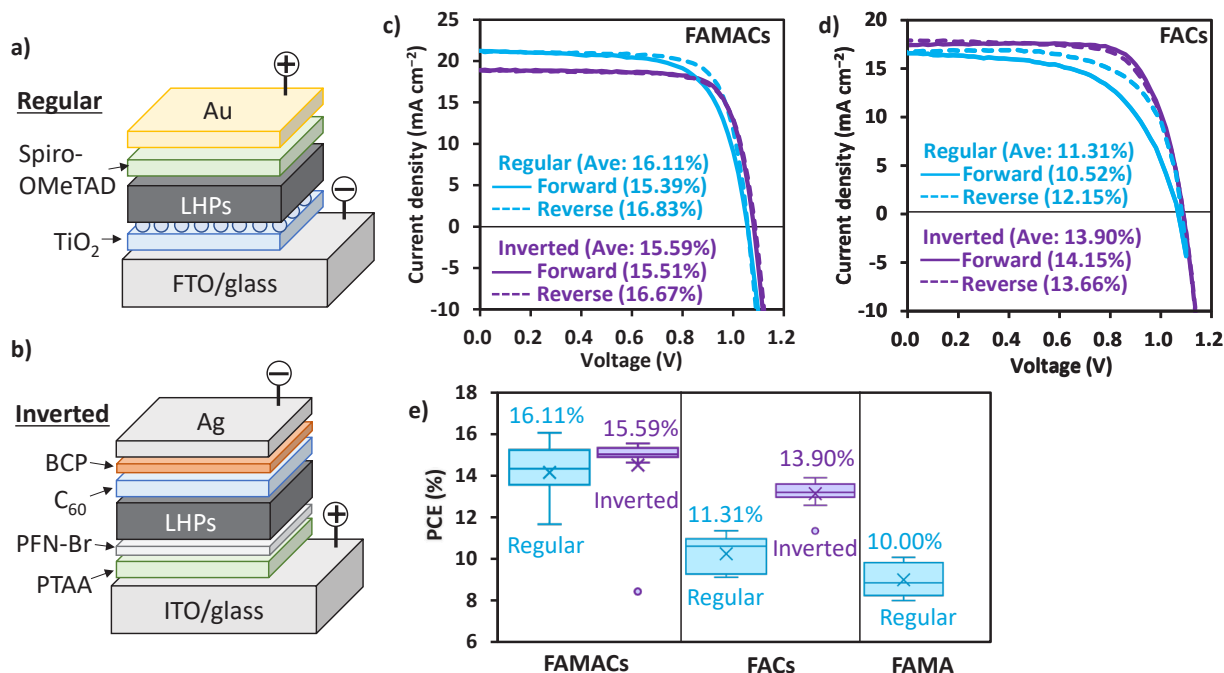| A-site cation	FAMACs			FACs			FAMA		
Layer	(i)	(ii)	(iii)	(i)	(ii)	(iii)	(i)	(ii)	(iii)
Br 20%	0.816	2.59	0.291	0.783	2.12	0.690	0.409	1.01	0.346
Br 33%	0.689	2.65	0.316	0.452	1.84	0.790	0.416	1.21	0.278
Br 50%	1.16	1.71	0.257	0.500	1.74	0.680	0.384	0.839	0.151

Fig. 5. Illustration of **(a)** regular and **(b)** inverted device structures. *J-V* curves of the best performed devices of **(c)** FAMACs-LHPs (Br-33%) and **(d)** FACs-LHPs (Br-33%). **(e)** The box plot of all the device performance. The highest PCE for each type of device is described in the figure.

particularly improved TRMC τ values on mp-TiO$_2$ and PTAA/PFN-Br, respectively. The illustrations of device structures, *J-V* curves of the best devices, and the summary of maximum and average PCEs are described in Fig. 5a, 5b, and 5c, 5d, and 5e respectively. Notably, FAMACs-LHPs exhibited higher performance in the regular structure (16.09%) than that of the inverted cell (15.59%). On the contrary, FACs-LHP showed the higher PCE in the inverted structure (13.91%) than that in the regular structure (11.31%). The devices showed a notable consistence with the PL and TRMC results. These compositional and scaffold layer-induced dependence are probably originated from the quality of LHP crystal such as defect density and/or the spatial inhomogeneity due to halide segregation [38,39].

4. Conclusion

We investigated the charge carrier dynamics of WG LHPs with varying A-site and X-site compositions, namely FA$_{0.8}$MA$_{0.15}$Cs$_{0.05}$PbBr$_{3x}$I$_{(3-3x)}$, FA$_{0.9}$Cs$_{0.1}$PbBr$_{3x}$I$_{(3-3x)}$, and FA$_{0.85}$MA$_{0.15}$PbBr$_{3x}$I$_{(3-3x)}$ ($x = 0.20, 0.33, 0.50$) on different underlying layers (mp-TiO$_2$ and PTAA/PFN-Br) by utilizing PL, TRMC, and *J-V* measurements. As a result, FAMACs-LHPs on mp-TiO$_2$ exhibited more efficient charge separation and suppressed non-radiative recombination than that on PTAA/PFN-Br, as evidenced by their enhanced PL intensity and

longer TRMC τ. Conversely, FACs-LHPs showed more suppressed recombination when overlying PTAA/PFN-Br than mp-TiO$_2$, which is contrary to FAMACs-LHPs. The TRMC results exhibited good consistency with the higher solar cell performances of the regular FAMACs-PSCs and the inverted FACs-PSCs. We speculate that the dependence on the LHP compositions as well as the underlying layers is originated from the defect density and/or the spatial inhomogeneity. These findings offer invaluable insight into optimizing the LHP composition as well as the device structure with improved performance of WG PSCs.

References
1. W. Zhang, G. E. Eperon, H, Snaith, *Nat. Energy*, **1** (2016) 16048.
2. A. K. Jena, A. Kulkarni, T. Miyasaka, *Chem. Rev.*,

119 (2019) 3036–3103.

3. S. Y. Kim, J.-W. Lee, H. S. Jung, H. Shin, N.-G. Park, *Chem. Rev.*, **120** (2020) 7867−7918.

4. E. L. Lim, A. Hagfeldt, D. Bi, *Energy Environ. Sci.*, **14** (2021) 3256–3300.

5. T. Wu, Z. Qin, Y. Wang, Y. Wu, W. Chen, S. Zhang, M. Cai, S. Dai, J. Zhang, J. Liu, Z. Zhou, X. Liu, H. Segawa, H. Tan, Q. Tang, H. Fang, Y. Li, L. Ding, Z. Ning, Y. Qi, Y. Zhang, L. Han, *Nano-Micro Lett.*, **13** (2021) 152.

6. H.-S. Kim, C.-R. Lee, J.-H. Im, K.-B. Lee, T. Moehl, A. Marchioro, J. S. Moon, R. Humphry-Baker, J.-H. Yum, J. E. Moser, M. Grätzel, N.-G. Park, *Sci. Rep.*, **2** (2012) 591.

7. M. M. Lee, J. Teuscher, T. Miyasaka, T. N. Murakami, H. J. Snaith, *Science*, **338** (2012) 643–647.

8. J. Jeong, M. Kim, J. Seo, H. Lu, P. Ahlawat, A. Mishra, Y. Yang, M. A. Hope, F. T. Eickemeyer, M. Kim, Y. J. Yoon, I. W. Choi, B. P. Darwich, S. J. Choi, Y. Jo, J. H. Lee, B. Walker, S. M. Zakeeruddin, L. Emsley, U. Rothlisberger, A. Hagfeldt, D. S. Kim, M. Grätzel, J. Y. Kim, *Nature*, **592** (2021) 381–385.

9. D. P. McMeekin, G. Sadoughi, W. Rehman, G. E. Eperon, M. Saliba, M. T. Hörantner, A. Haghighirad, N. Sakai, L. Korte, B. Rech, M. B. Johnston, L. M. Hrz, H. J. Snaith, *Science*, **351** (2016) 151–155.

10. Q. Ou, X. Bao, Y. Zhang, H. Shao, G. Xing, X. Li, L. Shao, Q. Bao, *Nano Mater Sci.*, **1** (2019) 268–287.

11. R. He, S. Ren, C. Chen, Z. Yi, Y. Luo, H. Lai, W. Wang, G. Zeng, X. Hao, Y. Wang, J. Zhang, C. Wang, L. Wu, F. Fu, D. Zhao, *Energy Environ. Sci.*, **14** (2021) 5723–5759.

12. Y. Tong, A. Najar, L. Wang, L. Liu, M. Du, J. Yang, J. Li, K. Wang, S. Liu, *Adv. Sci.*, **9** (2022) 2105085.

13. W. S. Yang, J. H. Noh, N. J. Jeon, Y. C. Kim, S. Ryu, J. Seo, S. I. Seok, *Science*, **348** (2015) 1234.

14. M. Saliba, T. Matsui, J.-Y. Seo, K. Domanski, J.-P. Correa-Baena, M. K. Nazeeruddin, S. M. Zakeeruddin, W. Tress, A. Abate, A. Hagfeldt, M. Grätzel, *Energy Environ. Sci.*, **9** (2016) 1989.

15. M. M. Byranvand, C. Otero-Martinez, J. Ye, W. Zuo, L. Manna, M. Saliba, R. L. Z. Hoye, L. Polavarapu, *Adv. Optical Mater.*, **10** (2022) 2200423.

16. E. H. Jung, N. J. Jeon, E. Y. Park, C. S. Moon, T. J. Shin, T.-Y. Yang, J. H. Noh, J. Seo, *Nature*, **567** (2019) 511.

17. H. Zhu, Y. Liu, F. T. Eickemeyer, L. Pan, D. Ren, M. A. Ruiz-Preciado, B. Carlsen, B. Yang, X. Dong, Z. Wang, H. Liu, S. Wang, S. M. Zakeeruddin, A. Hagfeldt, M. I. Dar, X. Li, M. Grätzel, *Adv. Mater.*, **32** (2020) 1907757.

18. Y. Niu, Y. Peng, X. hang, Y. Ren, R. Ghadari, J. Zhu, G. Tulloch, H. Zhang, P. Falaras, L. Hu, *ACS Energy Lett.*, **7** (2022) 3104−3111.

19. S. J. Sung, J. Im, G. kim, C. S. Moon, J. J. Yoo, S. S. Shin, N. J. Jeon, B. S. Ma, D. J. Kim, T.-S. Kim, J. Seo, *Adv. Energy Mater.*, **12** (2022) 2200758.

20. Q. Song, H. Gong, F. Sun, T. Zhu, C. Zhang, M. Li, F. You, Z. He, D. Li, C. Liang, *ACS Appl. Mater. Interfaces*, **15** (2023) 818−829.

21. R. D. J. Oliver, P. Caprioglio, F. Pena-Camargo, L. R. V. Buizza, F. Zu, A. J. Ramadan, S. G. Motti, S. Mahesh, M. M. McCarthy, J. H. Warby, Y.-H. Lin, N. Koch, S. Albrecht, L. M. Herz, M. B. Johnston, D. Neher, M. Stolterfoht, H. J. Snaith, *Energy Environ. Sci.*, **15** (2022) 714.

22. T. Duong, H. Pham, Y. Yin, J. Peng, M. A. Mahmud, Y. Wu, H. Shen, J. Zheng, T. Tran-Phu, T. Lu, L. Li, A. Kumar, G. G. Andersson, A. Ho-Baillie, Y. Liu, T. White, K. Weber, K. Catchpole, *J. Mater. Chem. A*, **9** (2021) 18454.

23. Y. Yu, R. Liu, C. Liu, X.-L. Shi, H. Yu, Z.-G. Chen, *Adv. Energy Mater.*, **12** (2022) 2201509.

24. D. Wang, H. Guo, X. Wu, X. Deng, F. Li, Z. Li, F. Lin, Z. Zhu, Y. Zhang, B. Xu. A. K.-Y. Jen, *Adv. Funct. Mater.*, **32** (2022) 2107359.

25. X. Huo, Y. Li, Y. Lu, J. Dong, Y. Zhang, S. Zhao, B. Qiao, D. Wei, D. Song, Z. Xu, *J. Phys. Chem. C*, **126** (2022) 1711−1720.

26. F. H. Isikgor, F. Furlan, J. Liu, E. Ugur, M. K. Eswarn, A. S. Subbiah, E. Yengel, M. D. Bastiani, G. T. Harrison, S. Zhumagali, C. T. Howells, E. Aydin, M. Wang, N. Gasparini, T. G. Allen, A. Rehman, E. V. Kerschaver, D. Baran, I. McCulloch, T. D. Anthopoulos, U. Schwingenschlögl, F. Laquai, S. D. Wolf, *Joule*, **5** (2021) 1566.

27. X. Zhuo, H. Lai, T. Huang, C. Chen, Z. Xu, Y. Yang, S. Wu, X. Xiao, L. Chen, C. J. Brabec, Y. Mai, F. Fuo, *ACS Energy Lett.*, **8** (2023) 502.

28. K. O. Brinkmann, T. Becker, F. Zimmermann, C. Kreusel, T. Gahlmann, M. Theisen, T. Haeger, S. Olthof, C. Tückmantel, M. Günster, T. Maschwitz, F. Göbelsmann, C. Koch, D. Hertel, P. Caprioglio, F. Peña-Camargo, L. Perdigón-Toro, A. Al-Ashouri, L. Merten, A. Hinderhofer, L. Gomell, S. Zhang, F. Schreiber, S. Albrecht, K. Meerholz, D. Neher, M. Stolterfoht, T. Riedl, *Nature*, **604** (2022) 280.

29. H. Lai, J. Luo, Y. Zwirner, S. Olthof, A. Wieczorek, F. Ye, Q. Jeangros, X. Yin, F. Akhundova, T. Ma,

R. He, R. K. Kothandaraman, X. Chin, E. Gilshtein, A. Müller, C. Wang, J. Thiesbrummel, S. Siol, J. M. Prieto, T. Unold, M. Stolterfoht, C. Chen, A. N. Tiwari, D. Zhao, F. Fu, *Adv. Energy Mater.*, **12** (2022) 2202438.

30. R. Murdey, Y. Ishikura, Y. Matsushige, S. Hu, J. Pascual, M. A. Truong, T. Nakamura, A. Wakamiya, *Sol. Energy Mater. Sol. Cells*, **245** (2022) 111885.

31. A. Saeki, S. Yoshikawa, M. Tsuji, Y. Koizumi, M. Ide, C. Vijayakumar, S. Seki, *J. Am. Chem. Soc.*, **134** (2012) 19035.

32. M. Tsuji, A. Saeki, Y. Koizumi, N. Matsuyama, C. Vijayakumar, S. Seki, *Adv. Funct. Mater.*, **24** (2014) 28.

33. H. Oga, A. Saeki, Y. Ogomi, S. Hayase, S. Seki, *J. Am. Chem. Soc.*, **136** (2014) 13818.

34. N. Ishida, A. Wakamiya, A. Saeki, *ACS Photonics*, **3** (2016) 1678.

35. N. Minoi, F. Ishiwari, K. Murotani, R. Nishikubo, T. Fukushima, A. Saeki, *ACS Appl. Mater. Interfaces*, **15** (2023) 6708.

36. A. Saeki, Y. Yasutani, H. Oga, S. Seki, *J. Phys. Chem. C*, **118** (2014) 22561.

37. R. Nishikubo, A. Saeki, *J. Phys. Chem. Lett.*, **9** (2018) 5392.

38. A. J. Knight, J. Borchert. R. D. J. Oliver, J. B. Patel, P. G. Radaelli, H. J. Snaith, M. B. Johnston, L. M. Herz, *ACS Energy Lett.*, **6** (2021) 799.

39. S. G. Motti, J. B. Patel, R. D. J. Oliver, H. J. Snaith, M. B. Johnston, L. M. Herz, *Nat. Commun.*, **12** (2021) 6955.

Communication

Insight into Charge Carrier Recombination Mechanisms in Lead Based Mixed Cation and Halide Perovskite

Keishiro Goshima[1,2], Wakana Matsuda,[3,4] Minh Anh Truong[5], Ryuji Kaneko[5], Ai Shimazaki[5], Tomoya Nakamura[5], Atsushi Wakamiya[5], and Yasuhiro Tachibana[1,3]*

[1] *School of Engineering, RMIT University, Bundoora, VIC 3083, Australia*
[2] *Aichi Institute of Technology, 1247, Yachigusa,Yakusa, Toyota, Aichi 470-0392, Japan*
[3] *Forefront Research Center, Faculty of Science, Osaka University, 1-1 Machikaneyama, Toyonaka, Osaka 560-0043, Japan*
[4] *Department of Molecular Engineering, Graduate School of Engineering, Kyoto University, Katsura, Kyoto 615-8510, Japan*
[5] *Institute for Chemical Research, Kyoto University, Gokasho, Uji, Kyoto 611-0011, Japan*
*yasuhiro.tachibana@rmit.edu.au; tachibana.yasuhiro.sci@osaka-u.ac.jp

Charge recombination dynamics inside a $Cs_{0.05}FA_{0.80}MA_{0.15}PbI_{2.75}Br_{0.25}$ perovskite film were studied by employing picosecond-microsecond transient absorption spectroscopy. A wide range of excitation intensity from 0.18 to 127 μJ cm^{-2} revealed two different charge recombination mechanisms. The charge recombination occurs in the 1st order with the excitation intensity of <2 μJ cm^{-2}, while with the higher excitation intensity of >2 μJ cm^{-2}, the recombination occurs in the addition of the 2nd order. The analysis of the 1st order reactions revealed that trap states with at least 3 different potential levels exist in the $Cs_{0.05}FA_{0.80}MA_{0.15}PbI_{2.75}Br_{0.25}$ perovskite film. From the transition of the reaction order from the 1st to the 2nd, the trap density inside the perovskite film is evaluated to be 1 x 10^{17} cm^{-3}.
Keywords: Lead halide perovskite, Transient absorption spectroscopy, Charge carrier recombination, Trap state

1. Introduction

Metal halide perovskite has emerged as one of the most promising materials, owing to the attractive opto-electronic properties, to be applied for solar cells [1-3], light emitting diodes [4, 5], optical detectors[6] and lasers[7]. Lead halide based perovskite has achieved solar energy conversion efficiency of 26% [2].

Perovskite solar cell functions by absorbing light by a solution processed lead halide perovskite film, followed by charge transfer, i.e. electron and hole transfer reactions. Photocurrent is detected by collection of separated electrons and holes at their respective electrode. Therefore, to detect photocurrent, these electron and hole transfer reactions must occur faster than the electron-hole recombination inside the perovskite film.

To improve perovskite solar cell performance, it is important to understand the mechanism of electron-hole recombination. Intensive studies have been conducted to understand hot charge carrier generation and relaxation, and their recombination dynamics [8-13]. Depending on the charge carrier density, the charge recombination process was analysed with the 1st , 2nd or 3rd order reaction rate laws [12-14]. Since the solar cell is operated under the low light intensity, it is important to understand the 1st order reaction process in detail. Although the 1st order reaction was interpreted as trap state mediated recombination [12, 14], the nature of the trap states, e.g. their potential levels and trap state density, have not been explicitly elucidated.

In this paper, we demonstrate new insights into charge carrier dynamics in lead halide perovskite by

employing picosecond-microsecond transient absorption spectroscopy (TAS). By altering excitation intensity from 0.18 to 127 μJ cm^{-2}, the transition of the 1st order reaction to the 2nd order is identified, and the charge trap density is evaluated. Based on the kinetic results, the implication to the perovskite solar cell performance is discussed.

2. Experimental

2.1. Preparation of perovskite films

A $Cs_{0.05}FA_{0.80}MA_{0.15}PbI_{2.75}Br_{0.25}$ perovskite film was prepared by spin coating drops of precursor solution [1, 15]. The precursor solution was prepared by dissolving CsI (69 mg, 0.27 mmol), MABr (85 mg, 0.76 mmol), $PbBr_2$ (96 mg, 0.26 mmol), PbI_2 (2235 mg, 4.85 mmol) and FAI (703 mg, 4.09 mmol) in a mixture of DMF (3 mL) and DMSO (0.9 mL). After stirring at 40 °C for 30 min, the solution was filtered with a 0.45 μm PTFE filter. 190 μL of the precursor solution was placed on a glass slide and spread by spin-coating (slope 1 s, at 1000 rpm for 10 s, slope 5 s, at 6000 rpm for 20 s, slope 1 s) 300 μL of chlorobenzene was dropped over the rotating substrate at 3 s before the end of the spin at 6000 rpm. The film was subsequently annealed on a hot plate at 150 °C for 10 min. The perovskite film thickness is ~600 nm [1]. The film was sealed by placing a UV curable resin film between the perovskite film substrate and a glass slide, and by irradiating it with UV light in Ar gas.

2.2 Characterisation

Absorption spectra were measured using a UV-Vis absorption spectrometer (Shimadzu, UV-2450).

Picosecond to microsecond TAS studies were conducted by a picosecond transient absorption spectrometer (UNISOKU Co., Ltd., RIPT Pico-TAS, time-resolution: 70 ps). The details of the spectrometer will be published elsewhere. Briefly, the sample was excited by a diode pumped picosecond Nd:YAG laser (EKSPLA, PL2210A-1K-TH) and an optical parametric generator (OPG, EKSPLA, PG403, ~25 ps pulse duration). Transient absorption signal was probed by a mode locked white light supercontinuum pulse laser (YSL Photonics Co., Ltd., SC-Pro-M-20, ~100 ps pulse duration). Transient data were collected with 570 nm excitation with a wide variety of excitation intensity from 0.18 to 127 μJ cm^{-2} with a repetition rate of 1 kHz at 22 °C. No change in steady state absorption spectra prior to and after the transient measurements was observed, indicating that the samples were stable during the experiments.

3. Results and discussion

$Cs_{0.05}FA_{0.80}MA_{0.15}PbI_{2.75}Br_{0.25}$ perovskite films used in this study have been employed for solar cells that show solar energy conversion efficiency of ~23%, and incident photon to current conversion efficiency of 85% at 570 nm [1]. Therefore any optical results from this study can be used as the benchmark data to develop perovskite materials/films in the future.

3.1. Steady state absorption spectrum

We first measured steady state absorption spectrum of this film. The resultant spectrum is shown in Fig. 1, and the spectral shape agrees with our previous study for MAPbI$_3$ films [16]. A clear exciton peak, i.e. a sharp rise near the bandgap, was observed around 760 nm, in agreement with those observed by other lead iodide based perovskite films, e.g. MAPbI$_3$ [12, 16, 17]. Following the model for the perovskite film absorption spectra, reported by Beard et al. [12, 17] and Herz et al. [11], the pump pulses at 570 nm for our TAS study most likely excite the continuum band, thereby generating charge carriers, i.e. free electrons and holes in the conduction band and the valence band, respectively. The absorbance at 570 nm is greater than 2, indicating that almost all excitation pulses are absorbed by the perovskite layer.
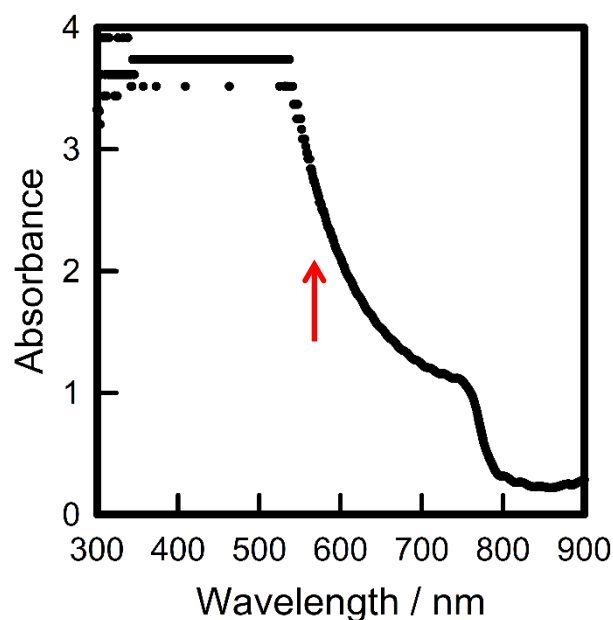

Fig. 1. Absorption spectrum of a $Cs_{0.05}FA_{0.80}MA_{0.15}PbI_{2.75}Br_{0.25}$ perovskite film. The red arrow indicates the excitation wavelength for the TAS studies.

3.2. Charge carrier dynamics

Picosecond-nanosecond transient absorption measurements were conducted for the prepared $Cs_{0.05}FA_{0.80}MA_{0.15}PbI_{2.75}Br_{0.25}$ perovskite films. Transient absorption spectra for the films excited at 570 nm with 0.9 µJ cm^{-2} are shown in Fig. 2. All spectra show a sharp negative bleach with a peak at 770 nm near the bandgap and a broad transient absorption above the bandgap (~730 nm). The bleach was interpreted as the bleach of exciton transition [12, 17, 18]. However, as discussed later, we assign it to the bleach of transition to the charge carrier trap states. The band width of the spectrum at 1 ns became narrower compared to that of the spectrum at 200 ps. Since we expect hot carriers cool by early picosecond time scale [12], we presume that the charge carrier trapping occurs from 200 ps to 1 ns.
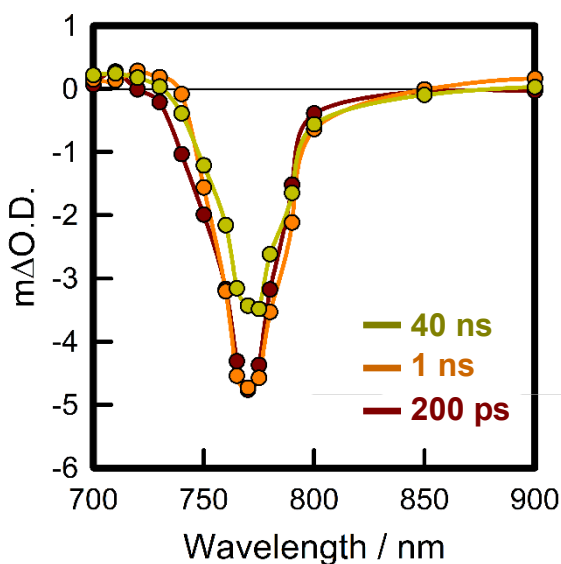

Fig. 2. Transient absorption spectra at 200 ps, 1 and 40 ns after 570 nm excitation with 0.9 µJ cm^{-2}.

Charge recombination dynamics were monitored by the decays of the bleach signals at 770 nm. The transient absorption decays obtained with different excitation intensities are shown in Fig. 3a. These decay dynamics with the different excitation intensity directly relate to the charge carrier recombination dynamics, i.e. electron-hole recombination dynamics, with the different initial carrier density. Therefore, these dynamics can be quantitatively described by the following rate equation [14, 16].

$$-\frac{dn}{dt} = k_1 n + k_2 n^2 \qquad (1)$$

where n is the photo-excited charge carrier density,

k_1 is the rate constant of trap state mediated recombination, k_2 is the rate constant of electron-hole recombination, and t is the time. The transient absorption decays obtained with the higher excitation intensities (>5 µJ cm^{-2}) were comfortably fitted with Equation 1. In fact, we find that the 2nd order recombination is dominant for the decays obtained with the high excitation intensity (>20 µJ cm^{-2}), while the first order recombination is dominant for the decays obtained with the low excitation intensity (<2 µJ cm^{-2}).
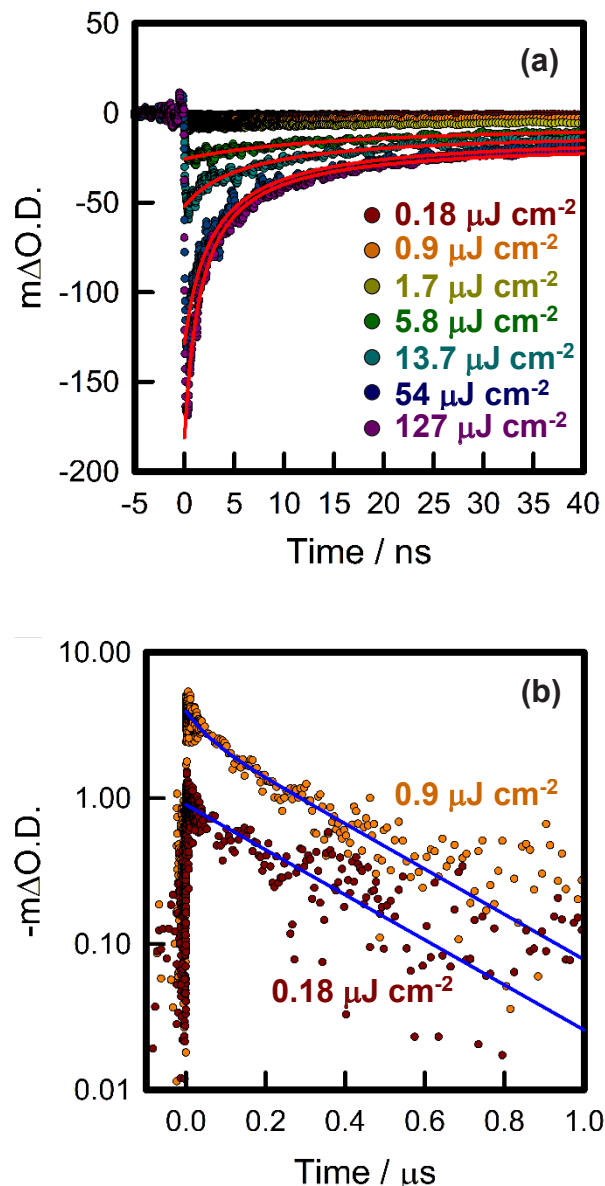

Fig. 3. (a) Transient absorption decays at 770 nm, obtained with a range of excitation intensity from 0.18 to 127 µJ cm^{-2}. The red solid lines indicate results of fitting with Equation 1. (b) Transient absorption decays at 770 nm, obtained with the excitation intensity of 0.18 or 0.9 µJ cm^{-2}. The blue solid lines indicate results of fitting with Equation 2.

Transient absorption decays obtained with the lower excitation intensity (0.9 or 0.18 μJ cm^{-2}) are shown in Fig. 3b. The decays can be quantitatively fitted with the single exponential dynamics, Equation 2.

$$n(t) = n_1 e^{(-t/\tau_1)} + n_2 e^{(-t/\tau_2)} \qquad (2)$$

where n is the photo-excited charge carrier density, n_1 and n_2 is the charge carrier density for the recombination via trap state 1 and 2, respectively, τ_1 and τ_2 is the lifetime of trap state mediated recombination, and t is the time. The transient absorption decay obtained with the excitation intensity of 0.18 μJ cm^{-2} was comfortably fitted with Equation 2, but with only a single component, while fitting the decay obtained with the excitation intensity of 0.9 μJ cm^{-2} requires at least two components, indicating that at least two different types of trap states are involved in the electron-hole recombination reactions.
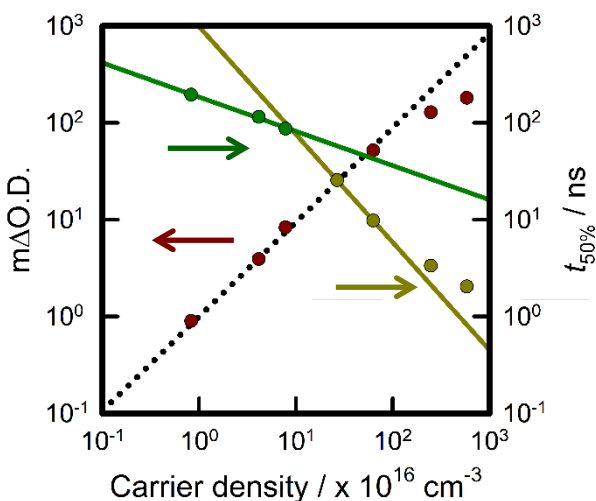

Fig. 4. Initial transient absorption amplitudes obtained from the kinetic fitting (see the text for the detail) and half lifetime ($t_{50\%}$) of the decay as a function of charge carrier densities generated by the pump pulse absorption. The black dotted line shows a slope of the linear fit. The green solid line indicates the linear fit to the half lifetimes obtained for the decays with the first order kinetics, i.e. charge recombination via the trap states, while the gold solid line shows the linear fit to the half lifetimes obtained or the decays with the second order kinetics, i.e. non-geminate electron-hole recombination.

To compare charge recombination dynamics over a wide range of excitation intensities, we first evaluated charge carrier density with the film absorbance and reflectance at 570 nm, and with the excitation intensities. Fig. 4 shows correlation of the resultant values with the initial bleach amplitude determined from fitting each decay with Equation 1

or 2. The linear relationship can be seen with the charge carrier density up to 1 x 10^{18} cm^{-3}. However with the charge carrier density greater than 1 x 10^{18} cm^{-3}, the bleach amplitude no longer increases linearly with increase of the charge carrier density probably owing to the bleach of the continuum band as a result of bandfilling of free charge carriers.

Since the charge recombination occurs with the 1st and/or 2nd order reaction rates, depending on the excitation intensity, it is not simple to compare reaction dynamics over a wide range of excitation intensity. Here we employ decay half lifetime, $t_{50\%}$, as it has been established in the theory of reaction kinetics, particularly for the 1st and 2nd order reactions. According to the rate law, the half lifetime of the 1st and 2nd order reactions are expressed below.

$$1^{st} \text{ order: } t_{50\%} = \frac{ln2}{k_1} \qquad (3)$$

$$2^{nd} \text{ order: } t_{50\%} = \frac{1}{k_2 n_0} \qquad (4)$$

where n_0 is the initial charge carrier density, k_1 is the rate constant of trap state mediated recombination, k_2 is the rate constant of electron-hole recombination. The half lifetime of each transient absorption decay is plotted as a function of the evaluated charge carrier density, shown in Fig. 4. With the low excitation intensity (<2 μJ cm^{-2}), where the decays are comfortably fitted with the 1st order rate equation, i.e. Equation 2, the lifetimes are not constant, unlike that expected from Equation 3, but rather linearly shorter with the increase of excitation intensity (The linear fit is shown in Fig. 4). These results indicate that trap states with at least 3 different potential levels are involved for charge carrier recombination reactions. With the higher excitation intensity (>2 μJ cm^{-2}), where the decays are comfortably fitted with the 2nd order rate equation or Equation 1, the half lifetime is inversely proportional with the initially generated charge carrier density, i.e. following Equation 4. The linear fit is shown in Fig. 4. Note that the data obtained with the excitation intensity of 54 and 127 μJ cm^{-2} were not included for the fit, since their initial charge carrier intensity does not linearly increase with the excitation intensity. Following Equation 4, the 2nd order rate constant is calculated from its slope, resulting in 1.4 ± 0.1 x 10^{-10} cm^3 s^{-1}. The similar value was reported for MAPbI$_3$ perovskite films by Beard et al [17].

From the linear fits for the half lifetimes of the transient absorption decays in which the 1st order reaction rate or the 2nd order reaction rate dominates,

shown in Fig. 4, it is clear that the reaction rate switches from the 1st to the 2nd order with the excitation intensity of >2 μJ cm^{-2} or the charge carrier density of 1 x 10^{17} cm^{-3}. If we assume that the 2nd order rate appears once all the trap states are filled with the generated charge carriers, then the trap state density of this perovskite film can be estimated to be 1 x 10^{17} cm^{-3}.

3.3. Implication to solar cell performance

A solar cell is usually assessed and/or operated under AM1.5 solar spectrum with 1 sun condition (100 mW cm^{-2}). Assuming that all the light at <800 nm is absorbed by the perovskite film, the charge carriers of 2.8 x 10^{15} cm^{-3} are generated every 1 μs [19]. According to the analysis of the data shown in Fig. 4, these generated carriers decay with the 1st order reaction rate with the half lifetime of 195 ns, and completed by 1 μs. To obtain the incident photon-to-current conversion efficiency (IPCE) of >90 %, either electron or hole transfer must occur at least one order of magnitude faster than the charge recombination lifetime (195 ns) [14, 16, 20, 21].

According to the analysis of the data shown in Fig. 4, if the trap density is minimized to 1 x 10^{16} cm^{-3}, then the charge recombination lifetimes would be around 1 μs, increasing both electron and hole transfer yield. Therefore, passivating the trap state is extremely important to improve solar cell efficiency.

Following the data shown in Fig. 2, the charge carrier trapping occur from 200 ps to 1 ns after the excitation. If the trapped carrier does not transfer to the electron or hole transporting material, the charge transfer reaction must occur faster than 200 ps. Unfortunately, we cannot distinguish the carrier trapping from electron or hole trapping, and therefore the kinetic requirement for electron or hole transfer reaction is unclear. We currently conduct TAS measurements to identify the trap states and distinguish charge transfer dynamics from charge carrier trapping dynamics. The results will be published shortly.

4. Conclusion

We conducted TAS measurements for a Cs$_{0.05}$FA$_{0.80}$MA$_{0.15}$PbI$_{2.75}$Br$_{0.25}$ perovskite film. With low excitation intensity (<2 μJ cm^{-2}), the charge recombination decay is comfortably fitted with the 1st order reaction rate equation, while with the higher excitation intensity (>2 μJ cm^{-2}), the fit requires addition of the 2nd order rate law. By comparing the half lifetimes of the 1st order reactions, trap states with at least 3 different

potential levels are identified. By comparing the 1st order reactions and the 2nd order reactions, the charge trap state density was estimated to be 1 x 10^{17} cm^{-3} in this Cs$_{0.05}$FA$_{0.80}$MA$_{0.15}$PbI$_{2.75}$Br$_{0.25}$ perovskite film.

Since a solar cell is generally assessed and/or operated under the low light intensity, i.e. 1 sun condition (100 mW cm^{-2}), equivalent to the charge carriers of 2.8 x 10^{15} cm^{-3} generated every 1 μs, the charge recombination reaction inside the Cs$_{0.05}$FA$_{0.80}$MA$_{0.15}$PbI$_{2.75}$Br$_{0.25}$ perovskite film occurs with the half lifetime of 195 ns. To optimize the solar cell performance, the electron or hole transfer must occur at least one order of magnitude faster than the charge recombination reaction.

References

1. M. A. Truong, T. Funasaki, L. Ueberricke, W. Nojo, R. Murdey, T. Yamada, S. Hu, A. Akatsuka, N. Sekiguchi, S. Hira, L. Xie, T. Nakamura, N. Shioya, D. Kan, Y. Tsuji, S. Iikubo, H. Yoshida, Y. Shimakawa, T. Hasegawa, Y. Kanemitsu, T. Suzuki, and A. Wakamiya, *J. Am. Chem. Soc.,* **145** (2023) 7528.
2. J. Park, J. Kim, H.-S. Yun, M. J. Paik, E. Noh, H. J. Mun, M. G. Kim, T. J. Shin, and S. I. Seok, *Nature,* **616** (2023) 724.
3. G. Li, Z. Su, L. Canil, D. Hughes, M. H. Aldamasy, J. Dagar, S. Trofimov, L. Wang, W. Zuo, J. J. Jeronimo-Rendon, M. M. Byranvand, C. Wang, R. Zhu, Z. Zhang, F. Yang, G. Nasti, B. Naydenov, W. C. Tsoi, Z. Li, X. Gao, Z. Wang, Y. Jia, E. Unger, M. Saliba, M. Li, and A. Abate, *Science,* **379** (2023) 399.
4. Y. Sun, L. Ge, L. Dai, C. Cho, J. Ferrer Orri, K.

Ji, S. J. Zelewski, Y. Liu, A. J. Mirabelli, Y. Zhang, J.-Y. Huang, Y. Wang, K. Gong, M. C. Lai, L. Zhang, D. Yang, J. Lin, E. M. Tennyson, C. Ducati, S. D. Stranks, L.-S. Cui, and N. C. Greenham, *Nature,* **615** (2023) 830.

5. D. Zhang, Q. Zhang, B. Ren, Y. Zhu, M. Abdellah, Y. Fu, B. Cao, C. Wang, L. Gu, Y. Ding, K.-H. Tsui, S. Fan, S. Poddar, L. Shu, Y. Zhang, D.-B. Kuang, J.-F. Liao, Y. Lu, K. Zheng, Z. He, and Z. Fan, *Nat. Photonics,* **16** (2022) 284.

6. Y. Zhou, C. Fei, A. M. Uddin, L. Zhao, Z. Ni, and J. Huang, *Nature,* **616** (2023) 712.

7. Y. Shi, R. Li, G. Yin, X. Zhang, X. Yu, B. Meng, Z. Wei, and R. Chen, *Adv. Funct. Mater.,* **32** (2022) 2207206.

8. X. Wang, D. Huo, X. Wang, M. Li, Y. Wang, and Y. Wan, *J. Phys. Chem. Lett.,* **12** (2021) 6907.

9. S. Sourabh, V. R. Whiteside, I. R. Sellers, Y. Zhai, K. Wang, M. C. Beard, V. Yeddu, M. T. Bamidele, and D. Y. Kim, *Phys. Rev. Mater.,* **5** (2021) 095402.

10. S. Feldmann, M. K. Gangishetty, I. Bravic, T. Neumann, B. Peng, T. Winkler, R. H. Friend, B. Monserrat, D. N. Congreve, and F. Deschler, *J. Am. Chem. Soc.,* **143** (2021) 8647.

11. C. L. Davies, M. R. Filip, J. B. Patel, T. W. Crothers, C. Verdi, A. D. Wright, R. L. Milot, F. Giustino, M. B. Johnston, and L. M. Herz, *Nat. Commun.,* **9** (2018) 1.

12. Y. Yang, D. P. Ostrowski, R. M. France, K. Zhu, J. van de Lagemaat, J. M. Luther, and M. C. Beard, *Nat. Photonics,* **10** (2016) 53.

13. J. S. Manser and P. V. Kamat, *Nat. Photonics,* **8** (2014) 737.

14. S. Makuta, M. Liu, M. Endo, H. Nishimura, A. Wakamiya, and Y. Tachibana, *Chem. Commun.,* **52** (2016) 673.

15. A. Jegorove, M. A. Truong, R. Murdey, M. Daskeviciene, T. Malinauskas, K. Kantminiene, V. Jankauskas, V. Getautis, and A. Wakamiya, *Sol. RRL,* **6** (2022) 2100877.

16. M. Liu, M. Endo, A. Shimazaki, A. Wakamiya, and Y. Tachibana, *ACS Appl. Energy Mater.,* **1** (2018) 3722.

17. Y. Yang, M. Yang, Z. Li, R. Crisp, K. Zhu, and M. C. Beard, *J. Phys. Chem. Lett.,* **6** (2015) 4688.

18. X. Chen, H. Lu, Y. Yang, and M. C. Beard, *J. Phys. Chem. Lett.,* **9** (2018) 2595.

19. L. D. Partain, *Solar Cells and Their Applications*. John Wiley & Sons, Inc.: **1995**.

20. M. Liu, M. Endo, A. Shimazaki, A. Wakamiya, and Y. Tachibana, *J. Photopolym. Sci. Technol.,* **31** (2018) 633.

21. M. Liu, H. Liu, S. R. Padmaperuma, M. Endo, A. Shimazaki, A. Wakamiya, and Y. Tachibana, *J. Photopolym. Sci. Technol.,* **32** (2019) 727.

Communication

Electron Generation in Tin-oxo Cage Extreme Ultraviolet Photoresists

Najmeh Sadegh[1], Quentin Evrard[1,2], Nicola Mahne[3], Angelo Giglia[3], Stefano Nannarone[3] and Albert M. Brouwer[1,2*]

[1] *Advanced Research Center for Nanolithography, Science Park 106, 1098 XG, Amsterdam, The Netherlands*
[2] *van 't Hoff Institute for Molecular Sciences, University of Amsterdam, Science Park 904, 1098 XH Amsterdam, The Netherlands*
[3] *IOM-CNR, 34149 Basovizza, Trieste, Italy*
*a.m.brouwer@uva.nl

Extreme Ultraviolet Lithography photoresists undergo chemical reactions initiated by ionizing radiation. Understanding the decay pathways in the photoresist following photoionization requires knowledge about the states and species that are generated during the ultrafast primary and secondary ionization processes while the energy of the photons (92 eV) is ultimately converted to heat and chemical reaction products. Here we use Total Electron Yield spectroscopy to investigate the electron generation following excitation of the resist with photons in the energy range from 5 to 150 eV. We estimate that each EUV photon gives rise to 3 – 4 electrons. Changes in the material during irradiation lead to changes in the yield of electrons, which is qualitatively explained by considering changes in the absorption spectrum and density that are due to chemical change.
Keywords: Extreme ultraviolet, Photoresist, Total Electron Yield, Organotin compound

1. Introduction

In the past few years, Extreme Ultraviolet Lithography has made the transition from the development stage to increasingly large-scale production [1]. Further development of the hardware follows a programmed route towards higher numerical apertures [2], but for the chemical software of photolithography, the photoresist, the pathway for improvement is less obvious. The chemically amplified resist (CAR) materials originally developed for 193 nm photolithography have been adapted for use with the 13.5 nm photon source, but the limitations of this approach have been pointed out: being organic polymer based, CARs have low absorption cross sections at 13.5 nm and their etch resistance may be insufficient when used in the thin layers that are required in small-sized patterns with a reasonably small aspect ratio [3]. As an alternative, metal-containing materials have been proposed, and they have been under investigation for more than a decade now [4,5].

From a more fundamental perspective, the development of EUV photoresists is hampered by a lack of knowledge and understanding of the chemistry induced by the ionizing radiation used. Photons with an energy of 92 eV cause the emission of photoelectrons from valence and shallow-core orbitals. These electrons, which may have kinetic energies up to ~85 eV, can cause further ionizations, generating a number of secondary electrons. It is often stated that the electrons are responsible for radiation induced chemistry, but a clear mechanistic picture is available only in few cases [6–8]. From the perspective of pattern fidelity, the secondary electrons raise the same questions as acids in CAR: to what extent do they blur the pattern projected in the areal image?

In our research we have investigated tin-oxo cages as a prototype material for EUV resist application. These have been introduced in the field by the Brainard group [9], and it has been suggested that they form the basis of the photoresists commercially developed by Inpria [10–12].

One aspect of the chemistry of these compounds

(and related organotin compounds) is clear: any form of activation, be it UV, XUV or EUV photons, or electrons (even of low energy), leads to the cleavage of tin-carbon bonds [13–20]. Unfortunately, direct experimental evidence for the molecular structure of the subsequent reaction products is lacking. We have detected photofragmentation products, which lost multiple butyl groups from the original *n*-butyltin-oxo cages, and proposed structures based on quantum-chemical calculations [21]. It is likely that the cages after loss of the alkyl groups cross-link to form higher molecular weight chains or cross-linked networks that are insoluble, but there is no experimental evidence for the chemical nature of the bonds between cages [11]. The main reason for this is that available spectroscopic methods lack the specificity and sensitivity to give the required quantitative insight. The problem is aggravated by the fact that only a relatively small conversion is needed to achieve the solubility switching, and that the spectroscopic signatures of the different bond types do not change much when few of the carbon-tin bonds are broken while most remain intact.

In previous work, we studied the photoelectron spectrum of different tin-oxo cages with photon energies in the range 60 – 150 eV, which showed that the ratio of $Sn(4d)$ electrons to valence electrons has a maximum near a photon energy of 92 eV [22].
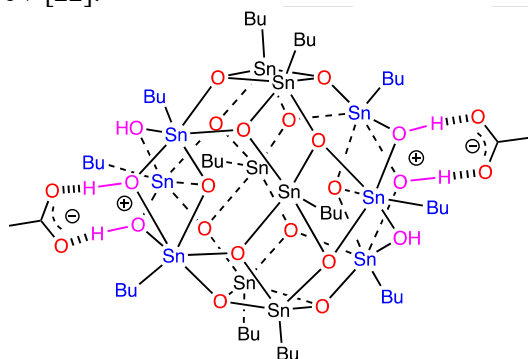
Scheme 1. Molecular structure of the TinOAc photoresist material investigated.

In the present work we describe Total Electron Yield (TEY) measurements in which we scan the photon energy over the much wider range from 5 to 150 eV and detect the total electron emission rate (drain current) from the sample, which results from the photoemission at the surface of the thin resist film.[23]

By comparing the shape of this TEY spectrum to the absorption spectrum, we obtain information on the electron yield as a function of the photon energy.

Because the irradiation leads to chemical change, the TEY changes during the measurement. Time traces of the electron yield vs. exposure dose reveal different responses in the low and high energy ranges.

2. Experimental

The TinOAc photoresist was prepared as described before [16]. Films with a thickness of ~20 nm were spin-coated on silicon substrates (2×2 cm^2) from toluene solutions (10 mg/mL).

Total Electron Yield measurements (TEY) were performed at the BEAR beamline of Synchrotron Elettra, Trieste, Italy [24]. The polarization of the synchrotron beam can be set, the wavelength monochromatized and filtered to remove higher orders contributions before being focused on the sample. The drain current generated in the refocusing mirror acts as continuous intensity monitor. It is used to normalize the incoming intensities and related signals among runs taken at different times.

To cover the whole photon energy range of interest (5 – 150 eV), two 1200 lines/mm gratings were used differing in monochromator inclusion angle. The photon beam was linearly polarized in the horizontal synchrotron orbit plane impinging at $45°$ in *s* (*TE*) incidence. The vertical slit of the monochromator in the dispersive plane was set to 50 μm, to ensure a band pass <0.1 eV. The horizontal slit width was 890 μm. The spot size on the sample was $\sim 70 \times 320$ μm^2 (vertical $\times$ horizontal). A -5 V bias was applied to the sample to maximize emission current signal.

To determine the electron yield, the current from the sample was measured. The TEY is obtained in electrons per photons as the ratio of rate of emitted electrons (derived from the drain current signal) to the rate of impinging photons obtained from the current signal of a calibrated photodiode inserted into the photon beam at different instant of time, then renormalizing the signals through the corresponding monitor signals from the mirror.

Because the photoresist sample is inherently radiation sensitive, for each photon energy a fresh unexposed spot on the sample was selected. Multiple acquisition is performed at each point to follow the time evolution of the TEY. The TEY spectrum presented in Fig.1 is composed of the data in the first time interval. By monitoring the signal over time, the effect of the radiation induced chemical change was detected.

3. Results and discussion

3.1. TEY spectrum

A representative Total Electron Yield spectrum of TinOAc on silicon is shown in Figure 1.
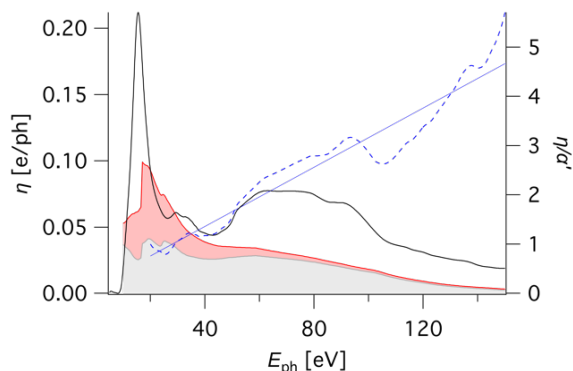

Fig. 1. TEY spectrum $\eta(E_{ph})$ of TinOAc (black) plotted together with the absorption spectrum (red), scaled to the same value at 20 eV, their ratio η/α' (blue dashed line) and a linear fit of the ratio vs. photon energy. The grey area is the unbleachable part of the absorption, the red area the bleachable part (see ref. [25]).

3.2. Time traces of the TEY

The TEY values shown in Fig. 1 were obtained for each energy from 0.5 s of data acquisition and ~2 s of exposure at a fresh point on the sample. The same spots were irradiated for 120 time intervals of ~2 s, which reveals the effect of the chemical change of the resist film under the influence of the radiation on the detected electron yield. As shown in Fig. 2, in the low photon energy regime, an initial decrease of the signal is observed, followed by a recovery. At energies near 100 eV the signal increases from the beginning of the irradiation.

3.3. Discussion

Spectral features. In fig. 1 the TEY spectrum of TinOAc is shown together with the absorption spectrum derived from the cross sections in the CXRO database [26]. As we have recently shown, this predicted spectrum is in very good agreement with the experimental data obtained by absorption and photobleaching experiments in the XUV range [25,27].

The onset of the TEY spectrum occurs near 8 eV constituting an indication of the value of the ionization energy. At this energy electrons originating from the highest occupied molecular orbitals (HOMO) can reach the vacuum level and be emitted into vacuum.
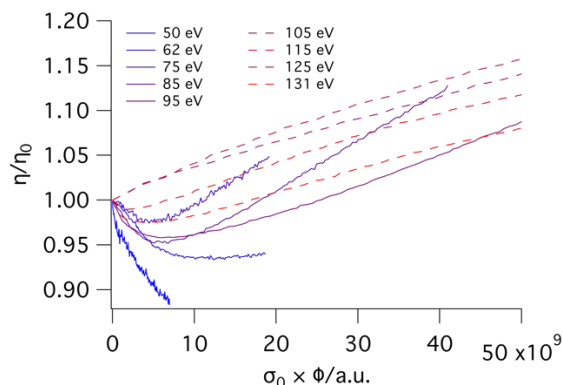

Fig. 2. Representative time traces of the TEY signal for selected photon energies. The horizontal axis displays the cumulative number of photons on the sample at the given photon energy multiplied by the absorption cross section at t = 0. The length of the traces is limited by the photon flux, which is low in the range <80 eV and peaks near 120 eV.

Since the HOMO-LUMO gap is ~5 eV, the electron affinity must be ~3 eV. In gas phase photofragmentation experiments we found the onset of ionization at 12 eV for the bare tin-oxo cage dication, and at 10 eV for a tin-oxo dication complexed with one monovalent counter-anion [21]. The electrostatic effect of adding the second counterion together with the dielectric effect of the matrix is responsible for another 2 eV shift.

The strongest peak in the spectrum is found at ~15.5 eV. In this energy range, a high density of electronically excited valence (σ*) and Rydberg states co-exists with ionized states. We tentatively attribute the strong TEY signal to efficient autoionization. Note that at hν <20 eV the CXRO predictions are not reliable because the high-energy valence transitions cannot be considered as purely atomic transitions. Thus, the low-energy peak in the TEY spectrum with its maximum at 15.5 eV should not be compared with the CXRO spectrum.

Strong absorption giving rise to ionization from the Sn(4d) level (binding energy ~29 eV) kicks in around 50 eV and is responsible for the broad band that extends up to ~100 eV.

Changes of TEY during exposure. As mentioned in the introduction, the characteristic radiation-induced chemical process in organotin-oxo cages is the loss of the hydrocarbon substituents due to breaking of the tin-carbon bonds. In a recent study we found that broadband XUV irradiation leads to a loss of 60-70% of the cleavable organic groups (including acetate and water) [25,27]. This leads to a decrease of the absorption, especially in the low energy region. The bleachable and non-

bleachable parts of the absorption are shown in Fig. 1. Without attempting a quantitative analysis, we can use these spectral changes to tentatively account for the evolution of the TEY $\eta(E_{ph})$ with exposure. At lower energies, η initially decreases due to the chemical conversion. The decrease of the absorption cross section is responsible for this, as a smaller cross section means that photons penetrate more deeply into the material, to depths where photoelectrons cannot escape because of their limited mean free path. Moving to higher energies the photobleaching becomes less important because of the smaller contribution of carbon to the absorption (Fig. 1), and the effect of increased density due to the loss of the butyl groups becomes dominant. Around 105 eV the TEY signal increases from the beginning of the exposure. When the hydrocarbon fraction is reduced due to outgassing, the photon absorption occurs on average more closely to the surface, allowing more efficient escape of the photoelectrons.

A more detailed quantitative analysis will be presented in a future paper.

TEY spectrum and electron yield. Primary photoelectrons with higher kinetic energies can induce more secondary ionizations via inelastic scattering. For example, Arumainayagam et al. state that typically 40,000 electrons are produced per MeV of radiation deposited [28]. In other words, the average energy consumed per electron generated amounts to ~25 eV. TEY measurements are frequently used as an indirect semi-quantitative way of measuring X-ray absorption spectra [23]. In that case the total electron yield η is treated as proportional to the absorption factor $\alpha(E_{ph})$ and the photon energy E_{ph}:

$$\eta(E_{ph}) \propto \alpha(E_{ph}) \times E_{ph} \quad (1)$$

The absorption coefficient α is related to the cross section σ by the Lambert-Beer law $\alpha = \sigma z \rho / M$, in which z is the film thickness, ρ the density and M the molecular weight. For our analysis we use the cross sections from the CXRO database [26] which were recently shown to match very well with experimental data in the XUV range 22 – 92 eV.[25]

The process of secondary electron generation has been depicted as a cascade, in which a photoelectron generates secondary electrons, which in turn generate more electrons [29]. Based on our results and discussions in the literature, however, it appears more likely that the primary photoelectrons lose energy by inelastic scattering in preferred quantities

that correspond to the plasmon energy [30], as illustrated in Scheme 2.
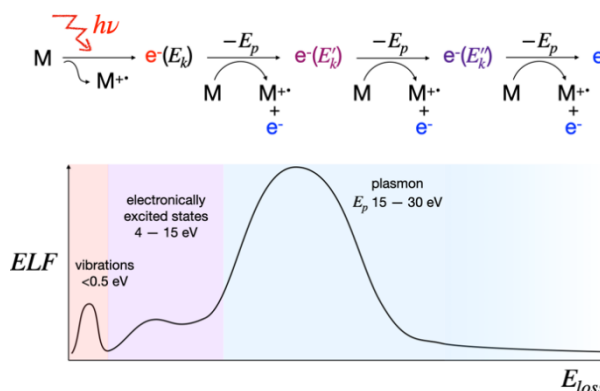
Scheme 2. Schematic representation of electron energy loss following valence excitation in the EUV range. Sketch of a typical Electron energy Loss Function (ELF), qualitatively indicating the energies and relative cross sections for the typical loss processes in molecular materials.

Among chemists, plasmons are well known as properties of metallic nanostructures, which give rise to visible absorption and light scattering [31]. More generally, plasmons occur in all materials as collective excitations of electrons. They are the most effective sink for the kinetic energy of electrons, that is, the plasmon dominates the electron energy loss function (ELF). Scheme 2 sketches the shape of a typical ELF for an organic material [32–34]. At the lowest loss energies, electrons can excite materials to higher vibrational energy levels. Next, electronic excitations are possible, and then in the range of 15 – 30 eV the plasmon loss can occur. Because this has a high cross section, electrons prefer to lose energy in amounts corresponding to the plasmon energy. In the low energy region additional loss mechanisms may play a role which lead to electron-induced reactions for example via dissociative electron attachment [35,36]. The excited plasmon dissociates to an electron hole pair, thus generating a low energy secondary electron [37].

When the ELF of a material is known, it is possible to simulate the decay of photoelectrons based on first principles, without any other experimental input.[30] Unfortunately, the electron energy loss function of the tin-oxo cage materials is unknown. An estimation of the plasmon energy, however, is provided by equation (2) [31].

$$E_p = \hbar \sqrt{\frac{ne^2}{\epsilon_0 m_e}} \quad (2)$$

In equation 2, n is the density of valence electrons,

e the electron charge, ε_0 the dielectric permittivity constant and m_e the electron mass. For poly(methylmethacrylate), equation 2 predicts $E_p = 22$ eV, in good agreement with experiment ($E_p = 21$ eV) [33]. For TinOAc, we find $E_p = 27$ eV, due to the higher valence electron density.

Although the proportionality in equation (1) is likely to break down at low energies, it is still interesting to consider its implications by comparing the measured TEY spectrum with the absorption spectrum. Considering that it takes $E_{ph} > 8$ eV to liberate an electron from TinOAc, we assume that $E_{ph} > 20$ eV is required to generate an electron that has enough energy to give rise to a secondary ionization with an appreciable probability. In Fig. 1 we plot the ratio η/α, scaled to $\eta/\alpha = 1$ at 20 eV, vs. E_{ph} and fit a straight line according to eq. 1. The slope is 0.03 e/eV, and the value of η/α at 92 eV is ~3. This corresponds to an average energy loss of ~27 eV per electron generated. This result depends on the details of the assumption made. For example, setting the onset of secondary electron generation at 25 eV gives a slope of 0.038 and a yield of 3.7 electrons at 92 eV. As can be seen in Fig. 1, the ratio η/α vs. E_{ph} deviates substantially from a straight line. We plan to analyze these data in more detail in future work.

The above analysis applies to the valence electrons, which are emitted with a kinetic energy mostly in the range 75 – 85 eV [22]. Electrons originating from Sn(4d) orbitals will have a lower kinetic energy, and thus generate fewer secondary electrons. In this case, however, the hole created in the Sn(4d) level is likely filled via an Auger process that releases another low energy electron [38].

The TEY spectrum reveals the yields of electrons that escape from the material. This would be proportional to electrons generated inside the material if the mean free path (MFP) of all electrons is the same. Examples in the literature suggest that the MFP is only a few nm but increasing with decreasing kinetic energy in the range <100 eV. Especially below the plasmon energy, the scattering cross sections are smaller.

Finally, another challenge not yet met is to relate the electron yield to the chemical reaction efficiency. In principle a thermalized electron hole pair could give rise to more than one Sn-C bond splitting. Moreover, the inelastic scattering of the electrons can lead to the formation of chemically reactive electronically excited states [15,21], in addition to low energy electrons. On the other hand, several electron-hole pairs created in a small volume in the material can readily undergo recombination, and even after Sn-C bond cleavage, bond recombination

is not unlikely, because the butyl radical cannot easily diffuse through the matrix. To investigate these ultrafast processes, time-resolved experiments are required.

4. Conclusion

Total Electron Yield spectra of thin films of an *n*-butyltin-oxo cage compound were studied in the photon energy range of 5 – 150 eV. The results suggest that at the EUV energy of 92 eV, 3 to 4 electrons could be generated. During exposure, hydrocarbon material is outgassed, which leads to opposing effects on the TEY: a decrease due to a decreasing absorption coefficient, an increase due to an increase of the density. In photon energy ranges where the contribution of the hydrocarbon fraction to the absorption is high, the decrease dominates; when the absorption by the tin-oxo core is relatively stronger, the TEY increases with conversion.

Our results are consistent with electron mean free paths of a few nm, but more work is needed to quantify the distances travelled by the primary and secondary photoelectrons.

References

1. H. J. Levinson, *Jpn. J. Appl. Phys.* **61** (2022) SD0803.
2. C. Zahlten, P. Gräupner, J. van Schoot, P. Kuerz, J. Stoeldraijer, and W. Kaiser, *Proc. SPIE* **11177** (2019) 111770B.
3. L. Li, X. Liu, S. Pal, S. Wang, C. K. Ober, and E. P. Giannelis, *Chem. Soc. Rev.* **46** (2017) 4855.
4. C. Luo, C. Xu, L. Lv, H. Li, X. Huang, and W. Liu, *RSC Advances* **10** (2020) 8385.

5. T. Manouras, and P. Argitis, *Nanomaterials* **10** (2020) 1593.

6. A. M. Brouwer, *J. Photopolym. Sci. Technol.* **35** (2022) 81.

7. A. Narasimhan, L. Wisehart, S. Grzeskowiak, L. E. Ocola, G. Denbeaux, and R. L. Brainard, *J. Photopolym. Sci. Technol.* **30** (2017) 113.

8. T. Kozawa, and S. Tagawa, *Jap. J. Appl. Phys.* **49** (2010) 030001.

9. B. Cardineau, R. Del Re, M. Marnell, H. Al-Mashat, M. Vockenhuber, Y. Ekinci, C. Sarma, D. A. Freedman, and R. L. Brainard, *Microelectron. Eng.* **127** (2014) 44.

10. S. T. Meyers, D. A. Keszler, K. Jiang, J. Anderson, and A. Grenville, US9310684B2, (2016).

11. W. D. Hinsberg, and S. Meyers, *Proc. SPIE* **10146** (2017) 1014604.

12. C. D. Needham, A. Narasimhan, U. Welling, L. S. Melvin III, P. De Schepper, J. Wouters, J. Severi, D. De Simone, and S. Meyers, *Proc. SPIE* **11323** (2020) 113230G.

13. I. Bespalov, Y. Zhang, J. Haitjema, R. M. Tromp, S. J. van der Molen, A. M. Brouwer, J. Jobst, and S. Castellanos, *ACS Appl. Mater. Interfaces* **12** (2020) 9881.

14. Y. Zhang, J. Haitjema, M. Baljozovic, M. Vockenhuber, D. Kazazis, T. A. Jung, Y. Ekinci, and A. M. Brouwer, *J. Photopolym. Sci. Technol.* **31** (2018) 249.

15. Y. Zhang, J. Haitjema, X. Liu, F. Johansson, A. Lindblad, S. Castellanos, N. Ottosson, and A. M. Brouwer, *J. Micro/Nanolitho., MEMS, MOEMS* **16** (2017) 023510.

16. J. Haitjema, Y. Zhang, M. Vockenhuber, D. Kazazis, Y. Ekinci, and A. M. Brouwer, *J. Micro/Nanolitho., MEMS, MOEMS* **16** (2017) 033510.

17. J. T. Diulus, R. T. Frederick, D. C. Hutchison, I. Lyubinetsky, R. Addou, M. Nyman, and G. S. Herman, *ACS Appl. Nano Mater.* **3** (2020) 2266.

18. M. C. Sharps, R. T. Frederick, M. L. Javitz, G. S. Herman, D. W. Johnson, and J. E. Hutchison, *Chem. Mater.* **31** (2019) 4840.

19. J. T. Diulus, R. T. Frederick, M. Li, D. C. Hutchison, M. R. Olsen, I. Lyubinetsky, L. Árnadóttir, E. L. Garfunkel, M. Nyman, H. Ogasawara, and G. S. Herman, *ACS Appl. Mater. Interfaces* **11** (2019) 2526.

20. R. P. Oleksak, R. E. Ruther, F. Luo, J. M. Amador, S. R. Decker, M. N. Jackson, J. R. Motley, J. K. Stowers, D. W. Johnson, E. L. Garfunkel, D. A. Keszler, and G. S. Herman, *ACS Appl. Nano Mater.* **1** (2018) 4548.

21. J. Haitjema, L. Wu, A. Giuliani, S. Castellanos, L. Nahon, and A. M. Brouwer, *Phys.Chem.Chem.Phys* **23** (2021) 20909.

22. Y. Zhang, J. Haitjema, S. Castellanos, O. Lugier, N. Sadegh, R. Ovsyannikov, E. Giangrisostomi, F. O. L. Johansson, E. Berggren, A. Lindblad, and A. M. Brouwer, *Appl. Phys. Lett.* **118** (2021) 171903.

23. J. Stöhr, *NEXAFS Spectroscopy*, Springer, Berlin, Heidelberg, **1992**.

24. S. Nannarone, F. Borgatti, A. DeLuisa, B. P. Doyle, G. C. Gazzadi, A. Giglia, P. Finetti, N. Mahne, L. Pasquali, M. Pedio, G. Selvaggi, G. Naletto, M. G. Pelizzo, and G. Tondello, *AIP Conf. Proc.* **705** (2004) 450–453.

25. N. Sadegh, Q. Evrard, P. M. Kraus, and A. M. Brouwer, *submitted* (2023)

26. B. L. Henke, E. M. Gullikson, and J. C. Davis, *At. Data Nucl. Data Tables* **55** (1993) 181.

27. N. Sadegh, M. van der Geest, J. Haitjema, F. Campi, S. Castellanos, P. M. Kraus, and A. M. Brouwer, *J. Photopolym. Sci. Technol.* **33** (2020) 145.

28. C. R. Arumainayagam, H.-L. Lee, R. B. Nelson, D. R. Haines, and R. P. Gunawardane, *Surf. Sci. Rep.* **65** (2010) 1.

29. J. Torok, R. Del Re, H. Herbol, S. Das, I. Bocharova, A. Paolucci, L. E. Ocola, C. Ventrice Jr, E. Lifshin, G. Denbeaux, and R. L. Brainard, *J. Photopolym. Sci. Technol.* **26** (2013) 625.

30. L.-L. Chua, M. Dipankar, S. Sivaramakrishnan, X. Gao, D. Qi, A. T. S. Wee, and P. K. H. Ho, *Langmuir* **22** (2006) 8587.

31. R. L. M. Gieseking, *Mater. Horiz.* **9** (2022) 25.

32. T. Okabe, *J. Phys. Soc. Jpn.* **35** (1973) 1496.

33. J. J. Ritsko, L. J. Brillson, R. W. Bigelow, and T. J. Fabish, *J. Chem. Phys.* **69** (1978) 3931.

34. H. Ahn, D. W. Oblas, and J. E. Whitten, *Macromolecules* **37** (2004) 3381.

35. R. Naaman, and L. Sanche, *Chem. Rev.* **107** (2007) 1553.

36. Y. Zheng, and L. Sanche, *Appl. Phys. Rev.* **5** (2018) 021302.

37. M. Pope, and C. E. Swenberg, *Electronic Processes in Organic Crystals and Polymers*, Oxford University Press, Oxford, **1999**.

38. M. Huttula, E. Kukk, S. Heinäsmäki, M. Jurvansuu, S. Fritzsche, H. Aksela, and S. Aksela, *Phys. Rev. A* **69** (2004) 012702.

Ultra-hydrophilic Diamond-like Carbon Coating on an Inner Surface of a Small-diameter Long Tube with an Amino Group by AC High-voltage Plasma Discharge

Yuichi Imai[1,2]*, Hiroyuki Fukue[2], Tatsuyuki Nakatani[2]**, Shinsuke Kunitsugu[3], Noriaki Kuwada[4], Yasuhiro Fujii[5], Daiki Ousaka[5], Susumu Oozawa[5], and Tomio Uchi[1]

[1] STRAWB Inc., [2] Okayama Univ. of Science,
[3] Industrial Technology Center of Okayama Prefecture,
[4] Kawasaki Medical School, [5] Okayama Univ.
*imai_y@strawb.jp, **nakatani@ous.ac.jp

Medical tubing includes artificial vascular grafts and catheters, each has a different purpose of use, but they both need to hydrophilize the lumen surface. Diamond-like carbon (DLC) is a dry coating technology, and its surface can be easily modified with hydrophilic functional groups. AC high-voltage plasma chemical vapor deposition has been developed for DLC deposition on the inner surface of small-diameter long tubes. In addition, oxygen plasma treatment of the DLC-deposited surface has been performed to enhance the hydrophilicity of the tube lumen and to inhibit biofilm adhesion in urinary catheters. However, the oxygen plasma treatment using silicone as the base material had only a slight inhibitory effect on biofilm adhesion, with a water contact angle of 104.4° for the DLC film and 90.6° for the DLC film, compared with oxygen plasma treatment, with an average value of 119.5° for the blank film. Recently, a new ammonia plasma treatment method has been developed, and an ultra-hydrophilic water contact angle of nearly 10° has been achieved with polyurethan (PU) as the base material. Furthermore, the zeta potential was found to be negative in oxygen plasma treatment and positive in ammonia plasma treatment, indicating that the hydrophilicity, and surface potential can be arbitrarily controlled by combining these plasmas, thereby achieving surface properties suitable for various applications.

Keywords: Plasma, DLC, Medical Tube, Catheter, Ultra Hydrophilic

1. Introduction

Amorphous carbon thin diamond-like carbon (DLC) film produced by plasma is primarily composed of the elemental symbols C and H, and it is not easily recognized as a foreign substance in the living organism, making it suitable for use as a biomaterial [1-3]. It has been applied to coronary artery stents [4, 5]. Recently, its application to small-diameter long tubes for medical use, such as artificial vascular grafts [6], ureteral stents [7], and catheters, has also been investigated. These small-diameter long tubes for medical applications have been subjected to secondary processing, such as the addition of hydrophilic properties [8], because of

issues such as stenosis and occlusion caused by thrombus and abnormal endothelial growth [9]. However, most of them are wet coating techniques, and problems such as thick wall, non-uniformity, and delamination [10-11] have been pointed out. Therefore, AC high-voltage plasma chemical vapor deposition (CVD) was developed to form DLC thin films on the inner surface of small-diameter long tubes using dry coating that enables dense and uniform film formation [12].

We have investigated the oxygen plasma treatment of the inner wall of small-diameter long tubes with DLC films to bring them closer to the biological environment. The water repellency of

DLC is reduced by the introduction of carbonyl or carboxyl groups, and a negative zeta potential (−15.9 mV) has been successfully obtained [13]. Polyurethane (PU) is a material that has been used in the production of PU films.

In the medical field, segmented polyurethane (SPU) with hard and soft microphase structures with mechanical properties and chemical stability has been developed for use in artificial hearts, artificial vascular grafts, balloon pumping for the aorta, balloon catheters, and high-calorie balloon catheters. SPU is used as a material for artificial hearts, artificial vascular grafts, balloon catheters for aortic balloon pumping, and indwelling catheters for high-calorie blood transfusion [14]. However, PU is not as durable as the other resins, and it's *in vivo* stability and hemocompatibility should be improved to inhibit thrombosis.

In this report, we investigated the changes in the surface properties of a PU material by forming a DLC film on a PU sheet encapsulated in a silicone tube using AC high-voltage burst plasma deposition and then applying NH$_3$ plasma treatment.

2. Experimental Method

2.1. Deposition conditions and sample

Figure 1 shows a schematic of the experimental equipment. DLC deposition on the inner surface of the tube was performed using an AC high-voltage plasma CVD system. The plasma power supply consisted of a voltage generator (IWATSU SG-

4105) and an amplifier (NF Corporation HVA4321). The voltage from the voltage generator was amplified 1000 times by using an amplifier to generate a high voltage. The deposition conditions are shown in Table 1. Notably, no Ar bombardment treatment was performed prior to deposition.

A commercially available 25 mm × 7 mm × 0.15 mm thick PU sheet was set inside a silicone tube for deposition on a PU sheet. Figure 2 shows the situation.

NH$_3$ treatment was performed by plasma discharge under NH$_3$ gas distribution after film deposition. The gas flow rate was kept constant at 96.2 sccm, and the plasma discharge duration varied from 5, 10, 20, 30, and 60 s.

2.2. Surface Characterization

The surface properties of the films were measured by measuring the contact angle of pure water and the zeta potential of the solid surface. For the pure water contact angle measurement, 1.5 μL of distilled water was dropped onto the film surface using a solid–liquid interface evaluation device (Dropmaster 500 manufactured by Kyowa Surface Science Co). The zeta potential of the fixed surface was evaluated by measuring the electrical mobility at different points in a flat cell using a zeta-potential-measuring device (ELSZ-1000 made by Otsuka Electronics Co., Ltd.) and by analyzing the electroosmotic flow using the "Mori/Okamoto formula." [15-17]. Polystyrene latex (particle
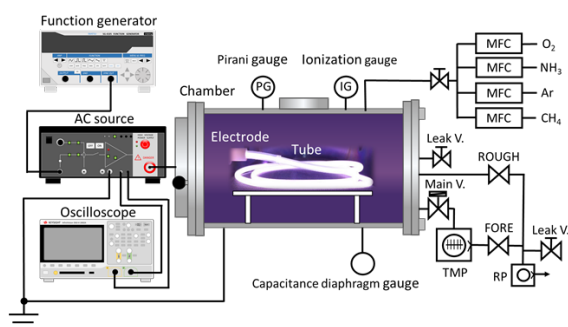
Fig. 1 Schematic of the experimental equipment.

Table 1. Deposition conditions.

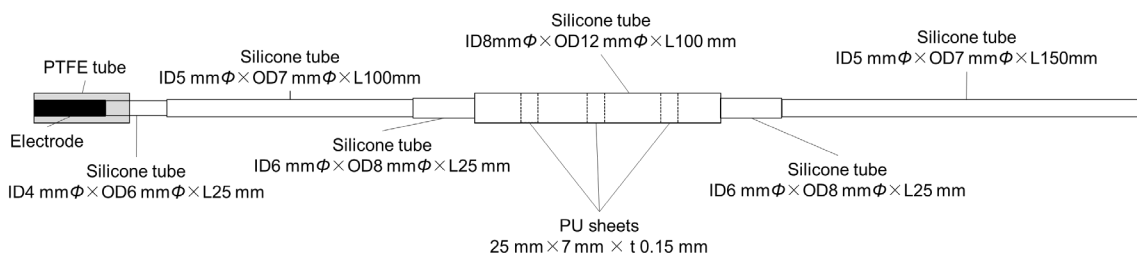| AC Voltage	5 kV
Offset Voltage	2 kV
Frequency	10 kHz
Gas	CH$_4$
Gas flow rate	96.2 sccm
Pulse Per Second	10 pps
Deposition time	20 min
Working Pressure	36.2 Pa

Fig. 2 Installation of PU sheet in a silicone tube.

$$f(x; A, \mu, \sigma, \alpha) = \frac{(1-\alpha)A}{\sigma\sqrt{2\pi}} \exp\left(-\frac{(x-\mu)^2}{2\sigma^2}\right) + \frac{\alpha A}{\pi}\left[\frac{\sigma}{(x-\mu)^2 + \sigma^2}\right] \quad (1)$$

diameter: approximately 500 nm) coated with hydroxypropyl cellulose (MW = 3000), which has almost zero surface potential, was used as the monitor particle, and the monitor–particle suspension was diluted 250-fold using a 10 mmol/L NaCl solution.

X-ray photoelectron spectroscopy (XPS) was used to investigate the chemical bonding state of the surface. A scanning X-ray photoelectron spectrometer (ULVAC PHI500 VersaProbe III) was used as the X-ray source, and the X-ray source was monochromatized at an Al–K wavelength of 1486.6 eV. The X-ray output was 25 W, and the analysis diameter was 100 μm. For fitting, each peak was fitted using the following equation (1), which is known as the pseudo-Voigt function. Here A refers to the amplitude; μ is the center position; σ is the full width at half maximum, and α is the Gauss–Lorentz component ratio. The Gauss–Lorentz component ratio of this pseudo-Voigt function was the one with the lowest error in the preliminary fitting (α = 0.3.) The fitting of the C1s peak was performed using nonlinear least squares with the Levenberg–Marquardt algorithm [18-19]. Fitting analysis was performed using a self-written program in Python.

3. Results and Discussion

3.1 Contact Angles in Pure Water

Figure 3 shows the contact angles. The contact angles of PU sheets and DLC-coated samples were 87.3° and 83.3°, respectively, showing slight hydrophobicity, whereas those treated with NH₃ plasma for 5 s were 20.6°, showing substantial hydrophilicity. The contact angle of the sample treated with NH₃ plasma for 20 s was further reduced to 12.2°, indicating the ultra-hydrophilicity.

Next, Fig. 4 shows the change in contact angle by NH₃ plasma treatment over time. However, the average values for n = 7 are obtained at 0 s (without DLC deposition) and 5 s, and the average values for n = 3 are obtained at 10, 20, 30, and 60 s. The average contact angle of the samples treated with NH₃ plasma treatment for 5 s was 21.2° ± 1.9°. The mean value of all data for treatments longer than 10 s was 15.6° ± 4.3° (n = 12).

3.2 Zeta potential measurement

Figure 5 shows the results of zeta potential measurement of the solid surface in relation to NH₃ plasma treatment time. The measurement of the PU
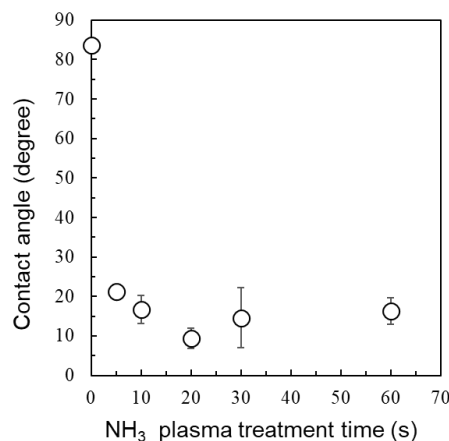

Fig. 4 Relationship between NH₃ plasma treatment time and pure water contact angle.
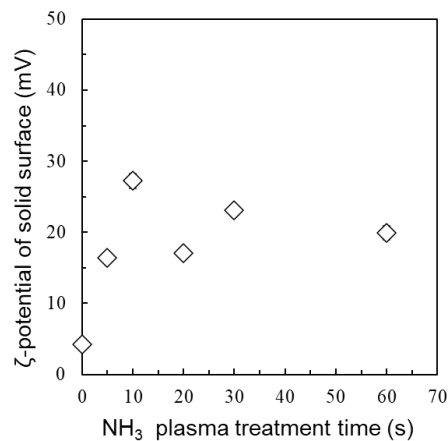(5s : n=7, 10s, 20s, 30s, 60s : n=3)

Fig. 5 Relationship between NH₃ treatment time and solid surface zeta potential.

sheet only showed a negative potential of –3.9 mV ± 0.5 mV. By contrast, the DLC-deposited sample was positively charged at 4.2 mV, and the NH_3 plasma treatment further increased the positive potential, with an average value of 20.7 ± 4.5 mV for the sample over 5 s. In previous studies, in the case of oxygen plasma treatment [13] , the potential changed to −12.4 mV and negative after 10 s of discharge. However, in the case of NH_3 plasma treatment, the surface charge was positive despite the superhydrophilicity (Figure 3).

3.3 Chemical bonding state of the surface

The chemical bonding state of the surface was investigated by XPS. Figure 6 shows the wide scan spectra of the DLC-coated PU sample and the NH_3 plasma-treated samples for 5 and 20 s. For the DLC-coated PU sample, C1s, and O1s peaks were observed. By contrast, the N1s peak was detected in NH_3 plasma-treated samples, indicating that NH_3 plasma treatment introduced N to the DLC surface. The semi-quantitative values estimated from the intensity of each peak using the relative sensitivity coefficient were C:N:O = 76:15:9 for both treatment times. This result is due to carbon dioxide and contamination adsorbed on the surface. On the other hand, in the NH_3 plasma treatment, approximately 9 at% O was detected in spite of the treatment in which only NH_3 gas was circulated, indicating that the O remaining on the DLC surface remained as it was, or that radicals and ions generated by the divergence and decomposition of NH_3 gas during NH_3 plasma discharge reacted with the O or moisture and O in the chamber may react with the O remaining on the DLC surface, resulting in the formation of bonds such as amide groups. Therefore, we performed narrow-scan measurements of the C1s, N1s, and O1s peaks to investigate the chemical bonding state in detail.

Figure 7 shows the narrow spectra of the C1s, N1s, and O1s peaks for the sample treated with NH_3 plasma for 20 s. The C1s peak is the strongest at 284.8 eV. First, for the C1s, the C–C, and C–H peaks at 284.8 eV are the strongest, but the presence of a large shoulder at higher binding energies can be confirmed.

Assuming the peak positions of the C–O and C–N, as well as O=C–O and N=C–O components to be 286.1 and 287.9 eV, respectively [20], and

Fig. 7 XPS narrow scan spectrum after 20 s of NH_3 plasma treatment.

Fig. 6 XPS wide scan spectrum.

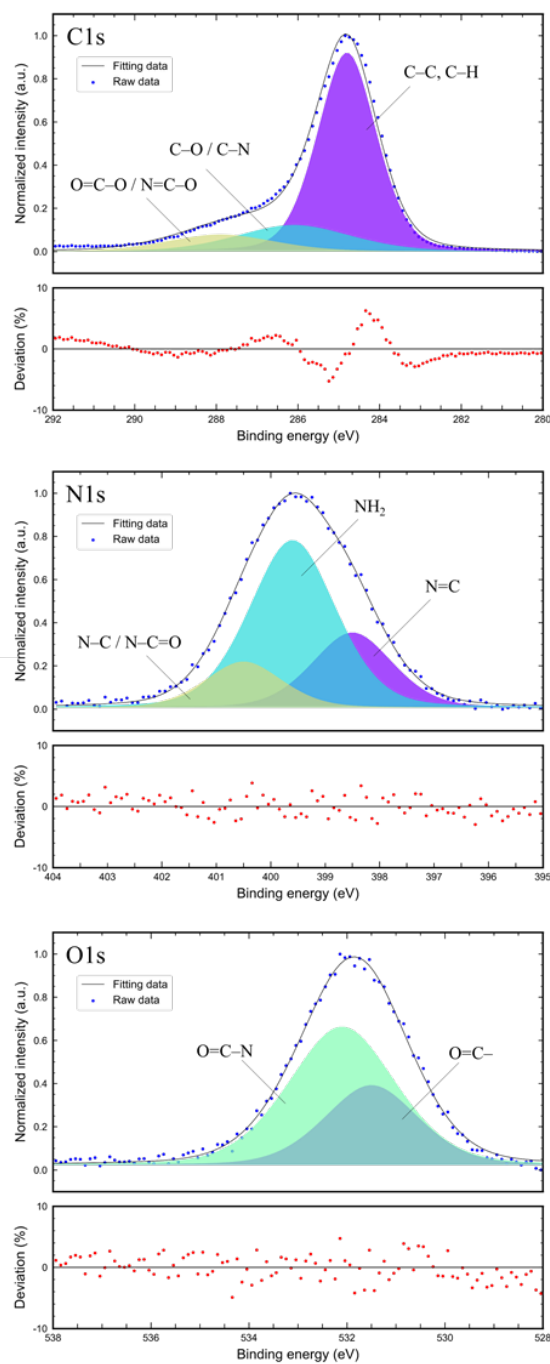performing curve fitting, the results show minor errors, which were indicated by red lines in the figure. The curve fitting results converged with a small error (R^2 = 0.995), which was indicated by a red dotted line in the figure. The C1s waveform separation results indicate the presence of bonds with chemical bonds between carbon and oxygen or nitrogen.

Similarly, the N1s peak shows a broad peak shape, indicating the presence of a multiple component. In addition, the C1s waveform indicates the presence of a carbon-bonded component. The waveforms were fitted to the three components assuming N=C, NH_2, and N–C or N–C=O bonding at 398.5, 399.6, and 400.5 eV, respectively [20], resulting in a highly accurate waveform separation (R^2 = 0.998). The main bond was shown to be -NH_2 (primary amino group). No -NH_3^+ (401.9 eV), which is formed by the ionization of NH_3, was detected.

In the case of O1s, as with the other peaks, the broad peak with a wide semi-valence bandwidth is a multiple component. In general, based on the database of organic materials, the peak position of the oxygen–carbon double bond (O=C) and oxygen–carbon single bond (C–O–C) of the carbonyl and carboxyl groups, appears as a difference of 1.6 eV, such as 531.8 and 533.4 eV, respectively [20]. The amide bond (O=C–N), which is a bond between nitrogen and oxygen found in C1s and N1s peaks, was reported at 531.2 eV, indicating a lower bond energy than the other peaks [20]. Therefore, curve fitting was attempted with three peaks based on these positions (the relative difference in bonding positions is fixed), and divergence was confirmed. Therefore, we attempted curve fitting with two peaks simultaneously, and waveform separation with two peaks was feasible (R^2 = 0.995). This result indicates the presence of polar bonds or end groups such as carbonyl and carboxyl because the main bond is O=C.

Furthermore, more O=C–N bonds than O–C single bonds may appear.

Table 2 summarizes the bonding states expected from the waveform separation results of the peaks obtained. As shown in the table, C–C, and C–H bonds, which are the main components of DLC, are the most abundant even after NH_3 plasma treatment, accounting for about half of the total bonds. The depth of XPS analysis is said to be 2 to 6 nm. Although only one atomic layer of the top surface is entirely modified by other bonds, the underlying DLC component can still be detected. C–O or C–N single bonds with a large ration are found, but the proportion of O–C single bonds found at 533.7 eV in the O1s is small, indicating that most of the components at 286.1 eV detected in the C1s are C–N single bonds. In N1s and O1s, a large fraction of N–C=O is present in the bonded state, including N–C single bonds. Based on these proportions, the chemical bonding on the surface consists of about 75% DLC (C–C, C–H) components, about 15% amide bonds (-NHCO-), about 10% C=O bonds such as carbonyl or carboxyl, and about 5% amino groups (-NH_2) in the surface area, which can be detected in this measurement.

4 Relationship between surface chemical bonding states and surface properties

The relationship among these surface functional groups, the contact angle of pure water and the zeta potential of the solid surface, are discussed. As shown in Figure 3, the NH_3 plasma treatment decreased the contact angle of pure water to 20°, confirming superhydrophilicity. Based on the observation of the chemical bonding state obtained from XPS, this phenomenon is due to the polar C=O bond and amino group with a strong hydrogen bond. On the contrary, the zeta potential of the solid surface was significantly more positive than that of DLC, whose surface would be hydrogen terminated.

Table 2. Chemical bonding state after 20 s of NH_3 plasma treatment.

	Content (at%)	B.E. (eV)	FWHM (eV)	Area (%)	Chemical bands
C1s	75.7	284.8	1.6	71.2	C–C,C–H
		286.1	3.1	17.9	C–O / C–N
		287.9	3.0	10.8	O=C–O / N=C–O
N1s	15.3	398.5	1.7	25.2	N=C
		399.6	1.7	60.0	NH_2
		400.5	1.5	14.8	N–C / N–C=O
O1s	9.0	531.5	2.1	33.8	O=C–N
		532.1	2.5	66.2	O=C–

In a nearly neutral 10 mol/L NaCl solution, -NH2 ionizes to -NH3+, which is considered to be a positive charge [21-22]. Notably, the zeta potential *in vivo* is slightly different because the salt concentration *in vivo* is approximately 150 mmol/L, and the pH is weakly alkaline (pH 7.4). In previous studies, oxygen plasma treatment imparts carbonyl or carboxyl groups, resulting in a negative potential (−15.9 mV) [13] . In this study, NH_3 plasma treatment resulted in a positive potential. Combining these plasma treatments makes it possible to arbitrarily control the hydrophilicity and surface potential, thereby achieving surface properties suitable to each application.

5 Conclusion

Biomimetic surfaces on the inner walls of small-diameter long tubes made of DLC films were formed on PU sheets encapsulated in silicone tubes through AC high-voltage burst plasma deposition, and NH_3 plasma treatment was applied.

The NH_3 plasma treatment for more than 10 s produced a super hydrophilic surface with a contact angle of less than 20° in pure water.
The surface after NH_3 plasma treatment showed a positive zeta potential. The super hydrophilic surface and positive zeta potential were attributed to the addition of amino groups (-NH_2) to the surface.

References

1. D. P. Monaghan, K. C. Laing and P. A. Logan, *Mater. World*, **1** (1993) 347.
2. S. J. Bull, *Diam. Relat. Mater.*, **4** (1995) 827.
3. T. Shuto, T. Nakatani, K. Okamoto, N. Saizaki, S. Mimura, S. Kunitsugu and H. Nikawa, *J. Photopolym. Sci. Technol.*, **29** (2016) 413.
4. T. Nakatani, K. Okamoto, I. Omura and S. Yamashita, *J. Photopolym. Sci. Technol*., **20** (2007) 221.
5. S. Kesavan, J. W. Strange, T. W. Johnson, S. F. Roese and A. Baumbach, *EuroIntervention*, **8** (2013) 1012.
6. Y Fujii, T Goyama, G Muraoka, D Ousaka, T Nakatani, HA Uchida, *European Journal of Vascular and Endovascular Surgery*, **58**, (2019) e419.
7. S. Watari, K. Wada, M. Araki, T. Sadahira, D. Ousaka, S. Oozawa, T. Nakatani, Y. Imai, J. Kato, R. Koriyama, T. Watanabe and Y. Nasu, *Int. J. Urol.*, **28** (2021) 1282.
8. P. Francois, P. Vaudaux, N. Nurdin, H.J. Mathieu, P. Descouts and D.P. Lew, *Biomaterials*, **17**, (1996) 667.
9. J. M. W. Donker, G. H. Ho, A. Te Slaa, H. G. W. Groot, J. C. H Van Der Waal, E. J. Veen, L. Van Der Laan, *Vasc. Endovascular Surg*. **45**, (2011) 598.
10. Amitabh M. Chopra, Monik Mehta, Jean Bismuth, Maksim Shapiro, Michael C. Fishbein, Alina G. Bridges, Harry V. Vinters, *Cardiovascular Pathology*, **30** (2017) 45.
11. Rashi I. Mehta and Rupal I. Mehta, *J Patient Saf*. Author manuscript; available in PMC (2019) September 19.
12. T. Nakatani, Y. Imai, Y. Fujii, T. Goyama and S. Ozawa, *J. Photopolym. Sci. Technol.*, **31** (2018) 373.
13. Y. Imai, H. Fukue, T. Nakatani, S. Kunitsugu, K. Kanda, T. Suzuki, S. Watari, Y. Fujii, D. Ousaka,S. Oozawa, T. Uchi, *J. Photopolym. Sci. Technol*., **35**, (2022) 289.
14. Y. Marois, R. Guidon, Madame Curie Bioscience Database, https://www.ncbi.nlm.nih.gov/books/NBK6422/. Accessed27 Sep (2022).
15. S. Mori, H. Okamoto, *Fusen*, **27**, (1980) 117 (in Japanese)
16. ISO 13099-2:2012, Colloidal systems−Methods for zeta-potential determination−Part 2: Optical methods (IDT).
17. S. Nakamura, Membrane, **30**, (2005) 344.
18. K. Levenberg, *Quarterly of applied mathematics*, **2**, (1944) 164.
19. D. W. Marquardt, *Journal of the society for Industrial and Applied Mathematics*, **11**, (1963) 431.
20. JEOL, Handbook of X-ray Photoelectron Spectroscopy (1991).
21. A. Mochizuki, T. Ogawa, K. Okamoto, T. Nakatani and Y. Nitta, *Mater. Sci. Eng. C*, **31** (2011) 567.
22. Y. Nitta, K. Okamoto, T. Nakatani, H. Hoshi, A. Honma, E. Tatsumi and Y. Taenaka, *Diam. Relat. Mat.*, **17** (2008) 1972.

Synthesis of High Refractive Linear to Branched Polyguanamines from 2-Amino-4,6-dichloro-1,3,5-triazine with Aromatic Diamines

Yuji Shibasaki*, Takanori Koizumi, and Yoshiyuki Oishi

*Department of Chemistry & Biological Sciences, Faculty of Science & Engineering,
Iwate University, 4-3-5 Ueda, Morioka, Iwate 020-8551, Japan
yshibasa@iwate-u.ac.jp

Polycondensation of 2-amino-4,6-dichloro-1,3,5-triazine (ADCT) with various aromatic diamines such as *m*-phenylenediamine (*m*PDA), 2,4,6-trimethyl-*m*-phenylenediamine (TMPDA), 4,4'-oxydianiline (ODA), 9,9-bis(4-aminophenyl)fluorene (BAFL), 4,4'-hexafluoroisopropylidenedianiline (BisAF) was investigated. High-molecular weight perfectly linear polyguanamines (PG)s, ($M_n \sim 46{,}000$) were successfully obtained for the polycondensation of ADCT with BisAF, while the polycondensation of ADCT with BAFL produced the branched PGs with the degree of branching of from 2.2 to 16.9%. The glass transition temperature and the 5% weight-loss temperature of PGs were in the range of 121 to 325 °C, and 419 to 490 °C, respectively. The optical transmittance of the polymers is higher than 90% at 400 nm wavelength, indicating the high transparency of the materials. The refractive indices of the resulting PGs were from 1.635 to 1.779 at D-line.
**Keywords: Polycondensation, Polyguanamine, Transparency, Refractive index**

1. Introduction

Cyanuric chloride has three active C-Cl bonds, which undergo sequential substitution reactions depending on the reaction temperature [1-3]. Therefore, many monosubstituted dichlorotriazine compounds have been synthesized and used as monomers for preparing functional polymers [4-13]. 2-Amino-4,6-dichloro-1,3,5-triazine (ADCT) is an AB$_2$-type monomer that is easily synthesized by the reaction of cyanuric chloride and aqueous ammonia [14]. However, the amino group on the triazine ring is extremely electron deficient; thus, it has little nucleophilicity. Wang et al reported the synthesis of high molecular weight polyguanamines (PG)s from ADCT with α,ω-alkylenediamines and the crystal structure was studied [15]. The NH$_2$ group on the triazine ring was intact for the polymerization; thus, the functional group was played as a multiple hydrogen bondable site in the crystal formation. We have already reported that the polycondensation of ADCT as a AB$_2$ monomer with 4,4'-oxydianiline (ODA) as an A$_2$ monomer produced an almost perfectly linear polymer free from branching unit [16]. This chemoselective polycondensation was

arisen by the above-mentioned weak nucleophilicity of the amino group on the triazine ring. On the other hand, the polycondensation of ADCT with 9,9-bis(4-aminophenyl)fluorene (BAFL) provided the polymers with slightly branched structure depending on the polymerization temperature.

Recent rapid progress of wearable small appliances requires further miniaturization of optoelectronic devices, and thus light and processable organic high temperature polymers are attracting more and more attention as an alternative to glass materials. The refractive index at 589.6 nm (D line, n_D) for such organic glasses are usually in the range from 1.30 to 1.70, but a very high exceeding 1.7 is frequently desired especially for CMOS image sensors [17]. Although several organic optical polymers such as aromatic heterocyclic polymers [18], polythiophene [19], and conjugated polymers [20] show high n_D values over 1.7, they have inadequate solubility, high optical dispersion, and low optical transparency in the visible region. Therefore, the development of organic polymers with high heat resistance and high n_D values remains an essential issue.

PGs are well-known polymers that possess multiple hydrogen-bonding ability due to guanamine units; thus, the PG obtained by the chemo-selective polycondensation of ADCT with diamines should show strong molecular interaction at the amino groups, resulting in well-packed polymer chains with higher n_D value. Changing diamines and the polymerization conditions may control the structure of the PGs from ADCT with the perfectly intact amino unit on the triazine ring to partially reacted one, which could affect the properties of the PG polymers. Therefore, in this study we investigated the relationship between structure and n values of polymers obtained by the polycondensation of ADCT with various diamines (Scheme 1).
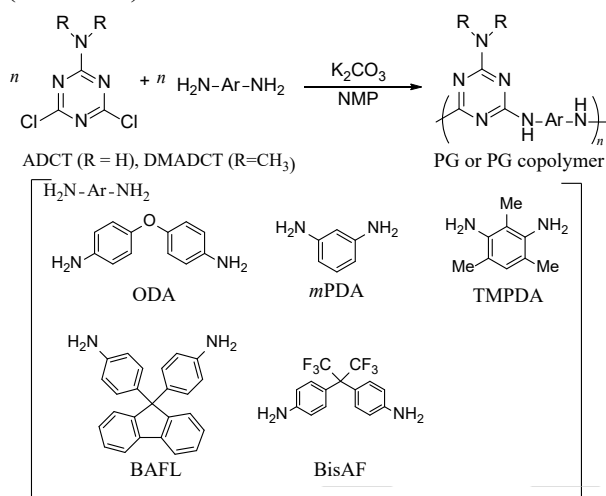
Scheme 1. PG syntheses using ADCT or DMADCT with various diamines.

2. Experimental

2.1. Materials

Cyanuric chloride, *N,N*-dimethylamine HCl complex, *p*-anisidine, *m*-phenylenediamine (*m*PDA), ODA, 2,4,6-trimethyl-1,3-phenylenediamine (TMPDA), BAFL, 4,4'-(hexafluoroisopropylidene)dianiline (BisAF) were purchased from Tokyo Chemical Industy Co. Ltd. and used as received. Ammonia aqueous solution, pyridine, K_2CO_3, Cs_2CO_3 were purchased from Kanto Chemical Co. Inc. and used as received. 1-Methyl-2-pyrrolidone, (NMP) super dehydrated was purchased from Fujifilm-Wako Chemicals and used as received. ADCT was prepared by the reported procedure using cyanuric chloride with the mixture of acetone and ammonia solution at 0 °C for 1 h [14]. 2-*N,N*-Dimethylamino-4,6-dichloro-1,3,5-triazine (DMADCT) was prepared according to literature [14]. The other reagents and solvents were used as received.

2.2. Measurements

Fourier transform infrared (FTIR) spectra were measured on a Jasco FT/IR-4200 spectrometer (Jasco. Ltd.) by transmittance absorption spectroscopy (KBr tablet method). The number-average molecular weights (M_n), weight-average molecular weights (M_w), and the molecular weight distribution (M_w/M_n) were determined by a Tosoh HLC-8220 gel permeation chromatograph (GPC), equipped with refractive index and UV detectors, and a consecutive polystyrene gel column (TSK-GEL α-M × 2), at 40 °C and eluted with NMP at a flow rate of 1.0 mL/min. Nuclear magnetic resonance (NMR) spectroscopy was performed on a Bruker AC-500 spectrometer at 500 MHz for ^{1}H measurement. Deuterated dimethyl sulfoxide (DMSO-d_6) was used as the solvent with tetramethylsilane as the internal reference. Thermogravimetric analysis (TGA) was conducted using a HITACHI TG/DTA 7220 system under exposure to air or N_2 flow at a heating rate of 10 °C min^{-1} from 20 to 800 °C. Differential scanning calorimetry (DSC) was performed on a HITACHI X-DSC7000 system under N_2 flow at a heating rate of 20 °C min^{-1} from 20 °C to 350 °C. Solubility tests were conducted by immersing polymer samples in eight different solvents for 24 h at room temperature. UV-Vis spectra were recorded on a Shimadzu UV spectrophotometer (UV-1800) at the concentration of 2.0×10^{-5} mol/L (as a repeating unit of a polymer) in NMP. The out-of-plane and in-plane refractive indices of the polymer films were measured with a prism coupler (Metricon Model 2010) equipped with a He–Ne laser light source (wavelength = 632.8 nm). Measurement of the refractive indices were carried out in transverse electric (TE) and transverse magnetic (TM) mode.

2.3. Synthesis of 2-*N*-(4-methoxyphenyl)-4-amino-6-chloro-1,3,5-triazine (ADCT-AN)

This compound was prepared according to the reported procedure [21]. Into a two-necked round bottom flask equipped with a reflux condenser, a three-way stopcock, and a stirrer bar were added ADCT (0.660 g, 4.00 mmol) and NMP (2 mL) under nitrogen. *p*-Anisidine (0.493 g, 4.00 mmol) solution in NMP (2 mL) was dropwise added via a syringe at 0 °C, and the reaction was allowed to continue at 40 °C for another 2 h. The reaction solution was poured into 3wt% $NaHCO_3$ aqueous solution, and the precipitate was collected. This was dried at 80 °C for 12 h under vacuum to give the title compound as pale purple powders. Yield 0.805 g (80.0%). ^{1}H NMR (400 MHz, DMSO-d_6, δ ppm):

3.734 (s, 3H, CH$_3$), 6.859 (br, 4H, NH$_2$, Ar-H), 7.589 (br, 2H, Ar-H), 9.151 (br, 1H, NH).

2.4. Synthesis of 2,6-bis(*N*-(4-methoxyphenyl))-4-amino-1,3,5-triazine (ADCT-2AN)

This compound was prepared in the modified method according to literature [22]. Into a two-necked round bottom flask equipped with a reflux condenser, a three-way stopcock, and a stirrer bar were added ADCT (0.1649 g, 1.000 mmol), potassium carbonate (0.304 g, 2.20 mmol), *p*-Anisidine (0.2647 g, 2.150 mmol), and NMP (2 mL) under nitrogen. The mixture was reacted at 150 °C for 2 h, and poured into water. The precipitate was collected and dried at 100 °C for 12 h under vacuum. This was recrystallized from ethyl acetate / hexane mixed solvent to give the title compound as pale purple powders. Yield 0.268 g (79.1%). ^{1}H NMR (400 MHz, DMSO-d_6, δ ppm): 3.735 (s, 3H, CH$_3$), 6.52 (br, 2H, NH$_2$), 6.861 (d, 2H, Ar-H), 7.590 (br, 2H, Ar-H), 8.910 (br, 2H, NH).

2.5. Polymerization (Typical procedure for poly(ADCT-ODA) (Run 2, Table 1))

Into a two-necked flask equipped with a three-way stopcock, a reflux condenser, and a magnetic stirrer bar, ODA (0.5006 g, 2.500 mmol), NMP (5 mL), and ADCT (0.4125 g, 2.500 mmol) were added in this order under nitrogen. Into this solution, K$_2$CO$_3$ (0.761 g, 5.50 mmol) was added, and the mixture was stirred at 150 °C for 3 h. The resulting mixture was poured into water (200 mL) containing a small amount of aqueous ammonia (28%, 5 mL), to precipitate the polymer. The polymer was dissolved in NMP, and reprecipitated in methanol twice, providing a white powder. Yield 0.7234 g (99%).

2.6. Copolymerization (Typical procedure for poly(ADCT-BAFL$_{74}$-*m*PDA$_{26}$) (Run 5, Table 3))

Into a two-necked flask equipped with a three-way stopcock, a reflux condenser, and a magnetic stirrer bar, *m*PDA (0.0811 g, 0.750 mmol), BAFL (0.6098 g, 1.750 mmol), NMP (5 mL), and ADCT (0.4125 g, 2.500 mmol) were added in this order under nitrogen. Into this solution, K$_2$CO$_3$ (0.761 g, 5.50 mmol) was added, and the mixture was stirred at 150 °C for 24 h. The resulting mixture was poured into water (200 mL) containing a small amount of aqueous ammonia (28%, 5 mL), to precipitate the polymer. The polymer was dissolved in NMP, and reprecipitated in methanol twice, providing a white powder. Yield 0.598 g (65%).

2.7. Film preparation

In a 20 mL vial tube were added poly(ADCT-BisAF) (0.5 g) and NMP (9.5 g), and the mixture was stirred at 20 °C for 24 h. The resultant viscous solution was drop-cast on a glass plate. This was dried in a glass desiccator at 20 °C for 6 h under 20 mmHg pressure, followed by in a vacuum oven at 50, 80, 120 °C for 3 h each, and 140 °C for 12 h under the reduced pressure to give a slightly yellow stiff film (film thickness 21.0 μm) (Fig. 5).

3. Results and discussion

3.1. Synthesis of the model compounds

To evaluate the degree of branching (*DB*) in the PG polymers, ADCT-AN and ADCT-2AN were synthesized. These can be a terminal and a linear model, respectively. The ^{1}H NMR spectra of these compounds are depicted in Fig. 1(A) and (B). The aromatic protons assignable to *c* and *c'* were observed at 6.859 and 6.861. The NH$_2$ protons of the linear model were appeared at 6.520 ppm while those of the terminal ones were observed at 6.859 ppm. The guanamine NH protons of the terminal and linear models were observed at 9.151 and 8.910 ppm, respectively. These spectra were compared with those of PG polymers to evaluate the branch structure.
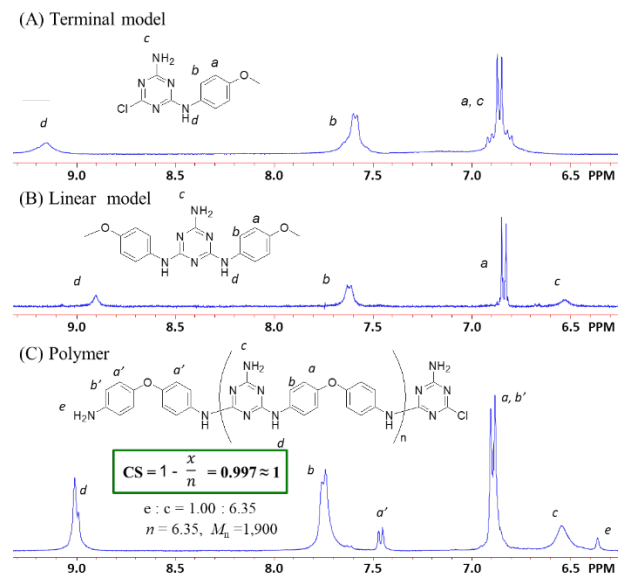

Fig. 1. ^{1}H NMR spectra of (A) ADCT-AN, (B) ADCT-2AN, and (C) poly(ADCT-ODA) in DMSO-d_6.

3.2. Synthesis of poly(ADCT-ODA)

Polymerization of ADCT with ODA was performed by changing proton scavengers as summarized in Table 1. In any case the corresponding PG polymers were obtained in good yields, but the M_n values were not very high. The
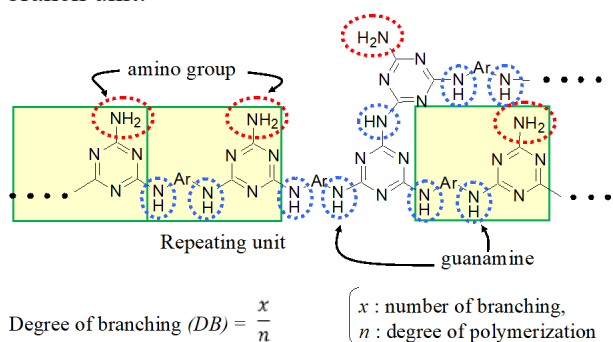
resulting poly(ADCT-ODA) showed poor solubility (only soluble in DMF and DMSO), probably because of the strong hydrogen bonding interaction between polymer chains. Figure 1(C) depicts the ^{1}H NMR spectrum of the poly(ADCT-ODA) polymer. In addition to the main chain proton signals a, b, c, and d, the terminal protons a' and e were observed at 7.455 and 6.356 ppm, respectively. From the integrated values of e and c the repeating numbers n was calculated to be 6.35, which can be converted to M_n of 1,900. The M_n was also evaluated by GPC to be 1500; thus, the expected PG polymer was successfully obtained in this condition. Since there are no clear signals arisen from the branched units, the DB value was calculated using the integration values of NH$_2$ and guanamine hydrogens in the ^{1}H NMR spectrum. As shown in Fig. 2, the number of hydrogens in NH$_2$ to that in guanamine is $2n$-2 to $2n + x$, from which x/n is determined and substituting it into the following formula.

$$DB = x/n \qquad (1)$$

The chemoselectivity (CS) of NH$_2$ group is calculated to be as follows.

$$CS = 1\text{-}DB \qquad (2)$$

With this formula, the CS for poly(ADCT-ODA) was calculate to be 0.997; therefore, it can be said that the polymer was obtained almost free from branch unit.

Fig. 2. Schematic illustration of a PG polymer having branched unit and the equation of DB.

3.3. Synthesis of PG polymers using ADCT with various diamines.

Since poly(ADCT-ODA) showed poor solubility, BAFL was applied for the polymerization. The results are summarized in Table 2. The PG (poly(ADCT-BAFL)) showed better solubility

(soluble in NMP, DMF, DMSO) due to the bulky fluorene pendant group, and thus the M_n reached up to 19000 in the polymerization at 180 °C for 24 h. However, in this case we detected the branched units (DB = 2.2%) from ^{1}H NMR calculation (Fig. 3).

Table 1. Polymerization of ADCT with ODA[a]

Run	Additive	Yield (%)	M_n[b]	M_w/M_n[b]	M_n(NMR)[c]
1	pyridine	90	1,900	20	1,700
2	K$_2$CO$_3$	99	1,500	18	1,900
3	Cs$_2$CO$_3$	99	1,800	11	2,000

[a] Conditions: 2.5 mmol of ADCT, 2.5 mmol of ODA, 5.5 mmol of base in 5 mL NMP, at 150 °C, 3 h. [b] Determined by GPC (NMP, PSt). [c] Determined by NMR (DMSO-d_6).

Table 2. Polymerization of ADCT with BAFL[a]

Run	Temp (°C)	Conc. (mol/L)	Yield (%)	M_n[b]	M_w/M_n[b]	n	DB[c] (%)
1	120	1.00	82	6,000	7.3	13.6	0
2	140	1.00	84	6,000	7.8	13.6	0
3	150	1.00	61	14,000	2.3	31.8	2.2
4	180	1.00	59	19,000	10.5	43.1	16.9
5	200	1.00	-	gel	-	-	-
6	180	0.67	69	18,000	7.5	40.9	5.5
7	180	0.50	64	5,000	8.4	11.4	0
8[d]	180	0.50	60	10,300	6.7	23.4	0

[a] Conditions: 2.5 mmol of ADCT, 2.5 mmol of BAFL, 5.5 mmol of K$_2$CO$_3$ in 5 mL NMP for 24 h. [b] Determined by GPC (NMP containing 0.01mol% of LiBr). [c] Determined by ^{1}H NMR spectroscpy. [d] For 72 h.
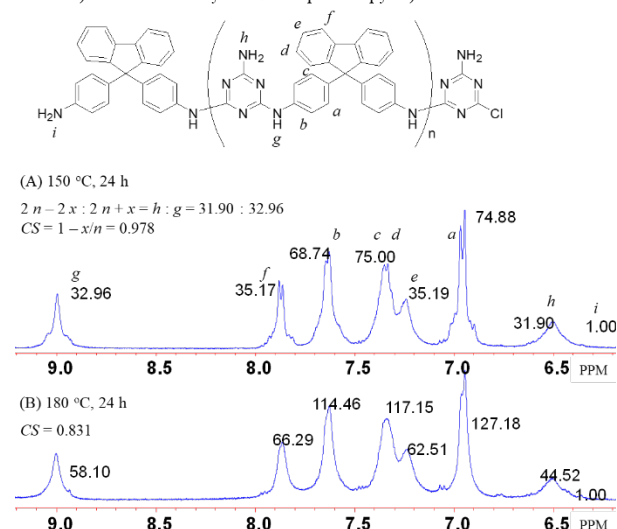

Fig. 3. ^{1}H NMR spectra of poly(ADCT-BAFL) obtained (A) at 150 °C for 24 h (Run 3, Table 2) and (B) at 180 °C for 24 h (Run 4, Table 2).

The branched units seem to increase with the polymerization temperature, and the almost linear-type high M_n PG of 14000 was obtained in the

polymerization at 150 °C for 24 h. The reactivity of NH_2 in ADCT against C-Cl groups at the terminals of the produced oligomers is the lowest due to the strong electron withdrawing two Cl atoms. However, the reactivity of NH_2 should increase by changing the Cl atom into NH function group after the reaction of ADCT with a diamine monomer. Therefore, it is reasonable that the branched units appear from this NH_2 group with the polymerization temperature. We thought that the formation of the branch units could be suppressed by using a diamine monomer having electron-withdrawing substituent.

Table 3. Polymerization of ADCT and BisAF [a]

Run	Diamine	CS (%)	T_g[a] (°C)	T_5[b] (°C)	T_{10}[b] (°C)
1	BAFL	>99	325	490	529
2	BAFL	97.8	293	472	524
3	BAFL	94.5	284	492	524
4	BAFL	83.1	288	419	517
5	ODA	99.7	248	468	520
6	BisAF	>99	280	488	519

a) Determined by DSC in nitrogen at a heating rate of 20°C/min.
b) T_5 and T_{10} are the temperatures for 5% and 10% decomposition of the polymer, respectively. (in N_2, heating rate 10°C/min)

$$2n - 2x : 2n + x = d : c = 86.82 : 86.83$$

$$CS = 1 - \frac{x}{n} \approx 1$$

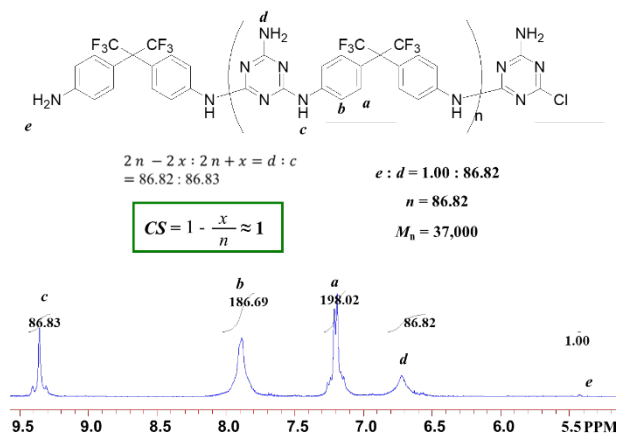$$e : d = 1.00 : 86.82$$
$$n = 86.82$$
$$M_n = 37,000$$

Fig. 4. ^{1}H NMR spectrum of poly(ADCT-BisAF) obtained at 180 °C for 12 h (Run 6, Table 3).

In this sense, BisAF was applied for the polymerization of ADCT. Table 3 summarizes the results of the polymerization. As can be seen, the corresponding polymer having the M_n up to 46000 was successfully obtained with the perfectly linear structure. The ^{1}H NMR spectra of poly(ADCT-BisAF) obtained at 180 °C showed the ideal spectrum with the reasonable integration values (Fig. 4). The CS of the PG polymer was calculated to be almost 1. The poly(ADCT-BisAF) polymer showed much better solubility even in THF in

addition to NMP, DMF, DMSO, probably because of weakening hydrogen network ability at the NH_2 function group.

Table 4. Thermal properties of PG polymers

Run	Temp (°C)	Time (h)	Yield (%)	M_n[b]	M_w/M_n[b]	M_n (NMR)[c]
1	150	3	88	1,000	32	1,300
2	150	6	67	3,500	11	12,000
3	150	12	58	16,000	3.1	18,000
4	150	24	41	15,000	3.2	14,000
5	170	12	52	26,000	1.9	30,000
6	180	12	33	46,000	2.3	37,000
7	200	12	-	gel	-	-

a) Conditions: 2.5 mmol of ADCT, 2.5 mmol of Bis-AF, 5.5 mmol of K_2CO_3 in 5 mL NMP. b) Determined by GPC (NMP, PSt). c) Determined by ^{1}H NMR.
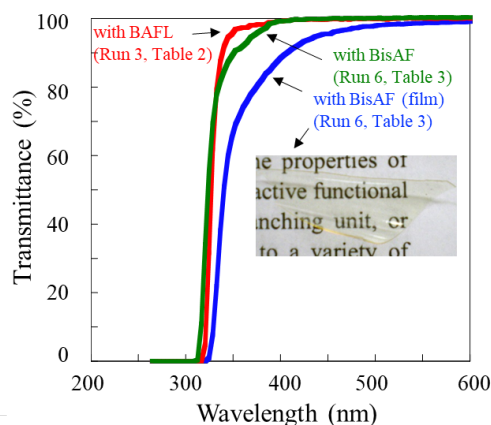

Fig. 5. UV-vis spectra of polymers in NMP (2.0×10^{-5} mol/L as the repeating unit) and in film (film thickness 21.0 μm) (inset is the film image of poly(ADCT-BisAF)).

3.4. Properties of poly(ADCT-BAFL) and poly(ADCT-BisAF)

Table 4 summarizes the thermal properties of PG polymers described above. The T_g decreased with the DB value from 325 to 288 °C. This phenomenon can be explained that the branching units prevent the polymer chain packing, resulting the increase of the chain mobility.

Figure 5 depicts the UV-vis spectra of the PG polymers. Since it was difficult to fabricate films using poly(ADCT-ODA) and poly(ADCT-BAFL) due to the low M_n value and the rigid-rod structure, the optical properties of the PG film (film thickness 21.0 μm) was only evaluated using the poly(ADCT-BisAF) polymer. Both of the poly(ADCT-BAFL) and poly(ADCT-BisAF) solution in NMP (2.0×10^{-5} mol/L as the repeating unit) similarly show good transparency of the λ_{cutoff} and $\lambda_{80\%}$ wavelength at 318, 332, and 310, 336 nm, respectively. The light

transmittance of the poly(ADCT-BisAF) decreased when the spectrum was measured in film state, probably because of the reflection at the surface of the film and the aggregation of the polymer chains within the film.

3.5. Copolymerization of ADCT with diamines.

To tune the solubility and the properties of the polymers, copolymerization of ADCT with diamines were studied. Table 5 summarizes the copolymerization of ADCT with BAFL/*m*PDA at 150 °C for 24 h. The M_n of the resulting copolymer decreased with the feed of *m*PDA due to the poor solubility. Figure 6 depicts the ^{1}H NMR spectrum of the poly(ADCT-BAFL)-*co*-poly(ADCT-*m*PDA) (Run 3, Table 5). From the integration values of *g* and *i*, the composition of the monomer was calculated to be 73 : 26, which agreed well with the feed ratio of the monomers. The *DB* values were calculated from the integration values similar to PG polymers described above to be in the range of only 1 to 3%.

Table 5. Polymerization of ADCT/BAFL/*m*PDA[a]

Run	BAFL : *m*PDA		Yield (%)	M_n [b]	M_w/ M_n [b]	DB
	feed	composition				
1	100 : 0	100 : 0	61	14,000	2.3	2.2
2	90 : 10	91 : 9	70	10,000	3.2	0.8
3	70 : 30	74 : 26	65	5,000	5.1	1.7
4	50 : 50	53 : 47	42	3,500	5.2	2.7
5	30 : 70	43 : 57	91	300	38	-

[a] 2.5 mmol of ADCT, 2.5 mmol of diamine, 5.5 mmol of K_2CO_3 in 5 mL NMP at 150 °C for 24 h. [b] Determined by GPC (NMP, PSt).

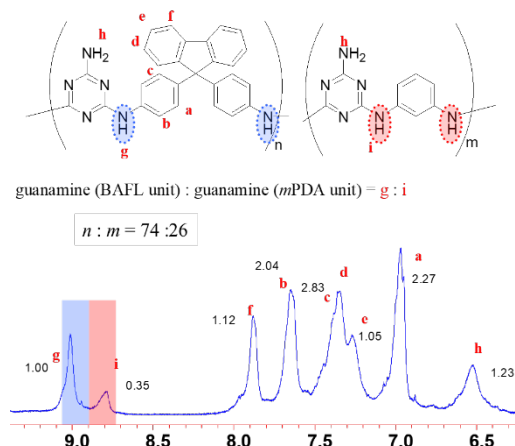guanamine (BAFL unit) : guanamine (*m*PDA unit) = g : i

n : *m* = 74 :26

Fig. 6. ^{1}H NMR spectrum of poly(ADCT-BAFL)-*co*-poly(ADCT-*m*PDA) obtained at 150 °C for 24 h (Run 3, Table 5).

To enhance the solubility of the PG polymer, the copolymerization was performed using ADCT with BAFL/TMPDA. The M_n values were similarly

decreased with the feed of TMPDA. ^{1}H NMR spectrum of this polymer (Run 2, Table 6) is depicted in Fig. 7. The composition of the polymer was calculated from the integration values of *a* and *b* to be 74 : 26, which were in good agreement with the feed ratio of the monomers. The *DB* values were also calculated from this spectrum to be nearly 0. When the polymerization was conducted with ADCT/BAFL at 150 °C, there was no branching unit. Whereas, some branched structure were observed in the poly(ADCT-BAFL)-*co*-poly(ADCT-*m*PDA). It shows that the introduced *m*PDA unit increases the nucleophilicity of the NH_2 group on the ADCT unit of the polymer chain. However, there was almost no branch unit in the produced copolymer using TMPDA instead of *m*PDA as a comonomer although TMPDA acts as electron-donating unit just like *m*PDA. This might be explained by the steric hindrance of TMPDA moiety with three CH_3 groups.

Table 6. Polymerization of ADCT/BAFL/TMPDA[a]

Run	BAFL : TMPDA		Yield (%)	M_n [b]	M_w/ M_n [b]	DB
	feed	composition				
1	100 : 0	100 : 0	61	14,000	2.3	2.2
2	70 : 30	74 : 26	54	2,500	3.7	0
3	50 : 50	52 : 48	59	3,500	2.5	0
4	30 : 70	29 : 71	47	2,000	2.8	0

[a] 2.5 mmol of ADCT, 2.5 mmol of diamine monomers, 5.5 mmol of K_2CO_3 in 5 mL NMP at 150 °C for 24 h. [b] Determined by GPC (NMP, PSt).

guanamine (BAFL unit) : guanamine (TMPD unit) = a : b
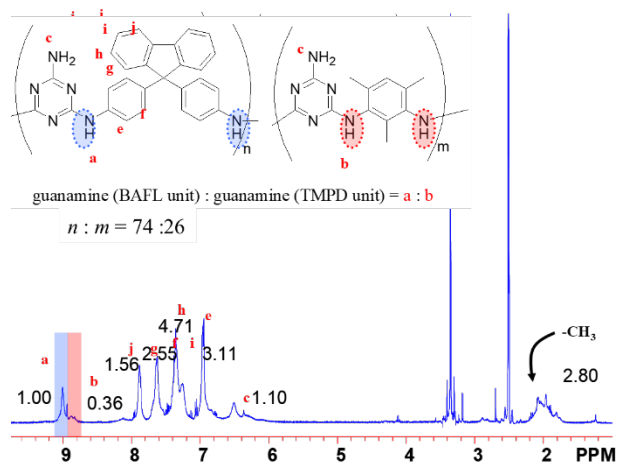
n : *m* = 74 :26

Fig. 7. ^{1}H NMR spectrum of poly(ADCT-BAFL)-*co*-poly(ADCT-TMPDA) obtained at 150 °C for 24 h (Run 2, Table 6).

Poly(ADCT-BAFL)-*co*-poly(ADCT-ODA) was then prepared and the results are summarized in Table 7. The corresponding PG polymers with the M_n values over 4100 were obtained. The *DB* value was calculated to be 0-3% using ^{1}H NMR

spectroscopy. Both BAFL and ODA provided the corresponding PG polymers with almost perfect linear structure. The thermal properties of the prepared PG polymers are also summarized in Table 7. As references, we also prepared *N,N*-dimethylated PG polymers, poly(DMADCT-BAFL) and poly(DMADCT-BisAF), which are perfect linear polymers. While poly(ADCT-BAFL) and poly(ADCT-BisAF) showed the T_g of 284-325 °C and 280 °C, respectively, those of their counterparts (ADCT → DMADCT) are 277 and 253 °C. These higher T_g values of ADCT-based polymers should be attributable to the free NH_2 function group, which can make dense hydrogen bond network in the films. In the series of poly(ADCT-BAFL-*m*PDA) copolymers, the T_g decreased with *m*PDA content (Run 3, 4, 5 in Table 7). The bulky BAFL is more efficient than the densely packable ADCT unit for high T_g. For the series of poly(ADCT-BAFL-TMPDA) copolymers, the T_g again decreased with the composition of TMPDA. This is due to the three bulky CH_3 groups on the TMPDA unit, which cause the twisted dihedral angles between triazine and TMPDA units (weaker chain packing). The T_g of poly(ADCT-ODA) was reasonably between those of poly(ADCT-BAFL-*m*PDA) and poly(ADCT-BAFL-TMPDA).

low polarization of fluorine atoms. Poly(DMADCT-BAFL) showed lower n_d of 1.7151 compared with poly(ADCT-BAFL) due to the absence of NH_2 function group on the triazine ring. This result supports well the lower T_g of the poly(DMADCT-BAFL) than that of the counterpart. It is notable that the n_d of poly(ADCT-BAFL) polymer increased from the DB of 0 to 5.5, but it decreased to 1.7286 at that of 16.9. Since the BAFL unit is too bulky in the polymer chain, and thus the less steric ADCT unit produces some space, resulting in lower density and lower n_d. Therefore, several branch structure can efficiently fill out this space, resulting in the n_d increase. However, excessive introduction of the branch structure produces much sparse within the polymer film, resulting in the n_d decrease. Because of the bulky structure of the BAFL unit in the polymer chain, introduction of *m*PDA as the substituent was effective to increase the n_d from 1.7453 (*DB* = 2.2) to 1.7788 of poly(ADCT-BAFL$_{43}$-*m*PDA$_{57}$). Again, TMPD was ineffective to increase n_d, because the bulky three CH_3 groups prevent the coplanar structure between triazine and *m*PDA unit; thus, the free volume increased, resulting in the n_d decrease.

Table 7. Thermal properties of PG polymer

Run	Monomers	DB	T_g [a] (ºC)	N₂		Air	
				T_{d5} [b] (ºC)	T_{d10} [b] (ºC)	T_{d5} [b] (ºC)	T_{d10} [b] (ºC)
1	DMADCT/BAFL	0	277	484	500	403	450
2	DMADCT/BisAF)	0	253	480	494	399	470
3	ADCT/BAFL$_{74}$/*m*PDA$_{26}$	1.7	309	483	526	447	481
4	ADC/BAFL$_{53}$/*m*PDA$_{47}$	2.7	302	479	513	457	496
5	ADCT/BAFL$_{43}$/*m*PDA$_{57}$	0.5	295	465	510	461	479
6	ADCT/BAFL$_{76}$/TMPD$_{24}$	0	290	472	524	445	492
7	ADCT/BAFL$_{52}$/TMPD$_{48}$	0	285	431	504	396	441
8	ADC/BAFL$_{29}$/TMPD$_{71}$	0	283	461	505	390	423
9	ADCT/BAFL$_{67}$/ODA$_{33}$	3	315	493	531	445	481
10	ADCT/BAFL$_{50}$/ODA$_{50}$	0	290	483	527	457	486

a) Determined by DSC in nitrogen at a heating rate of 20ºC/min. b) T_{d5} and T_{d10} (heating rate 10ºC/min).

The n_d value of the prepared PG polymers were measured by a prism coupler, and the results are summarized in Table 8. Poly(ADCT-BisAF) showed the lowest n_d of 1.6348 due to the effect of

Table 8. Refractive index of PG polymers

Run	Monomers	M_n	DB	n_D [a]
1	ADCT/BisAF	46,000	0	1.6348
2	DMADCT/BAFL	5,200	0	1.7151
3	ADCT/BAFL	6,000	0	1.7303
4	ADCT/BAFL	14,000	2.2	1.7453
5	ADCT/BAFL	18,000	5.5	1.7462
6	ADCT/BAFL	19,000	16.9	1.7286
7	ADCT-BAFL$_{91}$/*m*PDA$_9$	10,000	0.8	1.7580
8	ADCT-BAFL$_{74}$/*m*PDA$_{26}$	5,000	1.7	1.7650
9	ADCT-BAFL$_{43}$/*m*PDA$_{57}$	300	-	1.7788
10	ADCT-BAFL$_{76}$/TMPD$_{24}$	2,500	0	1.7391
11	ADCT-BAFL$_{52}$/TMPD$_{48}$	3,500	0	1.7055
12	ADCT-BAFL$_{29}$/TMPD$_{71}$	2,000	0	1.6844

a) Determined by ellipsometry

The *n* values were fitted by Cauchy's equation, and the fitting curves are depicted in Fig. 8 and 9. As seen in Fig. 8, the combination of ADCT and BAFL seems effective to enhance the polymer packing with high n_d value. Since in this polymerization condition the branch structure can be ignorable, the produced space in poly(ADCT-BAFL) may be efficiently filled with the compact poly(ADCT-*m*PDA) segment. Introduction of

BAFL unit can increase the solubility of the resulting polymer, but decrease the density and n_d.
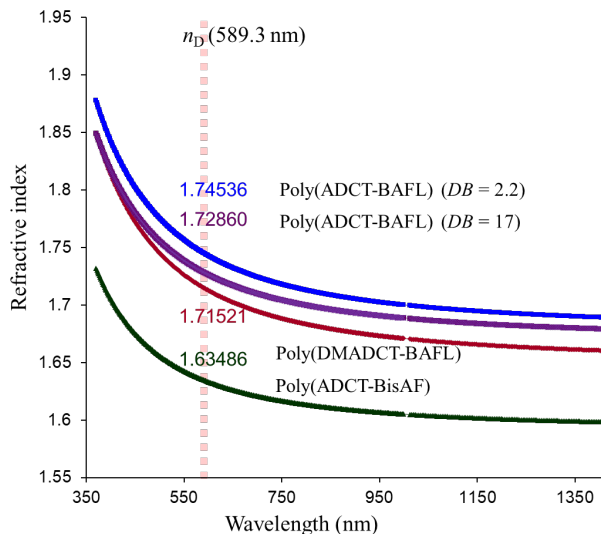

Fig. 8. Relationship between refractive index and wavelength of PG polymers. The measured data were fitted by Cauchy's equation.
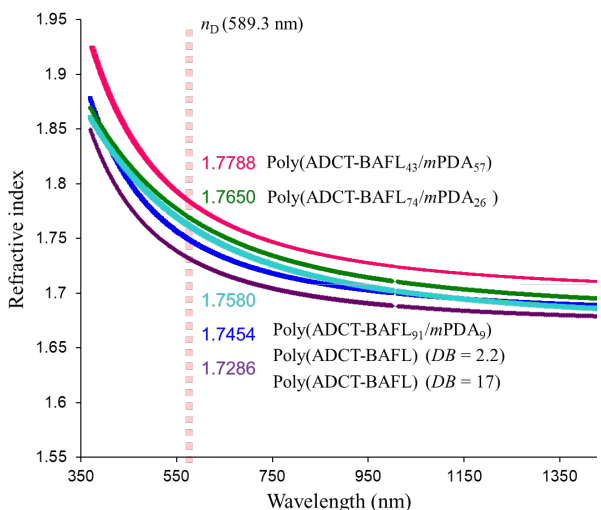

Fig. 9. Relationship between refractive index and wavelength of PG polymers. The measured data were fitted by Cauchy's equation.

Fig. 10 depicts the schematic illustration of the effect of the polymer structure on the n_d value. The PG having anilino pendant (poly(AnDCT-BAFL)) showed the n_d and T_g values to be 1.709 and 287 °C, respectively, in our previous work [11]. Two methyl substituents instead of the anilino moiety gave the polymer (poly(DMADCT-BAFL)) with the comparable n_d and T_g values to be 1.715 and 277 °C. On the other hands, the unsubstituted NH$_2$ moiety afforded the polymer (poly(ADCT-BAFL) with the improved n_d and T_g values to be 1.732 and 325 °C, clearly due to the multiple hydrogen bondable

ADCT function. The branched structure of the poly(ADCT-BAFL) (*DB* up to 17%) was able to modulate the n_d values from 1.729 to 1.746, probably due to the alternation of the free volume of the polymer. The poly(AnDCT-*m*PDA) was known to have a high n_d value of 1.783, but the M_n and T_g (209 °C) were both low because of the poor solubility in typical organic solvent including an aprotic polar solvent. The poly(ADCT-BAFL/*m*PDA) copolymers in the current study were revealed that they showed excellent n_d, T_g values, and good solubility in NMP, DMF, DMSO, thanks to the strong hydrogen bondable NH$_2$ and bulky BAFL moieties.
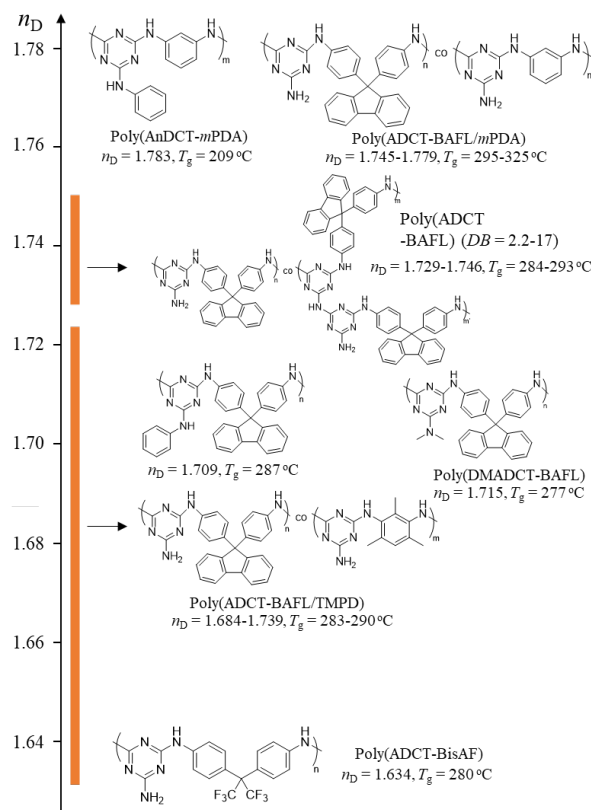
Fig. 10. Schematic illustration of the effect of polymer structure on the refractive index.

4. Conclusion

In this study, ADCT was polymerized with different kinds of diamines, and the thermal and optical properties were evaluated. ADCT has NH$_2$ group on it, and the functional group tended to react in high temperature condition, which produced brunch structure in the polymer chain. Depending on the branching density, the n_d values were changed, probably due to the fulfillment of the empty space within the polymer chains. In this sense, the values were affected by the DB and combination

of the used monomers. The highest n_d of the PG polymers reached to 1.779 when ADCT was copolymerized with BAFL and *m*PDA in 3/7 in molar ratio. This molecular design would be helpful to tune the n_d, T_g, and the optical transparency as an organic high refractive glass.

Acknowledgement

References
1. M. Goi, *Yuki Gosei Kagaku Kyokaishi*, **18** (1960) 327–331.
2. P. de Hoog, P. Gamez, W. L. Driessen, and J. Reedijk, *Tetrahedron Lett*., **43** (2002) 6783–6786.
3. A. Chouai and E. Simanek, *J. Org. Chem*., **73** (2008) 2357–2366.
4. J. K. Lin, Y. Yuki, H. Kunisada, and S. Kondo, *Polymer J.,* **22** (1990) 47–55.
5. H. Kunisada, Y. Yuki, S. Kondo, Y. Nishimori, and A. Masuyama, *Polymer J.*, **23** (1991) 1455–1465.
6. Y. Yuki, H. Kunisada, K. Iida, and S. Kondo, *Polymer J.*, **27** (1995) 1239–1245.
7. Y. Yuki, H. Kunisada, K. Iida, T. Kukaya, and S. Kondo, *Polymer J.*, **28** (1996) 337–342.
8. Y. Yuki, H. Kunisada, K. Iida, and S. Kondo, *Polymer J.*, **28** (1996) 553–555.
9. M. Maciejewski, E. Bednarek, J. Janiszewska, J. Janiszewski, G. Szczygiel, and M. Zapora, *J. Macromol. Sci., Pure and Appl. Chem.,* **A37** (2000) 753–783.
10. K. Saito, N. Nishimura, S. Sasaki, Y. Oishi, and Y. Shibasaki, *React. & Funct. Polym*., **73** (2013) 756–763.
11. T. Kotaki T., N. Nishimura, M. Ozawa, A. Fujimori, H. Muraoka, S. Ogawa, T. Korenaga, E. Suzuki, Y. Oishi, and Y. Shibasaki, *Polymer Chem*., **7** (2016) 1297–1308.
12. Y. Shibasaki, T. Kotaki, T. Bito, R. Sasahara, N. Idutsu, A. Fujimori, S. Miura, Y. Shidara, N. Nishimura, and Y. Oishi, *Polymer,* **146** (2018) 12–20.
13. H. Sasaki, T. Kotaki, A. Fujimori, T. Tsukamoto, E. Suzuki, Y. Oishi, and Y. Shibasaki, *RSC Advances*, **10** (2020) 1361–1370.
14. A. Baliani, G. J. Bueno, M. L. Stewart, V. Yardley, R. Brun, M. P. Barrett, and I. H. Gilbert, *J. Med. Chem*., **48** (2005) 5570–5579.
15. N. Irles, J. Puiggalí, and J. A. Subirana, *Macromol. Chem. Phys*., **202** (2001) 3316–3322.
16. Y. Shibasaki, T. Koizumi, N. Nishimura, and Y. Oishi, *Chem. Lett*., **40** (2011) 1132–1134.
17. J. Brandrup, E. H. Immergut, E. A. Gruike, A. Abe, and D. R. Bloch, ”*Polymer Handbook, 4th ed*.”; John Wiley & Sons: New York, 2005.
18. C. J. Yang and S. A. Jenekhe, *Chem. Mater.,* **6** (1994) 196−203.
19. T. Sugiyama, T. Wada, and H. Sasabe, *Synth. Met*., **28** (1989) C323−C328.
20. C. J.Yang and S. A. Jenekhe, *Chem. Mater*., **7** (1995) 1276−1285.
21. H. R. Bhat, U. P. Singh, A. Thakur, S. K. Ghosh, K. Gogoi, A. Prakash, and R. K. Singh, *Exp. Parasitol*., **157** (2015) 59−67.
22. P. X. Li, Q. L. Zhao, S. L. Wang, and Y. M. Lu, *Lat. Am. J. Pharm.,* **35** (2016) 529−536.

Synthesis of Thermosetting Polycarbonate with Ethynyl Terminals

Yuji Shibasaki[1]*, Tomoya Shirata[1], and Yoshiyuki Oishi[1]

[1] *Department of Chemistry & Biological Sciences, Faculty of Science & Engineering, Iwate University, 4-3-5 Ueda, Morioka, Iwate 020-8551, Japan*
*yshibasa@iwate-u.ac.jp

Thermosetting bisphenol A-carbonate resins with ethynyl and phenylethynyl terminals were successfully developed via an activated transcarbonate reaction. The terminal transformation efficiency from OH into ethynyl function was 74 to 87% determined by ^{1}H NMR spectroscopy, and the resin was sufficiently crosslinked with annealing treatment over 240°C. The glass transition temperature increased from 109 to 162°C with the char yield of 26% at 800°C.
Keywords: Polycarbonate, Thermosetting resin, Ethynyl group, Frame retardant

1. Introduction

Engineering plastics, which is endurable over 100°C with the elastic modulus over 2 GPa, tensile strength over 60 MPa, are widely used as metal substitute materials [1]. Thanks to the high moldability and low production cost, they have been applied in a variety of fields. On the other hand, flame resistance and high-temperature stability such as in solder reflow processes are often required, and even higher heat resistance is being demanded. In that sense, there is a certain demand for the development of thermosetting grades of the engineering plastics. For example, poly(2,6-dimethylphenylene ether) (PPE) is an amorphous engineering plastic with good heat resistance and mechanical properties. Its dielectric properties are particularly superior; thus, it has been continuously studied for the usage as a low-k material. However, in such fields its heat resistance of the T_g of 210°C is rather poor, and thus the thermosetting grades of PPE (allyl as pendant [2], epoxy [3], acryloyl [4] as terminal groups) have been developed so far. Epoxy, cyanate, and bismaleimide resins are thermosetting compounds with high rigidity, but they lack toughness and tend to absorb moisture, which limit their use in humid condition. As their substitute, thermosetting poly(arylether sulfone)s have been developed with the introduction of ethynyl [5], maleimide, and nadimide [6] groups at both ends of the polymer chains. In development of advanced

composite materials, polyimides (PI)s are widely studied such as P-13N (having norbornene terminals by TRW) [7], LARC-13 [8] (having norbornene-5,6-dicarboxylic anhydride terminals) [9], TriA-PI (having phenylethynyl terminals) [10].

Bisphenol A-polycarbonate (BisA PC) is a heat-resistant, highly transparent resin that boasts the largest production volume among the five major engineering plastics, and is used for lenses and optical substrates. Several attempts to combine thermoplastic BisA PC and carbon fiber have been reported [11], but research on thermosetting PC is quite limited. Lavrov et al. reported the epoxy compositions cured by products of the reaction of aminolysis from the secondary BisA PC (household waste with polyethylene polyamine [12]. Li et al. reported the synthesis and properties of benzocyclobutene (BCB) - functionalized thermosetting PC via copolymerization with BCB-functionalized bisphenol monomer, where The T_{d5} and char yield of the cured resin were improved to be 450°C and 33%, respectively [13]. Marks et al. reported the synthesis of oligocarbonate having ethynyl terminals by direct oligomerization of BisA/phosgene/m-ethynyl phenol (mEP), but the terminal functionality with mEP was below 50% [14]. These reports are interesting in terms of regeneration of BisA PC or modification by copolymerization, but they do not lead to the development of thermosetting grades utilizing the

current BisA PC manufacturing process. We, therefore, report the modification of carbonate oligomer with ethynyl or phenylethynyl groups at the terminals and their curing behavior with the thermal stability. Development of thermosetting BisA-carbonate resin would open new applications of heat resistant polycarbonate that can be mixed well with the additional inorganic fillers.

2. Experimental

2.1. Materials

4-Iodophenol, 3-bromophenol, BisA, diphenyl carbonate (DPC), *N,N*-dimethylaminopyridine (DMAP), ethynylbenzene, trimethylsilyl acetylene, *p*-nitrophenyl chloroformate, PPh$_3$, and Pd(PPh$_3$)Cl$_2$, and 3-ethynylphenol (*m*EP) were purchased from TCI Chemical and used as received. CuI was purchased from Merck and used as received. Triethylamine (TEA) and super dehydrated tetrahydrofuran (THF) were purchased from Kanto Chemical Co. Inc. and purified by distillation over calcium hydride. The other chemicals were used as received.

2.2. Measurements

Fourier transform infrared (FTIR) spectra were measured on a Jasco FT/IR-4200 spectrometer (Jasco Co. Ltd.) by transmittance absorption spectroscopy (KBr tablet method). The number-average molecular weights (M_n), weight-average molecular weights (M_w), and the molecular weight distribution (M_w/M_n) were determined by a Tosoh HLC-8220 gel permeation chromatograph (GPC), equipped with refractive index and UV detectors, and a consecutive polystyrene gel column (TSK-GEL α-M $\times$ 2), at 40°C and eluted with *N*-methyl-2-pyrrolidone (NMP) at a flow rate of 1.0 mL/min. Nuclear magnetic resonance (NMR) spectroscopy was performed on a Bruker AC-500 spectrometer at 500 MHz for ^{1}H and 125 MHz for ^{13}C measurements. Deuterated chloroform (CDCl$_3$) was used as the solvent with tetramethylsilane as the internal reference. Thermogravimetric analysis (TGA) was conducted using a HITACHI TG/DTA 7220 system under exposure to air or N$_2$ flow at a heating rate of 10°C/min from 20 to 800°C. Differential scanning calorimetry (DSC) was performed on a HITACHI X-DSC7000 system under N$_2$ flow at a heating rate of 20°C/min from 40°C to 340°C.

2.3. Synthesis of 4-(4-phenylethynyl)phenol (*p*PEP)

This compound was prepared according to the reported procedure [15]. Into a 500 mL three-necked flask equipped with a three-way stopcock

were added 4-iodophenol (8.828 g, 0.04000 mol), Pd(PPh$_3$)Cl$_2$ (0.4038 g, 0.5800 mmol), CuI (0.1107 g, 0.5800 mmol), PPh$_3$ (0.1515 g, 0.5800 mmol), ethynylbenzene (5.343 g, 0.005200 mol), and TEA (300 mL) at 20°C, and the mixture was stirred for 24 h. The resulting solution was filtered off, and the filtrate was mixed with diethyl ether and 0.1 mol/L HCl aq. solution. The organic phase was extracted three times with diethyl ether, and washed with water. The solvent was removed by a rotary evaporator, and the residue was separated by a column chromatography (CHCl$_3$). The product was further purified by sublimation at 40°C for 6 h under the reduced pressure to give the title compound as white powder (81.0% yield). ^{1}H NMR (400 MHz, CDCl$_3$, ppm): δ = 7.51 (m, 2H), 7.42 (d, 2H), 7.33 (m, 3H), 6.80 (d, 2H), 5.12 (s, 1H). ^{13}C NMR (100MHz, CDCl$_3$, ppm): δ =155.6, 133.3, 131.5, 128.3, 128.0, 123.5, 115.6, 115.5, 89.2, 88.1. FT-IR [KBr (cm^{-1})] : 3418 (O-H), 2230 (C≡C), 1510 (C=C), 1251 (Ph-O).

2.4. Synthesis of 3-(4-phenylethynyl)phenol (*m*PEP)

This compound was prepared in the modified method according to literature [16]. Into a 100 mL three-necked flask equipped with a three-way stopcock were added 3-bromophenol (9.985 g, 0.05800 mol), acetic anhydride (17 mL), and the mixture was reacted at 150°C for 2 h. After cooling the solution to room temperature, water (100 mL) was added. The organic phase was extracted with diethyl ether three times, dried over anhydrous MgSO$_4$, and the solvent was evaporated by a rotary evaporator to give 3-bromophenylacetate. This compound was used for the following reaction without further purification.

Into a 100 mL three-necked flask equipped with a three-way stopcock were added 3-bromophenylacetate (12.43 g, 0.05800 mol), Pd(PPh$_3$)Cl$_2$ (0.0722 g, 0.0100 mmol), CuI (0.0291 g, 0.153 mmol), PPh$_3$ (0.1445 g, 0.5010 mmol), ethynylbenzene (7.837 g, 0.007700 mol), and TEA (80 mL) at 20°C, and the mixture was stirred at 120°C for 12 h. The resulting solution was filtered off, and the filtrate was mixed with diethyl ether and 0.1 mol/L HCl aq. solution. The organic phase was extracted three times, and washed with water. The solvent was removed by a rotary evaporator. Into this flask], K$_2$CO$_3$ (9.678 g, 0.04100 mol) and methanol (70 mL) were added, and the mixture was reacted at 90°C for 4 h. The solution was diluted with water, and methanol was removed by a rotary evaporator. The solution was acidified with 0.1 mol/L HCl aq. solution, and the organic phase was

extracted with diethyl ether three times. After drying it with MgSO$_4$, the solvent was removed by a rotary evaporator, and the product was purified with a column chromatography (CHCl$_3$). The obtained product was further purified with recrystallization with hexane, and dried at 35°C for 6 h, to give the title compound as white powder (13.6% yield). ^{1}H NMR (400 MHz, CDCl$_3$, ppm): δ = 7.51 (m, 2H), 7.34 (m, 3H), 7.22 (t, 1H), 7.12 (d, 1H), 7.00 (s, 1H), 6.81 (d, 1H), 4.89 (s, 1H). ^{13}C NMR (100MHz, CDCl$_3$, ppm): δ = 155.2, 131.6, 129.7, 128.4, 124.5, 124.4, 123.1, 118.2, 115.7, 89.5, 88.9. FT-IR [KBr (cm^{-1})] : 3346 (O-H), 3048 (C-H), 2230 (C≡C), 1498-1475 (C=C), 1213 (Ph-O).

2.5. Synthesis of 4-trimethylsilyl ethynylphenol (*p*SEP)

This compound was prepared in the modified method according to the reported procedure [17]. Into a 500 mL three-necked flask equipped with a three-way stopcock were added 4-iodophenol (4.400 g, 0.02000 mol), Pd(PPh$_3$)Cl$_2$ (0.1403 g, 0.2000 mmol), CuI (0.1107 g, 0.5800 mmol), trimethylsilyl acetylene (2.161 g, 0.02200 mol), and TEA (50 mL) at 80°C, and the mixture was stirred for 12 h. The resulting solution was filtered off, and the filtrate was mixed with diethyl ether and 0.1 mol/L HCl aq. solution. The organic phase was extracted three times with diethyl ether, and washed with water. The solvent was removed by a rotary evaporator, and the residue was separated by a column chromatography (CHCl$_3$). The product was further purified by sublimation at 40°C for 6 h under the reduced pressure to give the title compound as pale brown liquid (65% yield). ^{1}H-NMR (400 MHz, CDCl$_3$, ppm): δ = 7.39 (d, 2H), 6.77 (d, 2H), 5.00 (s, 1H), 0.25 (s, 6H) ^{13}C-NMR (100MHz, CDCl$_3$, ppm): δ = 156.0, 133.8, 115.5, 115.0, 105.2, 92.6, 0.17. FT-IR [KBr (cm^{-1})] : 3381 (O-H), 2360 (C≡C), 1507 (aromatic C-H), 1249 (C-O, 832 (aromatic C-H).

2.6. Synthesis of BisA-carbonate oligomer Typical procedure (for Run 6 in Table 1)

Into a 300 mL separable flask equipped with a three-way stopcock were added BisA (3.424 g, 15.00 mmol), DPC (2.185 g, 10.20 mmol), and DMAP (0.0036 g, 0.0295 mmol (0.30 mol%)) under nitrogen. The mixture was stirred and heated up to 180°C for 1 h, and reacted another 1 h. After that, the pressure was reduced to 0.2-0.3 mmHg, and the temperature was increased to 270°C. The reaction was performed another 1 h, and then the temperature was decreased to 170°C. A small amount of dichlorobenzene was added to dissolve

the product, and the mixture was further cooled down to room temperature. The product was completely dissolved with the addition of CH$_2$Cl$_2$, and poured into methanol to precipitate the oligomer. It was dried at 100°C for 6 h under the reduced pressure to give the title compound as white powder (Yield 84%). M_n = 4,600, M_w/M_n = 1.6.

2.7. Synthesis of BisA-carbonate resin Typical procedure (for Run 1 in Table 2)

Into a 100 mL two-necked flask equipped with a three-way stopcock were added BisA-oligocarbonate (1.380 g, 0.3000 mmol), DMAP (0.0855 g, 0.700 mmol), and THF (15 mL) under nitrogen. Into the solution *p*-nitrophenyl chloroformate (0.1411 g, 0.7000 mmol) solution in THF (5 mL) was slowly added via a syringe at 0°C, and the reaction was continued for 12 h. The mixture of *p*PEP (0.1359 g, 0.7000 mmol) and DMAP (0.700 mmol) in THF (7 mL) were slowly added via a syringe at 0°C, and the reaction was continued for 12 h. The solution was neutralized with 0.1 mol/L HCl aq., and the organic phase was extracted with THF three times, followed by washing with water, dried over MgSO$_4$, filtered, and concentrated. The product was dissolved with a small amount of THF, and reprecipitated with methanol. The precipitate was collected dried at 80°C for 10 h under the reduced pressure (Yield 40%). M_n = 4,800, M_w/M_n = 2.5. Terminal functionality 74%.

2.8. Preparation of thermoset films

Three pieces of Upilex-75S PI films (UBE corporation, 75 μm thickness) each having a size of 8 cm × 8 cm were prepared. The center of one of these sheets was cut out into a square of 3 cm × 4 cm, and the PI film and the film with the center cut out were stacked in this order from the bottom on a SUS plate. Into the PI mold the above-mentioned BisA-carbonate resin was homogeneously placed and heated up to 320°C to melt the resin. After that, PI film and SUS plate were sequentially covered on the sample, and hot-pressed at 0.5 MPa for 5 min, and 3 MPa for 10 min. Finally, the resin was cross-linked at 320°C, 3 MPa for 1 h to give the thermoset film.

3. Results and discussion
3.1. Synthesis of crosslinking reagent

As the crosslinking agents, *p*PEP, *m*PEP, *m*EP, and *p*SEP were used here. Except for *m*EP, these were prepared via the conventional Sonogashira coupling reaction according to the reported procedure (Scheme 1) [15-17]. The structure of

these reagents was characterized by IR and ^{1}H NMR spectroscopy.
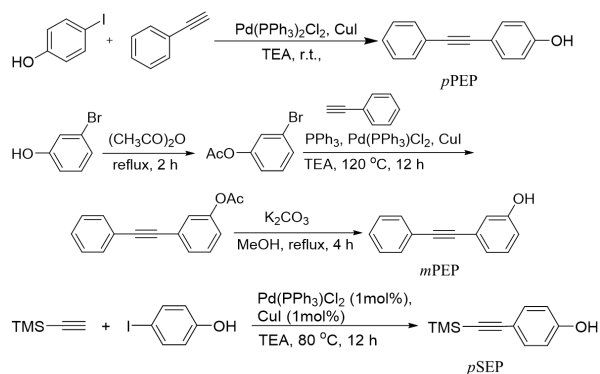
Scheme 1. Synthesises of the cross-linkers

Table 1. Synthesis of oligocarbonate[a]

Run	DMAP (mol%)	BisA:DPC (in mol)	Yield (%)	M_n[b]	M_w/M_n[b]
1	0.1	1:1	90	6,000	2.5
2	0.2	1:1	85	12,000	1.8
3	0.3	1:1	71	15,000	2.0
4	0.5	1:1	80	6,000	1.5
5	0.3	1:1	78	6,000	2.8
6	0.3	20:10.2	84	4,600	1.6
7[c]	0.3	20:10.2	81	2,620	2.6

[a] Conditions: at 180°C and 270°C for 1 h each under 0.2-0.3 mmHg. [b] Determined by GPC (CHCl$_3$, PSt). [c] At 180°C and 200°C for 1 h each.
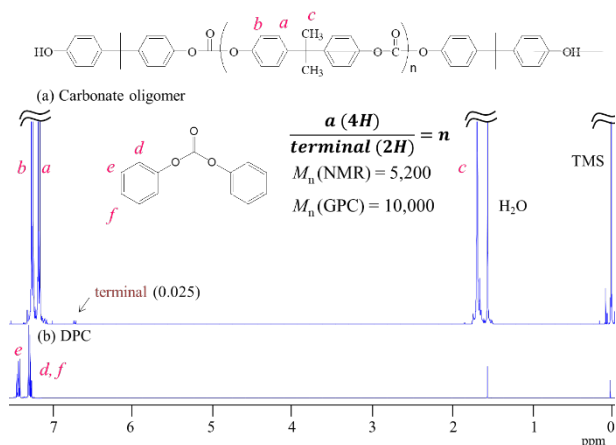
Fig. 1. ^{1}H NMR spectra of (a) carbonate oligomer and (b) DPC

3.2. Synthesis of BisA-carbonate oligomer

BisA-carbonate oligomers were prepared by melt polycondensation of BisA with DPC. To optimize the reaction conditions the amount of DMAP and the molar ratio of the two monomers were varied. As shown in Table 1 the M_n of the BisA-carbonate oligomer increased with the amount of DMAP (Run 1-3), while those values decreased with DMAP over 0.3 mol%. Excessive amount of DMAP might cause

not only the oligomerization but also deoligomerization to produce DPC, which easily sublimated under the reduced pressure, resulting in the M_n decrease. In fact, ^{1}H NMR spectrum indicated that both terminals of the resulting oligomer were BisA unit, and no DPC terminal was not detected (Fig. 1). Therefore, taking into account the usage of BisA terminal for the introduction of the thermosetting functional group, BisA-carbonate oligomer was synthesized with BisA/DPC (20/10.2) in molar ratio. The BisA-carbonate oligomer with M_n of 4,600 and 2,620 were successfully prepared at 270 and 200°C in the second heating condition, respectively (run 6 and 7, Table 1). These oligomers were used for the following reactions depicted in Scheme 2.
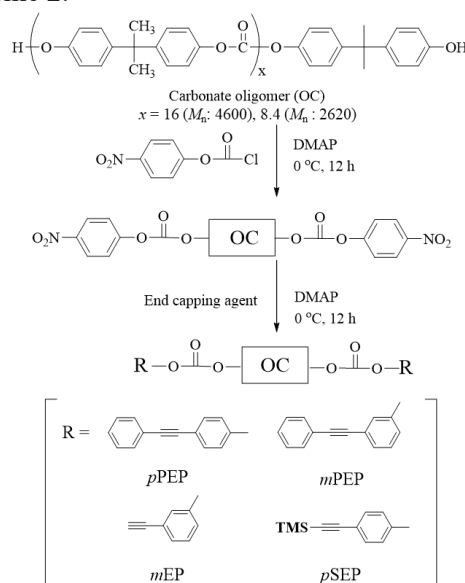
Scheme 2. Synthesis of BisA-carbonate resins

3.3. Synthesis of carbonate resin and the transformation of the end OH functions

The BisA-carbonate resin (thermosetting BisA-carbonate oligomer) was prepared as shown in Scheme 2. We first tried the preparation of the carbonate resin by the melt oligomerization of BisA (10.0 mmol) with DPC (10.0 mmol) in the presence of pPEP (2.0 mmol) at 270°C under the reduced pressure, but the resulting oligocarbonate did not have pPEP terminals, probably due to sublimation of the reagent during the reaction conditions. Therefore, we chose the two-step procedure via the active nitrophenyl intermediate method. The oligocarbonate having OH terminals was first prepared as described above, and the transformation of the terminal OH into cross-linkable ethynyl unit was performed via transcarbonate reaction. Fig. 2 depicts the ^{1}H and ^{13}C NMR spectra of the BisA-carbonate resin. In addition to the mainchain proton

signals *a*, *b*, and *c*, the protons at the terminal *p*PEP groups were observed at 7.60 ppm accompanying with the *o*-phenyl protons of the unreacted BisA terminals at 6.66 ppm. From the integration ratio the transformation efficiency was calculated to be 82%. In ^{13}C NMR spectrum, ethynyl carbon signal was clearly observed at 89.98 ppm. These results suggested that the two-step procedure via the active nitrophenyl intermediate method be effective to transform of OH into phenylethynyl groups. Table 2 summarizes the synthesis of the BisA-carbonate oligomer and the transformation reaction of the end groups. For BisA-carbonate oligomer, the M_n values determined by GPC agreed well with those by NMR spectroscopy. After the transformation reaction, the M_n increased in the range of 700 to 1900, which were close to the calculated value of 700, indicating that the transformation of the end group successfully occurred for all the samples. The transformation efficiency was calculated to be in the range of 74 to 87% determined by ^{1}H NMR spectroscopy.
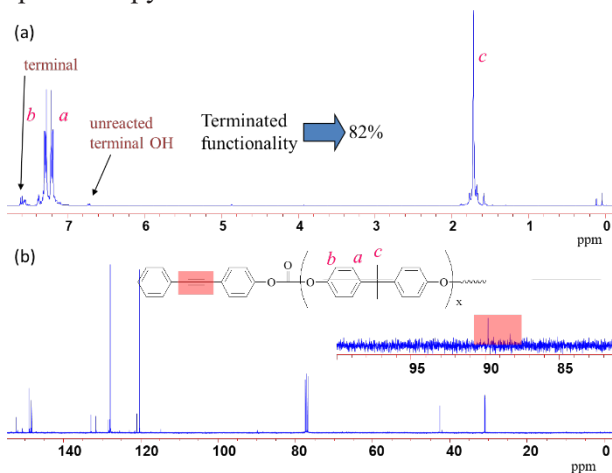
Fig. 2. (a) ^{1}H and (b) ^{13}C NMR spectra of BisA-carbonate resin with *p*PEP terminals (Run 2, Table 2)

Table 2. Synthesis of carbonate resin.

Run	Cross linker	Yield [a] (%)	Starting Oligocarbonate		Produced Carbonate resin		T.E. [c] (%)
			M_n (NMR)	M_n [b] (GPC)	M_n [b] (GPC)	M_w/M_n [b]	
1	*p*PEP	40	4,600	3,800	4,800	2.5	74
2	*p*PEP	55	2,620	2,400	3,300	1.8	82
3	*m*PEP	52	2,620	2,400	3,100	1.8	80
4	*m*EP	62	2,730	2,100	3,910	1.7	87
5	*p*SEP	52	2,630	2,250	4,200	1.5	85

[a]Methanol insoluble part. [b]Determined by GPC. [c]Transformation efficiency determined by ^{1}H NMR.

3.4. Thermal properties

The DSC profiles of the carbonate resin having *p*PEP and *m*PEP terminals are depicted in Fig. 3. For the *p*PEP terminal resin, T_g and the T_{onset} of thermosetting reaction were detected at 113 and 320°C, respectively. Although the DSC measurement was performed up to 340°C, in the 2nd heating process there was still small exothermic peak around over 260°C. The T_g in the 2nd heating process was 116°C, close to that in the 1st heating process. For *m*PEP terminal resin, there was almost no change in T_g between 1st and 2nd heating process. These results indicate that the carbonate resin having *p* and *m*PEP terminals do not work well for the thermal curing reaction because they require too high curing temperature.

Thermosetting PI and polystyrene with *p*PEP terminals [18] and *m*EP pendants [19] have been developed in different research groups. For the thermosetting PI, the quite high curing temperature of 360°C is required, while the curing at only 250°C is adequate for the thermosetting polystyrene. Based on these reports and the DSC results of our experiments, it can be said that the introduction of a low-temperature curable functional group such as *m*EP should be suitable for curing thermosetting carbonate resins. Therefore, *m*EP and *p*SEP were introduced instead of *p*PEP and *m*PEP. The DSC profiles of the carbonate resins are depicted in Fig. 4. For the *m*EP terminal resin, T_g and the T_{onset} of thermosetting reaction were detected at 113 and 238°C in conjunction with T_c and T_m at 180 and 218°C, respectively. In the 2nd heating process, the T_g increased to 142°C with disappearance of exothermic region over 230°C, clearly indicating that the resin was efficiently cross-linked with the terminal ethynyl function. For *p*SEP terminal resin, T_g, T_{onset}, T_c, and T_m were detected at 108 and 278, 139, 202°C, respectively. Again, the T_g increased to 138°C with disappearance of exothermic region over 270°C in the 2nd heating process, indicating the efficient cross-linking reaction with the terminal ethynyl function.

Table 3 summarizes the thermal properties of carbonate resins with the M_n adjusted to 2600-2700. A BisA-carbonate oligomer having OH terminals showed the T_g of 109°C with 17% char yield at 800°C under nitrogen. In contrast, *m*EP and *p*SEP terminal resins showed the T_g of 142 and 138°C with the char yield of 24 and 23%, respectively. Especially, the annealed *m*EP terminated carbonate resin at 240°C for 1 h showed the T_g of 162°C with the char yield of 26% (almost 10% higher than OH

terminated carbonate resin) while both T_g and char yield of *p*SEP terminated carbonate resin were remained the same. Thus, *m*EP should be an effective cross-linker for carbonate resin while *p*SEP be too bulky to induce an efficient cross-linking reaction.

Table 3. Thermal properties of carbonate resins

Run	Cross linker	Conditions	T_g [a] (°C)	T_{d5} (°C) [b]		T_{d10} (°C) [b]		Char (%) (800°C)
				N₂	air	N₂	air	
1	*m*EP	As made	142	423	376	451	398	24
2	*m*EP	Cured at 240°C	162	469	396	483	416	26
3	*p*SEP	As made	138	379	371	455	406	22
4	*p*SEP	Cured at 280°C	140	421	392	448	414	23
5	OH	As made	109	413	394	447	434	17

[a]Determined by DSC of the 2nd heating process in N₂, heating rate at 20°C/min. [b]5% and 10% weight loss temperature determined by TGA in N₂, heating rate 10°C/min.
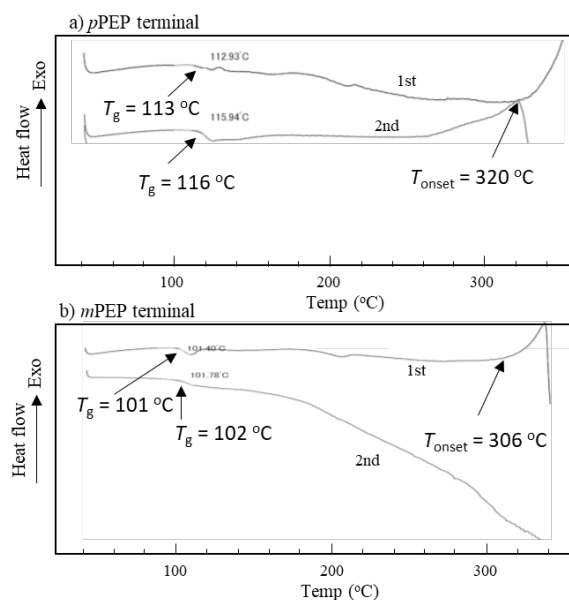
Fig. 3. DSC profiles of BisA-carbonate resin with a) *p*PEP and b) *m*PEP terminals

The T_{d5} of the *p*SEP terminated carbonate resin was lower than the others in Table 3, which could be explained by the thermal decomposition of trimethyl silyl group.

4. Conclusion

For the development of a thermosetting BisA carbonate resin, phenylethynyl and ethynyl groups were introduced into terminal OH group through the activated carbonate method, where the terminal functionality was 74 to 87%. The phenylethynyl groups did not work well to cross-link the carbonate resin by the thermal treatment up to 340°C,

probably because of the too high curing temperature. On the other hand, ethynyl terminals acted as an effective cross-linking group, and thus both T_g and the char yield at 800°C were improved from 109 to 162°C and 17 to 26%. The thermally cleavable carbonate bond itself made it difficult to improve the char yield. Further thermal improvement may be performed with shorten the chain length of the carbonate resin in the future study.
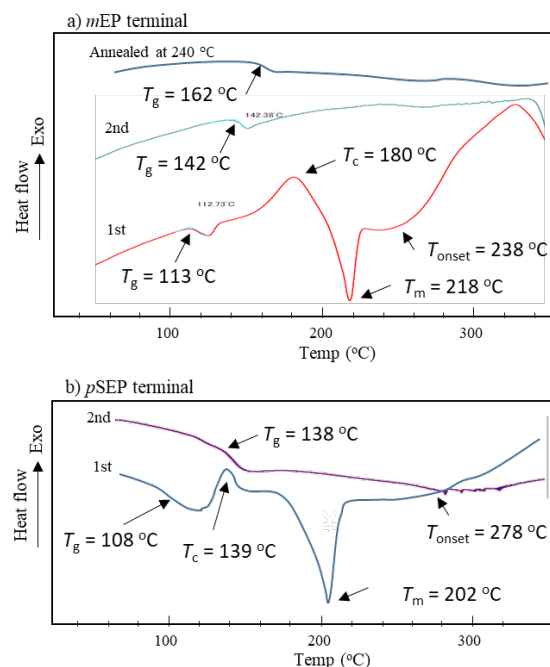
Fig. 4. DSC profiles of BisA-carbonate resin with a) *m*EP and b) *p*SEP terminals

Acknowledgement

References
1. J. M. Margolis, "*Engineering Plastics Handbook*", McGraw-Hill Professional Pub, 2005.
2. (a) Y. Wang, S. Cheng, W. Li, C. Huang, F. Li, and J. Shi, *Polym. Bull.*, **59** (2007) 391. (b) T. Fukuhara, Y. Shibasaki, S. Ando, and M. Ueda, *Polymer*, **45** (2004) 843. (c) Y. Ishii, Yoshiyuki Ishii, H. Oda, T. Arai, and T. Katayose, "Syntheses and Properties of Allylated Poly(2,6-dimethyl-1,4-phenylene ether)", in *"Microelectronics Technology" Polymers for Advanced Imaging and Packaging*, Ed by E. Reichmanis, C. K. Ober, S. A. MacDonald, T. Iwayanagi, and T. Nishikubo, ACS Symposium Series, **614** (1995) 485.

3. X. Wu, C. Xu, M. Lu, K. Wang, Z. Li, and H. Yang, *J. Appl. Polym. Sci.*, **139** (2022) e52858.

4. E.N. Peters, S.M. Fisher, and H. Guo, *Proceedings of the Annual Technical Conference Proceedings* (ANTEC 2011), 2011, 2823.

5. C. Bonfanti, L. Lanzini, R. Sisto, and C. Valentini, *J. Appl. Polym. Sci.*, **64** (1997) 1987.

6. P. Mison and B. Sillion, *Adv. Polym. Sci.,* **140** (1999) 137.

7. (a) H. R. Lubowitz, *U.S. Patent,* 3, 528, 950 (Sept. 15, 1970). (b) R. W. Vaughan, J. F. Jones, H. R. Lubowitz, and E. A. Bums, *SAMPE Proc.*, **15** (1969) 59. (c) H. H. Lubowitz, *Polym. Prepr.*, **12** (1971) 329. (d) S. L. Kaplan, *Plastic Design & Processing*, **10** (1972) 5.

8. (a) A. K. St. Clair, *Polym. Eng. & Sci.*, **22** (1982) 9. (b) T. L. St. Clair and D. J. *Progar, SAMPE Proc.*, **24** (1979) 1081.

9. (a) H. D. Stenzenberger, *Adv. Polym. Sci.*, **117** (1994) 163. (b) G. D. Roberts and R. W. Laver, *J. Appl. Polym. Sci.*, **33** (1987) 2893.

10. (a) R. Yokota, S. Yamamoto, M. Hasegawa, H. Yamaguchi, H. Ozawa, and R. Sato, *High Perform. Polym.*, **13** (2011) 61. (b) T. Ogasawara, Y. Ishida, R. Yokota, T. Watanabe, T. Aoi, and J. Goto, *Composites: Part A*, **38** (2007) 1296. (c) M. Miyauchi, Y. Ishida, T. Ogasawara, and R. Yokota, *Polym. J.*, **45** (2013) 594. (d) M. Miyauchi, Y. Ishida, T. Ogasawara, and R. Yokota,

Polym. J., **44** (2012) 959.

11. (a) M. Fang, Y. Ma, N. Zhang, M. Huang, B. Lu, K. Tan, C. Liu, and C. Shen, *Mater. Res. Expss*, **7** (2020) 045305. (b) F. Lambiase, V. Grossi, A. D. Llio, and A. Paoletti, Int. J. Adv. Manuf. Technol., **106** (2020) 2451.

12. M. B. Alikin, K. D. Alekseeva, D. A. Panfilov, I. M. Dvorko, and N. A. Lavrov, *Mech. Comp. Mater.*, **58** (2022) 697.

13. Z. Li, W. Cao, J. Sun, and Q. Fang, Chin. *J. Org. Chem.*, **36** (2016) 2442.

14. M. J. Marks, J. Newton, and S. E. Bales, *J. Polym. Sci.: PART A: Polym. Chem.*, **38** (2000) 2352.

15. (a) S. Kopolow, T. E. Hogen Esch, and J. Smid, *Macromolecules*, **4** (1971) 359–360. (b) M. J. Marsella and T. M. Swager, *J. Am. Chem. Soc.*, **115** (1993) 12214–12215. (c) D. P. Dickson, C. Toh, M. Lunda, M. V. Yermolina, D. J. Wardrop, and C. L. Landrie, *J. Org. Chem.*, **74** (2009) 9535.

16. M. S. M. Ahmed and A. Mori, *Tetrahedron*, **60** (2004) 9977.

17. D. X. Duc and N. V. Quoc, *Lett. Org. Chem.*, **19** (2022) 28.

18. A. L. Landis, N. Bilow, R. H. Boschan, and R. E. Lawrence, *Polym. Prepr.*, **15** (1974) 533.

19. F. Ishii, W. Hirahata, K. Yokota, K. Tuda, A. Hirao, and T. Kakuchi, *J. Polym. Sci.: PART B: Polym. Phys.*, **37** (1999) 3319.

Miniaturization of Scattered Random Patterns Formed by Lens·less Speckle Lithography

**Tomoki Iwaoka, Toshiyuki Horiuchi
and Hiroshi Kobayashi***

*Graduate School of Engineering, Tokyo Denki University,
5 Senju-Asahi- cho, Adachi-ku, Tokyo 120-8551, Japan
h_kobayashi@mail.dendai.ac.jp

A new method without using a projection lens for easily and inexpensively forming random micro-patterns on large area surfaces and three-dimensional shapes such as steps and curved surfaces was developed in the past research. In the method named "Speckle lithography", speckle light was used for forming scattered random patterns on surfaces coated with a resist film. In this paper, further miniaturization of patterns was investigated. In a renovated handmade exposure system, the beam diameter of laser beam irradiated to the diffusion plate was expanded from 4 mm to 17 mm using a beam expander. And, the distance between the diffusion plate and the wafer was shortened from 45 mm to 1 mm. As a result, random dot resist patterns with a minimum size of 1 μm or less were successfully formed on entire exposed areas limited to 10×10 mm.
Keywords: Speckle lithography, Random pattern, Scattered pattern, Lens·less

1. Introduction

In the field of bio-mimetics, observations and analyses of surface structures of plants and insects were eagerly carried out for producing characteristic surface functions by imitating their surface structures. Owing to the research efforts, water repellency of plant leaves in nature [1-7], antireflection of moth eyes [8-11], and antibacterial properties of cicada wings are known [12-14], for example. It is believed that these characteristic surface functions can be reproduced by artificially forming similar microstructures on the surfaces of industrial materials [15-19].

The purpose of this research is to form a scattered random patterns with sizes of between sub-micrometers and several hundreds micrometers on a large area using a simple and inexpensive exposure system that does not use a reduction projection lenses, and utilizing speckle light. This new method has been named speckled photolithography.

Most of the conventional exposure systems are fabricated to form patterns on flat surfaces such as silicon wafers. It is thought that this technology can be used for forming patterns on three-dimensional surfaces such as stepped surfaces and curved surfaces.

2. Characteristics of speckle lithography

Speckles are scattered irregular light intensity distributions that occurs when a rough surface is irradiated by coherent light such as laser light.

The speckles are scattered in various directions by a rough surface. And, because the scattered light rays interfere each other in a complex manner, spot-like patterns with random shapes and high contrasts are generated in the space.

Speckles are not generated by imaging optics such as a projection lens or a reflective mirror. Therefore, speckles are observed without depending on the distance between the rough surface and the irradiated object surfaces. As a result, speckles can be projected onto arbitrarily curved objects such as three-dimensional ones and stepped ones.

In addition, it is generally known that occurrences of speckle patterns vary depending on the characteristics of rough surface, wavelength and intensity of irradiated light.

Many researches using speckles have been carried out in the field of measurement [20-21].

However, applications to lithography have not been reported much [22].

The purpose of this research is to form fine patterns without using a reduction projection lens. How the patterns are formed and their sizes are reduced by changing the exposure time, position of diffusion plate, and others are discussed here.

3. Speckle pattern miniaturization factors

Figure 1 shows the principle of the speckle photolithography. A speckle light distribution is formed onto a resist-coated silicon wafer, and random patterns are formed on the silicon wafer by developing the exposed resist.
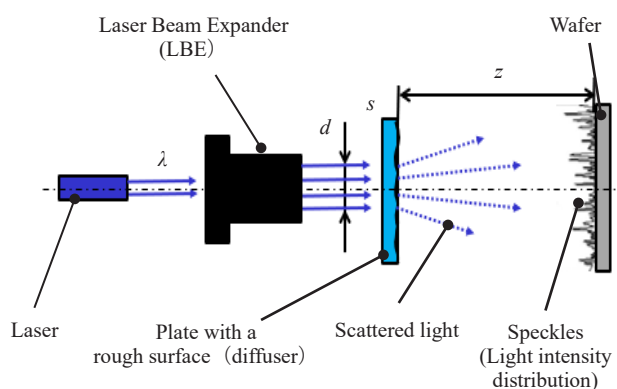
Fig. 1. Principle of speckle photolithography.

If the resist pattern size is R, the wavelength is λ, the irradiation beam diameter is d, the roughness of the diffusion plate is s, the distance between the diffusion plate and the silicon wafer is z, and the exposure time is t, the following relationship can be considered for the increase and decrease of the pattern size.

Increase factor of R: λ, z, t
Decrease factor of R: d, s

In this research, parameters that were relatively easy to change were chosen. It was thought that the pattern dimension could reduced by enlarging the irradiation beam diameter d, decreasing the proximity distance z between the diffusion plate and the silicon wafer, and reducing the roughness s of the diffusion plate.

4. Exposure system and experimental methods

A simple renovated experimental exposure system was assembled to investigate basic exposure characteristics of speckle photolithography. An appearance of the system is shown in Fig. 2. The system consists of a laser diode with a wavelength of 403 nm and a power of 16 mW, a shutter to control exposure time, A laser beam expander (LBE) for expanding the irradiation beam diameter, a diffusion plate (#1000 manufactured by Sigma Koki Co., Ltd.), and a wafer stage. The wafer was held by a vacuum chuck. They were arranged in a row and fixed on the guide rail.
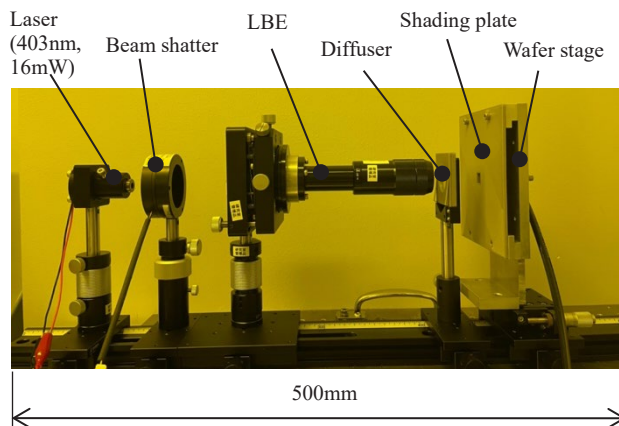
Fig. 2. Handmade exposure system assembled in this research.

In the experiment, all the wafers were coated with a positive resist THMR-iP3300 (Tokyo Ohka Kogyo Co., Ltd.) in approximately 1 μm using a spin coater. The exposure time was adjusted by turning the beam shutter on and off. To grasp patterning characteristics efficiently and systematically, under various exposure conditions were executed on a wafer. A light shielding plate was placed in front of the wafer stage for limiting the exposure area to 10 mm square.

5. Patterning results and discussions
5.1 Influence of irradiation beam diameter

At first, the distance between the diffusion plate and the silicon wafer was set to 45 mm, and the beam diameter of the laser beam irradiated to the diffusion plate was expanded from 4 mm to 10 and 17 mm by LBE. Before the experiments, the light intensity I on the wafer surface was measured. And the exposer time t was adjusted as the exposure dose D was almost constant using the following equation.

$$D = It \qquad (1)$$

The pattern was observed by a microscope.

Fig. 3 shows the patterns formed by a 4-mm irradiation beam. Fig. 4 shows the patterns formed by a 10-mm irradiation beam. Fig. 5 shows the patterns formed by a 17-mm irradiation beam.

Exposure dose (mJ)			
15		22.5	
30		37.5	
45		Resist Silicon wafer 20 μm	
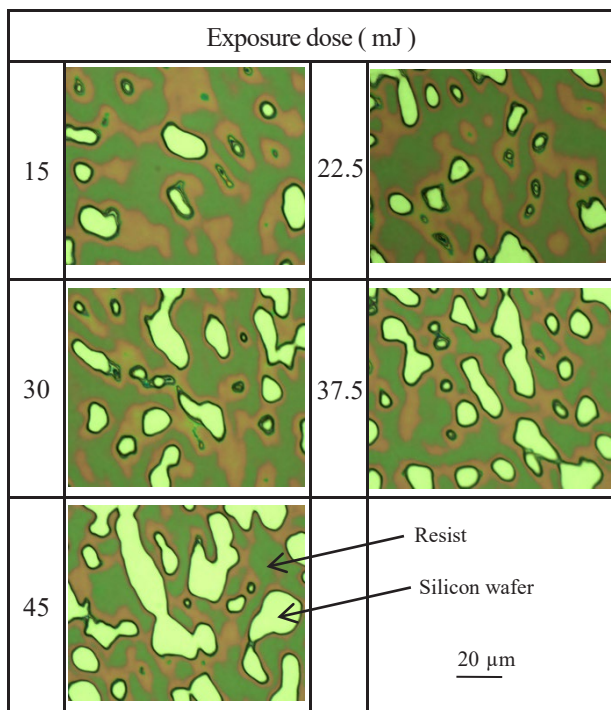
Fig. 3. Speckle patterns printed by a 4-mm irradiation laser beam.

Exposure dose (mJ)			
15		22.5	
30		37.5	
45		Resist Silicon wafer 20 μm	
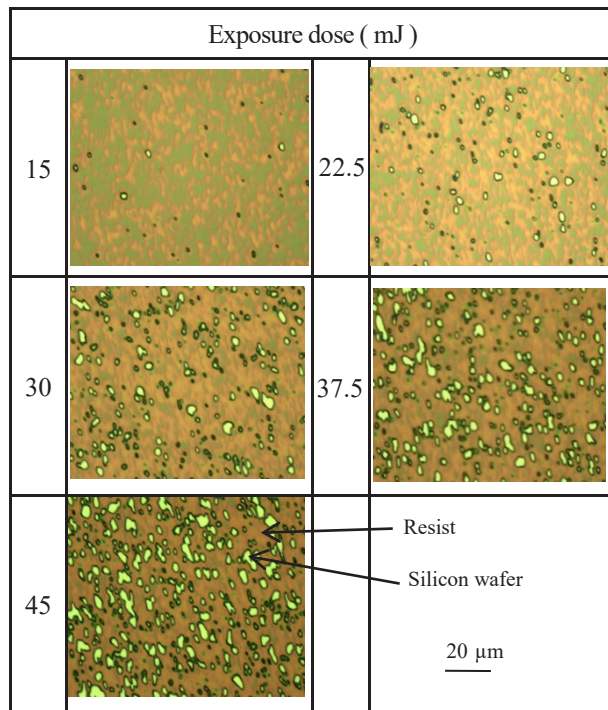
Fig. 5. Speckle patterns printed by a 17-mm irradiation beam.

Exposure dose (mJ)			
15		22.5	
30		37.5	
45		Resist Silicon wafer 20 μm	
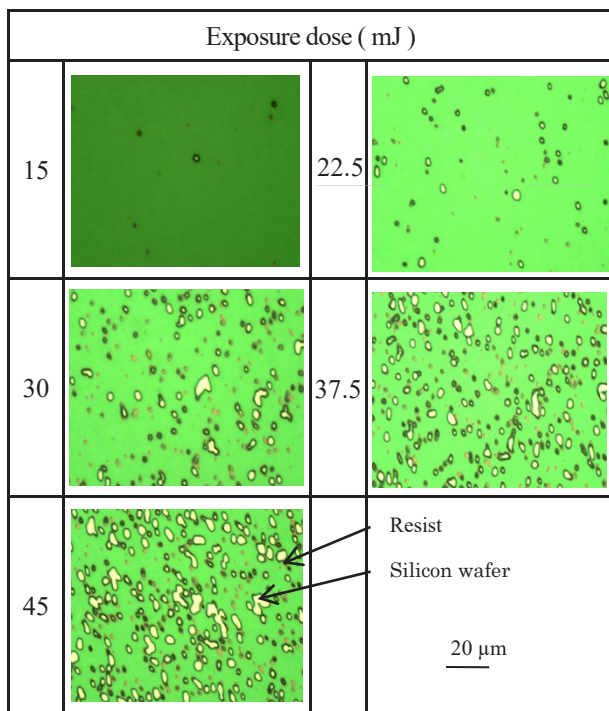
Fig. 4. Speckle patterns printed by a 10-mm irradiation beam.

The resist was dissolved in the development process in places where the speckle light intensity was sufficiently high.

The pattern sizes and numbers of patterns were measured using the image analysis software ImageJ (National Institutes of Health). The shapes of resist patterns exposed by the speckle light and developed were random ones. For this reason, each resist pattern was approximated to an ellipse using the software ImageJ. The pattern length in the major axis direction was measured as the pattern size, as shown in Fig. 6(a). The number of patterns in the measured area was counted by scanning entire images, and searching the area boundaries where the resist patterns were dissolved in a line. All the counted numbers were indicated in each pattern respectively by the software, as shown in Fig. 6(b). In the evaluation of the patern size and number of patterns, those partialy cut off by the evaluation area boundaries were not used.

Experimental results are shown next. Fig. 7 shows the relationship between the irradiation beam diameter and the average pattern size in the evaluation area of 93×112 μm. Figure 8 shows the relationship between the irradiation beam diameter and the number of patterns.
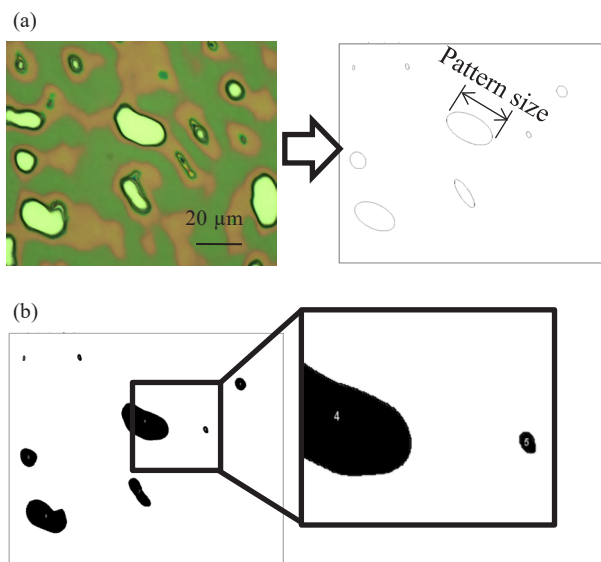
Fig. 6. Methods used for evaluating speckle pattern sizes and numbers.
(a); An example of measured speckle pattern size. The largest size was measured.
(b); An example of number counting of speckle patterns. All the counted numbers were indicated in each pattern respectively.
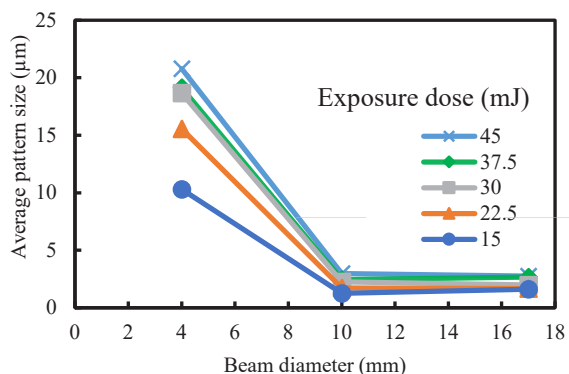
Fig. 7. Relationship between the pattern size and the beam diameter.
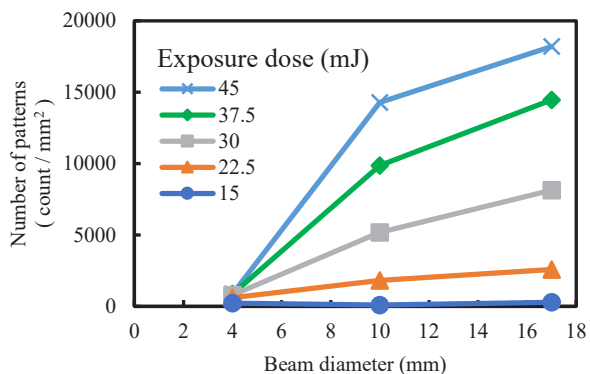
Fig. 8. Relationship between the number of patterns and the beam diameter.

It was found that pattern sizes decreased as the irradiation beam diameter was increased. Minimum patterns of approximately 1 µm were formed when the irradiation beam diameters were 10 and 17 mm and exposure dose was 15 mJ.

On the other hand, it was also found that the numbers of patterns increased as the irradiation beam diameter was increased.

Pattern sizes and numbers varied by the contrary trends each other for the irradiation beam diameter variation. Further investigation is necessary to clarify the reasons of this different variation trends of relationships shown in Figs. 7 and 8.

It was found also that both the sizes and numbers varied non-linearly. It was thought that one of the reasons of non-linear variations was the facts that the evaluation area shapes were rectangles in spite of the circular irradiation beam. However, it was considered possible to adjust the pattern size and number by controlling the irradiation diameter even if the variation trend were non-linear.

5.2 Irradiation diameter increase and proximity distance reduction between the diffusion plate and the wafer

Next, exposure experiments were carried out by setting the proximity distance between the diffusion plate and the silicon wafer to 1 mm and the irradiation beam diameter to 17 mm. The proximity distance of 1 mm was the minimum one. Using a microscope, the maximum and minimum dimensions of the formed patterns were measured in each 19 × 23 µm evaluation area.

Fig. 9 shows the patterns when the irradiation diameter was 17 mm and the proximity distance between the diffusion plate and the wafer was 1 mm. Fig. 10 shows the measurement results of the maximum and minimum pattern sizes.

By enlarging the irradiation diameter to 17mm and shortening the proximity distance between the diffusion plate and the silicon wafer to 1mm, the maximum pattern sizes increased as the exposure dose was increased. However, the minimum pattern size was reduced to 1µm or less. And, reduced minimum pattern sizes were almost fixed and did not varied. So, reasons of these facts were discussed. As a result, the reasons were considered as follows. When the exposure time was increased, pattern sizes increased. However, by the exposure time increase, new small patterns were formed one after another. For this reason, the maximum pattern sizes increased, and the minimum pattern sizes were almost fixed and did not varied.

Exposure dose (mJ)		
14.8		22.2
29.6		37
44.4		Resist Silicon wafer 2 μm
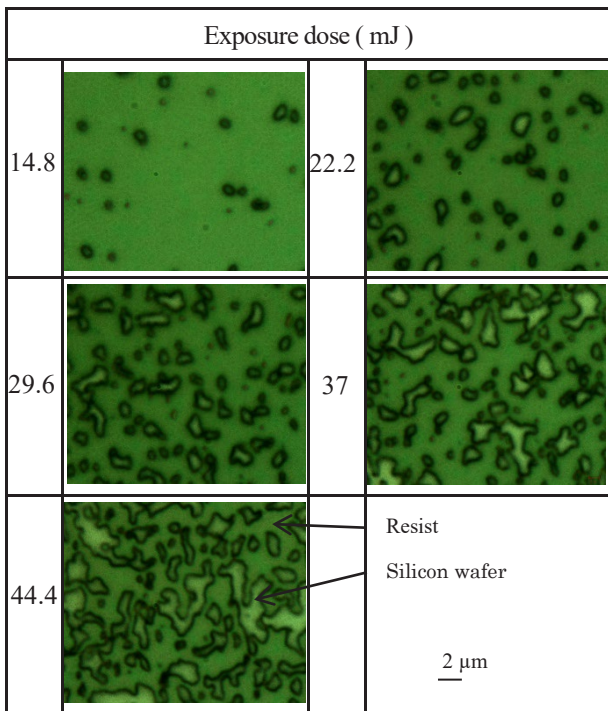
Fig. 9. Speckle patterns printed under 17-mm irradiation beam diameter and 1-mm proximity distance conditions.
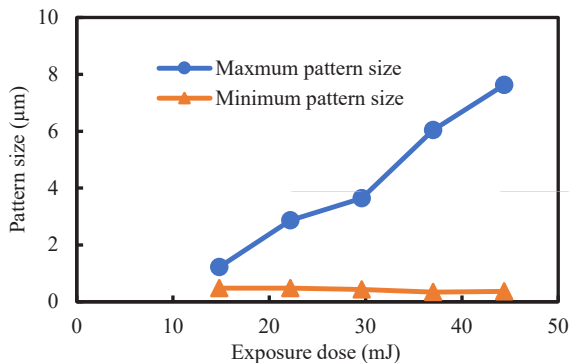
Fig. 10. Relationship between the number of patterns and the beam diameter.

5.3 Influence of diffusion plate roughness

Furthermore, influence of diffusion plate roughness was investigated. The proximity distance between the diffusion plate and the silicon wafer and the irradiation beam diameter were set to 45 mm and 4 mm, respectively. Thus, the roughness of the diffusion plate was changed to #240, #600, and #1000 in turn. The light intensity I on the silicon wafer surface was measured, and the exposure time t was adjusted using Eq. (1) so that the exposure dose D was approximately equal.

Figures 11, 12, and 13 show patterns for the diffuser plate #240, #600, and #1000, respectively. Figure 14 shows the relationship between the exposure dose and the average pattern size when the roughness of the diffusion plate was changed. Fig.

15 shows the relationship between the exposure dose and the number of patterns when the roughness of the diffusion plate was changed.

When the roughness of the diffusion plate was changed to #240, #600, and #1000 in turn, average pattern size became large when the #600 and #1000 diffusion plates were used. The reason why the average pattern sizes became large for the #600 and #1000 diffusion plates was considered as follows.

Exposure dose (mJ)		
15.8		23.7
31.6		39.5
47.4		Resist Silicon wafer 100 μm
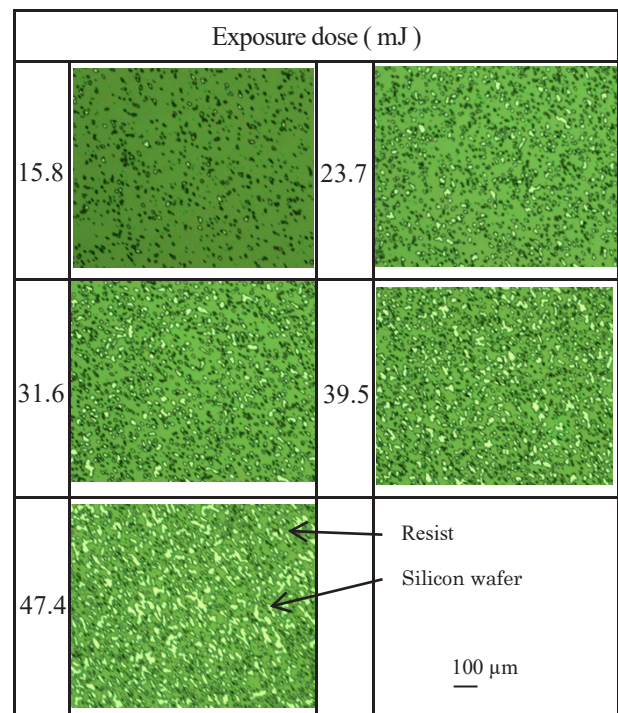
Fig. 11. Speckle patterns printed for diffuser #240.

Exposure dose (mJ)		
15.8		23.7
31.6		39.5
47.4		Resist Silicon wafer 100 μm
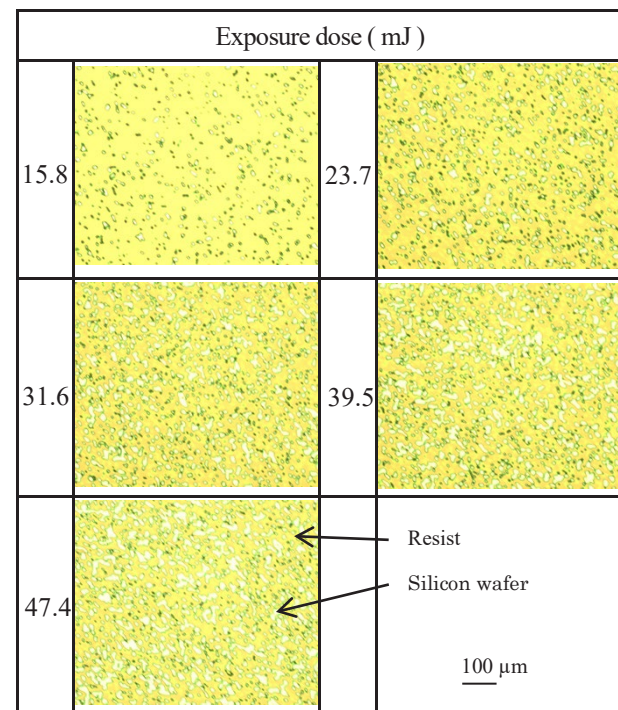
Fig. 12. Speckle patterns printed for diffuser #600.

Exposure dose (mJ)		
15.8		23.7
31.6		39.5
47.4		Resist / Silicon wafer / 100 μm
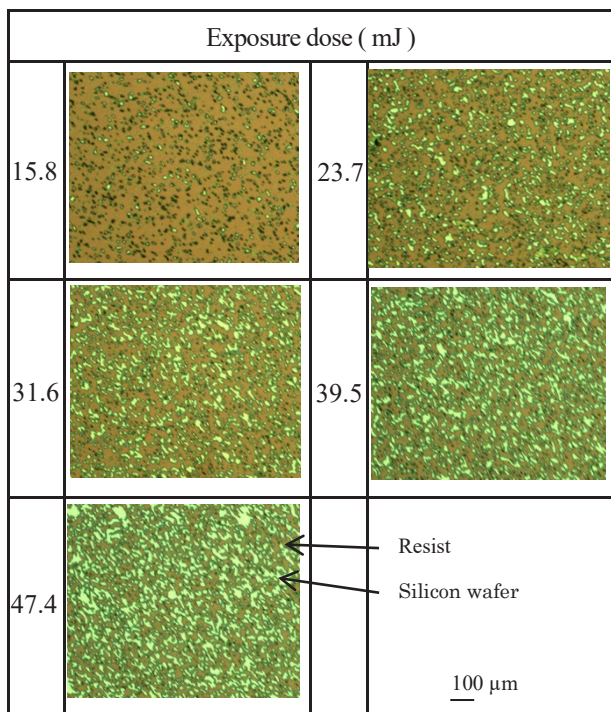
Fig. 13. Speckle patterns printed for diffuser #1000.
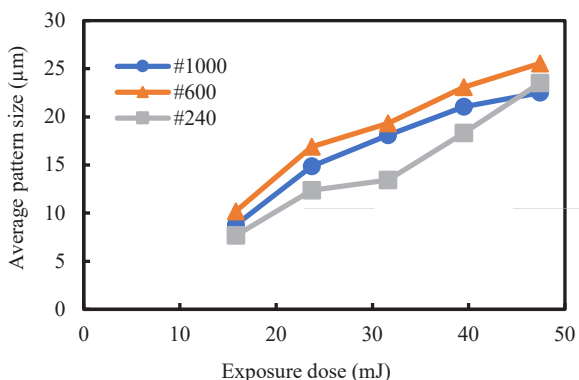
Fig. 14. Relationship between exposure dose and average pattern size due to roughness of diffusion plate.
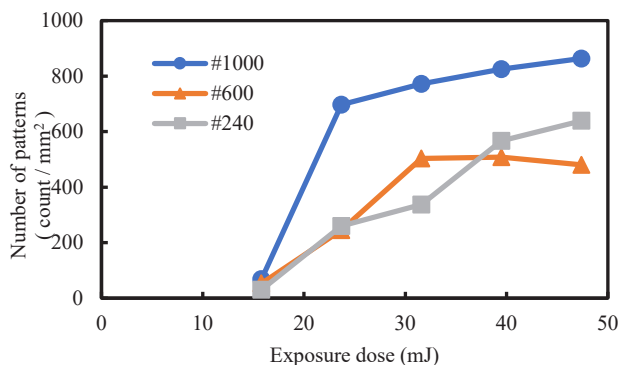
Fig. 15. Relationship between exposure dose and Number of patterns due to roughness of diffusion plate.

When resist pattern increased, small patterns combine each other, and form larger patterns. Measured number of patterns were increased for #600 and #1000 diffusion plates with large roughness. For this reason, pattern sizes became large by the combining of patterns.

6. Conclusions

Characteristics of speckle photolithography was investigated. And, influences of the irradiation beam diameter, the proximity distance between the diffuser plate and the silicon wafer, and the roughness of the diffuser plate were clarified.

When the irradiation beam diameter was expanded, the number of patterns increased. However, the resist pattern sizes decreased, and the pattern size was miniaturized to approximately 1 μm or less by expanding the irradiation beam diameter and shortening the proximity distance between the diffusion plate and the wafer.

In addition, it was found that the number of patterns increased when the roughness of the diffusion plate was large.

Although not examined this time, it was considered possible to form patterns even finer than 1 μm by changing the light source to a shorter wavelength laser and changing the diffusion plate material to the one with higher scattering property.

In the future, using the resist patterns as masking materials, surfaces of various industrial use materials may be etched. And improved surfaces with characteristic properties such as hydrophobicity and antireflection shall be obtained.

References
1. M. Sivabharathy, N. Lenin, R. R. Kanna, M. S. Dawood and A. Senthilkumar, *Mat. Today Proc.*, **49** (2022) 2048.
2. S. Martin, P. S. Brown and B. Bhushan, *Adv. Colloid Interface Sci.*, **241** (2017) 1.
3. B. L. Feng, S. Li, Y. Li, H. Li, L. Zhang, J. Zhai, Y. Song, B. Liu, L. Jiang and D. Zhu, *Adv. Mater.*, **14** (2002) 1860.
4. D. Zang, X. Xun, Z. Gu, J. Dong, T. Pan and M. Liu, *Ceram. Int.*, **46** (2020) 20328.
5. M. Karaman, N. Cʾabuk, D. Özyurt and Ö. Köysüren, *Appl. Surface Sci.*, **259** (2012) 542.
6. M.T.Z.Myint, G. L. Hornyak and J. Dutta, *J. Colloid and Int. Sci.*, (2013) 32.

7.   S. Ryu, S. Choo, H. Choi, C. Kim and H. Lee, *Appl. Suface Sci.*, (2914) 57.

8.   T. Okabe, T. Yano, K. Yatagawa and J. Taniguchi, *Microelectron Eng.*, **242-243** (2021) 111559.

9.   F. D. Nicola, P. Hines, M. D. Crescenzi and N. Motta, *Carbon*, **108** (2016) 262.

10. L. Shen, H. Du, J. Yang and Z. Ma, *Appl. Surface Sci.*, **325** (2015) 100.

11. K. Forberich, G. Dennler, M. C. Scharber, K. Hingerl, T. Fromherz and C. J. Brabec, *Thin Solid Films*, **516** (2008) 7167.

12. D. Chopra, K. Gulati and S. Ivanovski, *Mater. Today Adv.*, **12** (2021) 100176.

13. K. Jindai, K. Nakade, T. Sagawa, H. Kojima, T. Shimizu, S. Shingubara and T. Ito, *Mater. Today Proc.*, **7** (2019) 492.

14. F. Xue, J. Liu, L. Guo, L. Zhang, Q. Li and *J. Theor. Biol.*, **385** (2015) 1.

15. T. Horiuchi, Y. Imon, K. Sumimoto,

A.Yanagida and H. Kobayashi, *Key Eng. Mater.*,**813** (2019) 19.

16. M. Yamaguchi, S. Sasaki, S. Suzuki and Y. Nakayama, *J. Adhesion Sci. Techno.*, **29** (2015) 24.

17. J. Yu, S. Chary, S. Das and J. Tamelier, *Adv. Funct.   Mater.*, **21** (2011) 3010.

18. H. Shahsavan and B. Zhao, *Langmuir* (2011) 7732.

19. S. Li, H. Tian, J. Shao, H. Liu, D. Wang and W. Zhang, *ACS Appl. Mater. Interfaces,* **12** (2020) 39745.

20. J. Lettner and B. G. Zagar, *Meas. Sci. Technol.,* **24** (2013) 115204.

21. R. Balamurugan, K. Rathina, A. R. Arul, S. Inbakumar, and R. G. Sethuraman, *AIP Conf. Proc.*, **2270** (2020) 090003.

22.   H. Kobayashi, I. Tomoki, K. Oi, and T. Horiuchi, *J. Photopolym. Sci. Technol.*, **34** (2021) 35.

Metal Purifiers Specific to Lithography Related Chemicals

Robb Fang[1], Alexander Zhu[1], and Yoshiaki Yamada[2*]

[1] *Hangzhou Cobetter Filtration Equipment Co., Ltd,*
Heshang Industry Section, Xiaoshan, Hangzhou, 311265, China
[2] *Nippon Cobetter Co., Ltd.,*
1-9-10, Itachibori, Nishi-ku, Osaka city, Osaka, 545-0053, Japan
[*]y-yamada@cobetter.com

Metal impurities in lithography chemicals is critical to wafer fabrication processes. Since these trace amount of metal impurities is difficult to detect by existing in-line inspection systems, they should be removed as much as possible before wafer processing begins. Metal reduction media implemented as a filter is one strong candidate to remove metals. Ion-exchange type media is typical for metal reduction with the metal reduction mechanism of ion-exchange type media utilizing a strong acid function group such as a sulfonic group. However, lithography chemicals are very sensitive to acidic conditions. For instance, the reaction mechanism of chemically amplified resists utilizes acid catalysis and ester solvent such as PGMEA, which is very widely used as casting solvent for photo resists and underlayer coating materials may be decomposed under acid coexistence. The potential impact of acid presence in ion-exchange type media is a concern. For this reason, we have developed a new metal purifier called "Nylonpolar" to process lithography chemicals in advanced semiconductor applications. Nylonpolar consists of a nylon based membrane and carboxylic group for metal reduction. We were able to confirm that Nylonpolar doesn't decompose PGMEA solvent, while ion-exchange type media did. Also it was confirmed that Nylonpolar can remove a wide range of metal impurities. This data indicates that Nylonpolar is better metal purifier, especially for lithography process chemicals. Additionally, we have developed another different kind of metal purifier called "MGS2M". The membrane structure of this metal purifier consists of an ion-exchange type media and acid capture membrane. The acid that was released from the ion-exchange media can be captured by the second acid capture membrane. It was confirmed that MGS2M doesn't leach the acid, while a more typical ion-exchange type media did. And also, this MGS2M can remove more kinds of metal impurities than typical ion-exchange type media.

Keywords: Metal purifier, Defect reduction, Nylon membrane, Lithography friendly, Nylonpolar, Ion-exchange, MGS2M

1. Introduction

According to feature size reduction and wafer process complexities, further defect reduction from lithography chemicals is required. Especially, compared with organic impurities, metal impurities cause not only simple metal contamination, but also more complex defectivity issues such as cone defects, which are caused during the total semiconductor manufacturing process. Furthermore, in accordance with the introduction of three-dimensional structures such as 3D NAND devices and new generation transistors, thicker coating processes for burying and planarization have begun to be applied. Chemicals containing metal impurities in thick coating films can penetrate into substrates during the etching and dry ashing processes. Also, as film thickness increases, risk of metal penetration increases as well. As mentioned above, there is a chance that we will not be able to detect metal defectivity post the lithography process. Rework is impossible if metal related defects cannot be detected. Therefore, we have to remove metal impurities as much as possible before the wafer process starts.

There are several ways to remove metal impurities from lithography chemicals, including a traditional chemical engineering approach. However, introduction of metal purifier is the most convenient and the most cost-efficient method. Ion-exchange type metal purification media is well known for this application, but generally strong acid function groups, such as sulfonic group is applied to the ion-exchange media. At the same time, various kinds of chemicals used for lithography processes such as chemically amplified resists and ester solvents like PGMEA are sensitive to acid. Therefore, acid influence on the quality of lithography chemicals have to be evaluated when selecting metal purifiers and filters.

General ion-exchange type metal purifiers are widely used for metal ion reduction in various chemicals used in semiconductor manufacturing processes. However, ion-exchange type metal purifiers generally apply strong acidic groups. We know that lithography materials are generally very sensitive to acidity, and there is a risk of that acidity causing a deprotection reaction in chemically amplified resists, and the hydration decomposition of ester solvents, which are used as resist solvents. In this paper, we will attempt to demonstrate that a novel membrane purifier called Nylonpolar can drastically reduce metal contaminants in organic solvents used for chemically amplified photoresists.
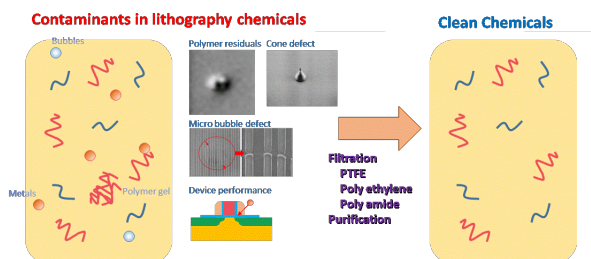
Scheme 1. Organic and metal impurities in lithography chemicals

2. Nylonpolar

2.1 Structure of Nylonpolar

As mentioned above, ion-exchange type metal purifiers are widely used in various kinds of industries and the general structure of ion-exchange type metal purifiers consist of a functional group and substrate media. Accordingly, we decided to use the same product format as general ion-exchange type metal purifiers. We then needed to fix three key technical components to develop new metal purifiers,

1. What kind of substrate media
2. What kind of functional group
3. How we should decorate the functional group onto the decided substrate.

Based on this idea, we will discuss our approach.

2.2 Metal removal performance of Nylon

Firstly, we have to decide which kind of substrate media should be applied from several possible substrate candidates. Next, we picked the key parameters to select it.

1. Media are familiar to the semiconductor industry
2. Cleanliness of the media is attainable to the leading-edge technology
3. If possible, the media can remove metal impurities.

PTFE, Polyethylene and nylon membranes are widely used in the leading-edge lithography processes of the semiconductor industry as a filtration media. Therefore, we can select metal purifier media among those three membranes. Among those three types of membranes, Nylon membrane is known for its adsorption effect of impurities and metal removal capability. We then checked metal removal performance of our Nylon membrane. The result is shown in Figure 1.

In this evaluation, a nylon coupon membrane of 47mm diameter was used. We prepared 300 ppb of Fe spiked organic solvent. The organic solvent that was used for this evaluation was a mixture of PGMEA and PGME. This OK73 thinner was provided by Tokyo Ohka Kogyo. We delivered this Fe spiked OK73 thinner by a pump system to the nylon coupon membrane, took samples after purification periodically, and measured the samples by ICP-MS (Agilent 7900). Figure 1 shows that the nylon membrane can remove the Fe ion impurity from OK73 thinner. This data indicates that the nylon membrane has the capability to remove metal impurities presented in the organic solvent. The same kind of evaluation was again carried out with the results shown in Table 1. In this evaluation, we added 300 ppb of each spiked metal in each organic solvent sample, and we measured total metal removal capacity. As shown in this table, 130μg of Fe ion was removed by the nylon filter. According to the recent paper, a more recent metal purifier coupon has shown an increased metal capacity of 250μg under the same conditions, demonstrating that our nylon has great potential as a substrate for organic solvent metal purifiers. Furthermore, Cobetter can manufacture in house nylon membranes with different pore size, thickness, and so on and we can customize the properties of nylon membrane. These results and nylon membrane availability led us to select the nylon membrane as our substrate.

In addition, Table 1 shows that metal removal performance depends on the solvent. Removal performance for PGME and IPA is relatively low, while for PGMEA is higher. Though we need to investigate more, we may assume that metal removal performance in protonic organic solvents such as IPA and PGME is lower, while it is higher for ester solvents such as PGMEA.
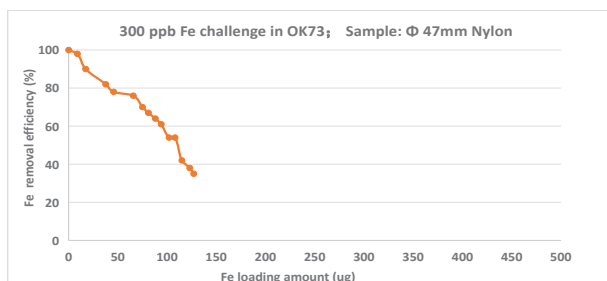

Figure 1. Metal removal test of Nylon membrane

Table 1. Removal capacities of metal ion species in organic solvent by nylon membrane

Metal species	PGME	IPA	PGMEA
Na	0.0	0.3	54
Fe	No data	54	130

2.3 Functional group of Nylonpolar

As mentioned above, ion-exchange metal purifiers are widely used in various industries, and generally sulfonic acid groups for strong cationic type ion-exchange are applied to ion exchange media. At the same time, several kinds of chemicals used for lithography processes are very sensitive to acid existence. For instance, chemically amplified photoresists have been used since the KrF lithography generation utilize acid catalysis. If undesired acid that originates from a metal purifier exists in chemically amplified photoresist, it may cause undesired chemical reactions, causing a pattern size change and defectivity. Also, ester organic solvents like PGMEA, which are widely used as casting solvents, can decompose through a hydration reaction by an acid catalyst. This also impacts the quality of lithography chemicals. Therefore, we must pay attention to the acid originated from metal purifiers when selecting the functional group.

Consequently, it is very critical to know the influence of the acid on the lithography related chemicals. We mentioned the two examples above. As resist polymer is not accessible for this evaluation, we investigated the effect of acid existence on the decomposition of PGMEA instead.

Table 2. Decomposition of PGMEA solvent under various kinds of acid sources

Function	Media	Test Conditions (24 hr at RT)	Analysis	Decomposed concentration
H2SO4	Solution	PGMEA (10%, 100mL) H2SO4 (10%, 20mL)	detected	950.8mg/L
HCl	Solution	PGMEA (100mL) HCl (5%, 20mL)	detected	307.3mg/L
COOH typed	Purifier	PGMEA (10%) 100 pieces of Φ47mm coupon	No detected	——
General ion-exchange	Purifier	PGMEA (10%) 100 pieces of Φ47mm coupon	detected	65.8mg/L

The results are shown in Table 2. In this evaluation, we prepared 4 kinds of acid sources. Two kinds of acids are general inorganic acids, H_2SO_4 and HCl, while another two kinds of acid come from metal purifiers. Firstly, we prepared 100 mL of PGMEA solvent. We added 20mL of 10% H_2SO_4 aqueous solution or 20mL of 5% HCl aqueous solution. For the metal purifier test, we used the general strong cationic typed ion-exchange media, branded as Iongard by Cobetter, and a newly developed nylon membrane that is grafted with carboxylic acid function group. One hundred pieces of 47mmΦ coupons were soaked in 100 ml of PGMEA solvent. We stored these 4 kinds of samples for 24 hours at room temperature. Each of the evaluation conditions are shown in Table 2. As shown in Table 2, in the case of only carboxylic acid on the nylon membrane, a decomposition product of PGMEA wasn't detected.

In this evaluation, PGMEA solvent is metal ion free. Therefore, the concentration of the acid that is released from the function group on an ion-exchange media were assumed to be low. However, some decomposition of PGMEA was confirmed. It indicates that even the exposure of PGMEA solvent to an ion-exchange media caused the acid released into PGMEA. As this is just one data point, to show that this new developed metal purifier is friendly with chemicals for lithography, we need further investigation. However, this data indicates that nylon membrane with carboxylic function group has lower risk on the influence of the acid that originates from metal purifiers. Therefore, we named Nylonpolar for this membrane.

Next, we need to decorate the carboxylic group onto a nylon membrane. We can choose several ways to graft it, but for cleanliness and functionality, we selected radiation grafting polymerization. Generally, we have two ways to initiate grafting polymerization. One is chemically initiated, while another is radiation initiated. On the point of metal purifier cleanliness, we selected radiation initiated grafting polymerization. The reason is that if chemicals used to initiate reaction remain inside metal purifier, we would need remove them to avoid contamination. Radiation initiation doesn't have such a concern.

Through these activities, we were able to fix the substrate media, functional group and surface modification process. This nylon membrane modified with a carboxylic group by radiation grafting modification reaction is called Nylonpolar.

2.4 Metal removal performance of Nylonpolar

We described how to establish the new metal purifier called Nylonpolar in previous section. Then, we checked metal removal performance of Nylonpolar. In order to briefly compare metal performance, we repeated the same metal removal tests as carried out in figure 1. The results are shown in Figure 2. At lower Fe loading input levels, Nylonpolar demonstrated higher Fe metal removal efficiency and also showed higher metal removal capacity. Thus, compared with the general nylon membrane, newly developed Nylonpolar showed higher metal purifier performance.

Next, we tested metal removal efficiency of 28 kinds of metal species. The results are shown in Figure 3. In this evaluation, 10ppb of each metal species was used to spike the PGMEA solvent, then we measured the remaining metal impurities after Nylonpolar purification. From this test, we calculated removal efficiency. As shown in Figure 3, most of the metal ions were removed by Nylonpolar. This data indicates that Nylonpolar works for removing most of the typical metal impurities that are discussed in lithography processes.
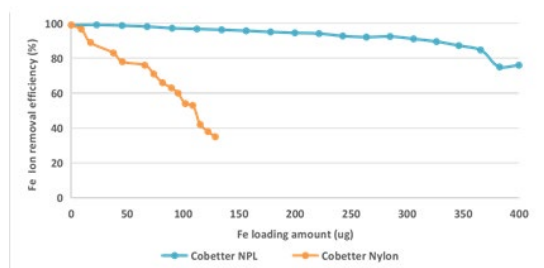
Fig. 2 Metal removal performance of Nylonpolar
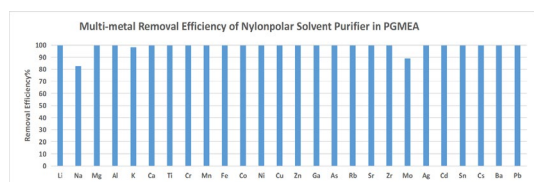
Figure 3 Metal removal efficiency of Nylonpolar

3. MGS2M

3.1   Acid concentration from an IEX media

In addition to Nylonpolar, we have developed another kind of metal purifiers which is called MGS2M to reduce the risk of imparting any

influence on lithography related materials and their stability. The concept of a new metal purifier is to add capability to capture the acid generated by metal purifier by another media right after metal purifier. In other words, it consists of double layers, a metal removal layer and an acid removal layer. We measured directly the acid concentration to know how much the second acid removal layer reduced the concentration of the acid released from an ion-exchange media via titration. We used potentiometric titration with NaOH aqueous solution to quantify the generated acid. Firstly, in order to measure the metal reduction performance and the acid concentration from metal purifiers at the same time, we prepared metal spiked PGMEA solvent. It was prepared by spiking 29 kinds of metal impurities into pure PGME solvent. Usually, standard chemical agents used as metal sources are metal compounds of metal and acidic anion such as metal nitrate. Therefore, metal spiked PGMEA solvent showed weak acidity. After that, we purified this solvent by passing it through metal purifiers. The metal purifier device used was a 4-inch capsule package with surface area of membrane, 1200 cm^2. The capsule package and the shell was made of HDPE, and the flow rate was 40ml/min. We took the initial 200mL of PGMEA after purification as a measurement sample. A Metrohm 916 autotitrator is used in potentiometric titration measurement. Titration was carried out by 2mM NaOH aqueous solution. 10 mL of Ethanol was added to 10 mL of PGMEA solvent after purification to improve the metal stability in PGMEA solvent.

The NaOH used in titration at 3 kinds of sample conditions are shown in Table 3, with each test conducted in duplicates. Titration volume for Ethanol was 2.4 and 0.0 ml. As it can be assumed to be neutral, these titration volumes were considered reasonable given the experimental error. Next, the titration volume for the metal spiked PGMEA solvent is slightly higher than that of Ethanol because of the influence of acidity in standard metal agents. The volume was 8.5 and 6.1mL respectively. We then measured metal spiked PGMEA after purification using our general ion-exchange typed media. The required volume was higher than 50mL. This result clearly shows that the exposure of PGMEA solvent to an ion-exchange typed media increases the acidity of PGMEA. As mentioned in the previous section, the exposure of an ion-exchange typed media to PGMEA decomposed the PGMEA compound. This data also shows the increased acid in PGMEA. In this evaluation, as we

used metal spiked PGMEA solvent, we can assume that the concentration of the acid released from an ion-exchange media is higher than the case without spiking metal in PGMEA. Both cases are a risk for lithography chemicals which are sensitive to the acid.

Table 3   NaOH volume for acid titration

Solvent	Required NaOH volume mL
Ethanol	2.4, 0.0
Spiked PGMEA in Ethanol	8.5, 6.1
After purification by IE media	>50.0, >50.0

3.2 Capture the acid

The scheme of an ion-exchange mechanism is shown in Figure 4. Metal impurity diffuses in PGMEA solvent. In this figure, Na metal ions diffuse in PGMEA solvent, and finally are captured by sulfonic group. When the sulfonic group captures the metal impurities, proton is released at the same time as the exchange reaction. This is the acid that we are discussing in this paper. In order to neutralize the influence of the acid on the stability and the performance of lithography related materials, we need to remove this acid immediately.
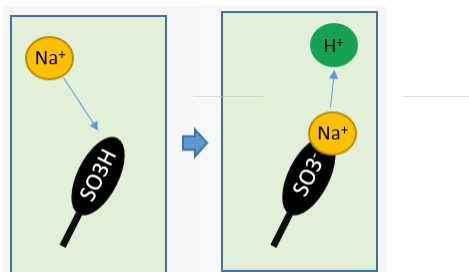
Figure 4.   Mechanism of ion-exchange reaction

Previous sections introduced Nylonpolar, nylon membrane with carboxylic acid, showed that this membrane didn't decompose in PGMEA solvent. We subsequently evaluated an alternative idea, which implements another media with a second layer to remove the released acid effectively and immediately with the original ion-exchange approach. It is essentially a kind of double-layer metal purifier consisting of a metal removal layer and an acid removal layer.
The new membrane structure in Figure 5 shows a blue layer and a green layer. The blue layer is an ion-exchange media, while the green one is newly developed media which can remove the released acid. The application chemical flows first through the blue layer and followed by the green one. In

Figure 5, the flow proceeds from top to bottom. The proton that was released from the ion-exchange function, when metal impurity is removed, is transported downstream and removed by the green layer. In order to confirm this idea, we measured the acid concentration in the same way as we did above.
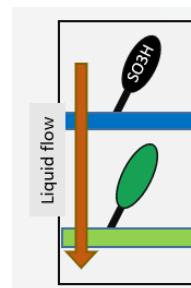
Figure 5.   Membrane structure concept

New data is shown in bold in Table 4. It was confirmed that the acid concentration decreased from > 50mL to 6.0 and 3.6 mL by implementing the additional acid removal layer. Also, the volume of NaOH aqueous solution required for neutralization is lower than spiked PGMEA in Ethanol in Table 4. It is concluded from the reduced titration amounts of NaOH used in titration that MGS2M can remove the acid originated from the standard reagent for metal impurities. We so named this new metal purifier MGS2M.

Table 4   NaOH volume for acid titration

Solvent	Required NaOH volume mL
Ethanol	2.4, 0.0
Spiked PGMEA in Ethanol	8.5, 6.1
After purification by IE media	>50.0, >50.0
After purification by MGS2M	**6.0, 3.6**

3.3 Metal removal performance.

Next, we confirmed metal removal performance of the newly developed MGS2M. Metal concentration was measured by Agilent ICP-MS 7900. The result is shown in Figure 6.
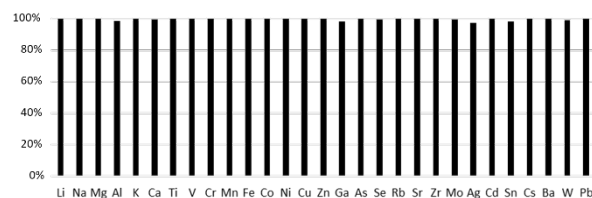
Figure 6.   Metal removal efficiencies of MGS2M

Metal removal efficiency for each kind of metal species was higher than 97%.

Next, in order to compare metal removal efficiency with ion-exchange typed media, we tested it against ion-exchange typed media. The result is shown in Figure 7. In this evaluation, 10ppb of 29 kinds of metal impurity are spiked into PGMEA solvent and the MGS coupons are soaked in this solvent. After that, metal impurities remaining in PGMEA solvent were measure by ICP-MS. The result shows that metal removal efficiency of MGS and Nylonpolar isn't as high for some kind of metal species. In contrast, Figure 6 shows that metal removal efficiency is kept high for all kinds of metals indicating that the implementation of the second layer can also improve the metal removal efficiencies.
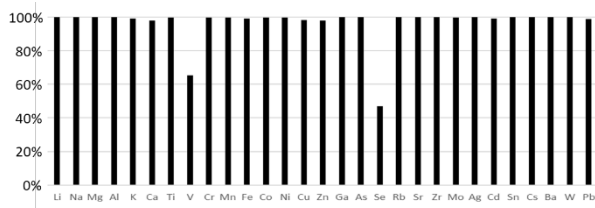
Figure 7.   Metal removal efficiency of   ion-exchange typed media

4. Conclusion

Our study confirmed that the acidic group generated from an ion-exchange type metal purifiers may negatively impact lithography materials and processes.   The new metal purifiers, Nylonpolar and MGS2M, can suppress the acid generation. These metal purifiers also demonstrated high metal removal efficiencies and also reduced influence from the acid.

5. Acknowledgement

References

1. Tetsu Kohyama, Fumiya Kaneko, Saksatha LY, James Hamzik, Jad Daber, and Yoshiaki Yamada. *Proc. SPIE* 10146.

2. Aiwen Wu, Tetsu Kohyama et a. *Proc. SPIE* 10586.

3. Toru Umeda, Shusaku Daikoku, et al., *Proc. SPIE* 10146.

4. Tetsu Kohyama, Fumiya kaneko, Alketa Gjoka, and Jad Jaber, *Proc. SPIE* 10960.

5. Tetsu Kohyama, Proc. SPIE 8325.

6. Toru Umeda, Shinichi Sugiyamada, Takashi Nakamura, Makoto Momota, Michael Sevegney, Shuichi Tsuzuki, and Toru Numaguchi, Proc. SPIE 8325.

7. Toru Umeda, Fumitake Watanabe, Shuichi Tsuzuki, and Toru Numaguchi, Proc. SPIE7520.

8. Toru Umeda, Shuichi Tsuzuki, and Toru Numaguchi, Proc. SPIE 7273.

9. Lucia D'Uzo, Toru Umeda, Takehito Mizuno, Atsushi Hattori, Amamauth Singgh, Rajan Beera, Philippe Foubert, and Waut Drent, Proc. SPIE 11612.

10.   Hassan Ait-Haddou, Timothy McKeon, Katsuhiko Tokuno, Jeambo Yang, Tomoyuki Takakura, and Makonnen Payne, SPCC2020.

11.   Siddarth Sampath, Kusum Maharjan, Anthony Ozzelo, and Ashutosh Bhabhe, SPCC 2020.

JOURNAL OF PHOTOPOLYMER SCIENCE AND TECHNOLOGY
Volume 36, Number 5, 2023